2015

Engineering of Polyamidoamine Dendrimers for Cancer Therapy

Leyuan Xu
Virginia Commonwealth University

ENGINEERING OF POLYAMIDOAMINE DENDRIMERS FOR CANCER THERAPY

A dissertation submitted in partial fulfillment of the requirements for the degree of

Doctor of Philosophy at Virginia Commonwealth University

by

Leyuan Xu

M.S., Virginia Commonwealth University, 2013

Director: Hu Yang, Ph.D.

Associate Professor, Biomedical Engineering

Virginia Commonwealth University

Richmond, Virginia

May, 2015

Acknowledgment

I would like to express my deep gratitude to my academic advisor, Dr. Hu Yang, for his extraordinary patience, mentoring, support and encouragement. I would like to give special thanks to Dr. Andrew Yeudall, who also teaches at daily basis during the past four years. I would like to thank Dr. Kristoffer Valerie, who gave me great opportunities and training working on different animal projects. I also would like to thank Dr. Rebecca L. Heise and Dr. Ning Zhang who gave many suggestions on my research projects serving as my advisory committee members.

I would like to thank all of my colleagues, current and past for making the lab a home away from home. I would like to particularly thank Dr. Olga Zolotarskaya, Dr. Quan Yuan, Jingfei Tian, Donald Aduba, Michael Lancina and Natasha Sheybani as well as Xu Wang, Xia-Juan Xia, Mary Tokarz, Dr. Ming Sun, Dr. Jinyang Cai, and Dr. Weihua Chen for their help.

Lastly but not the least, I would like to thank my friends and family for supporting me throughout this journey. Specially, I want to thank my wonderful girlfriend, Hao, for your sharing, caring and support. To my dear parents, especially my mom, thank you for your unconditional love, care, and prayers. You have made every possible opportunity to my life. I love you, mom and dad, and I will keep making you all proud.

Table of Contents

List of Tables

List of Figures

Abbreviations

PAMAM	Polyamidoamine dendrimer
G4	Polyamidoamine dendrimer generation 4
G4.5	Polyamidoamine dendrimer generation 4.5
DEN	Polyamidoamine dendrimer generation 4
FA	Folic acid
G4-FA	FA-coupled G4
FITC	Fluorescein isothiocyanate
FITC-G4	FITC-labeled G4
FITC-G4-FA	FITC-labeled, FA-coupled G4
NIR	Near-infrared fluorescent dye 800CW
NIR-G4	NIR-labeled G4
NIR-G4-FA	NIR-labeled, FA-coupled G4
PEG	Polyethylene glycol
FR(α)	Folate receptor (α)
GFP	Green fluorescent protein
YFP	Yellow fluorescent protein
pGFP	pMAX-GFP plasmid
pYFP	pCEFL-YFP plasmid
ACTB	β-actin
VEGFA	Vascular endothelial growth factor A
siRNA	Small interfering RNA
siVEGFA	siRNA against vascular endothelial growth factor A

siGFP	siRNA against green fluorescent protein
RNAi	RNA interference
NA	No addition
i.v.	Intravenous
i.t.	Intratumoral
s.c.	Subcutaneous
MW	Molecular weight
MWCO	Molecular weight cutoff
CPT	Camptothecin
DMEM	Dulbecco's modification of Eagle's medium
H&E	Hematoxylin and eosin
IHC	Immunohistochemistry
DMSO	Dimethyl sulfoxide
ELISA	Enzyme-linked immunosorbent assay
PBS	Phosphate buffer solution
HPLC	High-performance liquid chromatography
^{1}H NMR	Proton nuclear magnetic resonance
DLS	Dynamic light scattering
PCR	Polymerase chain reaction
UV-Vis	Ultraviolet-visible
N/P ratio	Nitrogen to phosphate ratio
SD	Standard deviation
SEM	Standard error of the mean
CuAAC	Copper-catalyzed alkyne-azide cycloaddition
RAW	RAW264.7 macrophages
DIBO	Dibenzocyclooctyne alkyne
NP(s)	Nanoparticle(s)
DAPI	4,6-diamidino-2-phenylindole
DMSO	Dimethyl sulfoxide
EDC	1-ethyl-3-[3-dimethylaminopropyl] carbodiimide hydrochloride

NHS	*N*-hydroxysuccinimide
HNSCC	Head and neck squamous cell carcinomas
PI	Propidium iodide

Abstract

ENGINEERING OF POLYAMIDOAMINE DENDRIMERS FOR CANCER THERAPY

by Leyuan Xu

A dissertation submitted in partial fulfillment of the requirements for the degree of Doctor of Philosophy at Virginia Commonwealth University

Virginia Commonwealth University, 2015

Major Director: Hu Yang, Ph.D., Associate Professor, Biomedical Engineering

Dendrimers are a class of polymers with a highly branched, three-dimensional architecture comprised of an initiator core, several interior layers of repeating units, and multiple active surface terminal groups. Dendrimers have been recognized as the most versatile compositionally and structurally controlled nanoscale building blocks for drug and gene delivery. Polyamidoamine (PAMAM) dendrimers have been most investigated because of their unique structures and properties. Polycationic PAMAM dendrimers form compacted polyplexes with nucleic acids at physiological pH, holding great potential for gene delivery.

Folate receptor (FRα) is expressed at very low levels in normal tissues but expressed at high levels in cancers in order to meet the folate demand of rapidly dividing cells under low folate conditions. Our primary aim was to investigate folic acid (FA)-conjugated PAMAM dendrimer generation 4 (G4) conjugates (G4-FA) for targeted gene delivery. The in vitro cellular uptake and transfection efficiency of G4-FA conjugates and G4-FA/DNA polyplexes were investigated in Chapter 4. It was found the cellular uptake of G4-FA conjugates and G4-FA/DNA polyplexes was in a FR-dependent manner. Free FA competitively inhibited the cellular uptake of G4-FA

conjugates and G4-FA/DNA polyplexes. G4-FA/DNA polyplexes were preferentially taken up by FR-positive HN12 cells but not FR-negative U87 cells. In contrast, the cellular uptake of G4 dendrimers and G4/DNA polyplexes was non-selective via absorptive endocytosis. G4-FA conjugates significantly enhanced cytocompatibility and transfection efficiency compared to G4 dendrimers. This work demonstrates that G4-FA conjugates allow FR-targeted gene delivery, reduce cytotoxicity, and enhance gene transfection efficiency.

The in vivo biodistribution of G4-FA conjugates and anticancer efficacy of G4-FA/siRNA polyplexes were investigated in Chapter 5. Vascular endothelial growth factor A (VEGFA) is one of the major regulators of angiogenesis, essential for the tumor development. It was found G4-FA/siVEGFA polyplexes significantly knocked down VEGFA mRNA expression and protein release in HN12 cells. In the HN12 tumor-bearing nude mice, G4-FA conjugates were preferentially taken up by the tumor and retained in the tumor for at least 21 days following intratumoral (i.t.) administration. Two-dose i.t. administration of G4-FA/siVEGFA polyplexes significantly inhibited tumor growth by lowering tumor angiogenesis. In contrast, two-dose i.t. administration of G4/siVEGFA polyplexes caused severe skin lesion, presumably as a result of local toxicity. Taken together, this work shows great potential for the use of G4-FA conjugates in targeted gene delivery and cancer gene therapy.

We also explored polyanionic PAMAM dendrimer G4.5 as the underlying carrier to carry camptothecin (CPT) for glioblastoma multiforme therapyin Chapter 6. “Click chemistry was applied to improve polymer-drug coupling reaction efficiency. The CPT-conjugate displayed a dose-dependent toxicity with an IC_{50} of 5 μM, a 185-fold increase relative to free CPT, presumably as a result of slow release. The conjugated CPT resulted in G_2/M arrest and cell death while the dendrimer itself had little to no toxicity. This work indicates highly efficient “click chemistry allows for the synthesis of multifunctional dendrimers for sustained drug delivery.

Immobilizing PAMAM dendrimers to the cell surface may represent an innovative method of enhancing cell surface loading capacity to deliver therapeutic and imaging agents. In Chapter 7, macrophage RAW264.7 (RAW) was hybridized with

PAMAM dendrimer G4.0 (DEN) on the basis of bioorthogonal chemistry. Efficient and selective cell surface immobilization of dendrimers was confirmed by confocal microscopy. It was found the viability and motility of RAW-DEN hybrids remained the same as untreated RAW cells. Furthermore, azido sugar and dendrimer treatment showed no effect on intracellular AKT, p38, and NFκB (p65) signaling, indicating that the hybridization process neither induced cell stress response nor altered normal signaling. This work shows the feasibility of applying bioorthogonal chemistry to create cell-nanoparticle hybrids and demonstrates the noninvasiveness of this cell surface engineering approach.

In summary, these studies indicate surface-modification of PAMAM dendrimer G4 with FA can effectively target at FR-positive cells and subsequently enhance in vitro transfection efficiency and in vivo gene delivery. G4-FA conjugates may serve as a versatile targeted gene delivery carrier potentially for cancer gene therapy. PAMAM dendrimers G4.5 may serve as a drug delivery carrier for the controlled release of chemotherapeutics. The immune cell-dendrimer hybrids via bioorthogonal chemistry may serve as an innovative drug and gene delivery carrier potentially for cancer chemotherapy. Taken together, engineering of PAMAM dendrimers may advance anticancer drug and gene delivery.

Chapter 1

Background and Significance

1.1 Head and neck squamous cell carcinoma (HNSCC)

Cancer, also known as a malignancy, is an abnormal growth of cells. In the body, normal cells grow, divide, and die in an orderly way. In contrast, cancer cells grow out of control. Instead of undergoing a normal cell cycle, cancer cells continue to grow and divide to make new abnormal cells. Moreover, cancer cells can invade other tissues. Cells become cancer cells mainly because of DNA damage or mutation. When DNA is damaged, normal cells either repair the damage or die. However, cancer cells do not repair the damaged DNA and do not die as they should. Instead, the cancer cells divide to make daughter abnormal cells, which contain the same damaged DNA as their parental cells do. Generally, the cancer cells form a tumor. Over time, tumors can replace normal tissue and push it aside. Some cancers, like leukemia, rarely form tumors. However, those abnormal white blood cells grow as they circulate through tissues.

To date, there are more than 100 types of cancer, including breast cancer, skin cancer, lung cancer, colon cancer, lymphoma, etc. Head and neck cancer includes malignancies arising in the mucosal surfaces of the oral cavity, pharynx, larynx, paranasal sinuses, and nasal cavity, and is generally referred to as head and

neck squamous cell carcinoma (HNSCC). HNSCC is estimated to have 53,640 new cases in US in 2013, accounting for 3% of all cancers [49]. HNSCC is the sixth most prevalent cancers in mankind, and presents high morbidity and low rates of survival [22]. Risk factors for HNSCC include exposure to tobacco and alcohol. At least 75 percent of head and neck cancers are caused by tobacco and alcohol use [179]. Infection with cancer-causing types of human papillomavirus (HPV) is another risk factor for some typescertain types of HNSCC. Particularly, such as oropharyngeal cancers involve the tonsils or the base of the tongue [70, 2, 27]. In the US, the incidence of oropharyngeal cancers caused by HPV infection is increasing, whereas the incidence of oropharyngeal cancers related to other causes is falling [27]. Other risk factors for HNSCC include paan (betel quid), mate, preserved or salted foods, oral health, occupational exposure, radiation exposure, Epstein-Barr virus infection, and ancestry [87, 212, 164, 79, 176, 72].

Treatment of HNSCC frequently requires multi-modality intervention involving surgical, medical, and radiation therapy. With improvements in radiation therapy and chemotherapy, organ-conserving treatments are increasingly employed to preserve speech, swallowing, and other regional functions [124]. These conventional therapies have been used for decades in HNSCC but they have limitations. Surgery may cause disfigurement, change patient's ability to chew, swallow, and talk, all of which reduce patient quality of life. After a laryngectomy or other surgery in the neck, parts of the neck and throat may feel numb because nerves have been cut. After removal of lymph nodes in the neck, the shoulder and neck may become weak and stiff. Radiation may cause redness, irritation, and sores in the mouth, a dry mouth or thickened saliva, difficulty in swallowing, changes in taste, nausea, loss of taste, and earaches [182]. Concurrent chemotherapy and radiation in HNSCC likely provides a better outcome in terms of local disease control and organ preservation compared to radiation alone or radiation plus induction chemotherapy, but concurrent therapy also leads to more severe toxicity [57]. Patients may also experience other side effects including dysphagia, xerostomia, radiation dermatitis, hematologic toxicity, neurotoxicity and/or ototoxicity, moist desquamation, nausea or vomiting, fever, weight

loss, fatigue, pneumonia and osteoradionecrosis, combinations of which may lead to termination of treatment or even death [264]. The toxicities of conventional therapies are in large part due to their non-selective nature. Molecular targeted therapies are therefore in development with the goal of developing selective approaches to inhibit the growth of HNSCC cells.

1.2 Anticancer drugs

Anticancer drugs can be broadly divided into three generations (Figure 1.1). The first-generation anticancer drugs are traditional anticancer chemotherapeutics, which mainly block DNA replication and cell division. These anticancer drugs have proved to be potent in treating some cancers, but they have severe side effects. These anticancer drugs can cause substantial toxicity to both normal cells and cancer cells. Therefore, they compromise not only the rapidly dividing cells of hematopoietic system, the gut and hair follicles, but also the function of post-mitotic tissues such as the heart muscle and peripheral nerves. The second-generation anticancer drugs target signaling intermediates that contribute to cancer growth. These signaling intermediates are oncoproteins that are primary products of gene fusions, gain-of-function mutations or overexpressed oncogenes. These anticancer drugs have shown to increased specificity and hereby reduce side effects, but they have limitations such as the development of acquired drug resistance, which often leads to relapse. The third-generation anticancer drugs are designed to target cellular machineries. Although they are not directly involved in DNA replication or cell division, they are essential for tumor growth and survival. However, a lack of absolute specificity for cancer cells will inevitably cause side effects [46].

Antibody-drug conjugates (ADCs) are a new class of highly potent biopharmaceutical drug, and become now one of the most active areas in anticancer drug development [46]. Brentuximab vedotin (trade name: Adcetris, marketed by Seattle Genetics and Millennium/Takeda) and ado-trastuzumab emtansine (trade name:

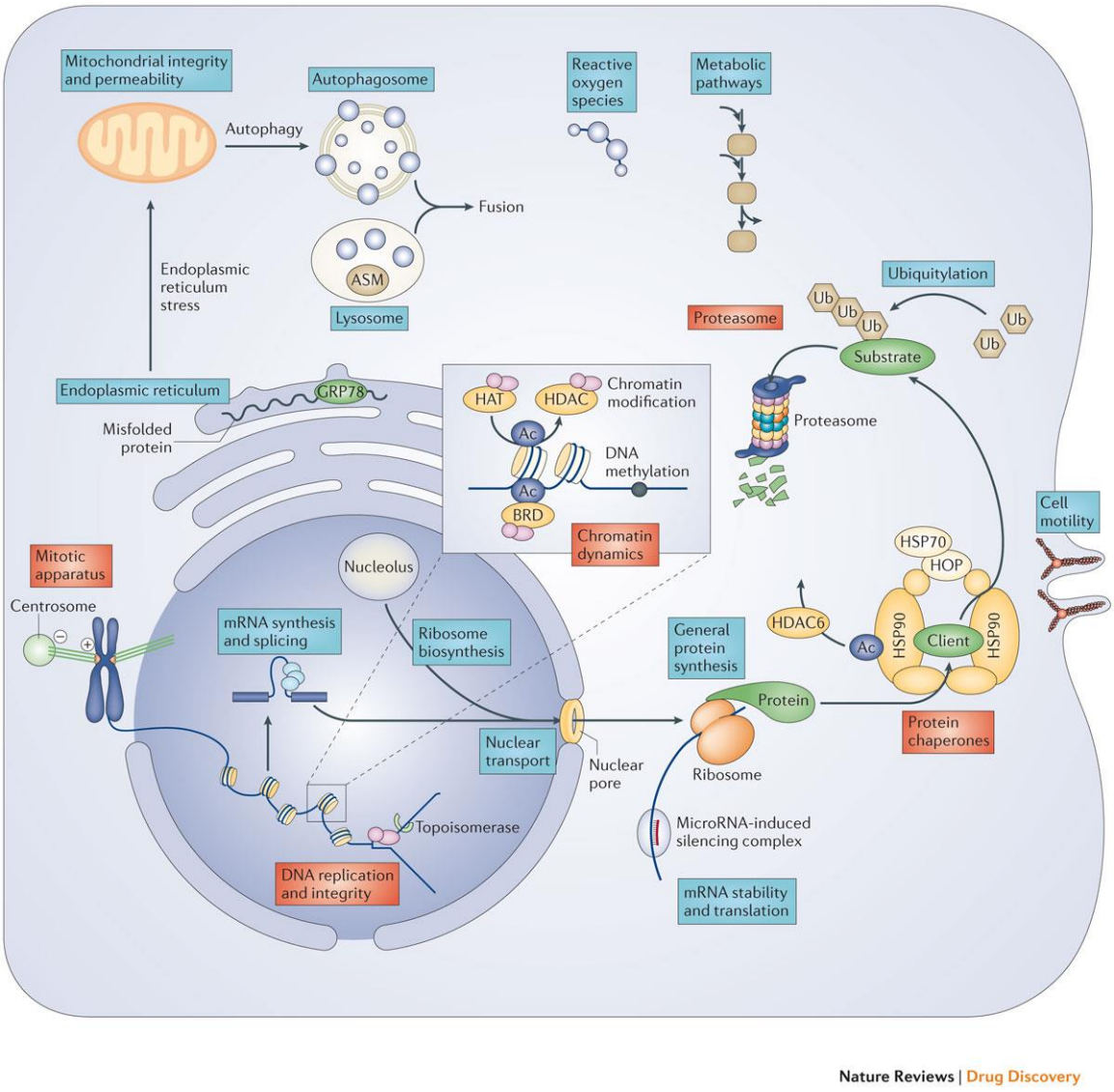

Figure 1.1: Cellular multicomponent machineries as current and future targets for anticancer drugs.
Current targets and future targets are illustrated in red and blue boxes, respectively. (Reproduced reference [46]. Copyright 2014 Macmillan Publishers Ltd.)

Kadcyla, marketed by Genentech and Roche) are marketed ADCs. Brentuximab vedotin is a conjugate of a CD30 specific antibody and five units of the antimitotic agent monomethyl auristatin E (MMAE) via a cathepsin cleavable linker. The peptide-based linker between the CD30 antibody and the MMAE is stable under physiologic conditions, helping prevent toxicity to healthy cells and ensure dosage efficiency. The antibody of brentuximab vedotin binds to CD30, which often occurs on tumor cells but rarely on normal tissues. Once bound, brentuximab vedotin is selectively taken up by tumor cells and internalized through endocytosis. The peptide-based linker is cleaved in lysosomes, which contain lysosomal cysteine proteases, particularly cathepsin B. MMAE is then rapidly released from the conjugate within the tumor cell. Brentuximab vedotin has showed promising results in Phase II trials for the treatment of patients with Hodgkin disease and patients with anaplastic large cell lymphoma [59, 316]. Ado-trastuzumab emtansine is a conjugate of a HER2 specific antibody and a cytotoxic maytansinoid (DM1) via a short heterobifunctional crosslinker. Ado-trastuzumab emtansine has shown clinical benefits for patients who had previously shown tumor progression with trastuzumab treatment [185, 268]. This approach combines the broad activity of first-generation anticancer drugs with an enhanced specificity for tumor cells [46]. However, severe side effects and drug resistance may arise for ADCs. Besides most common adverse reactions such as digestive distress, balding, digestive distress, nausea, vomiting, loss of appetite, anxiety, and depression, some severe adverse events identified in the ado-trastuzumab emtansine clinical trial included hepatotoxicity, heart failure, interstitial lung disease, thrombocytopenia, and peripheral neuropathy [129, 12].

Drug delivery systems have advanced over the last half century. Numerous drug delivery systems and controlled release formulations have been developed and used in clinical applications [133]. In particular, tumor-targeting drug delivery has received great attention, partly due to the emergence of nanomedicine.

1.3 Nanomedicine

Nanomedicine is the biomedical and pharmaceutical application of nanotechnology for making nanocarriers of therapeutics and imaging agents, nanoelectronic biosensors, and nanodevices. A number of nanocarrier delivery systems, including dendrimers [100, 101, 103, 150], liposomes [24, 64], polymeric micelles [231, 326], linear polymers [253, 338], quantum dots [18, 67], and iron oxide nanoparticles [54, 178], have been developed and have demonstrated promising properties in targeted drug delivery.

1.3.1 Liposomes

Liposomes are non-toxic, biocompatible and biodegradable carriers that are made up of lipid bilayers, typically phospholipid bilayers. A common method for liposome preparation is oil-in-water (o/w) emulsification, in which the oil phase is dispersed as the droplets of submicron size and then stabilized by surfactants. Liposomes made by o/w are suitable for delivery of lipophilic drugs. Liposomes can deliver hydrophilic, lipophilic and amphoteric drug molecules, which are entrapped either inside the carrier or on the micellar surface. However, liposomes have such problems as short clearance time and low transport rate. Liposomes with specificity may mitigate these disadvantages. For instance, liposomes surface modified with targeting ligands may facilitate encapsulated drug molecules to the target tissue or organ. Targeting ligands include monoclonal antibody (mAb) (e.g. mAb against transferrin receptor), cationized proteins (e.g. albumin), endogenous peptides or plasma proteins. Liposomal systems have been developed and evaluated for delivery of various drugs, such as chemotherapeutic compounds, antiretrovirals, anti-epilepsy drugs and anti-ischemia drugs. The mechanism for liposomes coupled with brain-targeting ligand to enter the brain through absorption- or receptor-mediated transcytosis. Liposome structural parameters such as surface charge, site membrane lipid packing and extent of steric stabilization can be modulated to prolong liposome circulation in the blood. In addition, polymers such as polypropylene oxide (PEO) and polyethylene glycol (PEG) as surface modifier help extend liposome circulation time, as a result of enhanced steric

stability, reduced phagocytosis, and weakened interaction between serum opsonins [305, 295, 4, 223, 286, 295].

1.3.2 Polymeric NPs

Synthetic and natural polymers with different structures (linear, branched, or dendritic) have attracted considerable attention for biomedical applications including CNS drug delivery. In general, polymers used for drug delivery are expected to possess biocompatibility, drug loading capacity, suitable biodegradation kinetics and mechanical properties and ease of processing [1]. Examples include poly(alkylacyano acrylates), poly(amino aicds), poly(acrylamides), poly(amides), ploy(esters), poly(orthoesters) and poly(urethanes). Aliphatic poly(esters) such as polylactic acid (PLA), polyglycolic acid (PGA), and copolymer poly(lactic-co-glycolic acid) (PLGA) have spurred tremendous interest in biomedical applications because of their excellent biocompatibility and biodegradability. PLGA degrades in the body through hydrolysis and breaks down into non-toxic lactic acid and glycolic acid monomers, which can be efficiently eliminated from the body. By virtue of their safety, PLGA copolymers have been approved by the FDA for the use in drug delivery. PLGA are commonly denoted by the molar ratio of lactic acid (LA) to glycolic acid (GA) in the polymer. The degradation rate of PLGA depends on several factors: the molar ratio of LA to GA, molecular weight of copolymer, degree of crystallinity and glass transition temperature (Tg) of the polymer [295, 1]. Single- and double-emulsion-solvent evaporation methods are most used to prepare PLGA NPs. The single-emulsion method is essentially o/w emulsification; whereas the double-emulsion process is water-in-oil-in-water (w/o/w) emulsification. The o/w emulsification method is ideal for hydrophobic lipophilic drug encapsulation, whereas the w/o/w emulsification method is more suitable for hydrophilic drug encapsulation. The solid/oil/water (s/o/w) emulsification method has been developed to utilize PLGA-based microspheres to deliver large amounts of hydrophilic peptides, such as insulin [295, 163].

1.3.3 Dendrimers

Dendrimers exhibit a highly branched, three-dimensional architecture and comprise an initiator core, interior layers, and a number of terminal groups. The branches and surface groups of dendrimers increase exponentially in number with the generation (G) of the dendrimers, whereas the diameter of dendrimers increases by about 1 nm with the generation, as shown in Figure 1.2 [262]. Dendrimers possess very low polydispersity and high functionality. The presence of numerous surface groups and a hydrophobic core allows for a high drug payload and multifunctionality [173, 105]. Dendrimers have been recognized as one of the most versatile compositionally and structurally controlled nanoscale building blocks. Dendrimers have received considerable attention in cancer drug delivery because of their capability of their advantages including (1) maintaining drug levels in a therapeutically desirable range, (2) increasing half-lives, (3) increasing solubility of drugs, (4) delivering a variety of drugs, (5) facilitating passage across biological barriers by transcytosis, (6) enabling rapid cellular entry, and (7) reducing side effects by targeted delivery [286, 173, 187, 297]. Dendrimers are capable to facilitate the transport of therapeutics across various cell membranes or biological barriers via different mechanisms such as modulation of tight junction proteins such as occludin and actin. However, such an event is reversible depending on the dose, generation, and surface charge of the dendrimers [297, 296, 222].

Surface groups and the molecular mass of dendrimers determine the dynamics of cellular entry [296]. The mechanism of a dendrimer-mediated drug-delivery system is illustrated in Figure 1.3. The internalization of dendrimers occurs mainly through a clathrin- and caveolae-mediated energy-dependentendocytosis and partly through marcopinocytosis [115, 160]. Dendrimers can then function as a proton sponge to facilitate the escape from endosomes and lysosomes. The proton sponge mechanism occurs because dendrimers contain a large number of secondary and tertiary amines. These amines enable the absorption of protons released from ATPase and subsequently cause osmotic swelling and rupture of the endosome membrane to release the

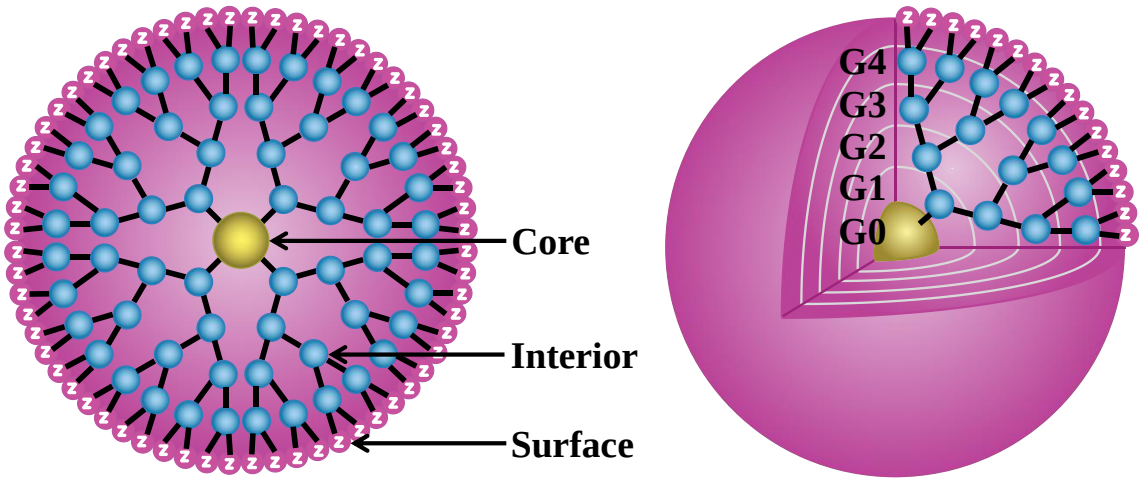

Figure 1.2: Schematic presentation of dendrimers as a nanoscaffold with a core, interior, and surface.
Abbreviations: G, generation; Z, surface group for host-guest interactions and functionalization. (Reproduced reference [297]. Copyright 2014 American Chemical Society.)

entrapped dendrimers [297, 242].

A variety of compositionally differentiated dendrimers have been exploited for drug delivery and imaging, including poly(amidoamine) (PAMAM), poly(etherhydroxylamine) (PEHAM), and poly(propyleneimine) (PPI) dendrimers [173]. Among these, PAMAM dendrimers have been the most investigated because of their unique structures and properties [296]. A full-generation PAMAM dendrimer is a polycationic dendrimer that presents primary amines on the surface, whereas a half-generation PAMAM dendrimer is a polyanionic dendrimer that presents carboxylic acids on the surface. Polycationic dendrimers are able to form compacted polyplexes with nucleic acids at physiological pH, which can be used for gene delivery [206, 225], whereas polyanionic dendrimers have anionic surface that are ideal for cationic drugs or for reversible coordination to platinum complexes [123]. Both polycationic and polyanionic dendrimers possess extremely high mucosal-serosal transfer rates, but polyanionic dendrimers are generally less toxic than polycationic dendrimers [297, 50]. The synthesis of PAMAM dendrimer nanocarriers suitable for targeting delivery of therapeutics involves four steps, as illustrated in Figure 1.4 [297]. First, dendrimers are modified with spacers or linkages on the surface to improve biocompatibility,

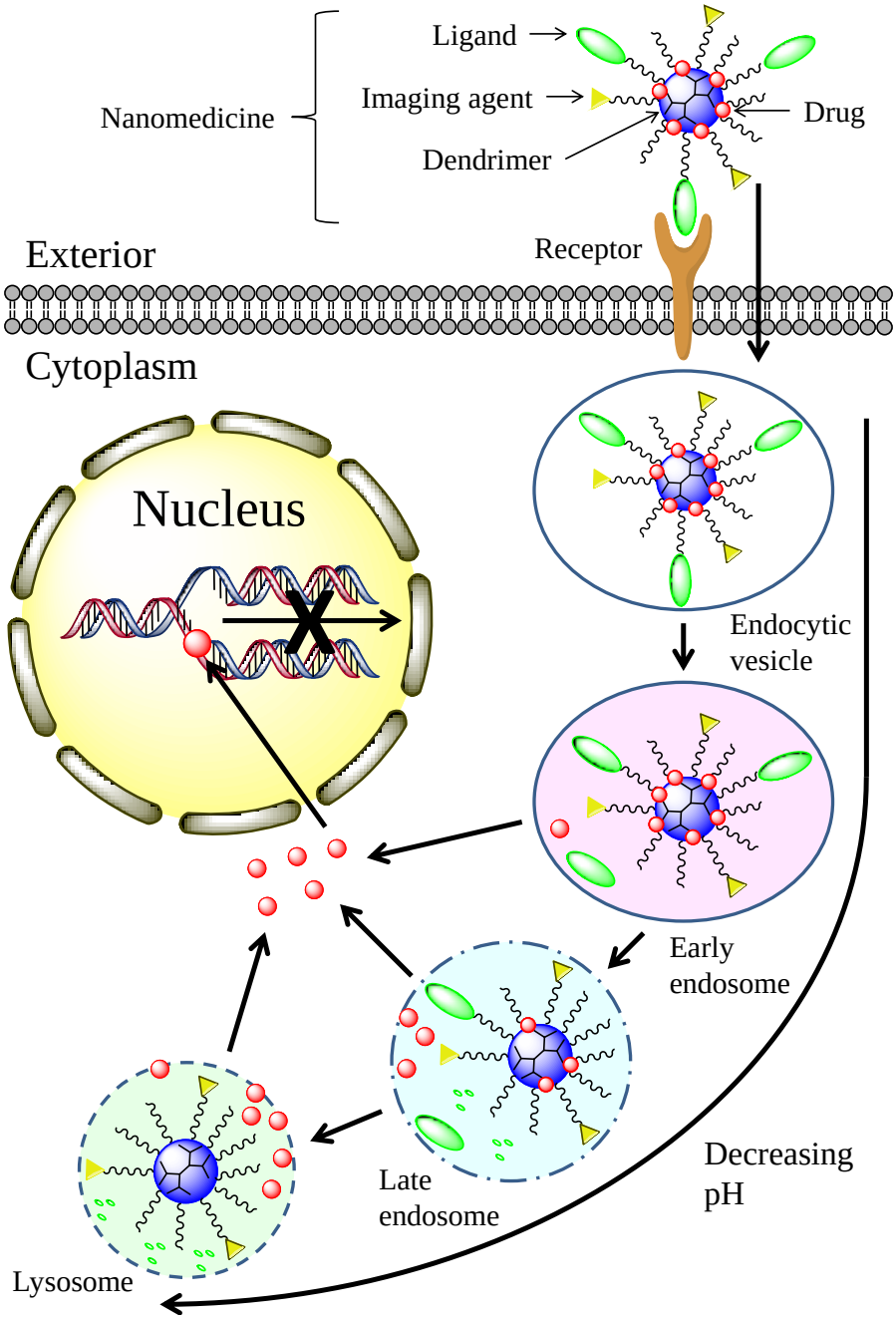

Figure 1.3: Mechanism of dendrimer-mediated intracellular delivery of therapeutics such asdoxorubicin (DOX) and camptothecin (CPT).
(1) Dendrimer nanomedicine is attracted to the cells by an electrostatic difference; (2) Ligand-receptor-mediated endocytosis occurs, and dendrimer nanomedicine is internalized into the cells; (3) reduction of the pH value from the endocytic vesicle to the lysosome triggers therapeutics to be cleaved from the dendrimer carrier and released into the cytoplasm; (5) released therapeutics diffuse into the nucleus, intercalate the DNA strand, and break the DNA chain to prevent its replication. (Reproduced reference [297]. Copyright 2014 American Chemical Society.)

buffering capacity, half-life, and drug-release kinetics. Second, specific ligands are conjugated to the surface-modified dendrimers for tumor targeting. Third, drug or gene therapeutics are bioconjugated or complexed with the surfaced-modified dendrimers. Notice that steps 2 and 3 can be switched depending on particular circumstances. Fourth, imaging agents can be covalently conjugated onto the dendrimer nanocarriers, allowing for the tracking of biodistribution and providing a modality for in vivo imaging and diagnosis [297].

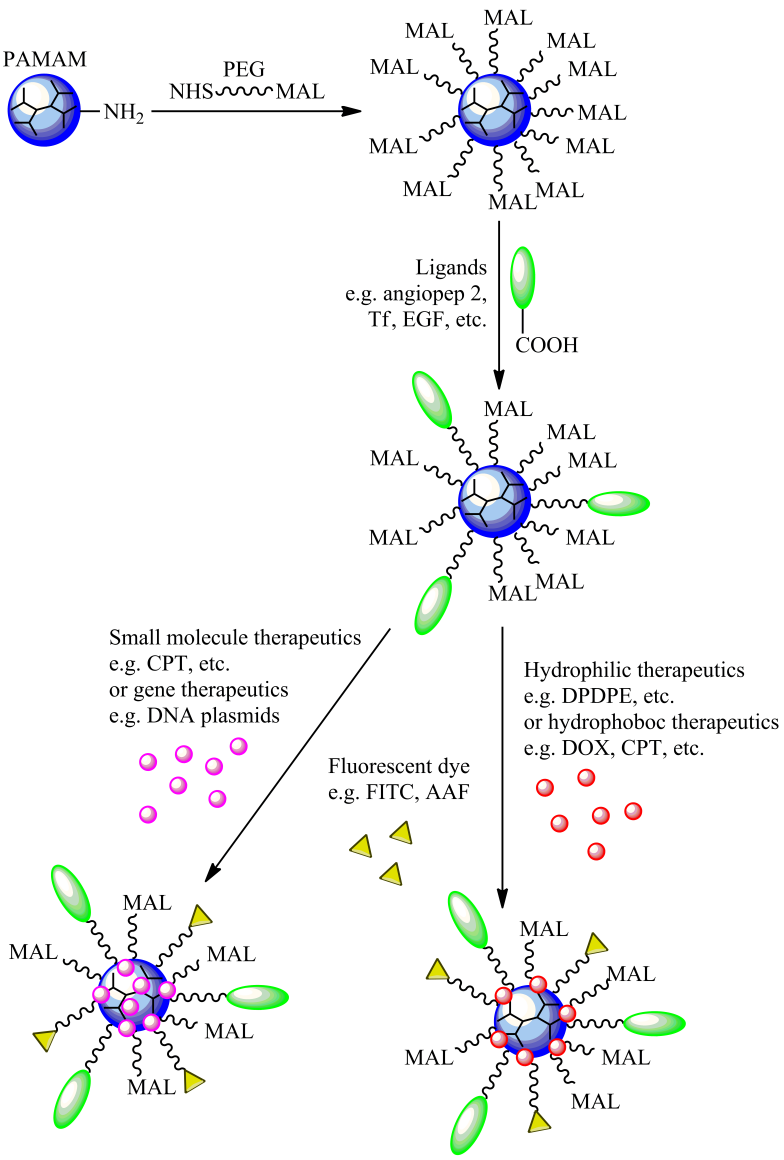

Figure 1.4: Dendrimer platform for targeted delivery of therapeutics and imaging reagents.
(1) Full-generation PAMAM dendrimer is reacted with NHS-PEG-MAL to express MAL on the surface. (2) Targeting ligands are reacted with MAL of the dendrimer to form a PAMAM-PEG-ligand nanoparticle. (3) Hydrophobic or gene therapeutics can be entrapped inside of the dendrimer core via hydrophobicity or electrostatics. (4) Hydrophilic or hydrophobic therapeutics can also be covalent conjugated onto dendrimer surface. (5) Imaging reagents are reacted with MAL of the dendrimer to form a PAMAM-PEG-drug-ligands-imaging reagent nanoparticle. Abbreviation: NHS, N-hydroxysuccinimide; MAL, maleimide; PEG, poly-(ethylene glycol); Tf, transferrin; EGF, epidermal growth factor; DOX, doxorubicin; FITC, fluorescein isothiocyanate; AAF, N-acetyl-2-aminofluorene; CPT, camptothecin. (Reproduced reference [297]. Copyright 2014 American Chemical Society.)

Chapter 2

Dendrimer-Based RNA Interference Delivery for Cancer Therapy: A Literature Review

Preface: This chapter has been published as a book chapter.

Leyuan Xu, W. Andrew Yeudall, Hu Yang

Tailored Polymer Architectures for Pharmaceutical and Biomedical Applications (Chapter 12), American Chemical Society Symposium Series: 2013; Volume 1135, pages 197-213.

2.1 Abstract

RNA interference (RNAi) has emerged as a promising tool for cancer treatment. A strenuous ongoing effort for translation of RNAi into clinically acceptable therapy is the development of vectors for efficient and targeted RNAi delivery. In this chapter, we review RNAi-based cancer treatment and the utility of dendrimers in RNAi delivery.

2.2 Introduction

To date, small-molecular-weight drugs remain dominant on the pharmaceutical market. In general, they interact with proteins such as enzymes within the cell or receptors on the cell surface to exert their desired therapeutic activities for treatment of various diseases. As for cancer chemotherapy, most of anticancer drugs are designed to be cytotoxic and induce apoptosis in cells. Nonetheless, lack of tumor specificity and acquisition of drug resistance are common problems associated with anticancer drugs and cause poor clinical outcomes. It is an important approach to modify existing drugs to improve their specificity and potency. Although discovery and development of new cytotoxic agents for cancer therapy remains a key focus, advances in fundamental understanding of cancer biology and identification of molecular targets have brought about new concepts in anticancer drug design and paved the way for development of molecularly targeted therapeutics. A paradigm shift in design of anticancer therapeutics has been brought about by a groundbreaking discovery-RNA interference (RNAi) [55]. In this chapter, we review RNAi for cancer treatment as well as the latest progress in RNAi delivery on the basis of dendrimers, which are an important class of macromolecules possessing highly branched nanoscale architectures with a high density of terminal groups on the surface.

2.3 Brief Overview of RNAi

RNAi refers to the process of gene silencing (Figure 2.1) [204]. In eukaryotic cells, the RNA endonucleases Drosha and Dicer recognize and cleave double-stranded RNA (dsRNA) into short double-stranded segment ($\sim$20-25 nt), which are known as small interfering RNA (siRNA) duplex, composed of a sense strand and an antisense strand. The siRNA duplex is phosphorylated at the 5' end and hydroxylated at the 3' end with two nucleotides overhung and, in turn, contributes to formation of the pre-RNA-induced silencing complex (pre-RISC), which includes (in mammals) one of four Argonaute proteins (AGO1-4) [114]. Within the pre-RISC, the siRNA duplex is

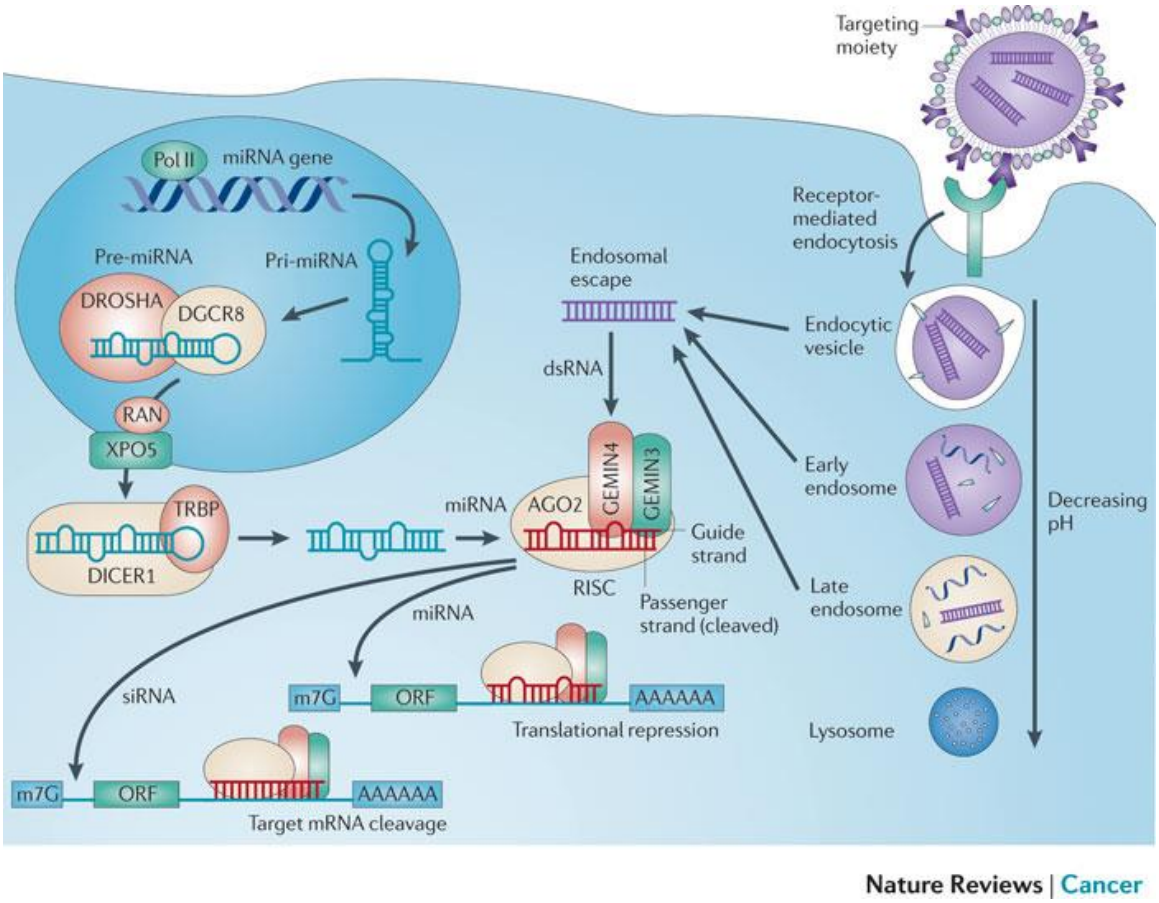

Figure 2.1: Mechanism of RNAi following intracellular dsRNA delivery. (Reproduced from reference [204]. Copyright 2011 Macmillan Publishers Ltd.)

unwound, the sense strand is degraded, and the antisense or guide strand is integrated into the RISC. Once the bound siRNA within the RISC recognizes and hybridizes to its complementary messenger RNA (mRNA), the specific nucleases in the RISC then cleave the mRNA/siRNA hybrid. Subsequently, the cleaved mRNA is destroyed by the cells. Naturally, as mRNA encodes information for production of cellular proteins, its degradation induced by RNAi directly reduces expression of the corresponding protein [208].

For experimental (and therapeutic) purposes, two methods are commonly used to produce siRNAs. The first is to synthesize a dsRNA corresponding to the chosen sequence within the target gene. This dsRNA is then inserted into the cell, usually by transfection by any of the standard methods available. An alternative method is

to generate a dsRNA corresponding to the target sequence in vivo from a precursor small hairpin RNA (shRNA). This involves synthesis of a double-stranded DNA of around 70bp, which is designed to contain tandem segments of both sense and anti-sense sequences corresponding to the target gene. This is ligated into a eukaryotic expression vector downstream of a suitable promoter (*e.g.*, U6), and is delivered to the cell. Once the vector is present in the cell and transcribed in the nucleus, it forms a dsRNA in a hairpin structure. This shRNA is transported into the cytoplasm and is processed, leading to the generation of a functional RISC.

2.4 RNAi in Cancer Therapy

Cell surface receptors such as receptor tyrosine kinases, anti-apoptotic genes, survival factors or key participants in signaling pathways are essential for processes such as cell division, proliferation, survival and migration [208]. Constant activation of these signaling pathways or overexpression of signaling molecules can lead to unchecked cell proliferation and migration, resulting in tumorigenesis.

Ligands such as epidermal growth factor (EGF) stimulate EGFR dimerization and activate the intrinsic intracellular tyrosine kinase activity of the receptor (Figure 2.2) [125]. This activation event enables recruitment of SH2-containing proteins to phosphotyrosine residues in the cytoplasmic portion of the receptor, including the adapter protein Grb2, phosphoinositide 3-OH kinase (PI3K) and phospholipase C [211]. These mediators trigger multiple signal transduction pathways such as MAPK, Akt and JNK pathways, leading to DNA synthesis and cell proliferation. EGFR overexpression on tumor cells, or mutation, can lead to hyperactivation and result in uncontrolled cell division that is characteristic of malignant disease. Based on the proposed role of EGFR as an oncoprotein, several anticancer therapeutics directly against EGFR have been developed, including the small molecule inhibitors Gefitinib and Erlotinib and the anti-EGFR antibody, Cetuximab, which have shown some utility in the treatment of several human cancers. In addition, EGFR-mediated drug delivery systems can be taken up more selectively by EGFR positive cells via EGFR-

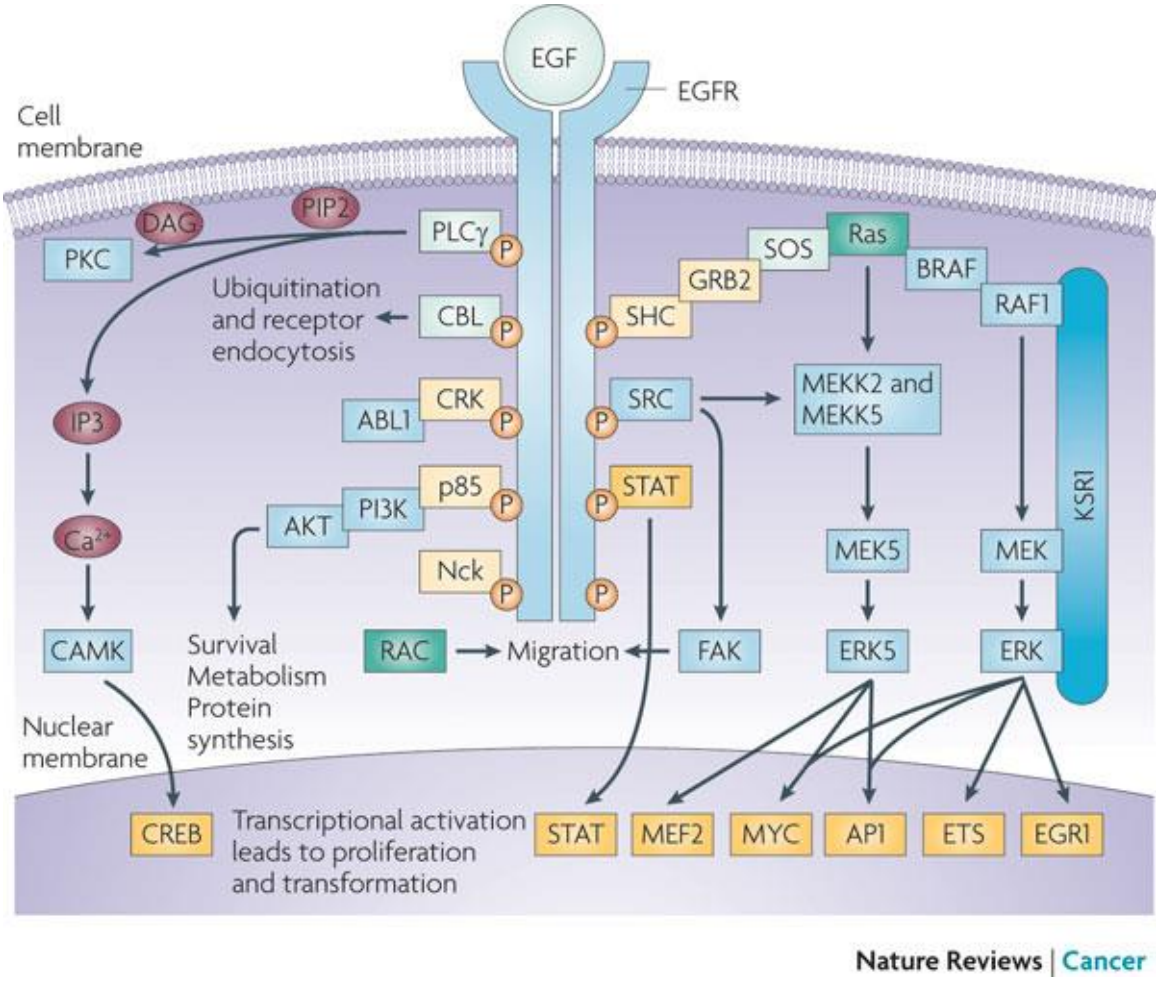

Figure 2.2: The epidermal growth factor receptor signaling pathway. (Reproduced from reference [125]. Copyright 2010 Macmillan Publishers Ltd.)

dependent endocytosis [320].

Inhibiting EGFR signaling or blocking its pathway intermediates during carcinogenesis offers a new strategy to treat cancer. For instance, Wang et al. reported the role of a signaling intermediate, EPS8, in human head and neck squamous cell carcinoma (HNSCC) progression [273, 272]. Overexpression of EPS8 in tumor cells results in increased cell proliferation and migration along with elevated expression of matrix metalloprotease MMP-9, which is dependent on protein kinase B (Akt) activity. They found that EPS8 knockdown decreases tumorigenicity and MMP-9 expression. Furthermore, in clinical samples of squamous cell carcinoma, EPS8 expression was observed at elevated levels and correlated to MMP-9 expression (Figure

2.3) [273, 272]. Therefore, EPS8 may be a good candidate target for RNAi in the treatment of some cancers. In fact, a variety of molecular targets (Table 2.1) have been identified and RNAi knockdown of those targets has been investigated for treating a broad spectrum of cancers including liver cancer, prostate cancer, etc [191]. These delivery systems have been shown to improve siRNA stability and cancer-specificity, thus minimizing off-target and nonspecific immune stimulations.

Currently, clinical trials are ongoing to tackle cancer via RNAi-based gene therapies. Trial CALAA-01, acclaimed as the first targeted delivery of siRNA in humans [39], examined a targeted delivery system to deliver siRNA to reduce expression of the M2 subunit of ribonucleotide reductase (R2) (RRM2) to achieve inhibition of tumor growth. The R2 siRNA was complexed with cationic cyclodextrin and stabilized with adamantane polyethylene glycol (AD-PEG). A targeting ligand, human transferrin (Tf), was coupled to AD-PEG for selective delivery and enhanced uptake via transferrin receptor-mediated endocytosis [40]. The evidence suggests that systematic administration of siRNA can result in specific gene (RRM2) inhibition at both mRNA and protein levels at the site predicted for an RNAi mechanism of action. Analysis of tumor biopsies from melanoma patients following the treatment revealed that amounts of nanoparticles accumulated intracellularly correlated well with doses of nanoparticles administered.

Another trial evaluated bi-shRNA-furin and granulocyte macrophage colony stimulating factor (GM-CSF) augmented autologous tumor cell vaccine for advanced cancer (FANG). The FANG vector was introduced to autologous tumor cells ex-vivo by electroporation, enabling transcription of the bi-shRNA furin and expression of the GM-CSF protein. Transfected tumor cells were irradiated, aliquoted, and cryopreserved until the time of injection (13). Autologous FANG vaccine produced both recombinant human GM-CSF(rhGMCSF) and bi-shRNAfurin. The GM-CSF protein helped recruit immune effectors to the site of intradermal injection and promote antigen presentation, while bi-shRNAfurin inhibited furin protein production at the post transcriptional and translational levels and consequently decreased both TGFβ1

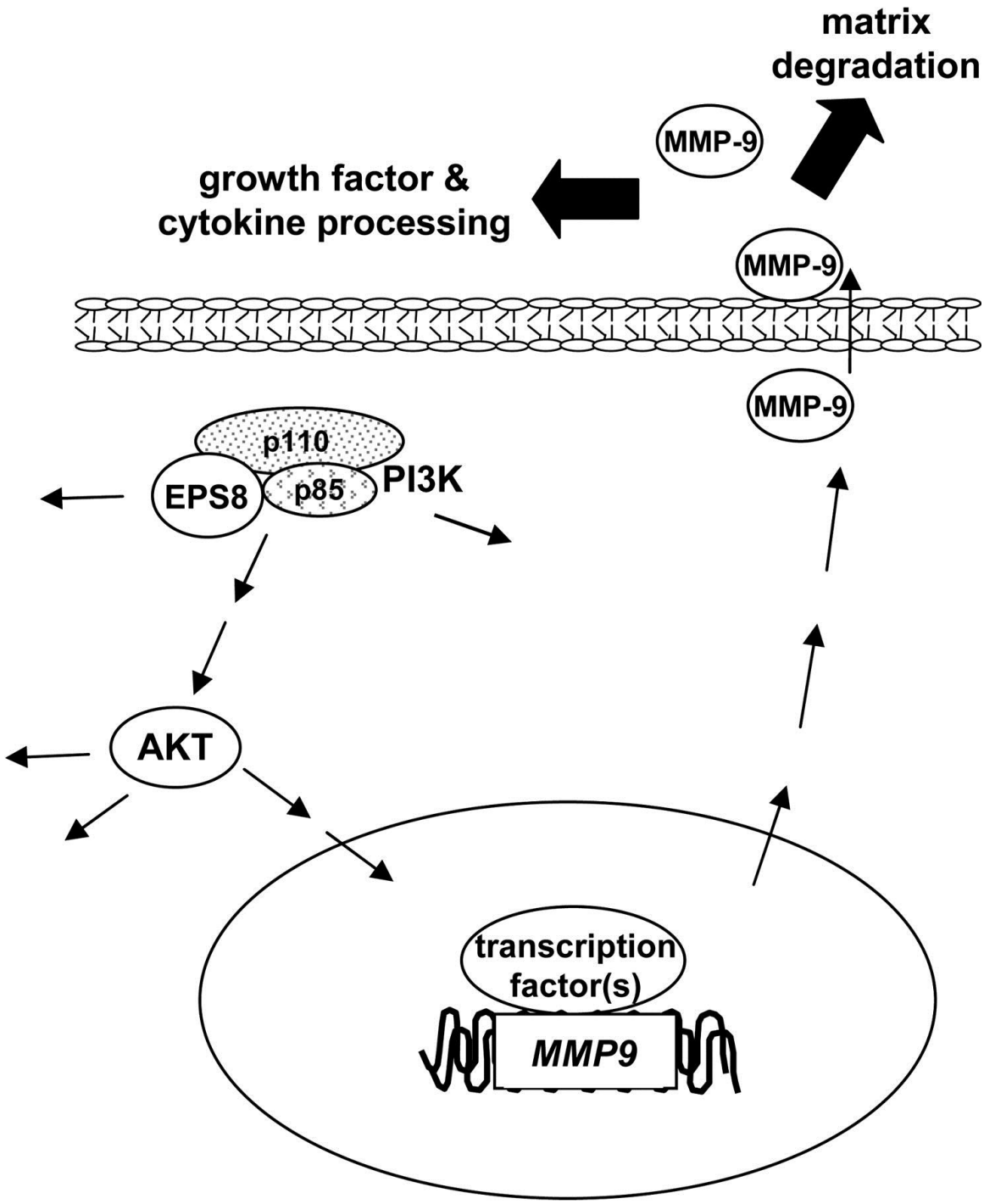

Figure 2.3: Overexpression of EPS8 potentiates AKT activation in a PI3K-dependent manner, resulting in elevated transcription of MMP9 by a yet-to-be-determined mechanism.
This results in enhanced MMP-9 activity, which is available to participate in degradation of extracellular matrix, thereby enhancing invasion. MMP-9 may also process growth factors, cytokines and chemokines, further stimulating cell growth and motility. (Reproduced from reference [272]. Copyright 2009 Oxford University Press.)

Table 2.1: RNAi for Cancer Therapy. SOURCE: adapted from reference [191]. Copyright 2009 Elsevier

Cancer type	Target gene	Administration Route	Ref(s).
Liver	Bcl-2	i.v.	[312]
Prostate	Integrin v	i.t.	[17]
	CD31	i.v.	[226]
	Bcl-2	i.t.	[312]
	Raf-1	i.v.	[194]
Breast	c-raf	i.v.	[34]
	RhoA	i.v.	[302]
	Her-2	i.v.	[91]
Ovarian	EphA2	i.v./i.p.	[135, 136]
	FAK	i.p.	[86]
	ADRB2	i.p.	[257]
	IL-8	i.p.	[174]
	Her-2	i.p.	[265]
Lung	EGFR	i.v.	[166]
	Akt1	Inhalation	[290]
	TERT	i.t.	[333]
Gastric	VEGF	i.t.	[90]
Nasopharyngeal	Her-2	i.t.	[315]
Glioblastoma	PTN	i.c.	[78]
Cervical	HPV18 type E6 and E7	i.t.	[62]
Metastatic Ewings sarcoma	EWS-FLI1	i.v.	[96]
Melanoma	c-myc, MDM2, VEGF	i.t./i.v.	[243]
	EGFP	i.t.	[75]

Abbreviations: i.v., intravenous; i.p., intraperitoneral; i.t., intratumoral; i.c., intracerebral

and TGFβ2 expression. As a result of the phase I trial, local immunosuppression was reduced and tumor antigens and major histocompatibility complex (MHC) proteins promoted. Phase II trial in advanced melanoma has begun recently to examine immune responses to FANG.

2.5 Challenges to RNAi Therapy

In spite of high gene silencing potency, RNAi can cause specific and non-specific off-target effects. Specific off-target effects are usually caused by unintended suppression of an unrelated mRNA due to a certain degree of siRNA complementarity to unintended mRNAs. Nonspecific off-target effects include activating an immune response and toxicity (activation of Toll-like receptors) triggered directly by the siRNA/shRNA plasmid itself or the delivery system [107, 217].

In addition to the off-target effects that impede therapeutic efficacy, barriers exist that reduce bioavailability of RNAi therapeutics. First, RNA encounters RNA-degrading ribonucleases present in the extracellular fluids during transport. Second, RNA may be absorbed nonspecifically by the liver, accessible mucosal surfaces, or body cavities [208]. Third, RNA by itself has no specificity towards target cells and hardly enters the cell due to the presence of negative charges on the cell surface.

To address the barriers facing RNAi therapy, the use of vectors to deliver RNAi therapeutics has become an important approach. Vectors are expected to protect these molecules from degradation, reduce non-specific absorption, enhance cellular uptake and specificity, and facilitate transfection. As such, vectors need to be biocompatible and nonimmunogenic. In general, vectors are divided into two categories: viral vectors and synthetic vectors. Viral vectors have evolved functions to enter cells efficiently, but safety concerns have restricted their practical application. Synthetic vectors, particularly cationic polymers [152, 167, 42], have attracted considerable attention for gene transfer as they can potentially avoid toxicity and immunogenicity, provide high carrying capacity, achieve prolonged delivery, and allow low-cost manufacturing [193, 165]. Nonetheless, delivery efficiency of synthetic vec-

tors for RNAi therapy is affected by factors such as assembly of nucleic acid/vector polyplexes, specificity,uptake, endosomal escape, disassembly of polyplexes, and stability of siRNA in the cytoplasm [165]. Endocytosis is a process involving multiple steps: binding, internalization, formation of endosomes, fusion with lysosomes, and lysis [219]. Following endocytosis, endosomal escape is an important step that affects transfection efficiency.

In the past, a variety of synthetic vectors have been developed or studied to deliver DNA plasmids. Those vectors can be readily applied to deliver RNAi therapeutics in that both types of genetic material are packaged with vectors through electrostatic interactions. Because of the distinct tumor microenvironment and the unique surface characteristics of cancer cells, *e.g.*, overexpression of EGFR, it seems practical to develop vectors to deliver RNAi molecules specifically to tumors through targeted delivery to avoid undesirable gene silencing effects on normal cells.

2.6 Dendrimers for RNAi Delivery

Numerous types of synthetic vectors and nanoparticulate delivery systems have been developed for delivery of nucleic acids including DNA and RNA. In this chapter, we review RNAi delivery on the basis of one important class of nanovectors, namely dendrimers.

2.6.1 Structures and Properties of Dendrimers

Different from traditional polymers, dendrimers have a highly branched, three-dimensional architecture with very low polydispersity and high functionality, comprising an initiator core, several interior layers composed of repeating units, and multiple active terminal groups (Figure 2.4) [158, 53, 184, 249]. The number of branches and surface groups increase exponentially with increasing generation (G). The presence of numerous surface groups allows for high drug payload and multifunctionality. Dendrimer toxicity is generation- and dose dependent [306]. Higher generations tend to be more toxic and carboxylate-or hydroxyl-terminated PAMAM dendrimers are more cyto-

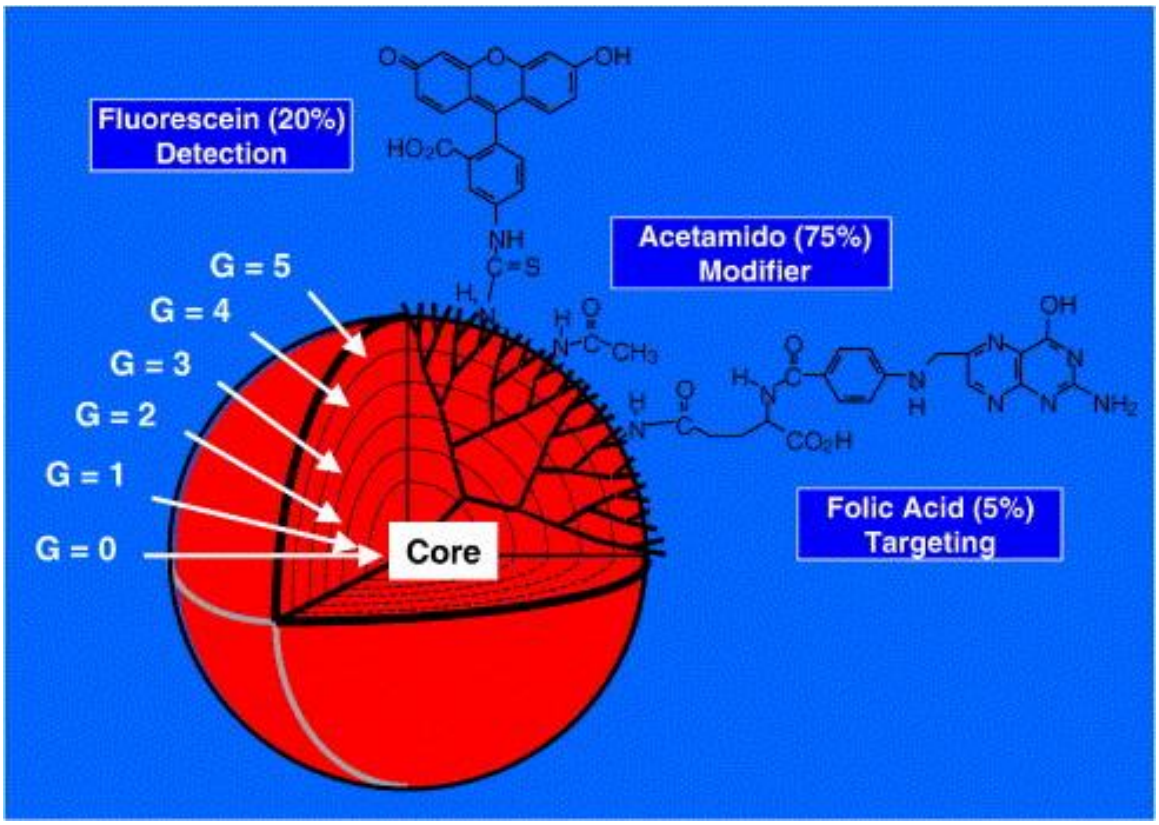

Figure 2.4: Schematic presentation of dendrimers as nano-scaffold for the attachment of cell-specific ligands, modifiers, and fluorescence tags.
Abbreviation: G: generation. (Reproduced from reference [249]. Copyright 2005 Elsevier)

compatible than amine-terminated dendrimers. Dendrimers have been recognized as the most versatile compositionally and structurally controlled nanoscale building blocks throughout the fields of engineering, materials science, chemistry, and biology.

By virtue of their unique structures and properties, polycationic polyamidoamine (PAMAM) dendrimers have been extensively investigated for gene transfer [158, 51, 16, 228]. Polycationic dendrimers can form compacted polyplexes with nucleic acids in physiology pH. Furthermore, dendrimers can act as a "proton-sponge" to facilitate the escape of polyplexes from endosomes and lysosomes [250, 242]. In general, "proton-sponge" polymers contain a large number of secondary and tertiary amines with a pK_a at or below physiological pH. They can adsorb protons released from ATPase and subsequently cause osmotic swelling and rupture of the endosome

membrane to release the entrapped polyplexes.

Additionally, dendrimers facilitate transport of therapeutics across various cell membranes or biological barriers. For instance, PAMAM dendrimers rapidly cross adult rat intestine at high serosal transfer rates following endocytosis-mediated cellular internalization. Surface groups and molecular mass affect the dynamics of dendrimer cellular entry.

2.6.2 Examples of Dendrimer-Mediated RNAi Delivery

Dendrimers can be functionalized to carry a variety of functional moieties to enhance knockdown efficiency, achieve targeted delivery, and reduce off-target effects.

2.6.2.1 PEGylated Dendrimers

Tang et al. reported the application of PEG-modified PAMAM dendrimers for siRNA delivery [254]. They modified PAMAM dendrimer generations 5 and generation 6 with MPEG-5000. They found that PEG-modified dendrimers were capable of protecting complexed siRNA from RNase digestion. The in vitro studies revealed that PEG-modified dendrimers achieved similar knockdown effects in Cos7 cells compared to Lipofectamine 2000. They went on to study siRNA knockdown by the synthesized PEGylated PAMAM dendrimers in animals. In this study, the authors intramuscularly injected PEG-modified dendrimer/siRNA against green fluorescence protein (GFP) polyplexes to C57BL/6 mice transiently infected with adenovirus or GFP transgenic mice and observed GFP suppression in both models. Interestingly, the authors noted that PEGylated PAMAM dendrimer G5.0 has higher transfection efficiency than PEGylated PAMAM dendrimer G6.0 and attributed it to a more flexible structure and a smaller size of G5.0 in contrast to G6.0. A structurally flexible vector tends to enhance compaction of siRNA and increase the fusion of the polyplexes with the cell membrane. A smaller size of polyplexes would bring about increased cellular uptake and enhanced release of the siRNA in the cell.

2.6.2.2 PEGylated Dendrimers with Bis-aryl Hydrazone (BAH) Linkages

The "proton sponge" property conferred by amines in the dendrimer is crucial for successful gene delivery. However, surface modification of PAMAM dendrimers with PEG or other moieties has to utilize surface amine groups and inadvertently impairs dendrimer buffering capacity. To address this issue, Yuan et al. employed a new methodology to make PEGylated dendrimers by using a bis-aryl hydrazone (BAH) linker (Figure 2.5) [321]. To use BAH to connect PEG to the dendrimer, PAMAM dendrimer G4.0 is activated with succinimidyl 4-hydrazinonicotinate acetone hydrazone (SANH), whereas monofunctional methoxypolyethylene glycol amine (PEG5000) is activated with succinimidyl 4-formylbenzoate (SFB). A subsequent coupling reaction between SFB-activated PEG and SANH-activated PAMAM forms a bis-aryl hydrazone linkage. It was found that use of BAH linkage simultaneously enables a high degree of PEGylation and an increase in buffering capacity of the dendrimer vector. Higher transfection efficiency was also observed for this vector compared to unmodified dendrimer [321]. Although the utility of this new PEGylated dendrimer for RNAi delivery has yet to be reported, this new linker can be broadly used for dendrimer surface modification without compromising buffering capacity required for endosomal escape during RNAi intracellular transport.

2.6.2.3 Dendrimer-EGF Conjugates

Epidermal growth factor receptor (EGFR) is preferentially overexpressed in multiple human solid tumors, including cancers of head and neck, lung, breast, colon, and brain. Tumor cells expressing a high level of EGFR can be more specifically targeted by a delivery system carrying EGFR ligand such as EGF. Following this rationale, Yuan et al. designed a dendrimer-EGF delivery system, in which EGF is covalently conjugated to PAMAM dendrimer G4.0 through a triglycine spacer (Figure 2.6) [320]. They observed that dendrimer-EGF conjugates facilitated intracellular uptake in an EGFR-dependent manner without triggering EGFR signaling pathways in EGFR-overexpressing cells. Furthermore, they confirmed that dendrimer-

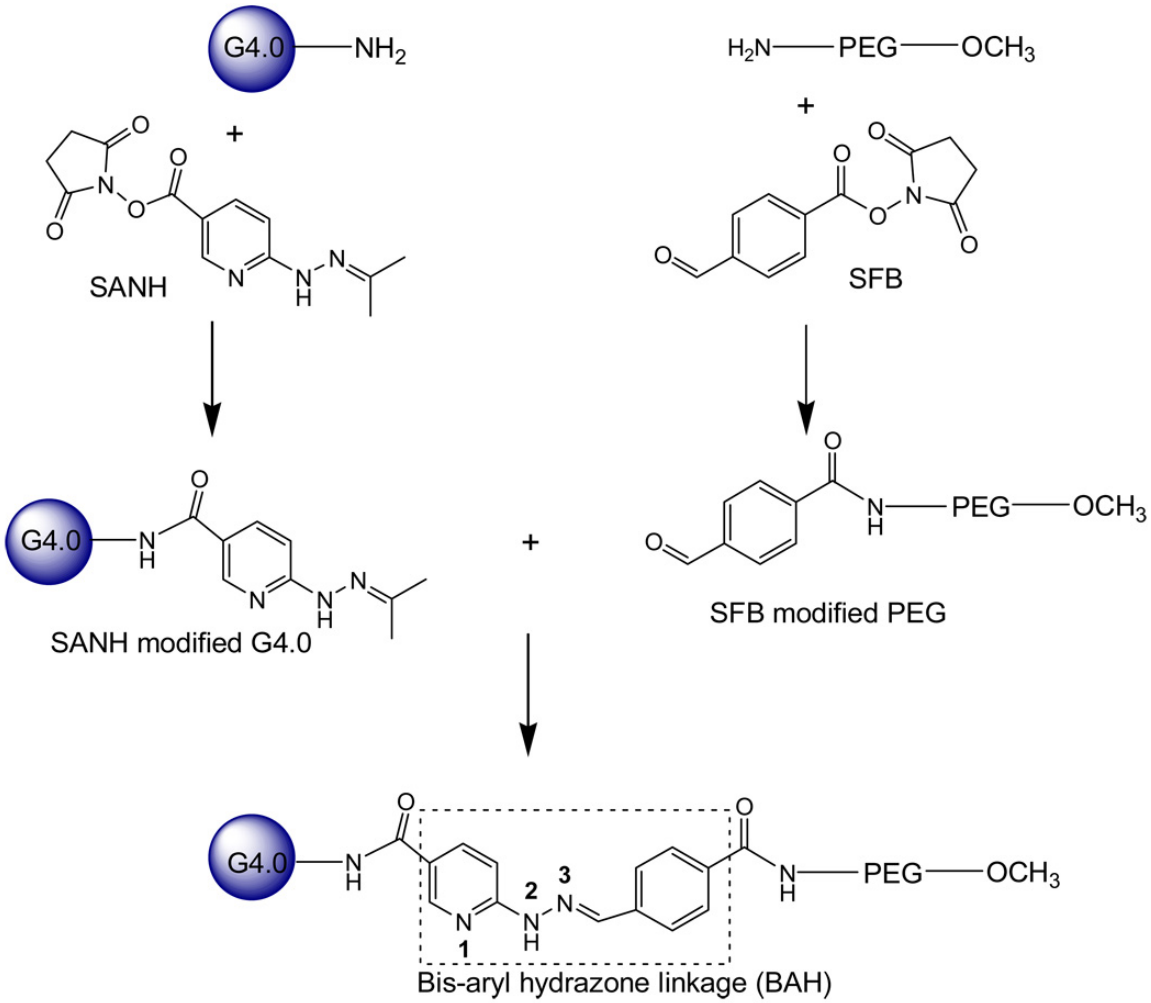

Figure 2.5: Synthesis of PEGylated PAMAM dendrimers with BAH linkages.
(Reproduced from reference [321]. Copyright 2010 American Chemical Society.)

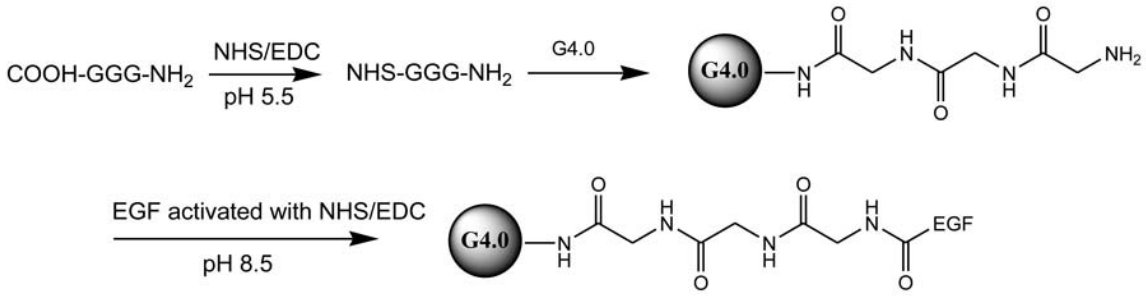

Figure 2.6: Synthesis of dendrimer-EGF conjugates through triglycine spacer (GGG).
(Reproduced from reference [320]. Copyright 2010 Elsevier.)

EGF conjugates improved siRNA delivery and gene knockdown efficiency compared to commercial vectors and to unconjugated dendrimers. Particularly, they examined delivery of siRNA against yellow fluorescent protein (YFP siRNA) and shRNA against vimentin (shVIM). Approximately 70% suppression of YFP expression in YFP-expressing cells was achieved while approximately 40% suppression of vimentin expression was achieved. The enhanced knockdown efficiency of dendrimer-EGF conjugates compared to unmodified dendrimer or TransIT (a commercial keratinocyte transfection reagent) transfections indicates this delivery system is suitable for introduction of nucleic acids into cells via a receptor-targeted mechanism [320].

2.6.2.4 Dendriworms

Agrawal et al. developed a modular platform, namely dendriworm, for siRNA delivery (Figure 2.7) [3]. To make dendriworms, cystamine core PAMAM dendrimers (generation 4) were reduced to dendrons and then coupled to near-infrared dye-labeled iron oxide nanoworms via a heterobifunctional linker, N-succinimidyl 3-(2-pyridyldithio)-propionate (SPDP). SPDP is a reducible linker, allowing rapid removal of dendrons from the conjugates in the reducing intracellular environment, which in turn helps improve siRNA delivery and diffusion inside the cell. The obtained dendriworms had 16-25 mV zeta potential and 80-110 nm hydrodynamic diameter. The authors used dendriworms to deliver EGFR siRNA for brain cancer treatment. In vitro studies

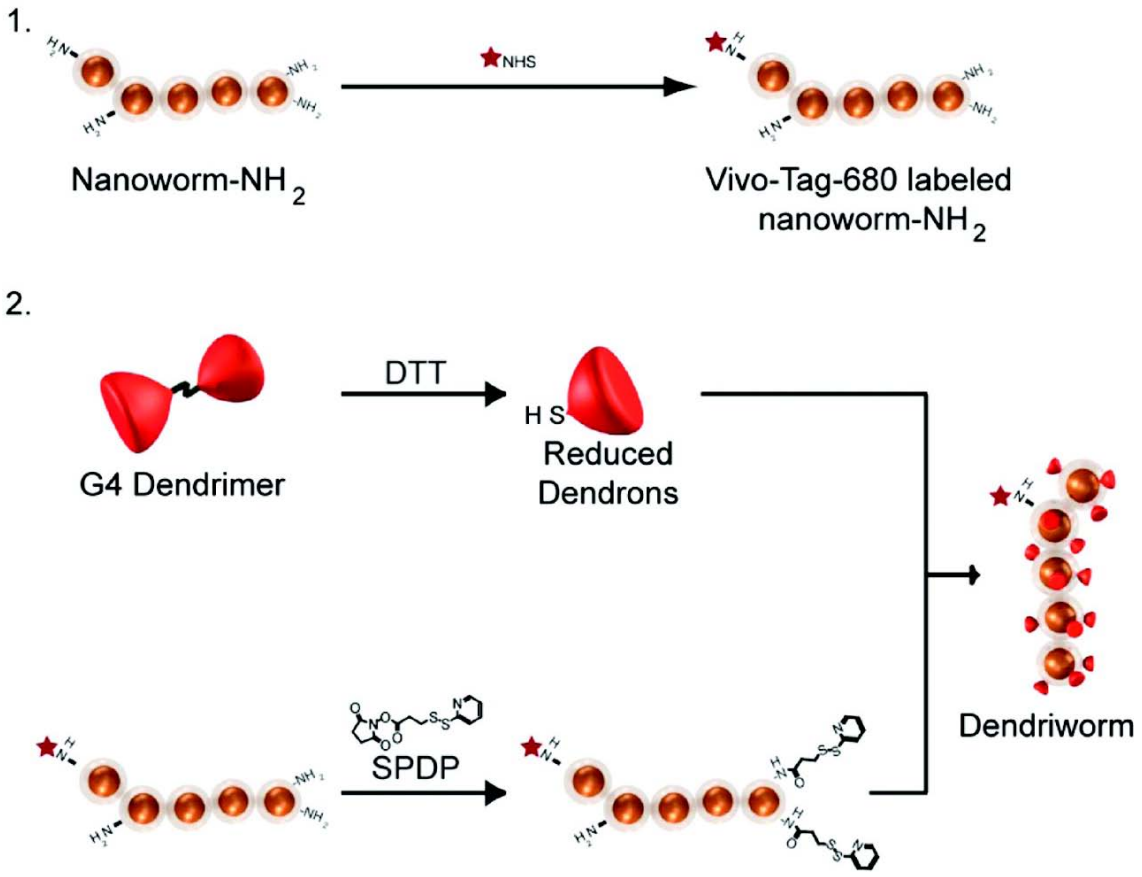

Figure 2.7: Synthesis of dendriworms.
(Reproduced from reference [3]. Copyright 2009 American Chemical Society.)

show that EGFR expression in human glioblastoma cells was reduced by 70-80%, which was 2.5-fold more efficient than commercial cationic lipids. In particular, 0.5 mg/ml of dendriworm (11 μg of total siRNA) was infused into the EGFR-driven transgenic mice of glioblastoma in a period of 7 days. A significant amount of nanoparticles were delivered to the brain and lead to suppression of EGFR in the tumor.

2.7 Summary

Dendrimers display the evolving nature needed to incorporate a number of functionalities desirable for efficient delivery of RNAi. The biocompatibility, tumor specificity, and immunocompatibility of dendrimer-based nanovectors can be achieved through proper chemical modification at the periphery, and their composition, shape, and size

can be precisely tuned to maximize transfection efficiency. Thus, dendrimer-based RNAi delivery is likely to meet the strict regulatory requirements of polymer-based therapeutics intended for use in humans.

Chapter 3

Folic Acid-Mediated Cancer Chemotherapy and Diagnosis: A Literature Review

3.1 Introduction

Folate receptors (FRs), especially FRα, are highly expressed in numerous cancers in order to meet the folate demand of rapidly dividing cells under low folate conditions [198, 52, 221]. As a potential targeting agent, folic acid (FA) has several advantages including lower molecular weight and less immunogenicity than most antibodies, relatively high stability, and ease of synthesis [322]. Because the solubility of FA in water is 1.6 mg/L at 25 °C, FA cannot readily dissolve in water. However, integration of FA to water soluble nanoparticles (NPs) can excellently guide anticancer drugs to tumors [322]. In this chapter, the mechanism of FR-targeting drug delivery systems are discussed. The latest applications of FA in the anticancer drug delivery with an emphasis on in vivo tumor xenograft models are reviewed. FA-mediated tumor imaging and diagnosis is also reviewed.

3.2 Structural basis of folic acid and folate receptors

Folate, also known as vitamin B_9 occurs naturally in food.Folic acid (FA), the synthetic form of this vitamin, is shown in Figure 3.1. In adult tissues, folate or FA is mainly transported by two transporters, reduced folate carrier (RFC) and folate receptor. RFC is a ubiquitously expressed anion channeland is a ubiquitous low affinity but high capacity transporter. RFC possesses low folate-binding affinity (K_m = 1-10 μM) but a high FA-binding affinity ($k_d < 1$ nM) [6, 335]. Folate receptor is a high affinity, low capacity transporter found in specific tissues such as kidney, lung, placenta. There are three subtypes of folate receptors (FRs): FRα, FRβ, and FRγ. Among these three FRs, FRα is most widely expressed at very low levels in normal tissues, but it is highly expressed in numerous cancers including ovarian, pediatric ependymal brain, mesothelioma, breast, colon, renal, lung tumors, and head and neck carcinomas, in order to meet the folate demand of rapidly dividing cells under low folate conditions [198, 52, 221, 29]. Recently, a molecular simulation and docking study revealed the ligand-receptor (FA-FRα) binding sites (Table 3.1) [29]. FA is docked into an extended groove of FRα in the direction roughly perpendicular to the plane formed by helices α1, α2 and α3. Both hydrogen bonds and hydrophobic interactions occur around the pteroate moiety. The ligand-binding affinity study showed that mutation of D81 in FRα significantly increases the dissociation constant (K_d) value by 11.7 fold (Table 3.1), suggesting that replacement of D81 decreases FA binding affinity by more than one order of magnitude. The interaction of the aspartate carboxyl oxygens with the pterin N1 and N2 nitrogens is very strong, contributing to high-affinity ligand binding. In contrast, mutations of K136 and R106 have little effect, and mutations of W102, R103, W140, and S174 have moderate effects on folic acid binding [29]. Their work illustrates that -$NH_2{}^a$ is a key binding site for FA to bind to FRα. The structural and mutational analysis provides a structural rationale for the absolute requirement of the pterin group, especially -$NH_2{}^a$ group, for anchoring folate in the binding pocket of the receptor. Additionally, the glutamate group

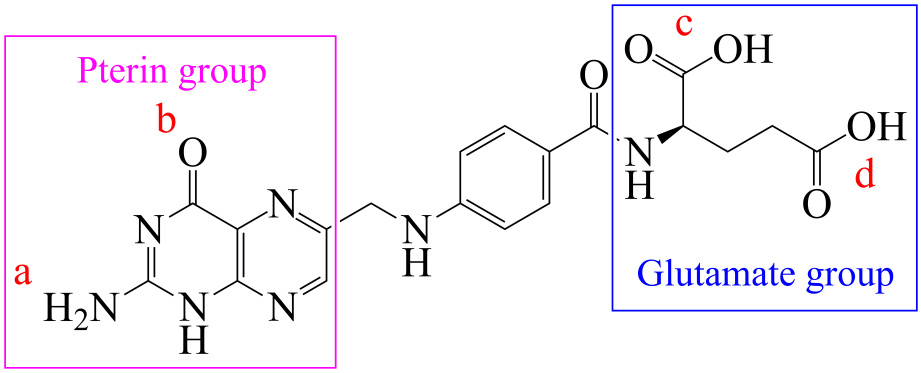

Figure 3.1: Chemical structure of folic acid (FA).
-$NH_2{}^a$, =O^b, -$COOH^c$, and -$COOH^d$ are the major binding sites of FA to the ligand-binding-pocket of folate receptor α.

Table 3.1: FA binding affinities of FRα ligand-binding-pocket mutants

Binding site of FA	Binding site in FRα ligand-binding pocket	Fold increase in K_d at the site mutation of FRα relative to wild type FRα
-$NH_2{}^a$	D81A	11.7
=O^b	R103A	2.5
...	R106A	1.2
...	S174A	2.0
-$COOH^c$	W140A	3.6
-$COOH^d$	W102A	3.1
...	K136A	1.1

Data taken from Chen et al [29]. FA, folic acid; FRα, folate receptor α.

is available for conjugation with drugs and imaging reagents, without compromising the interactions between receptor and ligand.

3.3 Folate-decorated anticancer drug delivery systems

To date, numerous FA-decorated nanostructures in various forms have been developed for active targeted anticancer drug delivery. The schematic diagram of FA-decorated

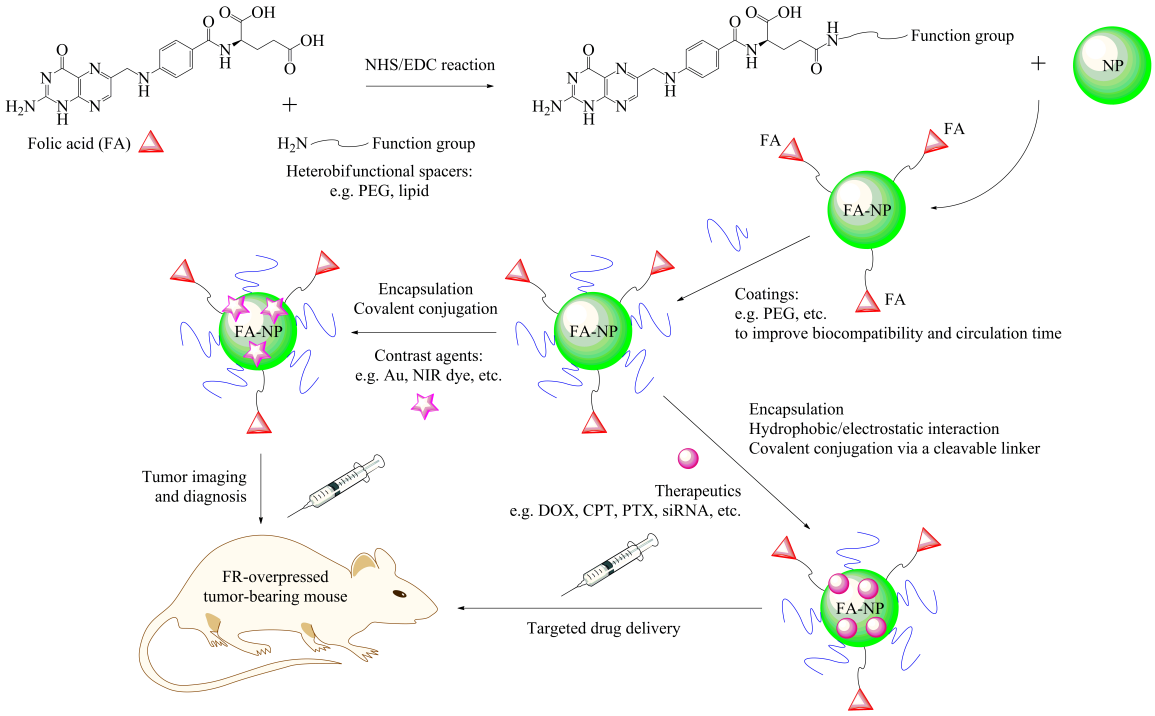

Figure 3.2: Schematic representation of a folic acid-decorated nanoparticle (FA-NPs) for in vivo anticancer drug delivery and bioimaging.
Abbreviation: EDC, 1-ethyl-3-(3-dimethylaminopropyl)carbodiimide; NHS, *N*-hydroxysuccinimide; PEG, polyethylene glycol; DOX, doxorubicin; CPT, camptothecin, PTX, paclitaxel; siRNA, small interference RNA; Au, gold; NIR dye, near infrared fluorescent Dye; FR, folate receptor.

anticancer drug delivery systems is illustrated in Figure 3.2.

3.3.1 Liposomes

A carboplatin-encapsulated folate receptor-targeted (FRT) liposomal system was developed for the treatment of metastatic ovarian cancer [28]. In vitro evaluation showed that FRT carboplatin liposome increases carboplatin potency by two-fold. In the IGROV-1 ovarian tumor-bearing SCID BC-17 mice, a superior survival rate (5 out of 6) was observed in the mice treated with FRT carboplatin liposome via intraperitoneal (i.p.) injection twice a week for 3 weeks, and no metastasis was observed in these mice. In contrast, no survivor was observed in the mice treated with saline, free carboplatin or non-folate receptor-targeted carboplatin liposome, and the cancer cells metastasized to the lung and liver tissues in these mice [28].

Folic acid and TAT peptide conjugated, octadecyl-quaternized, lysine-modified chitosan-cholesterol polymeric liposomes (FA-TATp-PLs) were designed for tumor-targeted drug delivery [334]. Paclitaxel (PTX) was loaded in the FA-TATp-PLs. In vitro evaluation of FA-TATp-PLs revealed the targeting effects of folate decoration, the transmembrane ability of TAT peptide, and their synergistic effects. In the KB nasopharyngeal tumor-bearing SCID mice, the tumor growth rate of the mice intravenously (i.v.) injected with PTX-loaded FA-TATp-PLs and free Taxol was reduced by 71% and 49%, respectively, compared with the one of PBS-treated mice. The drug delivery system, FA-TATp-PLs, had no effect on tumor growth [334].

Folic acid-coupled PEGylated nano-paclitaxel liposome (FA-NP) was developed to reverse drug resistance in paclitaxel-resistant (SKOV3/TAX) ovarian cancer [263]. In vitro evaluation showed that FA-NP but not NP markedly inhibited the growth of ovarian cancer cells and caused more G_2/M cell cycle arrest and apoptotic changes in ovarian cancer cells than NP or free paclitaxel. These effects were blunted in the presence of free FA, which competitively inhibited the receptor-mediated uptake of FA-NP. In the SKOV3/TAX ovarian tumor-bearing nude mice, i.p. administration of FA-NP but not free paclitaxel and non-targeted NP significantly prolonged the survival and reduced tumor nodule number. However, i.v. administration of FA-NP

failed to achieve these antitumor effects at the same dose following i.p. administration [263].

Folate targeted docetaxel (DTX)-lipid-based-nanosuspensions (tLNS) were developed for active-targeted cancer therapy [274]. In the B16 tumor-bearing Kunming mice, an obvious tumor regression was observed in the mice treated with tLNS, non-targeted docetaxel-lipid-based-nanosuspensions pLNS and Duopafei. Here, the tumor inhibition rate in the tLNS mice was higher than pLNS and Duopafei groups. In addition, both tLNS and pLNS generated less toxicity to the mice than Duopafei via i.v. administration. The pharmacokinetic (PK) profiles for DTX showed that the DTX serum concentration was measurable after 12 hours after i.v. injection of tLNS and pLNS but not Duopafei group. Compared to the ones in Duopafei group, the area under the plasma concentration-time curve (AUC) following i.v. administration of tLNS and pLNS significantly increased by about 1.59 and 1.66 times, respectively, clearance significantly decreased, and the mean residence time (MRT) was significantly prolonged by about 2.40 and 2.41 times, respectively. The overall targeting efficiency of pLNS was 1.09 times better than that of Duopafei; whereas the targeting efficiency of tLNS was 1.13 times better than that of pLNS [274].

The presence of folic acid within the cholesterol domain could promote more productive liposome-based transfection in cultured cells [299]. In the KB tumor-bearing nude mice, lipoplexes that included FA within the cholesterol domain showed significantly higher plasmid accumulation and transfection in tumors after intratumoral (i.t.) injection, as compared to lipoplexes in which FA was excluded from the domain [299].

3.3.2 Linear polymers

A heparin-folate-paclitaxel (HFT) backbone with an additional paclitaxel (T) loaded in its hydrophobic core (HFT-T) was designed for folate receptor-targeting cancer therapy [279, 280]. In vitro evaluation showed that the HFT-T NPs enhanced cytotoxicity in both KB-3-1 and paclitaxel-resistant KB-8-5 cancer cells, compared to free paclitaxel or nontargeted nanoparticle (HT-T). In both KB-3-1 and KB-8-5 tumor-

bearing nude mice, i.v. administration of HFT-T enhanced the specific delivery of paclitaxel into tumor tissues, prolonged retention within tumor tissues, and markedly retarded tumor growth, which were associated with a higher degree of microtubule stabilization, mitotic arrest, antiangiogenic activity, and inhibition of cell proliferation [279, 280].

A biodegradable, folic acid conjugated poly(ester amine) (FP-PEA) was synthesized to deliver TAM67 gene for cancer gene therapy [9]. In vitro evaluation showed that the transfection efficiency of FP-PEA was drastically decreased in the presence of an excess free folic acid in the FR-positive cells, and it exhibited very less significant transfection against FR-negative cells. In the KB tumor-bearing BALB/c mice, the tumor growth was suppressed after i.t. injection of FR-PEA/TAM67 polyplexes [9].

siRNA-loaded folic acid-PEG-chitosan oligosaccharide lactate (siRNA/FA-PEG-COL) NPs were prepared for targeted ovarian gene therapy [149]. Blood compatibility assay showed that FA-PEG-COL NPs possessed superior compatibility with erythrocytes in terms of degree of aggregation and hemolytic activity and low effect on cell viability. In the OVK18#2 ovarian tumor-bearing BALB nude mice, i.v. administration of FA-PEG-COL NPs showed significant greater tumor accumulation than non-targeting COL NPs [149].

3.3.3 Branched polymers

Folated PEG-chitosan-graft-polyethylenimine (FPCP) was designed for folate receptor-targeting cancer cell gene delivery [121]. In vitro evaluation showed that FPCP was much less cytotoxic than PEI, and the FA covalently linked with PEG had no negative effect on cytocompatiblity. In the H-ras12V transgenic mice, i.v. administration of FPCP-GFP complexes showed high levels of GFP expression in liver cancer tissues compared with GFP only and PEI-GFP; while i.v. administration of FPCP-Pdcd4 complexes showed a significant decrease in tumor numbers compared with Pdcd4 only but not PEI-Pdcd4 complexes [121].

2-hydroxypopyl-β-cyclodextrin (HP-β-CD) and folic acid cross-linked with low

molecular weight polyethyleneimine (FA-HP-β-CD-PEI) was synthesized for tumor-targeted delivery of siRNA [147]. Intracellular uptake of FA-HP-β-CD-PEI/siRNA polyplexes was greater than non-targeted HP-β-CD-PEI/siRNA polyplexes in HeLa cells. Additionally, administration of FA-HP-β-CD-PEI/siVEGF complexes to HeLa cells reduced 92% VEGF protein expression in the presence of 20% serum. In the HeLa tumor-bearing nude mice, four doses of i.v. administration of FA-HP-β-CD-PEI/siRNA polyplexes markedly decreased VEGF expression in the tumor, which in turn reduced tumor growth, compared to the ones treated with HP-β-CD-PEI/siRNA polyplexes [147].

Folic acid-decorated ethylenediamine-surface modified fullerene (C60-PEI-FA) was synthesized for tumor-targeted delivery of docetaxel (DTX) [234]. In the S180 tumor-bearing BALB/c mice, i.v. administration of C60-PEI-FA/DTX every 2 days significantly inhibited tumor growth, compared to untreated, C60-PEI-FA-, free DTX-, C60-PEI/DTX-treated mice. PK profiles showed that C60-PEI-FA/DTX significantly increased the blood circulation time of DTX by increasing the area under the curve (AUC) and the mean residence time (MRT) 2 and 6 times, respectively, compared to free DTX. More importantly, the uptake of DTX in tumor significantly higher in C60-PEI-FA/DTX-treated mice than in C60-PEI/DTX- and DTX-treated mice [234].

3.3.4 Polymeric micelles

Folate-targeted docetaxel (Dtxl) encapsulated PLGA-lecithin-PEG core-shell NPs (FT-NP Dtxl) were synthesized as a new class of radiosensitizers for cancer radiotherapy [284]. Both in vitro and in vivo evaluations showed that the radiosensitization efficacy of FT-NP Dtxl is dependent on the timing of radiotherapy. In the KB tumor-bearing nude mice, i.v. administration of free Dtxl, FT-NP Dtxl and non-targeting NP Dtxl (NT-NP Dtxl) led to significant tumor growth delay when tumors were irradiated, but FT-NP Dtxl significantly delay tumor growth rate compared to NT-NP Dtxl [284].

Folic acid-modified stealthy PEOz corona micelles (FA-PEOz-PCL) were syn-

thesized to deliver doxorubicin (DOX) [214]. In the KB tumor-bearing BALB/c nude mice, i.v. administration of DOX entrapped FA-PEOz-PCL micelles effectively inhibited the tumor growth and reduced the toxicity to mice compared with free DOX [214].

Folic acid (FA) and paclitaxel (PTX) loaded polymeric micelles [FA-M(PTX)] were prepared by coassembling FA-polymer conjugate [MPEG-b-P(LA-co-DHP/FA)] and PTX-polymer conjugate [MPEG-b-P(LA-co-MCC/ PTX)] for the treatment of human esophageal cancer [287]. In the human esophageal EC9706 tumor-bearing nude mice, i.v. administration of FA-M(PTX) micelles was more efficient in inhibiting tumor growth and extending the survival rate of the mice than free paclitaxel and non-targeting PTX micelles. Compared with non-targeting micelles, FA-M(PTX) micelles were preferentially uptaken by EC9706 cells in folic acid-free medium, while their uptake could be competitively inhibited by free FA [287].

Folate-decorated biodegradable polymeric micelles [FA-M(Pt)] were prepared by coassembling FA-polymer conjugate (FA-PEG-PLA) and diaminocyclohexane platinum (DACH-Pt) of oxaliplatin-polymer complex [mPEG-b-P(LA-co-MCC/Pt)] [277]. Plasma pharmacokinetics of Pt showed that FA-M(Pt) possessed greater steady-state area under the plasma clearance curve (AUC), slower plasma clearance rate (CL) and longer mean residence time (MRT) than free oxaliplatin. M(Pt) had peak plasma Pt concentration within 4 h; whereas FA-M(Pt) had peak plasma concentration after 4 h. Compared to M(Pt), FA-M(Pt) displayed a bigger AUC, slower CL, and the same MRT, indicating FA-M(Pt) was not as good as M(Pt) as far as the plasma drug concentration was concerned. In the H22 liver tumor-bearing Kunming mice, i.v. administration of FA-M(Pt) was more effective inhibiting the tumor growth and prolonging the survival rate of the mice than M(Pt) and free oxaliplatin [277].

Folic acid-decorated self-organized NPs (FADex NPs) were fabricated by complexation of doxorubicin-conjugated dextran with FA-grafted chitosan for cancer therapy [142]. In in vitro competition evaluation, the uptake of FADex NPs was significantly decreased by pre-treatment of free folic acid (2 mM) to the KB cells, which, in turn, reduced Dox cytotoxicity potency. In the KB tumor-bearing BALB/c nude

mice, two doses of i.v. administration of FADex NPs efficiently suppressed the tumor growth compared to non-targeted PEGylated NPs (CPDex NPs) and free DOX. However, this tumor growth suppression was greatly prohibited in the presence of free FA (2 mM). This could explain the observation that the tumor growth tendency of FADex NPs and FA-treated mice became similar to the one of CPDex NPs-treated mice [142].

A pH-sensitive folic acid-PEG-chitosan-PAMAM was designed (FPCPHD) to deliver plasmid DNA [276]. FPCPHD was prepared on the basis of a pH-sensitive core-shell system, which contains PEG tethered carboxylated chitosan modified FA, PAMAM dendrimer generation 4, high mobility group box 1 (HMGB1). In vitro evaluation showed that FPCPHD was resistant to heparin replacement and DNase I digestion at N/P ratio above 8 and 2, respectively. In vitro transfection analysis indicated that FPCPHD significantly enhanced luciferase and red fluorescence protein (RFP) gene transfection and expression in KB cells, compared to PAMAM/pDNA (PD), PAMAM/HMGB1/pDNA (PHD), CCTS/PAMAM/HMGB1/pDNA (CPHD), and PEG-CCTS/PAMAM/HMGB1/p-DNA (PCPHD) nanocomplexes. This enhancement could be significantly inhibited by pre-treatment of free FA at 1 mM in KB cells. Intracellular trafficking of FPCPHD in KB cells showed that FPCPHD rapidly escaped from endo-lysosomes and exclusively located in the nucleus at 3 h post transfection. In the S180 tumor-bearing BALB/c nude mice, i.v. administration of FPCPHD significantly increased RFP expression at the tumor site, compared to PD, PHD, CPHD, and PCPHD [276].

Self-assembled polyelectrolyte polyplexes of folate-dextran-siRNA via disulfide bonds and linear polyethylenimine (folate-DSC/LPEI) were reported for tumor-targeted systemic delivery of siRNA [118]. In vitro evaluation showed that the intracellular uptake of folate-DSC/LPEI was 3.2 times higher in the absence of free FA than presence of free FA at 1 mg/L in KB cells. In the GFP overexpressing-HeLa tumor-bearing nude mice, i.v. administration of folate-DSC/LPEI containing siGFP efficiently surpressed tumor GFP expression, compared to the ones treated with PBS and DSC/LPEI.[26] The biodistribution result showed that much higher

fluorescence intensity was observed in the tumor region compared to that from the mice treated with the naked siRNA/LPEI complexes. However, significant amounts of the folate-DSC/LPEI polyplexes accumulated in the liver and kidney [118].

3.3.5 Others

A molecular hydrogelator system of FA-Taxol conjugates was designed to improve Taxol therapeutic efficacy [303]. The hydrogels, made of glutathione (GSH), could trigger sustained release of Taxol through ester bond hydrolysis. In the 4T1-luciferase breast tumor-bearing mice, a single dose of i.t. administration of FA-Taxol hydrogel more potent than four doses of i.v. injection of free Taxol [303].

A folate receptor-targeted rhaponticin (FRHA) was synthesized via a releasable disulfide linker to improve RHA therapeutic efficacy [151]. In the FR-positive KB and M109 tumor-bearing Balb/c mice, i.v. administration of FRHA three times per week significantly inhibited tumor growth, compared to PBS and free RHA treatment. However, in the FR-negative 4T1 tumor-bearing Balb/c mice, i.v. administration of FRHA failed to suppress tumor growth, similar to PBS and free RHA treatments. Markedly, unlike free RHA, the mice treated with FRHA did not loss body weight, indicating no gross toxicity or adverse effects after FRHA therapy. PK profiles showed that FRHA was rapidly removed (half-life: about 10 min) from systemic circulation after i.v. administration to mice bearing FR-positive M109 cells, which was much faster than that in FR-negative 4T1 tumor-bearing mice or normal mice [151].

Folate-appended methyl-b-cyclodextrin (FA-M-β-CyD) was synthesized for delivery of doxorubicin [192]. In vitro evaluation showed that FA-M-β-CyD possessed increase cytotoxicity to KB cells, compared to M-β-CyD. This increase was significantly suppressed by pre-treatment of free FA at 1 mM. In the Colon-26 tumor-bearing BALB/c mice, single i.t. or i.v. administration of FA-M-β-CyD drastically inhibited the tumor growth, compared to control, doxorubicin, and M-β-CyD treated mice. Markedly, all of the tumor-bearing mice treated with FA-M-β-CyD survived for at least more than 140 days; whereas the others only survived for around 60 days. Additionally, FA-M-β-CyD treated mice showed no significant change in blood chemistry

values, including creatinine, blood urea nitrogen, aspartate aminotransferase, alanine aminotransferase, and lactate dehydrogenase [192].

Folic acid-anchored cucumber mosaic virus (FA-CMV) was synthesized for tumor-targeted delivery of doxorubicin (DOX) [323]. DOX was loaded into the interior cavity of CMV through the formation of DOX-RNA conjugate. In vitro evaluation showed that the intracellular uptake of DOX by FA-CMV-DOX was increased by 3 times in OVCAR-3 cells, compared to CMV-DOX or free DOX. This increase was significantly reduced in the presence of free FA at 1 mM. In the OVCAR-3 tumor-bearing BALB/c nude mice, i.p. administration of FA-CMV-DOX every five days significantly decreased the accumulation of DOX in mouse myocardial cells but increased the uptake of DOX in the ovarian cancer cells, compared to negative control, free DOX, and CMV-DOX treatment. Thus, FA-CMV-DOX possessed less cardiotoxicity but enhanced antitumor effect [323].

Folic acid conjugated single-walled carbon nanotubes (FA-SWNT) were developed to deliver paclitaxel. Non-toxic lipid molecule docosanol-conjugated paclitaxel (PTX) was loaded onto FA-SWNT via hydrophobic interactions (FA-SWNT-lipid-PTX) [232]. In vitro evaluation showed that FA-SWNT-lipid-PTX improved drug efficacy in MCF-1 cells, compared to free PTX and non-targeted SWNT-lipid-PTX. In the MCF-1 breast tumor-bearing nude mice, 4 doses of i.v. administration of FA-SWNT-lipid-PTX significantly suppressed tumor growth compared to free PTX and PBS treatment. At notice, no mortality and adverse effect was observed in SWNT-lipid-PTX-treated mice. Hematologic assessment (hematocrit, hemoglobin, red blood cell count and white blood cell count) and histological staining (liver, heart, lung, and kidney) showed no difference between control and SWNT-lipid-PTX-treated mice [232].

Folic acid-decorated poly(ethylene oxide)-*b*-poly(methacrylic acid)-cross-linked nanogels (FA-nanogels) were developed to deliver cisplatin (CDDP) or doxorubicin (DOX) [188]. The uptake of FA-nanogels in human ovarian carcinomas A2780 (FR-positive cells) greatly exceeded the uptake of the non-targeted nanogels. The in vitro competitive assay illustrated that FA-nanogels possessed much higher affinity

to cellular FR than free FA. In the A2780 ovarian tumor-bearing nude mice, tumor uptake of FA-nanogels was significantly higher than free CDDP and non-targeted nanogels at 4 days post i.v. administration. The increased uptake was significantly reversed by co-administration of free FA. As a result, i.v. administration of FA-nanogel/CDDP every four days significantly reduced tumor growth, compared to dextrose, nanogel alone, free CDDP, nanogel/CDDP, and FA-nanogel/CDDP in the presence free FA treatment.[32] It was observed that in the presence of 0.5 mM folate, the uptake of FA-nanogels was nearly 50% of the initial. In the presence of 10 mM FA, the uptake of FA-nanogels was suppressed to the level of the untargeted nanogels (20-25%), indicating FA-nanogels displayed much higher affinity to cellular FR than free FA. This may be beneficial for targeting in the body environment, where FA-nanogels would compete with free folate [188].

Doxorubicin-loaded folate-decorated silica nanorattles (DOX-FA-SNs) were developed to improve anti-tumor effects [65]. In HeLa tumor-bearing BALB/c nude mice, near infrared-labeled FA-SNs (ICG-FA-SNs) were distributed into the tumor at 4 hours post i.v. administration, and it retained in the tumor up to 24 hours. Subsequently, i.v. administration of DOX-FA-SNs every three days significantly suppressed tumor growth, compared to control, FA-SNs alone, free DOX, and non-targeted DOX-SNs [65].

3.4 Folate receptor-targeted nanoparticles for tumor imaging

Nanotechnology has been extensively applied to improve tumor imaging and diagnosis, including near-infrared (NIR) fluorescence imaging, magnetic resonance imaging (MRI), computed tomography (CT), ultrasonic imaging.

NIR fluorescence imaging is a highly sensitive, non-invasive, non-radiant technique for real-time in vivo monitoring of biological information [126]. Heparin-folic acid-IR-780 nanoparticles (HF-IR-780 NPs) were designed for in vivo tumor imaging

[322]. HF-IR-780 NPs were synthesized by self-assembly of the heparin-folic acid conjugates and NIR fluorescence dye-780 through ultrasonication [322]. In the MCF-7 tumor-breaing nude mice, the fluorescence signal was mainly located in the lung and liver at 1 h post-i.v. injection. The fluorescence signal in the tumor was detected at 3 h post-i.v. injection, and the signal intensity was observed at a much stronger in tumor tissue than in the lung and liver at 72 h post-i.v. injection. HF-IR-780 NPs treated mice showed stronger fluorescence intensity in the tumor tissue than free IR-780 in the excised tissue evaluation at 72 h post-injection [322].

Folic acid-modified trypsin-stabilized gold nanoclusters with NIR fluorescence (FA-try-AuNCs-NIR) was designed for cancer imaging [155]. In the Hela tumor-bearing nude mice, the fluorescence signal was detected immediately after i.t. injection of FA-try-AuNCs-NIR, and the signal in the tumor can remain up to 12 h. Moreover, after subcutaneous injection of FA-try AuNCs-NIR, the fluorescence signal was detected all over the whole body of the mice within 5 min. However, the signal intensity elevated at in the tumor site diminished at a slower rate than in the normal tissues [155].

A folate receptor-targeted aggregation-enhanced NIR emitting silica nanoprobe (SiNP-DFP-PEG-FA) was reported for in vivo tumor imaging [281]. Fluorenyl derivative DFP was encapsulated in the silica NPs, to which folic acid was conjugated via a PEG linkage, yielding SiNP-DFP-PEG-FA. In the HeLa tumor-bearing nude mice, fluorescence signal was detected in the tumor after 30 min post-i.v. injection of SiNP-DFP-PEG-FA. The tumor fluorescence intensity steadily increased and reached a peak at 6 h post-i.v. injection. However, no significant fluorescence signal was detected in the tumor of the mice injected with SiNP-DFP-PEG [281].

A stable self-assembled NP-gadolinium complex was designed to serve as a paramagnetic MRI contrast agent for in vivo tumor imaging [85]. The NPs were assembled via an ionotropic gelation process between poly-γ-glutamic acid-folic acid conjugates (PGA-FA) and fluorescently labeled chitosan conjugates (CH-A546). They were further complexed with gadolinium (Gd) to form a PGA-FA/CH-A546-Gd contrast agent. In the HeLa tumor-bearing nude mice, the MRI signal intensity in the

tumor site increased 34% at 2 h i.v. injection of PGA-FA/CH-A546-Gd contrast agent, compared to the untreated mice [85].

Folate-attached superparamagnetic iron oxide NPs (SPIONs) were used as a MRI contrast agent for in vivo tumor imaging [93]. SPIONs were encapsulated within poly(ethylene glycol)-poly(ε-caprolactone) (PEG-PCL) micelles, which contain folic acid at the distal ends of PEG chains. The resulting FA-PEG-PCL-SPIONs were tested in the BEL-7402 tumor-bearing nude mice. The change of MRI signal intensity was -41.2% in the tumor site at 3h post-i.v. injection of FA-PEG-PCL-SPIONs, a 2.5-fold increase compared to non-targeting PEG-PCL-SPIONs treated mice. It was observed that an ideal post-i.v. injection time window for MRI scanning was within 6 h for FA-PEG-PCL-SPIONs [93].

Radioiodinated tyrosine-click-folic acid conjugates (125I-tyrosine-click-folate) were synthesized for single-photon emission CT of tumor [218]. In the KB tumor-bearing nude mice, the CT signal in both tumor and kidney was achieved at 1 h post-i.v. injection of 125I-tyrosine-click-folate. Preinjection of potassium iodide and antifolate pemetrexed to the mice effectively reduced CT signal in the non-trageted organs, including thyroid gland and kidney, improving tumor-to-background contrast [218].

Folic acid-modified dendrimer-entrapped gold NPs (Au DENPs-FA) were used for X-ray CT imaging of human lung adenocarcinoma [271]. In the SPC-A1 tumor-bearing nude mice, Au DENPs-FA were uptaken by tumor tissue via i.v., i.t. or i.p. injection, allowing for effective CT imaging of tumor. Besides the tumor accumulation of Au DENPs-FA, a large amount of Au element was found in lung, spleen and liver, allowing these NPs to be cleared through the renal route and reticuloendothelial system (RES) [271].

Later, gadolinium (Gd) loaded Au DENPs-FA (Gd-Au DENPs-FA) were designed for targeted dual CT/MR imaging of tumors [32]. In the KB tumor-bearing nude mice, both CT value and MR signal in the tumor site increased by 200% and 152.7%, respectively at 24 h post-i.v. injection of Gd-Au DENPs-FA, compared to the Gd-Au DENPs-injected ones, allowing targeted dual mode CT/MR imaging of

tumors overspressing FR. These nanoprobes could be cleared out from the body in 96 h [32].

3.5 Summary

PEG-modified NPs can prolong the NPs half-life in the body, promote ligand-receptor binding, and hereby enhance accumulation of drug at the tumor site. When FA-decorated NPs arrive at a FR-positive tumor cell, FA can not only increase the retention of the NPs in the tumor mass but also facilitate the uptake of the NPs by FR-mediated endocytosis to exert their pharmacological effect. However, liver is a major storage organ of excess folate [171, 269]; liver and spleen are major organs that harbor large numbers of macrophages [255]; and kidney is a major organ for folate resorption [29]. Indeed, the weakness of this strategy remains that FA-decorated NPs can still be captured by the liver, spleen, and kidney.

Chapter 4

Folic Acid-Decorated PAMAM Dendrimer for Targeted Gene Delivery: Synthesis, Characterization, and In Vitro Evaluation

Preface: This chapter has been prepared as a research article.

Leyuan Xu, Shannon Andrews, W. Andrew Yeudall, Hu Yang

4.1 Abstract

In this work, a folic acid (FA)-conjugated polyamidoamine (PAMAM) dendrimer generation 4 labeled with fluorescein isothiocyanate (FITC) was designed for targeted nucleic acid delivery and tumor imaging. ^{1}H NMR, HPLC, and DLS were applied to characterize the synthesized dendrimer derivatives. Cellular uptake efficiency, targeting specificity, cytocompetibility, and transfection efficiency were evaluated using HN12 cells and coculture model of HN12-YFP cells with U87 cells. It was found that the cellular uptake of FITC-G4-FA conjugates and G4-FA/DNA polyplexes was in a

folate receptor (FR) dependent manner, as the evidence shown free FA significantly inhibited the cellular uptake of both conjugates and polyplexes. In the coculture model, G4-FA/DNA polyplexes were preferentially uptaken by FR-positive HN12 cells but not by FR-negative U87 cells. In contrast, the cellular uptake of FITC-G4 conjugates and G4/DNA polyplexes was non-selective. At the same weight ratio, G4-FA conjugates have been shown to be capable of both transfecting more cells and inducing higher gene expression than native G4 dendrimer. This work demonstrates that FA decoration on dendrimer/DNA polyplexes allows targeted nucleic acid delivery and results in enhanced gene transfection efficiency.

4.2 Introduction

Nanoparticles (NPs) have shown great potential for gene delivery. A number of nanocarrier delivery systems including dendrimers [132, 201, 270], liposomes [131, 143, 301, 311], polymeric micelles [177, 189, 122, 36, 317], linear polymers [327, 48], quantum dots [213, 304, 230, 148], and iron oxide nanoparticles [66], have been utilized to deliver genes and have demonstrated promising properties in gene delivery. Among these, dendrimers have been attracted considerable attentions. Dendrimers possess very low polydispersity and high functionality and have been recognized to be one of the most versatile compositionally and structurally controlled nanoscale building blocks for drug and gene delivery [297]. Dendrimers have received considerable attention in cancer drug delivery because of their capability of their advantages including (1) maintaining drug levels in a therapeutically desirable range, (2) increasing half-lives, (3) increasing solubility of drugs, (4) delivering a variety of drugs, (5) facilitating passage across biological barriers by transcytosis, (6) enabling rapid cellular entry, and (7) reducing side effects by targeted delivery [173, 187, 286].

Polyamidoamine (PAMAM) dendrimers bearing positive amine functionalities at the surface appear to be an ideal class of building blocks for ionic condensation with negatively charged nucleic acid (DNA/RNA) molecules. These polycationic dendrimers can form stable polyplexes with nucleic acids and aid efficient internalization

of nucleic acids mainly through endocytosis and membrane destabilization. Additionally, these dendrimers harbor tertiary amines within their interior. Both primary and tertiary amines can preferentially promote the intracellular release of nuclei acids in endosomes and lysosomes where the physiological pH drops to 5.5-6.0 and 5.0, respectively, via the "proton sponge" effect [117, 140, 172, 193, 249]. High generation polycationic dendrimers are excellent nanovectors able to deliver nucleic acids in vitro and in vivo, showing great potential for clinical applications [159, 209]. However, synthesis of high generation dendrimers on a large scale is technically demanding and difficult to meet the "good manufacturing practice" (GMP) grade required for further clinical trials [154]. Therefore, developing lower generation polycationic dendrimers via surface modification to enhance effective delivery constitutes a worthwhile goal.

Folate or folic acid (FA), also known as vitamin B_9, is essential for numerous body functions. Folate is a one-carbon donor for the synthesis of purine and thymidine, which are essential for synthesis of nuclei acids and indirectly for methylation of DNA, proteins, and lipids, via S-adenosyl methionine [29, 10]. Therefore, folate is important to facilitate rapid cell division and growth. Not only children, but also adults require folate to produce healthy red blood cells and prevent megaloblastic anemia [285]. However, humans cannot synthesize folates de novo; therefore, folate has to be supplied through diet to meet daily requirements. In adult tissues, folate or FA is mainly transported by two transporters, reduced folate carrier (RFC) and folate receptor. RFC is a ubiquitously expressed anion channeland is a ubiquitous low affinity but high capacity transporter. RFC possesses low folate-binding affinity (K_m = 1-10 μM) but a high FA-binding affinity (k_d < 1 nM). Folate receptor is a high affinity, low capacity transporter [6, 335]. Currently, three subtypes of folate receptors (FRs) have been identified, which are FRα, FRβ, and FRγ. These three FRs are cysteine-rich plycoproteins, which mediate folate uptake via endocytosis [29]. The expression of FRs is highly restricted to the cells important for embryonic development, including placenta and neural tubes, and folate resorption such as kidney [29]. Among them, FRα is most widely expressed at very low levels in normal tissues but at high levels in cancers including ovarian, pediatric ependymal brain, mesothelioma,

breast, colon, renal, lung tumors, and head and neck carcinomas, in order to meet the folate demand of rapidly dividing cells under low folate conditions [198, 52, 221].

In the last decade, FR-targeting drug delivery systems have been developed using different polymers such as liposomes [28, 334], polymeric micelles [214, 284], linear polymers [9, 149], and branched polymers [128, 121]. Dendrimer have also been developed for FR-targeted cancer drug delivery. For instance, methotrexate (MTX) and FA-conjugated, partially acetylated PAMAM dendrimer generation 5 (G5-FA-MTX) conjugates were shown to preferentially kill FR-positive cells in a coculture assay with both FR-positive and FR-negative cells and in a heterogeneous xenograft tumor model [180]. Noteworthy is that 70-90% of primary amines on the PAMAM dendrimer G5 surface were acetylated in order to decrease polydispersity during the synthesis and more importantly to neutralize positive surface charge of dendrimer, which can in turn reduce non-specific cellular uptake [128].

With this in mind, we hypothesized that FA-conjugated PAMAM dendrimer generation 4 (G4-FA) conjugates can enhance gene delivery in FR-positive cells in vitro. Plasmid DNA was complexed with G4-FA conjugates to form G4-FA/DNA polyplexes, as a means to neutralize positive surface charge of G4 dendrimer, and subsequently reduce non-specific cellular uptake of polyplexes. In this work, the fundamental aspects of the constructed G4-FA conjugates, including synthesis, characterization, mechanism of intracellular uptake, and transfection efficiency, were examined.

4.3 Materials and Methods

4.3.1 Materials

Diaminobutane (DAB) core polyamidoamine (PAMAM) dendrimer generation 4.0 (technical grade) was purchased from NanoSynthons (Mt. Pleasant, MI). Dimethyl sulfoxide (DMSO), folic acid (FA), Trifluoroacetic acid (TFA), formaldehyde solution (37 wt. % in H_2O), 1-ethyl-3-[3-dimethylaminopropyl] carbodiimide hydrochloride

(EDC), *N*,*N*-diisopropylethylamine (DIPEA), deuterium oxide (D2O; 99.9 atom % D), deuterated dimethyl sulfoxide (DMSO-*d*6), and fluorescein isothiocyanate (FITC) were purchased from Sigma-Aldrich (St. Louis, MO). Acetonitrile (ACN), water (HPLC grade), triton X-100, 4',6-diamidino-2-phenylindole (DAPI), sodium hydroxide, and phosphate-buffered saline (PBS) were purchased from Fisher Scientific (Pittsburgh, PA). Ethidium bromide, Dulbeccos modified Eagle medium (DMEM), trypsin-EDTA (0.25%), and penicillin-streptomycin (10,000 U/mL) were purchased from Life Technologies (Carlsbad, CA). Label IT Cy3 control plasmid was purchased from Mirus Bio (Madison, WI). Vectashield mounting media were purchased from Vector Laboratories (Burlingame, CA). Polyvinylidene difluoride (PVDF) membrane was purchased from Millipore (Billerica, MA). Western lightning Plus ECL was purchased from Perkin-Elmer (Waltham, MA). Cosmic calf serum (CS) and pMAX-GFP (pGFP) plasmid were purchased from Lonza (Walkersville, MD). GFP (sc-9996) and β-actin (ACTBD11B7) antibody were purchased from Santa Cruz Biotechnology (Santa Cruz, CA). SnakeSkin dialysis tubing with 7,000 molecular weight cut-off (MWCO) and folate receptor (FR) antibody were purchased from Thermo Scientific (Rockford, IL). Goat anti-rabbit antibody conjugated to horseradish peroxidase and goat anti-mouse antibody conjugated to horseradish peroxidase were purchased from Bio-Rad (Hercules, CA). WST-1 cell proliferation reagent, protease inhibitor and phosphatase inhibitor cocktail tablets were purchased from Roche Applied Science (Grand Island, NY). Propidium iodide (PI) was purchased from BD Biosciences (San Jose, CA).

4.3.2 Synthesis of PAMAM dendrimer conjugates

4.3.2.1 Synthesis of G4-FA conjugates

FA (18.6 mg, 42.2 μmol, MW = 441.4 g/mol) was allowed to react with EDC (113.3 mg, 590.9 μmol, MW = 191.71 g/mol) in a mixture of 12 mL of DMF and 4 mL of DMSO for 1 h. The organic reaction mixture was added dropwise to 50 mL of DI water solution containing 100 mg (7. 03 μmol) of PAMAM dendrimer G4 (MW = 14215 g/mol). The reaction mixture was vigorously stirred for 2 days and

then dialyzed against DI water using dialysis tubing with MWCO of 7 kDa for 2 days. After lyophilization (Flexi-Dry^{TM} MP corrosion resistant freeze-dryer), the resultant G4-FA conjugates were obtained. The number of FA molecules coupled to each G4 dendrimer was quantified by using GENESYS 6 spectrophotometer (Thermo Scientific, Rockford, IL).

4.3.2.2 Synthesis of FITC-G4-FA conjugates

FITC (4.9 mg, 12.67 μmol, MW = 389.38 g/mol) was dissolved in 1 mL of DMSO. The FITC solution was added dropwise to 9 mL of PBS containing 40 mg (2.53 μmol) of G4-FA conjugates (MW = 15783 g/mol by UV-Vis spectrophotometer) in the presence of 9.8 mg (76.03 μmol) of DIPEA (MW = 129.25 g/mL). The reaction mixture was stirred in the dark for 1 day and then dialyzed against DI water using dialysis tubing with MWCO of 7 kDa for 2 days. After lyophilization, the resultant FITC-G4-FA conjugates were obtained. The number of FITC molecules coupled to each G4-FA conjugate was quantified by using GENESYS 6 spectrophotometer.

4.3.2.3 Synthesis of FITC-G4 conjugates

FITC (5.5 mg, 14.07 μmol, MW = 389.38 g/mol) was dissolved in 1 mL of DMSO. The FITC solution was added dropwise to 9 mL of PBS containing 40 mg (2.81 μmol) of G4 dendrimer (MW = 14215 g/mol) in the presence of 10.9 mg (84.42 μmol) of DIPEA (MW = 129.25 g/mL). The reaction mixture was stirred in the dark for 1 day and then dialyzed against DI water using dialysis tubing with MWCO of 7 kDa for 2 days. After lyophilization, the resultant FITC-G4 conjugates were obtained. The number of FITC molecules coupled to each G4 dendrimer was quantified by using GENESYS 6 spectrophotometer.

4.3.3 High-performance liquid chromatography (HPLC)

The purity of the resultant G4-FA, FITC-G4-FA, and FITC-G4 conjugates were determined by HPLC. The reverse-phase HPLC (RP-HPLC) system (Waters, Milford,

MA) consisting of a system Waters 1515 isocratic HPLC pump, a model Waters 717plus autosampler, and a model Waters 2487 dual λ absorbance detector was used in this work. An XTerra particle-based RP-HPLC column (length 150mm, particle size 5 μm, RP18) was purchased from Waters (Milford, MA). The mobile phase for elution of PAMAM dendrimer and its derivatives was H_2O:ACN:TFA (750:250:0.38, v/v/v) at a flow rate of 1 mL/min [181]. All the samples were dissolved into the aqueous mobile phase. The detection of eluted samples was performed at 275 nm and 485 nm. The analysis was performed using the Breeze^{TM} software (Waters, Milford, MA).

4.3.4 Proton nuclear magnetic resonance (^{1}H NMR) spectroscopy

^{1}H NMR spectra were recorded on a Varian superconducting fourier-transform NMR spectrometer (Mercury-300) in the Nuclear Magnetic Resonance Center at Virginia Commonwealth University. D_2O and DMSO-*d*6 were used as the solvent. The ^{1}H chemical shift for D_2O residue and DMSO-*d*6 are 4.8 ppm and 2.5 ppm.

4.3.5 Paticle size and zeta potential measurements

PBS was filtered through a 20 nm filter. G4 dendrimer and its derivatives were dissolved in the filtered PBS at the concentration of 0.5 mg/mL. Various amounts of G4-FA conjugates (0 μg, 10 μg, 50 μg, and 200 μg) and G4 dendrimers (50 μg) were dissolved in 600 μL of filtered PBS; while 10 μg of pMAX-GFP plasmid was diluted in 400 μL of filtered PBS. The solutions were vortexed for 10 s and then equilibrated for 10 min at room temperature. The dendrimer solution was added to the plasmid solution, homogenized for 10 s with a vortex, and equilibrated for 30 min at room temperature. The size and zeta potential of G4 dendrimer, its derivatives, and polyplexes were measured at room temperature using a Malvern Zetasizer Nano ZS90 apparatus (Malvern Instruments, Worcestershire, U.K.).

4.3.6 Gel retardation assay

A series of G4-FA/plasmid polyplexes were prepared. 0 μg, 0.4 μg, 1 μg, 2 μg, 10 μg, 20 μg, and 40 μg of G4-FA conjugates were diluted in 300 μL of DMEM; while 2 μg of plasmid (p53 or pGFP) was diluted in 200 μL of DMEM. The solutions were mixed by vortexing for 10 s and then equilibrated for 10 min at room temperature. The G4-FA conjugates solution was added to the plasmid solution, homogenized for 10 s with a vortex, and equilibrated for 30 min at room temperature. The formation of G4-FA/DNA polyplexes was examined by electrophoretic mobility in an agarose gel. 20 μL of each polyplex was loaded into a 1% agarose gel containing ethidium bromide (0.5 μg/mL) and subjected to electrophoresis at 100 V for 1 h. The DNA bands were detected by a UV transilluminator (Alpha Innotech, ProteinSimple, San Jose, CA) [321].

4.3.7 Cell culture

Multiple cell lines including HN4 cells and HN6 cells, derived from a primary squamous cell carcinoma of the head and neck, HN12 cells derived from a synchronous lymph node metastasis, T98, U87, and U1242 glioblastoma cells were used in the studies; and NIH3T3 mouse fibroblasts were used as a negative control. All the cells were cultured in Dulbeccos modified Eagles medium (DMEM) supplemented with 10% Cosmic calf serum, 100 units/mL of penicillin, and 100 μg/mL of streptomycin at 37 °C in 95% air/5% CO_2 as described previously [215, 200, 272, 273, 73, 320].

4.3.8 Polyplex formation

For in vitro cellular uptake assessment, a solution of G4-FA/Cy3-plasmid, G4/Cy3-plasmid, or FITC-G4-FA/Cy3-plasmid polyplexes was prepared accordingly. 5 μg of G4-FA conjugates, G4 dendrimer, or FITC-G4-FA conjugates was diluted in 300 μL of DMEM; while 1 μg of Cy3-plasmid was diluted in 200 μL of DMEM.

For in vitro gene transfection assessment, a series of G4-FA/plasmid and G4/plasmid polyplex solutions were prepared accordingly. 2 μg, 10 μg, and 40 μg of

G4-FA conjugates or 40 μg of G4 were diluted in 300 μL of DMEM; while 2 μg of plasmid (pMAX-GFP or pCEFL-YFP) was diluted in 200 μL of DMEM.

All the solutions were well mixed by vortexing for 10 s and then equilibrated for 10 min at room temperature. The G4-FA conjugates solution or G4 dendrimer solution was added to the plasmid solution, homogenized for 10 s with a vortex, and equilibrated for 30 min at room temperature. Then 2.5 mL of the complete medium containing 10% serum was added into the polyplex solution, and the final volume brought to 3 mL. PBS was used as experimental negative controls [159, 154].

4.3.9 Fluorescence microscopy

For in vitro cellular uptake assessment, HN12 cells were seeded in the 6-well plates at a density of 20,000 cells/well and allowed to attach overnight. In the coculture assessment, YFP-overexpressed HN12 cells (HN12-YFP) and U87 cells were seeded in the 6-well plates at the same density of 10,000 cells/well and allowed to attach overnight. Before addition of the transfection medium, the spent medium was removed, and the cells were washed with PBS once. The cells were treated with FITC-G4 (10 μg/mL), FITC-G4-FA (10 μg/mL), FITC-G4/Cy3-plasmid and FITC-G4-FA/Cy3-plasmid polyplexes (described above) in the absence or presence of free FA (0.5 mg/mL) at 37 °C for 0, 1, 6, and 24 h.

For in vitro GFP transfection assessment, HN12 cells were seeded in the 6-well plates at a density of 20,000 cells/well and allowed to attach overnight. Before addition of the transfection medium, the spent medium was removed, and the cells were washed with PBS once. The cells were treated with G4-FA/pGFP polyplexes and G4/pGFP polyplexes (described above) in the absence of free FA at 37 °C for 48 h. The spent medium was then replaced with the complete medium containing 10% serum and maintained under normal growth conditions for another 48 h.

At the end of each treatment, HN12 cells were washed with PBS for three times, fixed with 4% formaldehyde at room temperature for 20 min, washed with PBS for three times, permeated with 0.1% Triton X-100 for 5 min, and washed with PBS for three times. The cell nuclei were counterstained with DAPI for 5 min, and

the cells were washed with PBS for three times. Fluorescent images were taken using a Zeiss Axiovert 200 inverted fluorescence microscope using a magnification of 20× (Carl Zeiss Microimaging, Thornwood, NY). A 405 laser line was selected for DAPI, a 488 laser line was selected for GFP/YFP/FITC, and a 543 laser line was selected for Cy3 [321].

4.3.10 Intracellular trafficking studies

HN12 cells were seeded onto microscope glass coverslips (Fisher Scientific, Pittsburgh, PA) in the 6-well plates at a density of 20,000 cells/well and allowed to attach overnight. Before addition of the transfection medium, the spent medium was removed, and the cells were washed with PBS once. The cells were then treated with FITC-G4-FA/Cy3-plasmid polyplexes (described above) at 37 °C for 24 h. At the end of treatment, the cells were washed with PBS for three times, fixed with 4% formaldehyde at room temperature for 20 min, washed with PBS for three times, permeated with 0.1% Triton X-100 for 5 min, and washed with PBS for three times. The cell nuclei were counterstained with DAPI (blue) for 5 min, and the cells were washed with PBS for three times. The coverslips were mounted on the slides and imaged under a Zeiss LSM 700 confocal laser scanning microscope using a magnification of 630× in the Microscope Core Facility at Virginia Commonwealth University [298].

4.3.11 Flow cytometry

HN12 cells were first seeded in the 60-mm dishes at a density of 50,000 cells/dish and allowed to attach overnight. Before addition of the transfection medium, the spent medium was removed, and the cells were washed with PBS once.

For in vitro cellular uptake assessment, the cells were treated with FITC-G4 (10 μg/mL), FITC-G4-FA (10 μg/mL), FITC-G4/Cy3-plasmid and FITC-G4-FA/Cy3-plasmid polyplexes (described above) in the absence or presence of free FA (0.5 mg/mL) at 37 °C for 0, 1, 2, 6, and 24 h. Then, HN12 cells were washed with PBS for three times, resuspended using trypsin for 5-10 min, centrifuged, washed with

PBS once, and transferred to microcentrifuge tubes. The mean fluorescence intensity (MFI) of FITC and Cy3 of the cells were analyzed by using a Guava EasyCyte mini flow cytometry system (Millipore, Billerica, MA) [159, 154].

For in vitro GFP transfection assessment, the cells were treated with G4-FA/pGFP polyplexes and G4/pGFP polyplexes (described above) in the absence of free FA at 37 °C for 48 h. The spent medium was replaced with the complete medium containing 10% serum and maintained under normal growth conditions for another 48 h. Then, HN12 cells were washed with PBS for three times, resuspended using trypsin for 5-10 min, centrifuged, washed with PBS for three times, fixed in 4% formadehyde at room temperature for 20 min, washed with PBS for three times, permeated with 0.1% Triton X-100 for 5 min, and washed with PBS for three times, and incubated with 50 μg/mL of PI and 40 μg/mL of RNase at 37 °C for 30 min. The GFP-expressing cell population was then analyzed by using a Guava EasyCyte mini flow cytometry system [321].

4.3.12 Cell viability assessment

HN12 cells were seeded in a 96-well plate at a density of 10,000 cells/well and allowed to attach overnight. For polymer cytocompatibility assessment, the cells were treated with G4 (0-1000 μg/mL) and G4-FA (0-1000 μg/mL) at 37 °C for 48 h. For polyplex cytocompatibility assessment, the cells were treated with G4/pGFP plasmid and G4-FA/pGFP plasmid polyplexes (described above) at 37 °C for 48 h, followed by another 48 h culture in a medium supplemented with 10% Cosmic calf serum. At the end of each treatment, the cell viability was determined by WST-1 cell proliferation assay following the manufacturer's protocol. The relative cell viability was normalized with respect to the viability of the control PBS-treatment group. Briefly, immediately following treatment, the spent media were removed, and the cells were incubated with 100 μL of fresh cell culture media and 10 μL of WST-1 reagent in for 30 min. The absorbance of each sample solution was then measured at 450 nm against a background control as blank. The wavelength of 650 nm was used as the reference wavelength [298, 293, 294].

4.3.13 Western Blotting

For FR expression assessment, HN4, HN6, HN12, T98, U87, U1242, and NIH3T3 cells were seeded in the 6-well plates at a density of 20,000 cells/well. The cells were harvested using cell lysis buffer containing protease and phosphorylase inhibitors when they reached 80% confluence.

For gene transfection assessment, HN12 cells were first seeded in the 6-well plates at a density of 20,000 cells/well and allowed to attach overnight. Before addition of the transfection medium, the spent medium was removed, and the cells were washed with PBS once. The cells were then treated with G4-FA/pGFP polyplexes and G4/pGFP polyplexes (described above) at 37 °C for 48 h. At the end of the GFP transfection, the spent medium was replaced with the complete medium containing 10% serum and maintained under normal growth conditions for another 48 h. At the end of each treatment, the cells were harvested using cell lysis buffer containing protease and phosphorylase inhibitors.

Western blot analysis of total cellular protein was carried out following procedures described previously [298, 293, 294]. Briefly, total cell lysates (30 μg) were separated on a 10% SDS-PAGE gel and transferred onto a polyvinylidene difluoride (PVDF) membrane. The membrane was blocked in Tris-buffered saline (TBS) containing 5% non-fat dry milk for 2 h at room temperature and then incubated in a 1:1000 dilution of primary antibody in blocking buffer overnight at 4 °C with shaking. The membrane was washed with TBS containing 0.5% Tween 20 (TBST) for three times and then incubated in a 1:3000 dilution of appropriate secondary antibody in TBST at room temperature for 2 h. The specific antigen-antibody interactions were detected using enhanced chemiluminescence. The protein expression of β-actin (ACTB) was used as a loading control.

4.3.14 Statistical Analysis

The curve fitting models were compared by running Akaike information criterion (AIC) test to determine a model that best fits experimental data using GraphPad

Prism 5 (La Jolla, CA). Models with lower AIC values are more likely to be correct [293, 310]. All the data were expressed as means ± standard deviation (SD) or standard error of the mean (SEM). The statistical analysis was performed by Students t-test for comparison. A value of $p < 0.05$ was considered statistically significant.

4.4 Results and Discussion

4.4.1 Relative folate receptor α (FRα) expression level

As reported, both human head and neck cancer cell line KB-3-1 and esophageal cancer cell line EC9706 have high expression of FRα. In the current work, the FR expression levels were evaluated in head and neck cancer cell lines and glioblastoma cell lines. The NIH3T3 cells were used as FRα-negative control. As shown in Figure 4.1, glioblastoma T98 and U1242 cells possessed relatively high expression levels of FRα. In contrast, all three head and neck squamous cell carcinoma HN4, HN6, and HN12 cells possessed high expression level of FRα. Noteworthy is that HN12 cell, derived from a primary synchronous lymph node metastasis, can be used to establish a clinically relevant model. Therefore, HN12 cells were used in the study of drug delivery for head and neck squamous cell carcinoma.

4.4.2 Design and synthesis of folic acid-decorated DAB-core PAMAM dendrimers

4.4.2.1 Synthesis of G4-FA conjugates

The strategy used to synthesize FITC-G4-FA conjugates is illustrated in Scheme 4.2. The purity of G4-FA conjugates was analyzed using HPLC. TFA was included in the mobile phase as a counterion to neutralize dendrimer surface charges [235]. The detection wavelength was selected at 275 nm, which was the characteristic maximum absorption wavelength of FA according to the UV-Visible absorption spectrum shown in Figure 4.3. Free FA has a retention time at 1.48 min (Figure 4.4a). After coupling

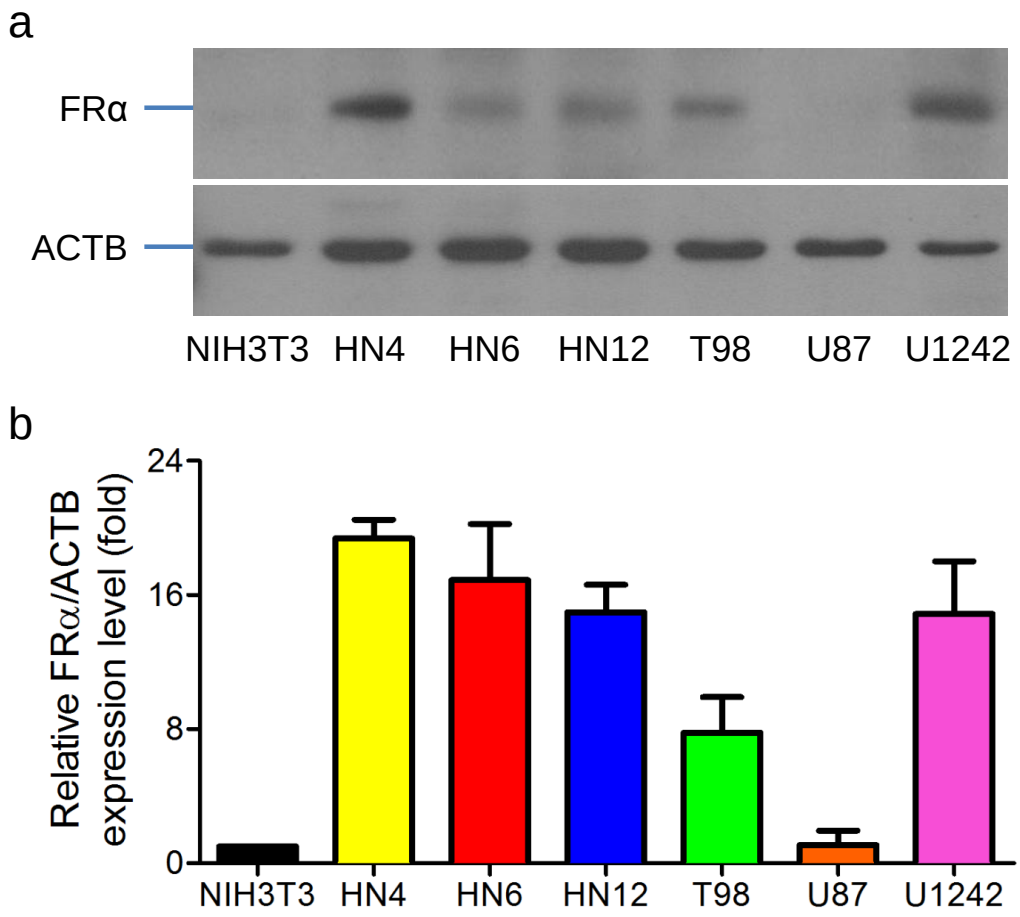

Figure 4.1: Endogenous expression level of folate receptor (FR). Total cell lysates of NIH3T3, HN4, HN6, HN12, T98, U87, and U1242 cells were harvested at 80% confluence. The protein expression level of FR was determined by Western blot analysis, and the expression level of β-actin (ACTB) was used as a loading control of total cellular protein (a). Each positive FR band was normalized to ACTB and was quantified by NIH ImageJ (b). The data represents typical one of three experiments. The bars and error bars are mean $\pm$ SEM. n = 4.

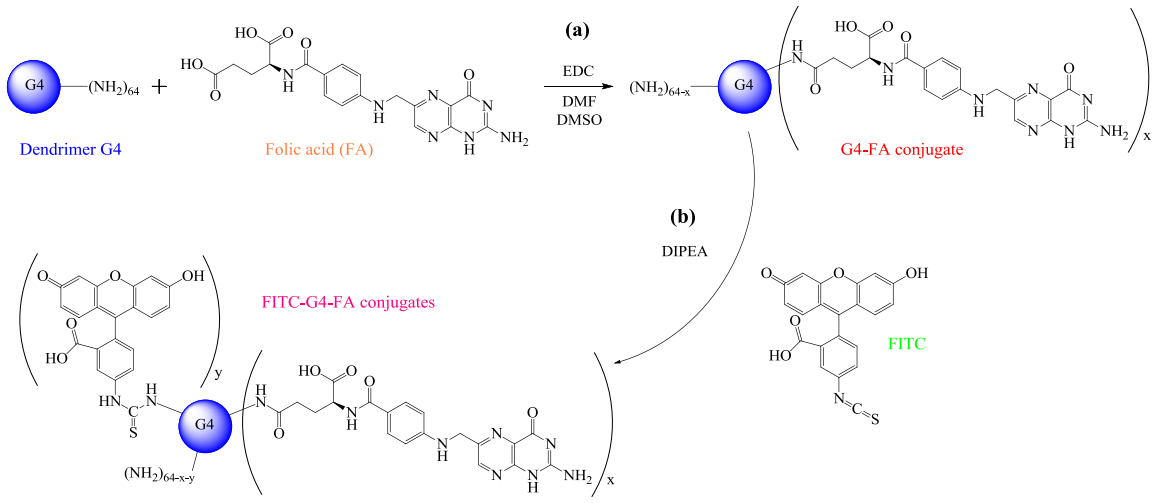

Figure 4.2: Synthetic scheme of FITC-G4-FA conjugate.
Synthesis of dendrimer-folic acid (G4-FA) conjugates (a). Labeling G4-FA conjugates with FITC (b).

reaction of G4 dendrimer and FA, the HPLC chromatogram of the resulting conjugates displays two separated peaks at 1.02 and 1.40 min. Because G4-FA conjugates are much more hydrophilic than free FA, G4-FA conjugates move faster than free FA through the C18 column. Thus, the peak at 1.02 min denotes G4-FA conjugates, whereas the peak at 1.40 min denotes unconjugated FA (Figure 4.4b). By calculating the area under the curve (AUC), the conjugation efficiency of G4-FA was about 80%. The conjugates were then purified using a dialysis tubing with 7,000 MWCO against DI water. The HPLC chromatogram of the purified G4-FA conjugates exhibits only one peak at 1.03 min (Figure 4.4c), indicating free FA was mostly removed. By calculating the AUC, the purity of G4-FA conjugates was above 97%.

Similar, ^{1}H NMR was employed to further confirm the presence of FA in the G4-FA conjugates. The ^{1}H NMR spectrum of FA is shown in Figure 4.5. The ^{1}H NMR spectra of purified G4-FA conjugates in DMSO-*d*6 and D_2O are shown in Figure 4.6 and 4.7, respectively. Both ^{1}H NMR spectra confirm the presence of the aromatic proton peaks of FA (8.5, 7.6, 6.6 ppm) and G4.0 (multiple methylene proton peaks between 3.8 and 2.1 ppm), indicating FA was successfully conjugated onto

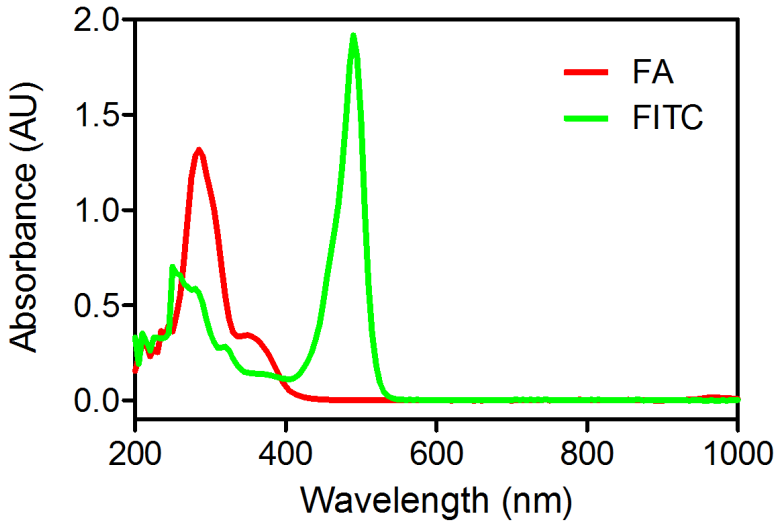

Figure 4.3: Absorption spectra of folic acid (FA) and fluorescein isothiocyanate (FITC).
The absorption spectrum of FA and FITC were determined by ultraviolet-visible (UV-Vis) spectroscopy.

G4 dendrimer.

UV-Visible spectroscopy was employed to determine an average number of FA coupled to G4 dendrimer. A standard curve of FA at serial concentrations measured at a wavelength of 275 nm was generated (Figure 4.8a). UV-Visible spectroscopy analysis confirmed that an average of 3.5 FA molecules was successfully conjugated onto G4 dendrimer, yielding G4-FA conjugates with a molecular weight of 15783 g/mol.

4.4.2.2 Synthesis of FITC-G4-FA and FITC-G4 conjugates

In order to determine and track intracellular uptake of G4-FA conjugates, we further labeled G4-FA conjugates with FITC and used FITC-labeled G4 for comparison. The detection wavelength was 485 nm, one of the characteristic maximum absorption wavelengths of free FITC, and it has limited absorption interference with FA (Figure

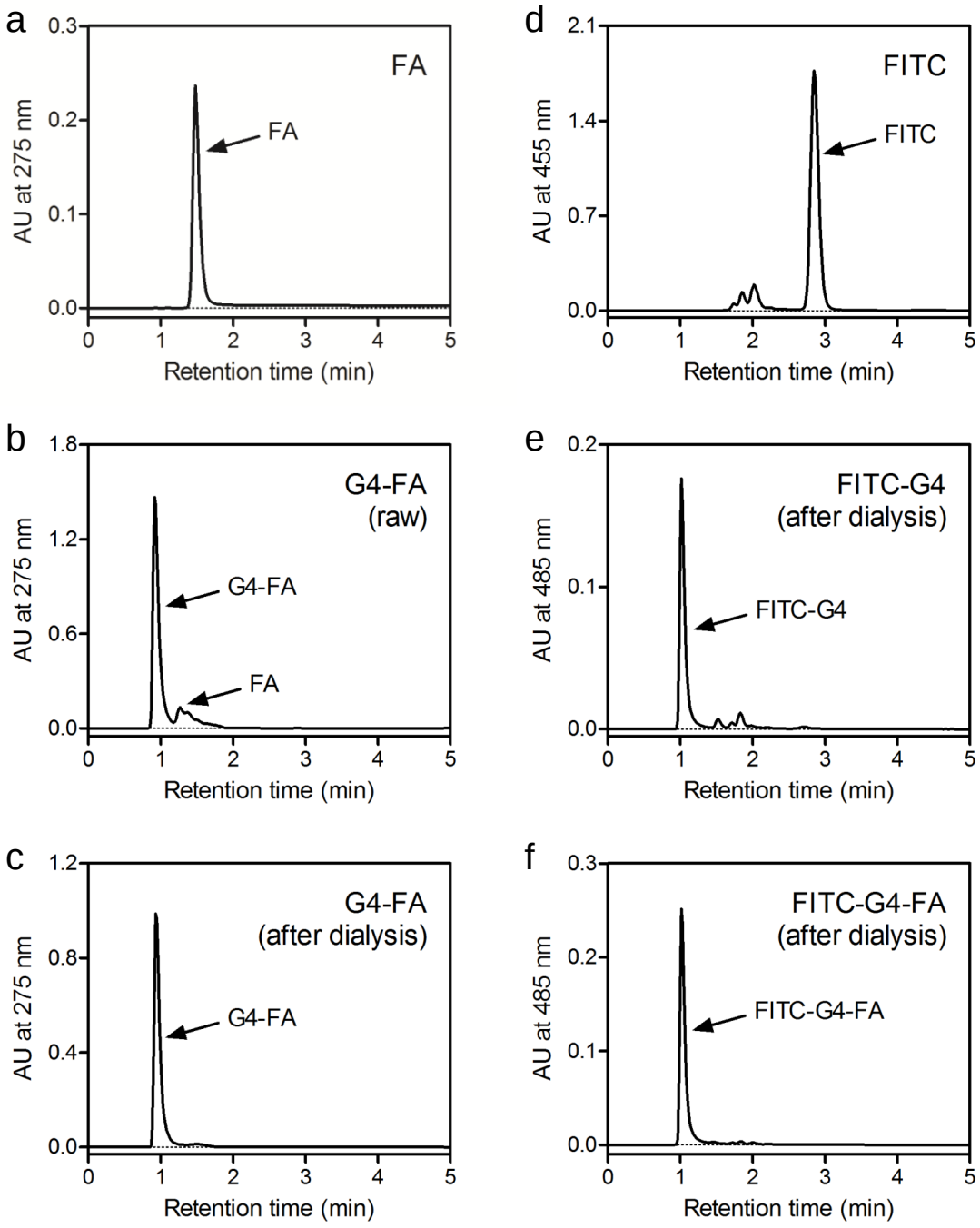

Figure 4.4: HPLC analysis of dendrimer derivatives.
FA standard (a), unpurified G4-FA conjugates (b), G4-FA conjugates after dialysis (c), FITC standard (d), FITC-G4 conjugates after dialysis (e), and FITC-G4-FA conjugates after dialysis (f).

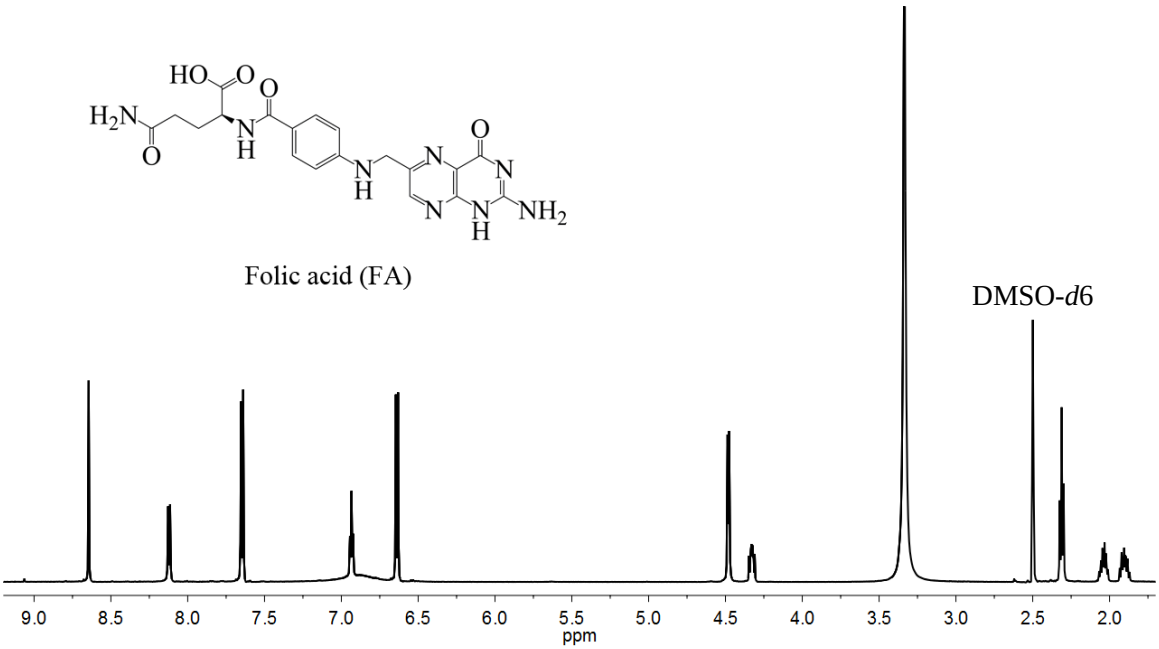

Figure 4.5: ^{1}H NMR spectrum of FA in DMSO-*d*6.

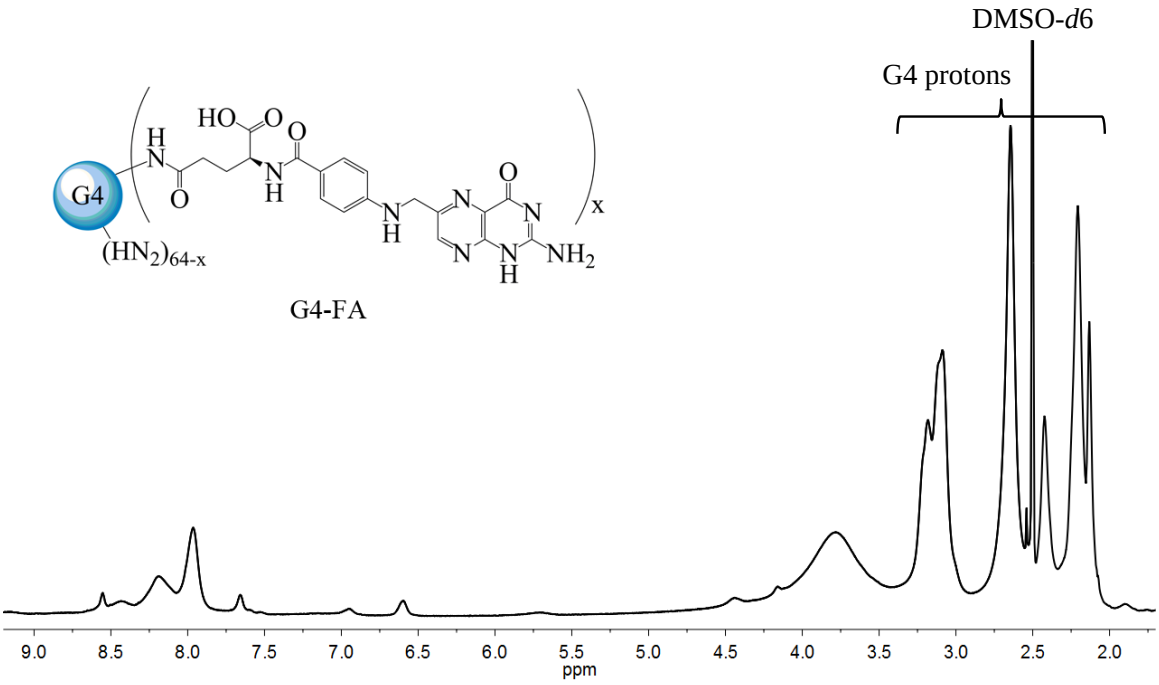

Figure 4.6: ^{1}H NMR spectrum of G4-FA conjugates in DMSO-*d*6.

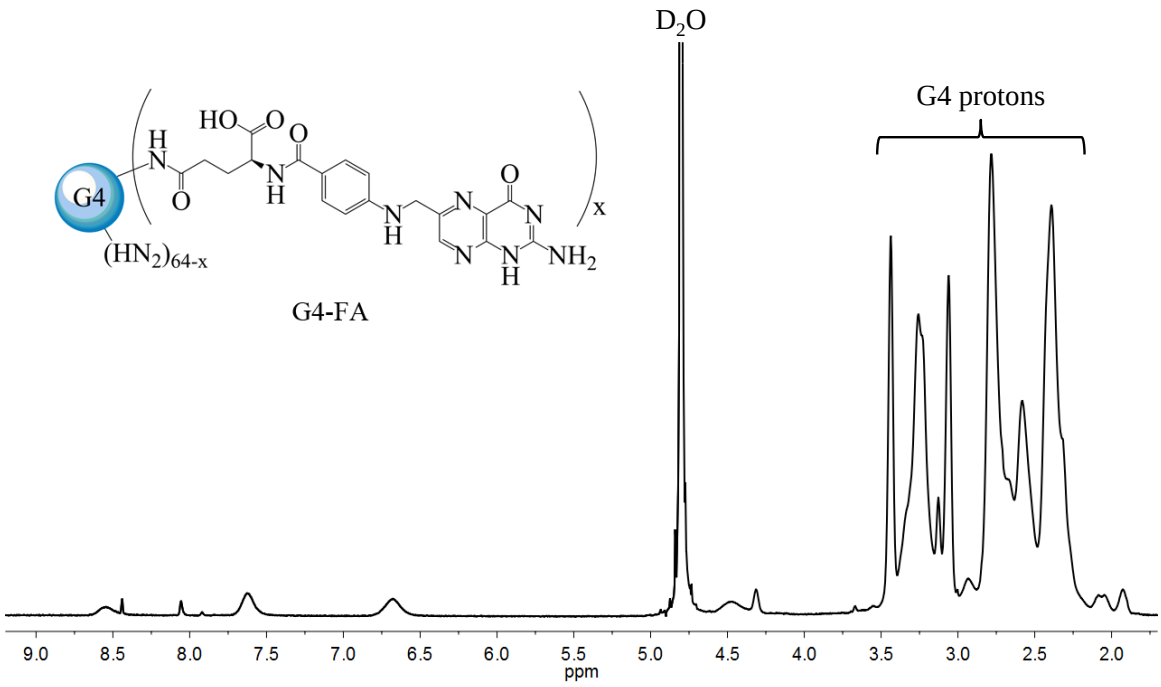

Figure 4.7: ^{1}H NMR spectrum of G4-FA conjugates in D_2O.

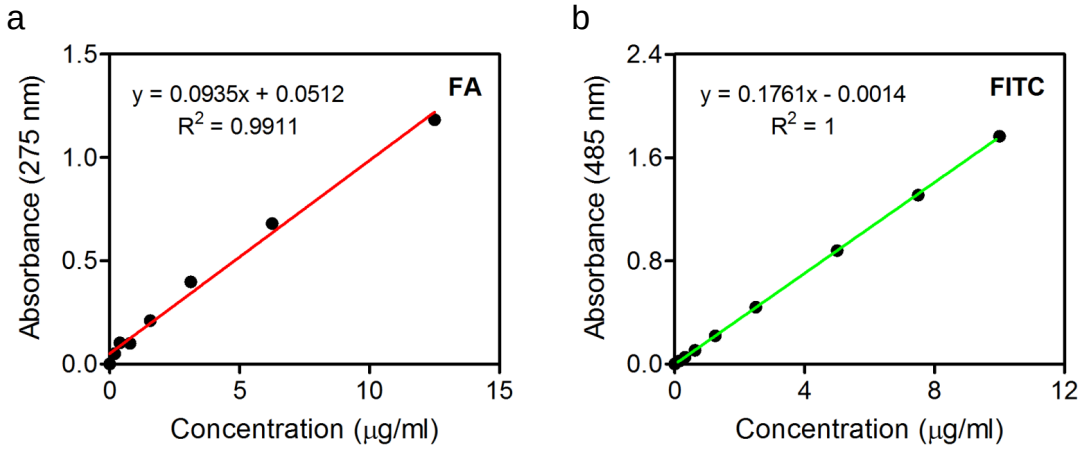

Figure 4.8: Standard curves of FA (a) and FITC (b).

Table 4.1: Molecular weight of dendrimer and its derivatives

Dendrimer and its derivatives	Coupling ratios	Molecular weight (g/mol)	Moles of 10 μg of polymers (nmol)
G4	n/a	14215	0.7035
G4-FA	1 : 3.5	15783	0.6336
FITC-G4-FA	2.3 : 1 : 3.5	16676	0.5997
FITC-G4	2.2 : 1	15070	0.6636

Abbreviation: n/a, not applicable.

4.3). HPLC analysis was applied to confirm purity of FITC-labeled dendrimers. Free FITC has a retention time of 2.85 min (Figure 4.4d). The small peaks at retention times of 1.73 and 2.02 min were attributed to the impurity of commercial FITC ($\geq$ 90%). The HPLC chromatogram of the purified FITC-G4-FA and FITC-G4 conjugates exhibits mainly one peak at 1.02 min (Figure 4.4e-f), indicating free FITC was mostly removed from the conjugates. By calculating the AUC, the purity of FITC-G4-FA and FITC-G4 conjugates is 97% and 95%, respectively. Because very limited absorption of FA at absorption wavelength of 485 nm, UV-Visible spectroscopy analysis at 485 nm was employed to determine the efficiency of coupling FITC to G4-FA conjugates and G4 dendrimer (Figure 4.8b). The results confirmed that an average of 2.3 and 2.2 FITC molecules were successfully conjugated onto each G4-FA conjugate and G4 dendrimer, respectively. The molecular weight of dendrimer and its derivatives were summarized in Table 4.1.

4.4.3 Characterization of dendrimer and its derivatives

PAMAM dendrimers generation 4 (G4) possess cationic primary amine groups at the surface that can beused to complex nuclear acids, including plasmids and small interference (si)RNA, and foster the cellular uptake of these nuclear acids [297]. We first determined whether surface modification of G4 dendrimer with FA could affect the zeta potential and particle size. DLS results showed the zeta potential of G4-FA, FITC-G4-FA, and FITC-G4 conjugates remained positive, which is essential for polyplexation (Figure 4.9). Noteworthy is that the zeta potential of G4-FA conjugates

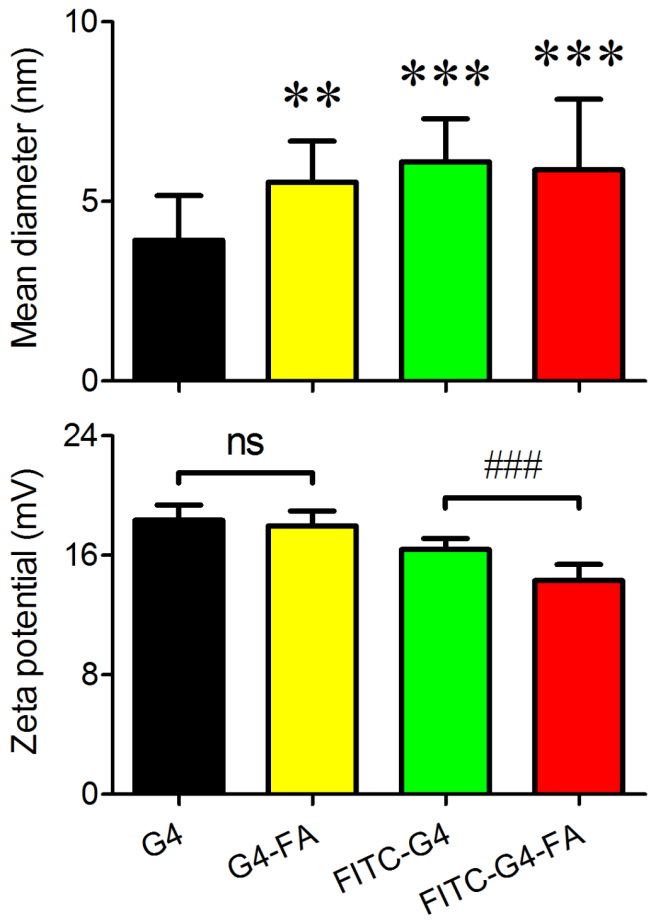

Figure 4.9: Particle sizes and zeta potentials of G4 dendrimer, G4-FA, FITC-G4-FA, and FITC-G4 conjugates were determined by dynamic light scattering (DLS).
The bars and error bars are means ± SD. n = 6-9. * $p < 0.05$, ** $p < 0.01$, and *** $p < 0.001$ versus G4 dendrimer. ### $p < 0.001$ versus FITC-G4 conjugates.

was not significantly different from that of G4 dendrimer; however, the zeta potential of FITC-G4-FA conjugates was significantly lower than that of FITC-G4 conjugates. Generally, higher zeta potential of NPs can result higher non-specific cellular uptake [30, 89]. Thus, the cellular uptake of FITC-G4 conjugates may be reasonably believed to be higher than that of FITC-G4-FA conjugates in the later study. The size of G4-FA, FITC-G4-FA, and FITC-G4 conjugates significantly increased compared to that of G4 dendrimer (Figure 4.9), reflecting the surface modification made on the dendrimer in this work.

Cytocompatibility of dendrimer and its derivatives play an important role in successful gene delivery. Our previous work showed that the cytocompatibility of PAMAM dendrimers are dependent on multiple factors including dose, generation, surface composition, and incubation period [319]. The current study showed both G4 dendrimer and G4-FA conjugates decreased HN12 cell viability in a dose-dependent manner (Figure 4.10a). In details, the viabilities of HN12 cells treated with both G4 dendrimer and G4-FA conjugates at 1 μg/mL or below for 48 h were over 86% and 91%, respectively. However, the viability of HN12 cells treated with G4 dendrimer at 10 μg/mL for 48 h reduced to 58%, whereas that the viability of HN12 cells treated with G4-FA conjugates at 10 μg/mL for 48 h remained 89%. By plotting cell viability against concentration in log scale, a linear regression was observed for both G4 dendrimer and G4-FA conjugate treatment (Figure 4.10b). By calculation, the half maximal inhibitory concentrations (IC_{50}) of G4 dendrimer and G4-FA conjugates were 67 μg/mL and 159 μg/mL, respectively. By converting weight concentration to molar concentration, the IC_{50} of G4 dendrimer and G4-FA conjugates were 4.7 μM and 10.1 μM, respectively (Figure 4.10c). A 2.4-fold increase (weight concentration) or 2.1-fold increase (molar concentration) in cytocompatibility was achieved after surface modification of G4 dendrimer with FA.

4.4.4 Characterization of polyplexes

G4-FA/pGFP polyplexes at different weight ratios were prepared (4.2). With the information on the molecular weights and the quantities of primary amines of G4 dendrimer and G4-FA conjugate as well as the quantities of bases and phosphates of pMAX-GFP plasmid, the molar ratios and the nitrogen/phosphate (N/P) ratios of polyplexes were calculated and are presented in Table 4.2. The stability of polyplex formation was characterized by a gel retardation assay to indicate the biophysical properties of G4-FA vectors. G4-FA conjugates were complexed with p53 plasmid at various weight ratios (0-10). According to the gel retardation assay (Figure 4.11a), at a weight ratio of 1 or higher, the polyplexes of G4-FA/p53 plasmid remain immobile.

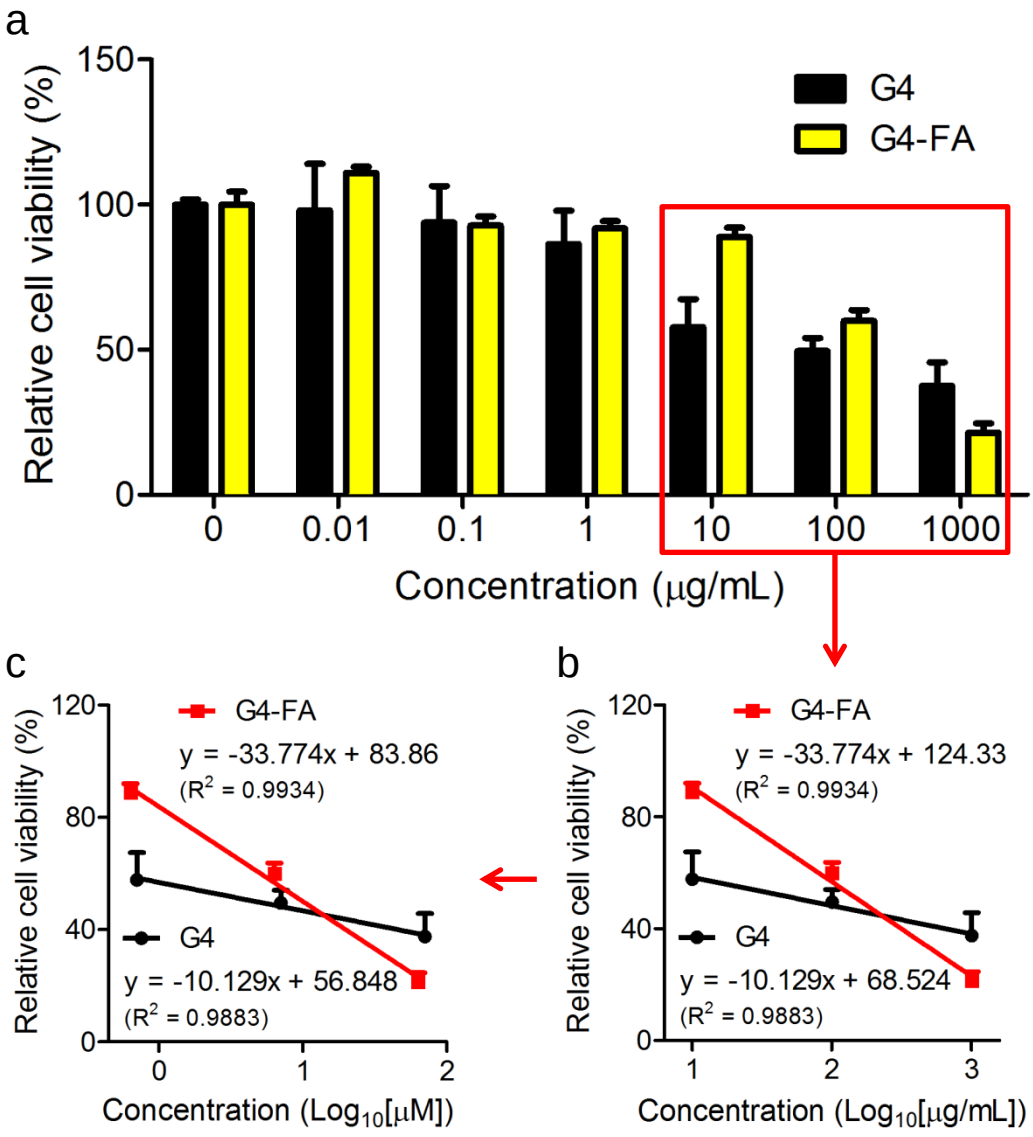

Figure 4.10: Cytocompatibility of G4 dendrimer and G4-FA conjugate. Cell viabilities of HN12 cells treated with G4 dendrimer and G4-FA conjugates at indicated concentrations were determined by WST-1 assay and normalized to untreated cells (a). Concentration-response curves of G4 dendrimer and G4-FA conjugate were determined at the concentration of 10 μg/mL and above. Concentrations in $\text{Log}_{10}(\mu\text{g/mL})$ against cell viability (b), concentration in $\text{Log}_{10}(\mu\text{M})$ against cell viability (c). The bars/dots and error bars are means $\pm$ SD. n = 4-6.

Table 4.2: Weight, molar, and nitrogen/phosphate (N/P) ratios of G4-FA conjugate and G4 dendrimer to plasmid

Polyplex	Weight ratio	Molar ratio	N/P ratio
G4-FA/pMAX-GFP	0.2	27	0.2
	0.5	67	0.6
	1	134	1.2
	2	268	2.5
	5	671	6.2
	10	1342	12.3
	20	2683	24.6
G4/pMAX-GFP	5	745	6.8

This result was further confirmed by using pMAX-GFP plasmid. G4-FA conjugates were complexed with pMAX-GFP plasmid at various weight ratios (0-20). According to the gel retardation assay (Figure 4.11b), at a weight ratio of 1 or higher, the polyplexes of G4-FA/pGFP plasmid remain immobile. Additionally, at weight ratios of 0.2 and 0.5, the DNA plasmid also showed retarded mobility on the gels. At weight ratios of 10 and 20, the DNA plasmid migrated in the opposite direction on the gels. Taken together, these results indicate that 1 is a minimal weight ratio for tight condensing of plasmid with G4-FA conjugates. This study illustrates the minimal weight ratio required for G4-FA vectors to neutralize the negatively charged plasmid and form stable polyplexes.

Furthermore, the zeta potential of polyplexes was measured by DLS. pMAX-GFP plasmid is a circular and double-stranded DNA molecule, composed of about 4700 base pairs. Each base pair contains a phosphate group, which results an overall negative charge of DNA plasmid. As expected, pMAX-GFP plasmid has a negative zeta potential of -19 mV (Figure 4.12). At a weight ratio of 1, G4-FA/pGFP polyplexes displayed a negative zeta potential of -22 mV, which was not significantly different from that of pMAX-GFP plasmid. At weight ratios of 5 and 20, the zeta potential of G4-FA/pGFP polyplexes significantly increased from -19 mV to -2 mV. These results suggest that G4-FA/pGFP polyplexes can be formed at a weight ratio of 1 or above; however, at a weight ratio of 1 (molar ratio of 134), the number of G4-

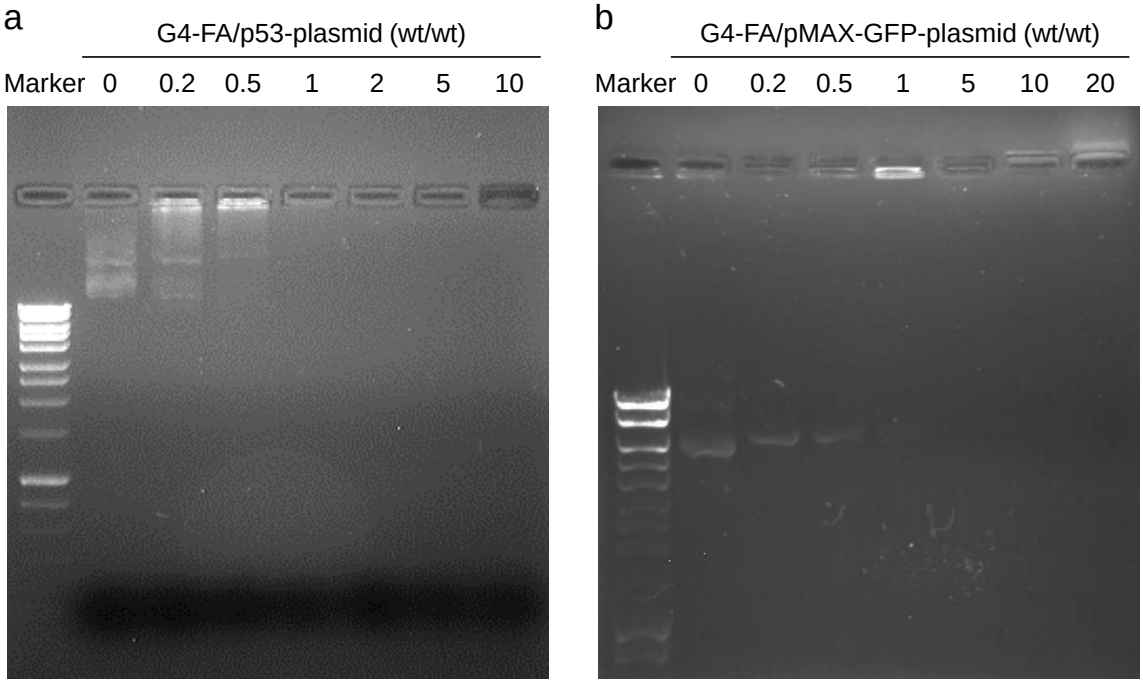

Figure 4.11: Gel retardation assay.
G4-FA/p53-plasmid polyplexes at weight ratios of 0, 0.2, 0.5, 1, 2, 5, and 10 (a). G4-FA/pMAX-GFP-plasmid polyplexes at weight ratios of 0, 0.2, 0.5, 1, 5, 10, and 20 (b).

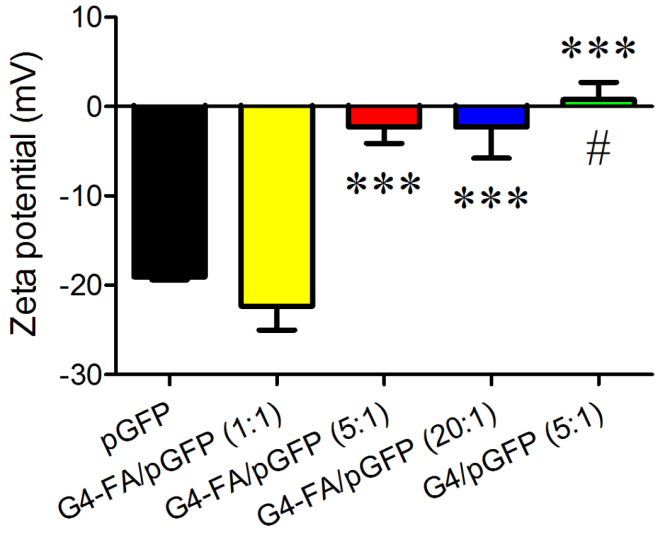

Figure 4.12: Zeta potentials of pMAX-GFP plasmid (pGFP), G4-FA/pGFP polyplexes at weight ratios of 1, 5, and 20, and G4/pGFP polyplexes at a weight ratio of 5 were determined by dynamic light scattering (DLS).
The bars and error bars are means ± SD. n = 5-6. *** $p < 0.001$ versus pGFP plasmid; # $p < 0.05$ versus G4-FA/pGFP polyplexes at a weight ratio of 5.

FA conjugates may be not high enough to complex the pMAX-GFP plasmid, which results an overall negative surface charge of -22 mV. At weight ratios of 5 and 20 (molar ratio of 671 and 2683), the pMAX-GFP plasmid can be sufficiently shielded by G4-FA conjugates in complexation, bringing the surface charge of polyplexes up to -2 mV. In contrast, the zeta potential of G4/pGFP polyplexes at a weight ratio of 5 was determined to be 1 mV. The increased zeta potential of G4/pGFP polyplexes may lead to a higher non-specific uptake than G4-FA/pGFP polyplexes because of the net positive charge of polyplexes [106].

4.4.5 Intracellular uptake

The cellular uptake efficiency of nanoparticles directly affects the therapeutic effects [190]. Fluorescent dyes labeled nanoparticles are frequently used to study cellular uptake. Fluorescein isothiocyanate (FITC) is a common fluorescent dye for dendrimers

labeling to study the cellular uptake behavior [109, 207, 205, 130]. We studied the cellular uptake of FITC-labeled G4 dendrimer and G4-FA conjugate by FR-positive HN12 cells.

HN12 cells were shown take up both FITC-G4-FA (Figure 4.13) and FITC-G4 (Figure 4.14) conjugates in a time-dependent manner. Notably, more and stronger FITC fluorescence was observed in the cells treated with FITC-G4 conjugates than that of the cells treated with FITC-G4-FA conjugates at each predetermined time point. This observation is likely due to the following two reasons. As earlier determined, an average of 2.3 and 2.2 FITC molecules was successfully conjugated onto each G4-FA conjugate and G4 dendrimer, respectively. The number of FITC molecules was close in the cells treated with FITC-G4 and FITC-G4-FA conjugates. However, the zeta potential of FITC-G4 conjugates was higher than that of FITC-G4-FA conjugates (Figure 4.9). As we suspected earlier, the higher zeta potential could lead to a more fluorescence uptake in the cells treated with FITC-G4 than the cells treated with FITC-G4-FA. On the other hand, FA, as a targeting moiety, was conjugated onto the G4 dendrimer. The cellular uptake mechanism of G4-FA conjugates was suspected to be receptor-mediated endocytosis, which was different from that of G4 dendrimer.

To confirm the fluorescence microscopy results, we quantified the cellular uptake of FITC-G4 and FITC-G4-FA conjugates in FR-positive HN12 cells by using flow cytometric analysis. The FITC fluorescence histogram of cells treated with FITC-G4-FA conjugates (Figure 4.15) was similar to that of cells treated with FITC-G4 conjugates (Figure 4.16). A distinguishable right shift was observed in the cells treated with both conjugates in a time-dependent manner. A further right shift was observed in the cells treated with FITC-G4 conjugates, compared to the cells treated with FITC-G4-FA conjugates. These results indicated more and stronger FITC fluorescence in the cells treated with FITC-G4 conjugates, consistently with fluorescence microscopy results. By plotting the mean intensity of FITC against incubation time, we determined the cellular uptake kinetics of FITC-G4 and FITC-G4-FA conjugates

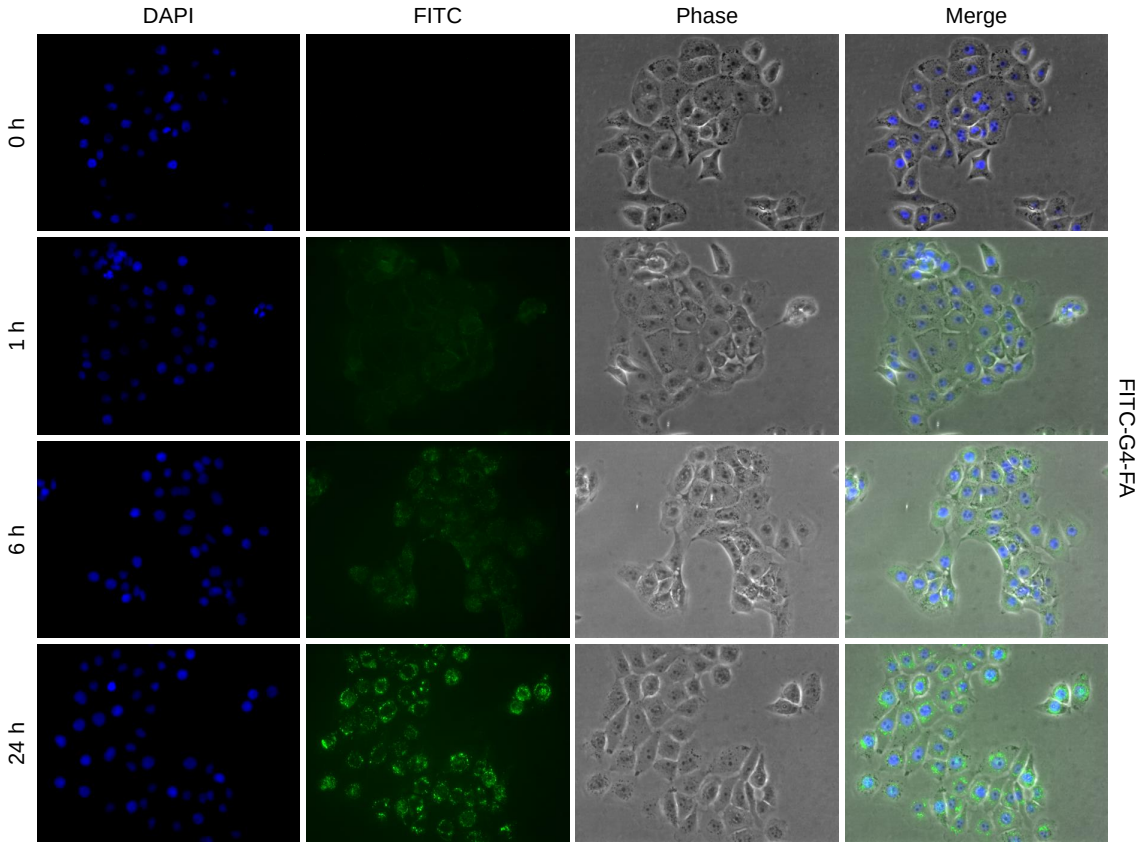

Figure 4.13: Cellular uptake of FITC-G4-FA conjugates in HN12 cells. HN12 cells were treated with FITC-G4-FA conjugates (10 μg/mL) for 0, 1, 6, and 24 h, then fixed, counterstained with DAPI and imaged using fluorescence microscope. Original magnification, 200×. The images are representative of experiments conducted on three independent occasions.

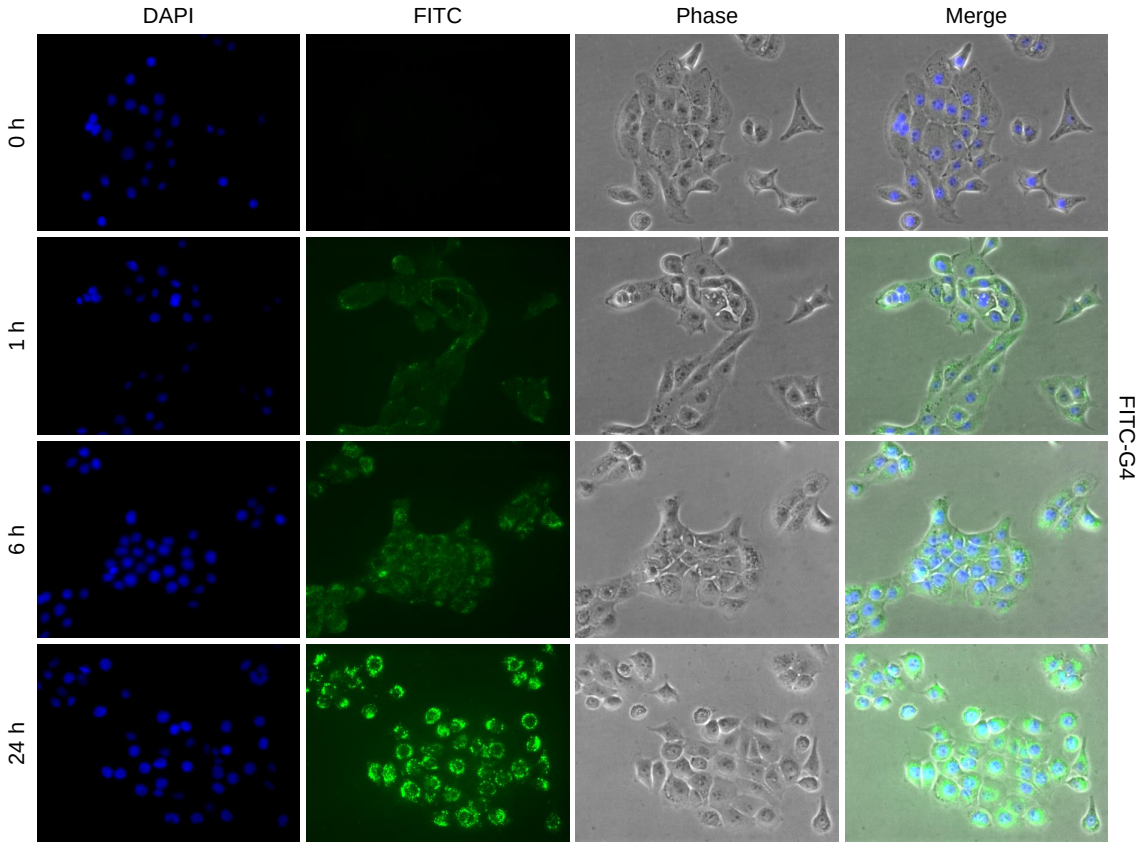

Figure 4.14: Cellular uptake of FITC-G4 conjugates in HN12 cells. HN12 cells were treated with FITC-G4 conjugates (10 μg/mL) for 0, 1, 6, and 24 h, then fixed, counterstained with DAPI and imaged using fluorescence microscope. Original magnification, 200×. The images are representative of experiments conducted on three independent occasions.

(Figure 4.17a). By curve fitting, a dose-response-stimulation [log(agonist) vs. response - variable slope] model was found to best describe the data (Figure 4.17b). Compared to the cells treated with FITC-G4 conjugates, the cellular uptake of FITC in the cells treated with FITC-G4-FA conjugates reached plateau within 24 h, suggesting that the mechanism of cellular uptake may be different from G4 dendrimer to G4-FA conjugates. It is clear that the cellular uptake of FITC-G4 conjugates is nonspecific absorptive endocytosis via electrostatic interaction between cells and conjugates. Therefore, HN12 cells kept taking up FITC-G4 conjugates within 24 h. In contrast, it is reasonable to hypothesize that the cellular uptake of FITC-G4-FA conjugates is receptor-mediated endocytosis. The saturated receptor can then limit further cellular uptake of conjugates, which causes the plateau in the uptake kinetics curve.

According to the literature, free FA at 1 mM (i.e., about 0.5 mg/mL), has been reported to efficiently competitively inhibit FA-conjugated nanoparticles cellular uptake in FR-positive cells [192, 323]. To prove our hypothesis, we then used free FA (0.5 mg/mL) as a competitive inhibitor to study the cellular uptake of FITC-G4-FA and FITC-G4 conjugates in HN12 cells. In the absence of free FA, FITC-G4-FA conjugates were taken up by HN12 cells as FITC fluorescence in the cells was observed at 1 h-post treatment. In the presence of free FA, limited FITC-G4-FA conjugates were taken up by HN12 cells as very little FITC fluorescence was observed in the cells (Figure 4.18). In contrast, in the presence and absence of free FA, FITC-G4 conjugates were taken up by HN12 cells as FITC fluorescence was observed in the both treated cells (Figure 4.18). These results suggest that free FA was able to competitively bind to and saturate FR, subsequently inhibiting cellular uptake of FITC-G4-FA conjugates in HN12 cells. However, such competitive inhibition was withdrawn in 6 h- and 24 h-treatment (Figures 4.19, 4.20). It is likely due to two reasons: non-specific cellular uptake and recycling of FR. First, FITC-G4-FA conjugates remained positive-charged as early determined (Figure 4.9), which may cause non-specific cellular uptake in either FR-

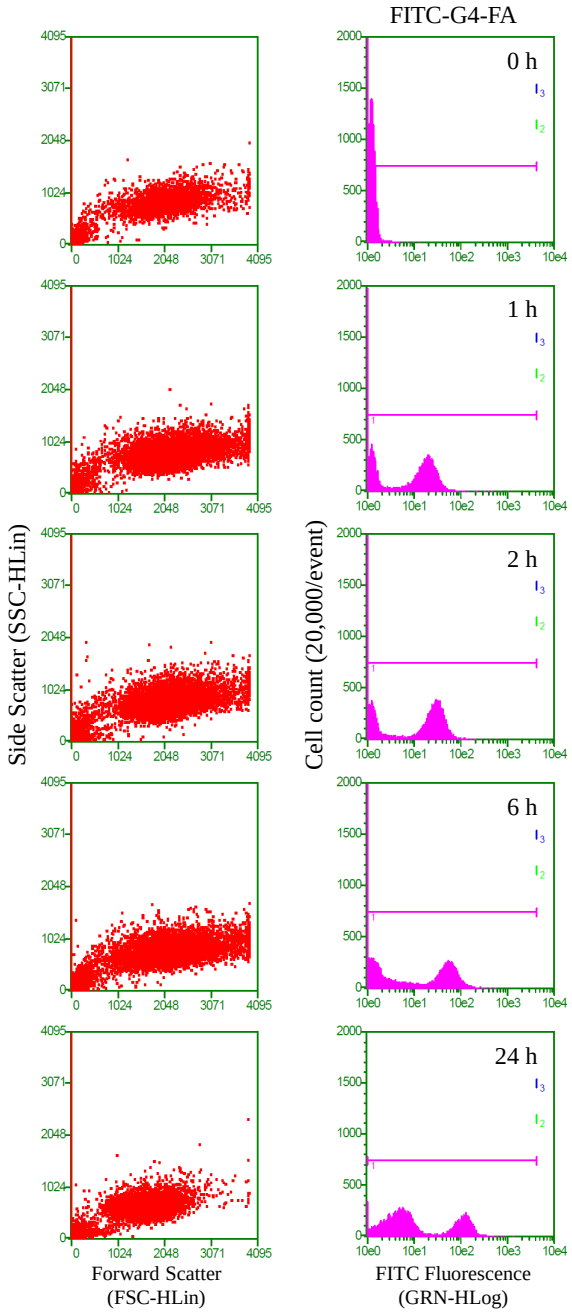

Figure 4.15: FITC fluorescence histogram of cells treated with FITC-G4-FA conjugates.

HN12 cells were treated with FITC-G4-FA conjugates (10 μg/mL) for 0, 1, 2, 6, and 24 h. The FITC fluorescence histogram of the cells at each treatment was determined by flow cytometry. The dot plot of cell scattering (forward verse side scattering) was presented on the left, and the histogram of FITC intensity against cell number was presented on the right. The histograms are representative of experiments conducted on three independent occasions.

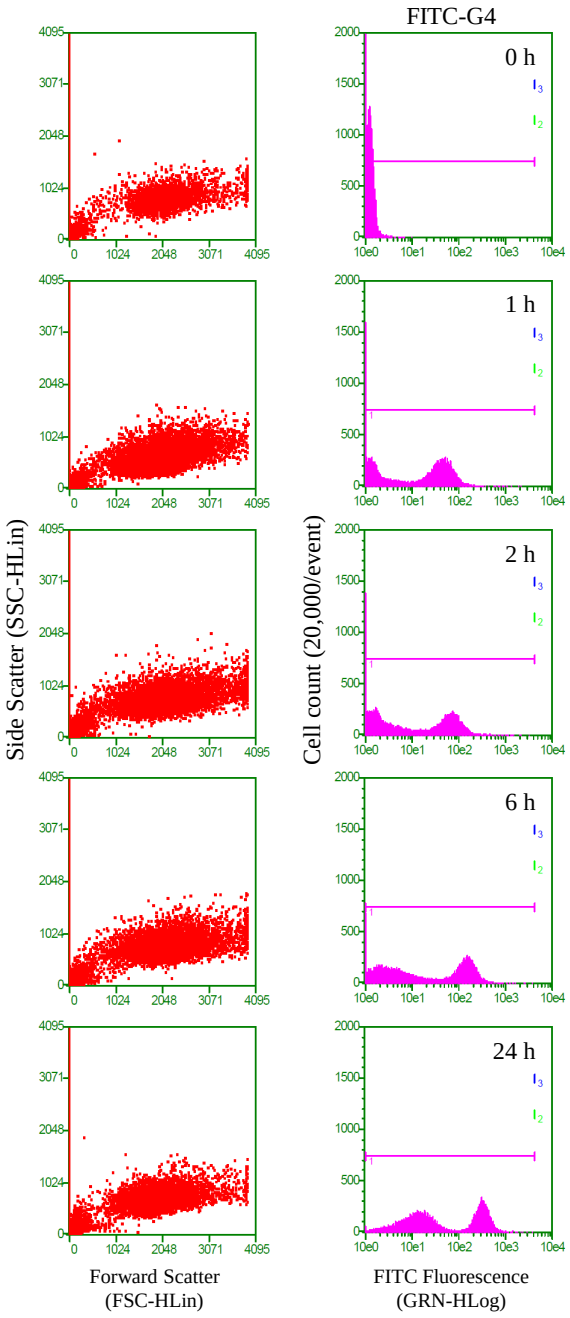

Figure 4.16: FITC fluorescence histogram of cells treated with FITC-G4 conjugates.

HN12 cells were treated with FITC-G4 conjugates (10 μg/mL) for 0, 1, 2, 6, and 24 h. The FITC fluorescence histogram of the cells at each treatment was determined by flow cytometry. The dot plot of cell scattering (forward verse side scattering) was presented on the left, and the histogram of FITC intensity against cell number was presented on the right. The histograms are representative of experiments conducted on three independent occasions.

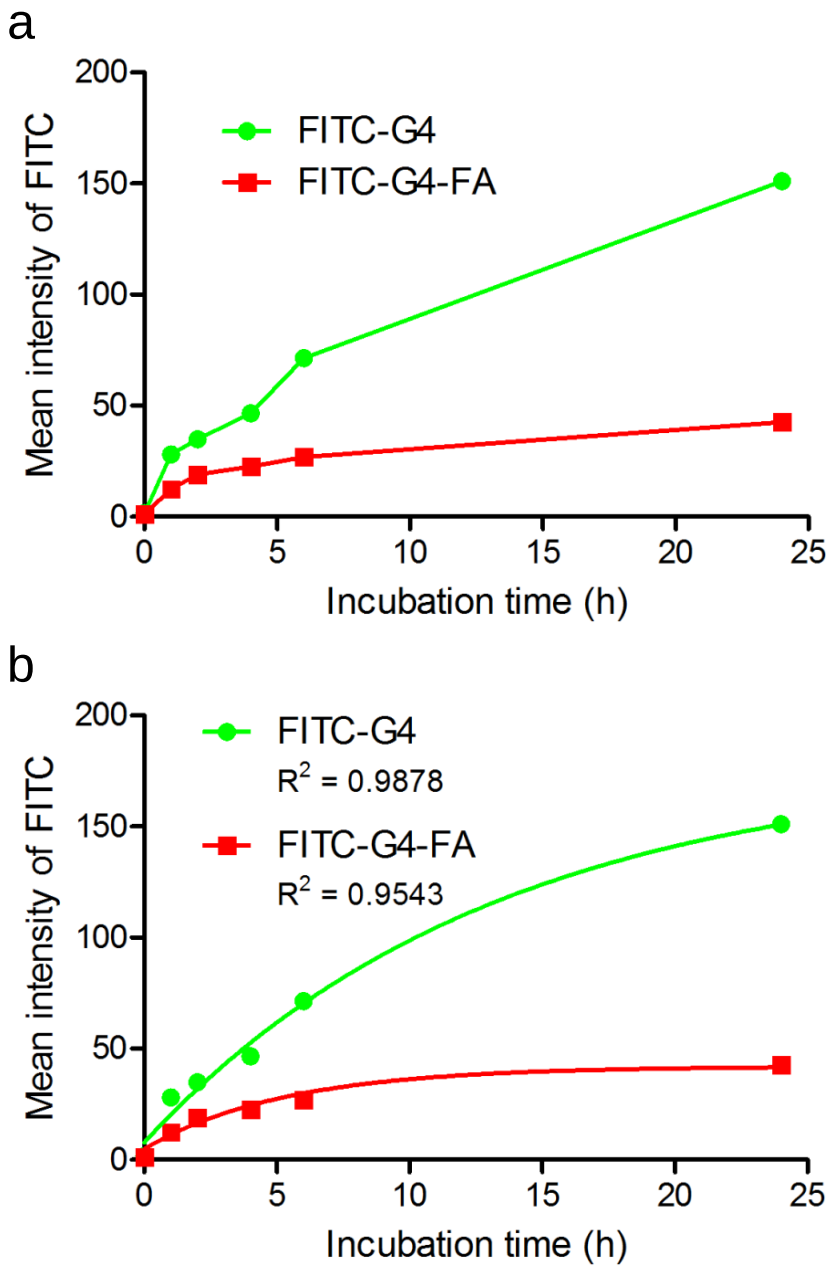

Figure 4.17: Cellular uptake kinetics of FITC-G4 and FITC-G4-FA conjugates in HN12 cells.
HN12 cells were treated with FITC-G4 and FITC-G4-FA conjugates (10 μg/mL) for 0, 1, 2, 6, and 24 h. The FITC fluorescence intensity of the cells at each treatment evaluated by flow cytometry (a). Time-response curves of FITC-G4 and FITC-G4-FA conjugates were determined (b). The dots and error bars are means ± SD. n =3.

positive and FR-negative cells. Second, folate or FA binds to FR, internalizes, and gets released from FR in the acidic environment of endosomes. The FR is then transported into the cytoplasm by proton-coupled folate transporter for recycling [249]. It has been reported that folate conjugates including folate-FITC, [^{3}H]folate, and folate-diethylenetriaminepentaacetic acid-ethylenediamine-^{111}indium chloride (folate-DTPA-^{111}In) were endocytosed as efficiently as free FA in FR-positive cells. More interestingly, the rate of FR recycling was estimated to be slightly less than 5.7 h for L1210A cells, and near 13.3 to 20 h for Line 01 and M109 cells [203]. Thus, to our best knowledge, the fast recycling time of FR in HN12 cells may result the increase of cellular uptake of FITC-G4-FA conjugates in the presence of free FA for 6- and 24 h-treatment. However, this interpretation needs to be validated by additional experiments in the future.

To confirm the fluorescence microscopy results, we quantified the cellular uptake of FITC-G4 and FITC-G4-FA in the presence or absence of free FA by using a series of flow cytometric analysis. Compared to the cells treated with FITC-G4-FA conjugates in the absence of free FA, a distinguishable left shift of FITC fluorescence was observed in the cells treated with FITC-G4-FA conjugates in the presence of free FA for 1 h and 2 h (Figure 4.21). In contrast, there was no significant FITC fluorescence shift in the cells treated with FITC-G4 conjugates in the absence and presence of free FA (Figure 4.22). By plotting mean intensity of FITC against incubation time, we observed a significant decrease of mean intensity of FITC in the cells treated with FITC-G4-FA in the presence of free FA, compared to that in the absence of free FA. In contrast, no significant difference of mean intensity of FITC was observed in the cells treated with FITC-G4 conjugates in the absence and presence of free FA (Figure 4.23). To further validate the cellular uptake mechanism of FITC-G4-FA conjugates, we quantified the cellular uptake efficiency of FITC-G4-FA conjugates in the presence of various concentrations of free FA by using a series of flow cytometric analysis. From the FITC fluorescence histogram of cells incubated

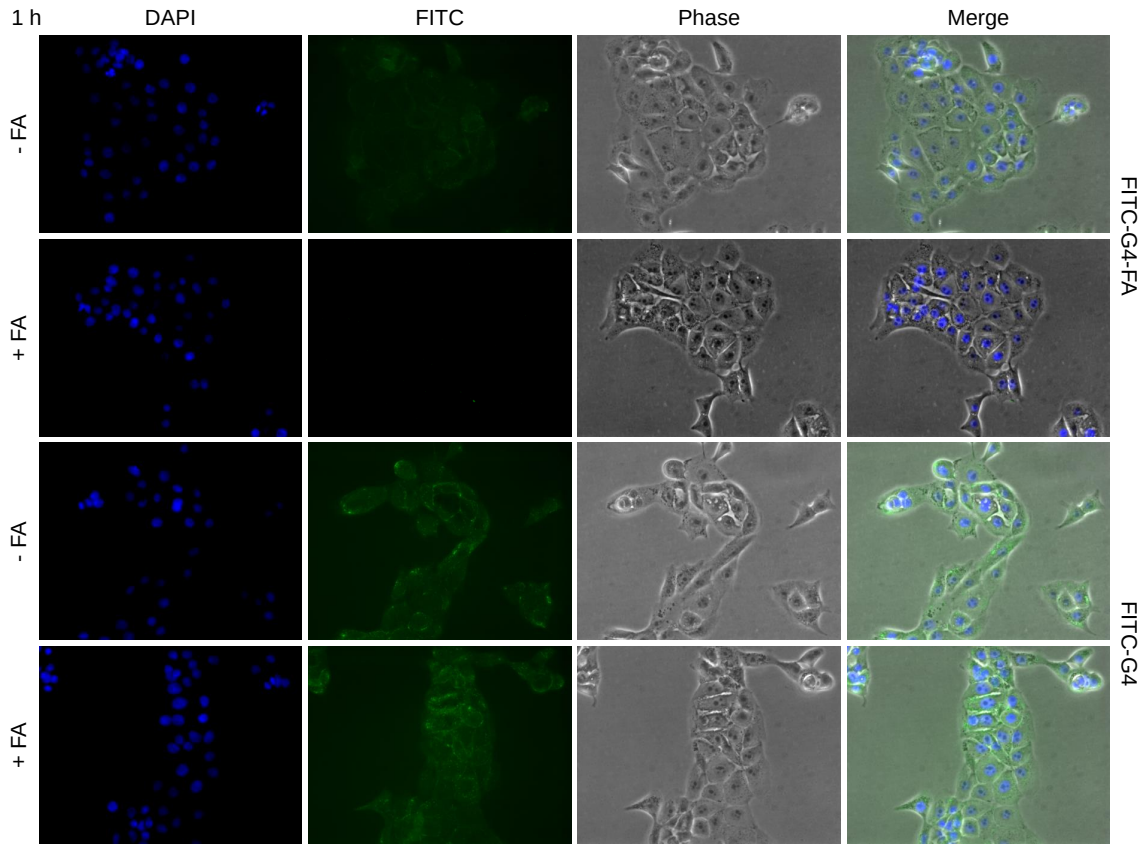

Figure 4.18: Effect of free FA on cellular uptake of FITC-G4 and FITC-G4-FA conjugates in HN12 cells.
HN12 cells were treated with FITC-G4 and FITC-G4-FA conjugates (10 μg/mL) for 1 h in the absence or presence of free FA (0.5 mg/mL), then fixed, counterstained with DAPI and imaged using fluorescence microscope. Original magnification, 200×. The images are representative of experiments conducted on three independent occasions.

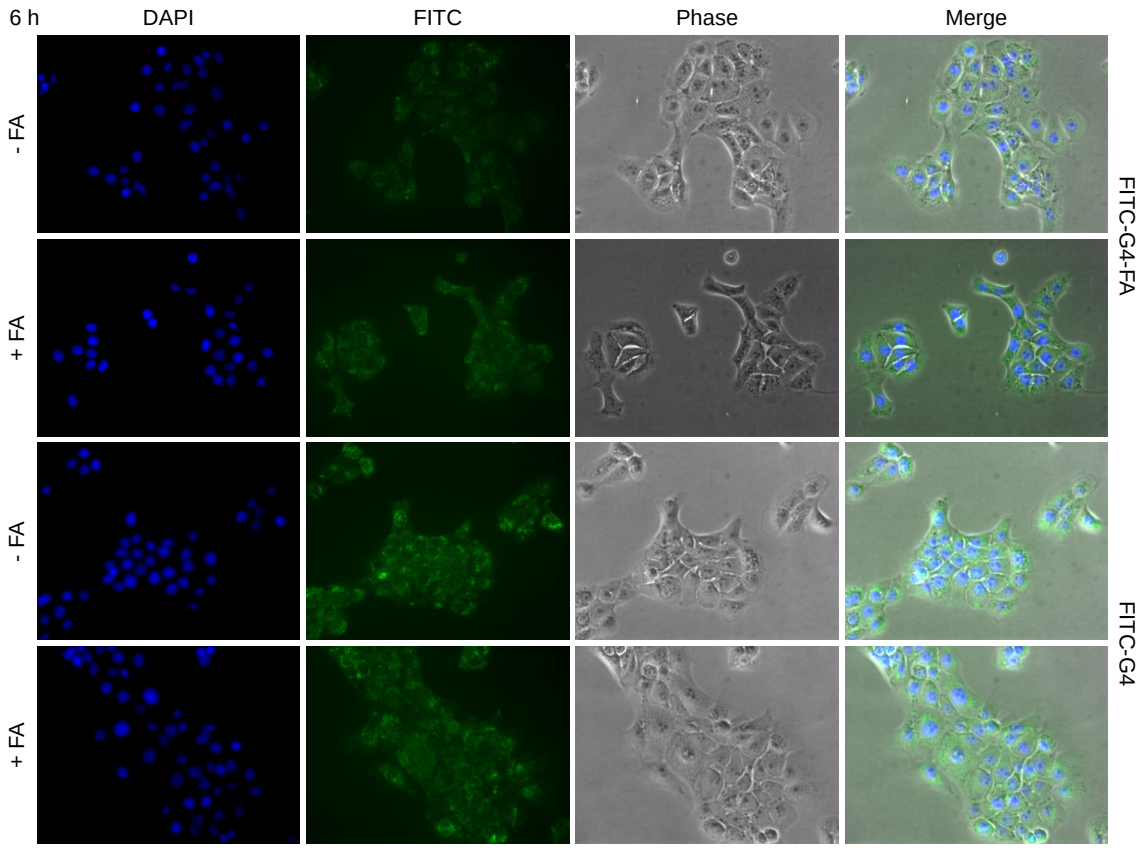

Figure 4.19: Effect of free FA on cellular uptake of FITC-G4 and FITC-G4-FA conjugates in HN12 cells.
HN12 cells were treated with FITC-G4 and FITC-G4-FA conjugates (10 μg/mL) for 6 h in the absence or presence of free FA (0.5 mg/mL), then fixed, counterstained with DAPI and imaged using fluorescence microscope. Original magnification, 200×. The images are representative of experiments conducted on three independent occasions.

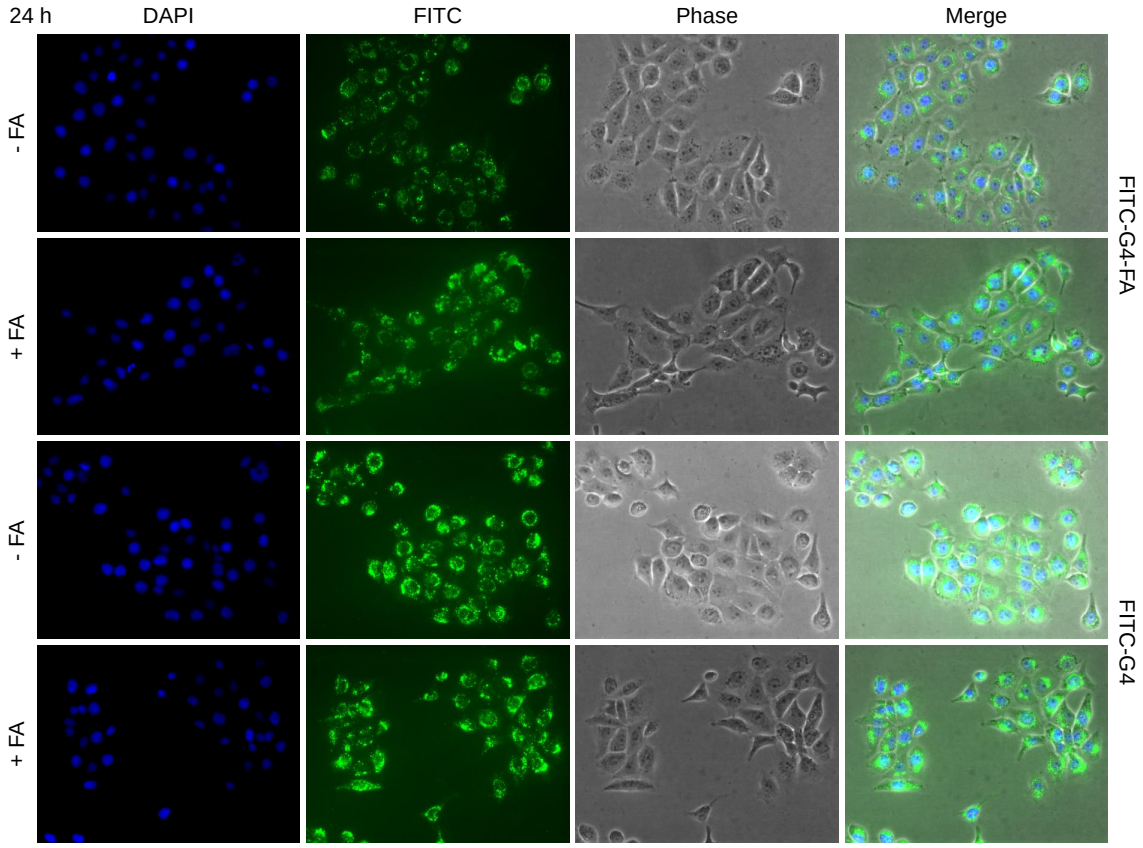

Figure 4.20: Effect of free FA on cellular uptake of FITC-G4 and FITC-G4-FA conjugates in HN12 cells.
HN12 cells were treated with FITC-G4 and FITC-G4-FA conjugates (10 μg/mL) for 24 h in the absence or presence of free FA (0.5 mg/mL), then fixed, counterstained with DAPI and imaged using fluorescence microscope. Original magnification, 200×. The images are representative of experiments conducted on three independent occasions.

with FITC-G4-FA conjugates, a distinguishable left shift of FITC fluorescence was observed in the cells treated with FITC-G4-FA conjugates (Figure 4.24). By plotting mean intensity of FITC against free FA concentration, we observed a significant decrease in mean intensity of FITC in the presence of free FA in a dose-dependent manner (Figure 4.25). Taken together, our results demonstrate that FA-decorated dendrimers can induce cellular uptake through FR-mediated endocytosis, which is highly FR-dependent. Free FA can competitively bind to FR on the cell surface in early incubation time, and subsequently inhibit cellular uptake of FITC-G4-FA conjugates. The expression level and recycling time of FR on cell membrane may serve as a rate-limiting step in cellular uptake of G4-FA conjugates, which is different as that of naive G4 dendrimer. Additionally, positive-charged FITC-G4-FA conjugate may still be able to trigger cellular uptake via electrostatic interaction. However, the precise mechanism of FR transport into cells remains yet to be resolved.

To understand the intracellular trafficking pattern of the internalized dendrimer/plasmid polyplexes in living cells, we performed colocalization assays to assess the distribution of the polyplexes in HN12 cells at various time points post-transfection using fluorescence microscopy. FITC-labeled G4-FA conjugates and a Cy3-labeled plasmid were employed for in vitro trafficking of vector and plasmid, respectively. Time lapse imaging and colocalization results qualitatively show a time-dependent internalization of G4-FA/plasmid polyplexes (Figure 4.26). As time progressed, more polyplexes of G4-FA/plasmid were internalized. At noticed, both FITC and Cy3 fluorescence was observed in more than 90% of HN12 cells at 24 h-post transfection, indicating 24 h transfection could give a good transfection efficiency using G4-FA conjugates as vectors.

Theoretically, the internalization of dendrimer occurs mainly through a clathrin- and caveolae-mediated energy-dependent endocytosis and partly through marcopinocytosis. Dendrimers can then function as a proton sponge to facilitate the escape from

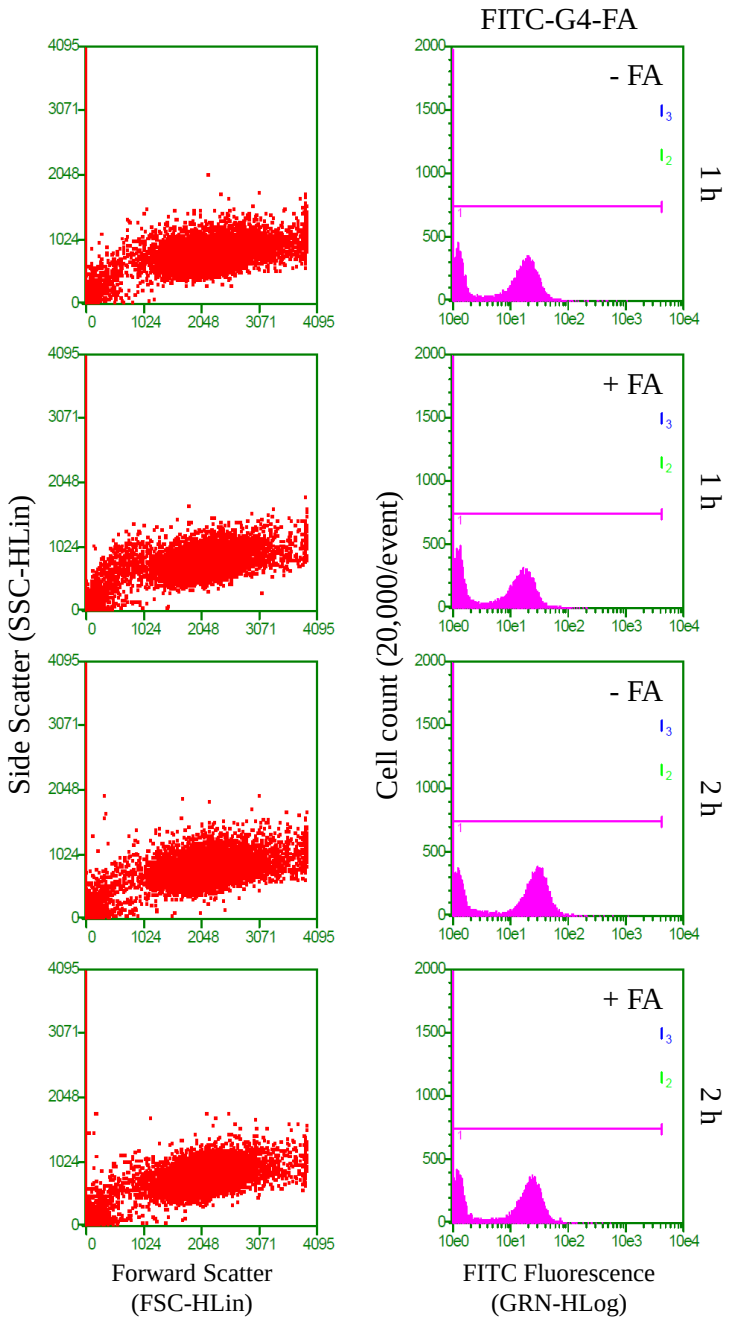

Figure 4.21: Effect of free FA on cellular uptake of FITC-G4-FA conjugates in HN12 cells.

HN12 cells were treated with FITC-G4-FA conjugates (10 μg/mL) for 1 and 2 h in the absence or presence of free FA (0.5 mg/mL). The FITC fluorescence histogram of the cells at each treatment was determined by flow cytometry. The dot plot of cell scattering (forward verse side scattering) was presented on the left, and the histogram of FITC intensity against cell number was presented on the right. The histograms are representative of experiments conducted on three independent occasions.

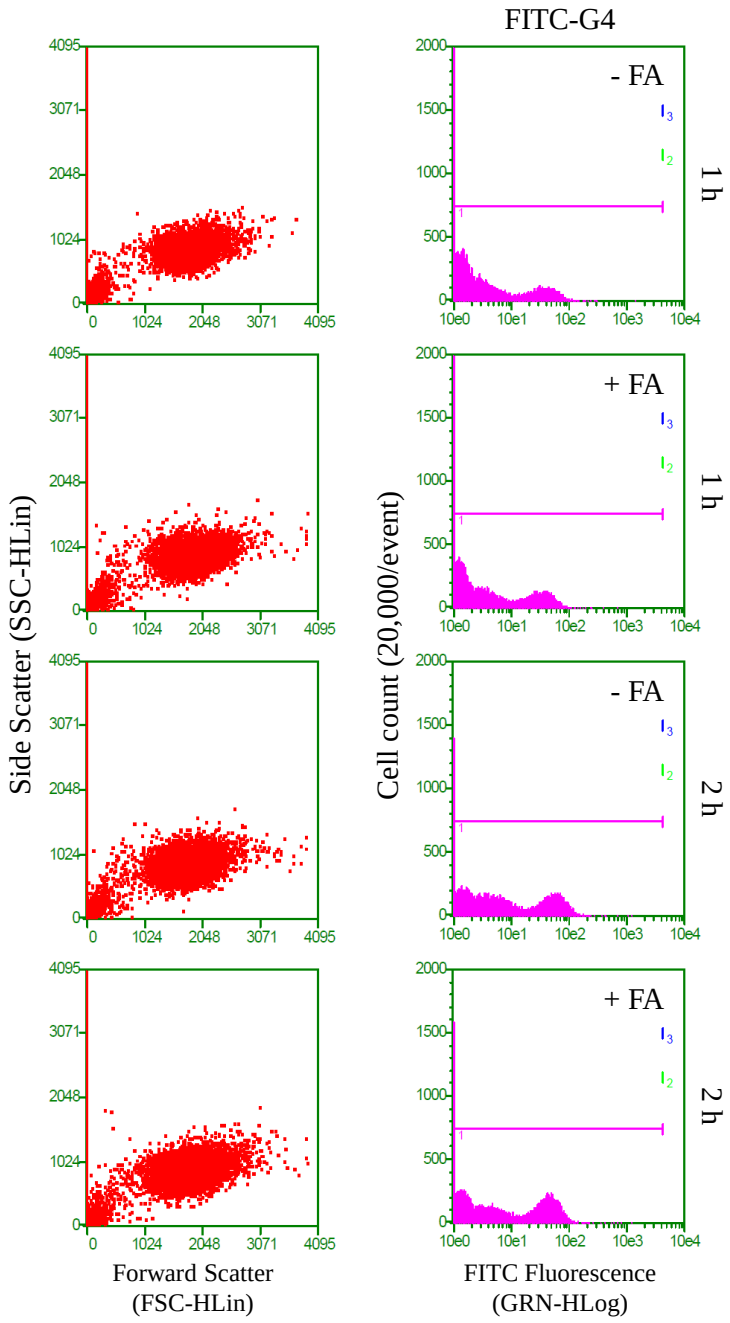

Figure 4.22: Effect of free FA on cellular uptake of FITC-G4 conjugates in HN12 cells.

HN12 cells were treated with FITC-G4 conjugates (10 μg/mL) for 1 and 2 h in the absence or presence of free FA (0.5 mg/mL). The FITC fluorescence histogram of the cells at each treatment was determined by flow cytometry. The dot plot of cell scattering (forward verse side scattering) was presented on the left, and the histogram of FITC intensity against cell number was presented on the right. The histograms are representative of experiments conducted on three independent occasions.

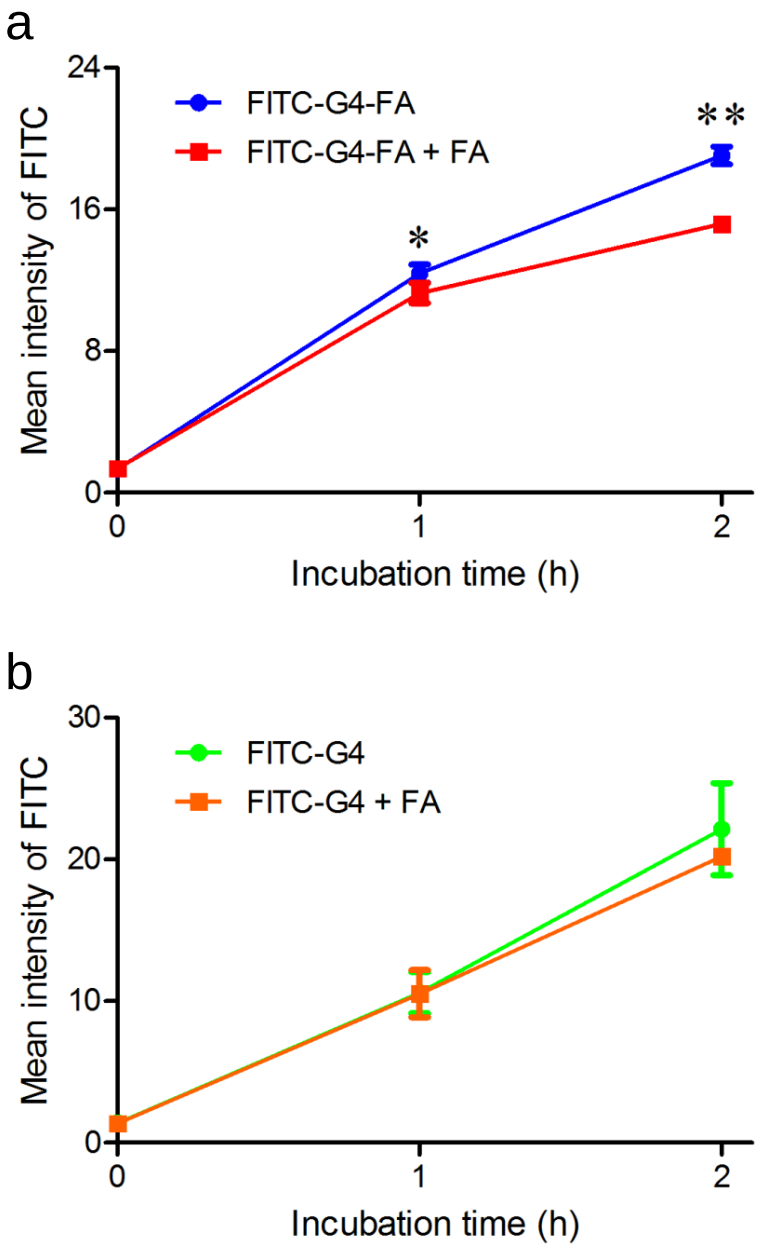

Figure 4.23: Effect of free FA on cellular uptake kinetics of FITC-G4 and FITC-G4-FA conjugates in HN12 cells.
HN12 cells were treated with FITC-G4 and FITC-G4-FA conjugates (10 μg/mL) for 1 and 2 h in the absence or presence of free FA (0.5 mg/mL). The FITC fluorescence intensity of the cells treated with FITC-G4-FA conjugates was evaluated by flow cytometry (a). The FITC fluorescence intensity of the cells treated with FITC-G4 conjugates was evaluated using flow cytometric analyses (b). The dots and error bars are means ± SD. n = 6. * $p < 0.05$ and ** $p < 0.01$ versus FITC-G4-FA conjugates at each indicated time point.

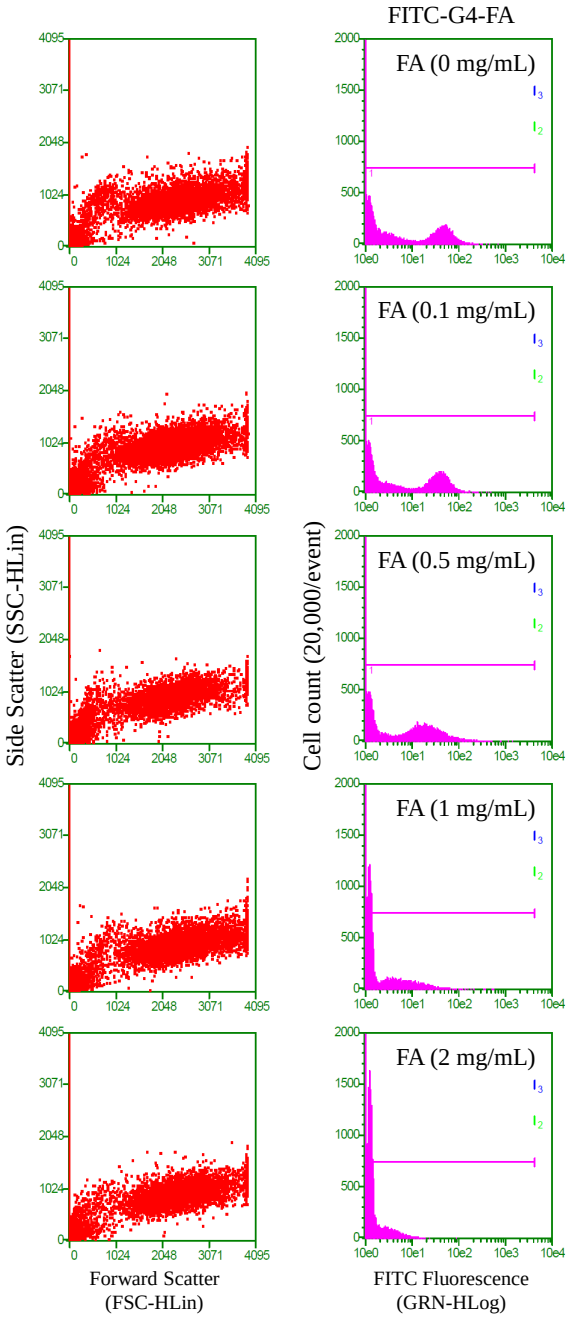

Figure 4.24: Effect of free FA on cellular uptake of FITC-G4-FA conjugates in HN12 cells.

HN12 cells were treated with FITC-G4-FA conjugates (10 μg/mL) for 2 h in the absence or presence of free FA (0.1, 0.5, 1, and 2 mg/mL). The FITC fluorescence histogram of the cells at each treatment was determined by flow cytometry. The dot plot of cell scattering (forward verse side scattering) was presented on the left, and the histogram of FITC intensity against cell number was presented on the right. The histograms are representative of experiments conducted on three independent occasions.

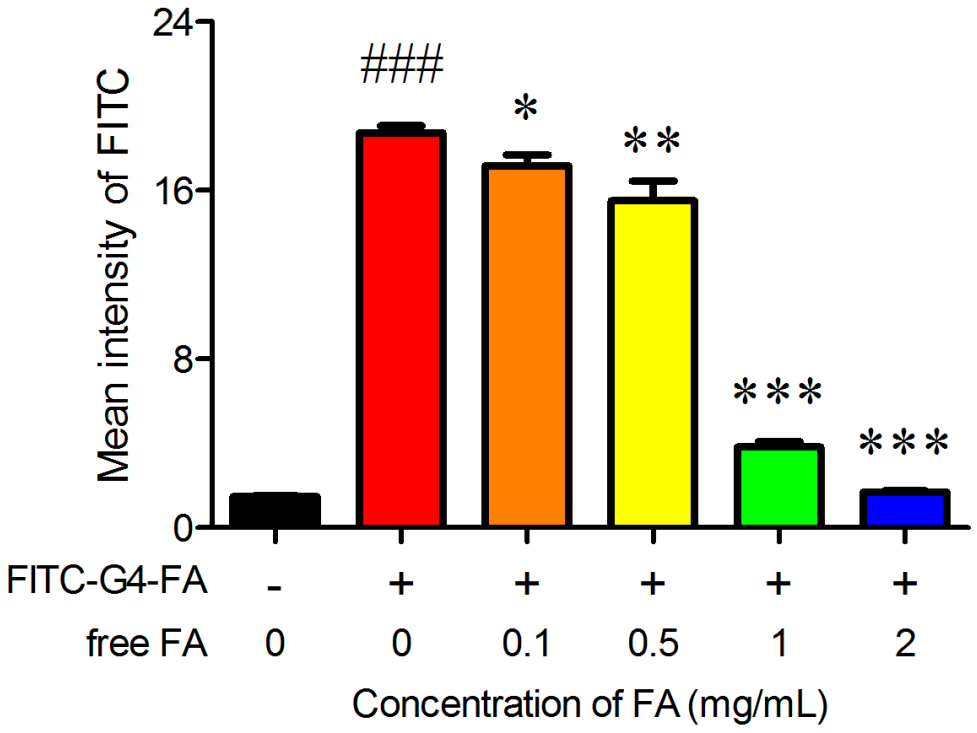

Figure 4.25: Effect of free FA on cellular uptake of FITC-G4-FA conjugates in HN12 cells.

HN12 cells were treated with FITC-G4-FA conjugates (10 μg/mL) for 2 h in the absence or presence of free FA (0.1, 0.5, 1, and 2 mg/mL). The FITC fluorescence intensity of the cells treated with FITC-G4-FA conjugates was evaluated by flow cytometry. The bars and error bars are means $\pm$ SD. n = 6. ### $p < 0.001$ versus no treatment; * $p < 0.05$, ** $p < 0.01$, and $p < 0.001$ versus FITC-G4-FA conjugates in the absence of free FA.

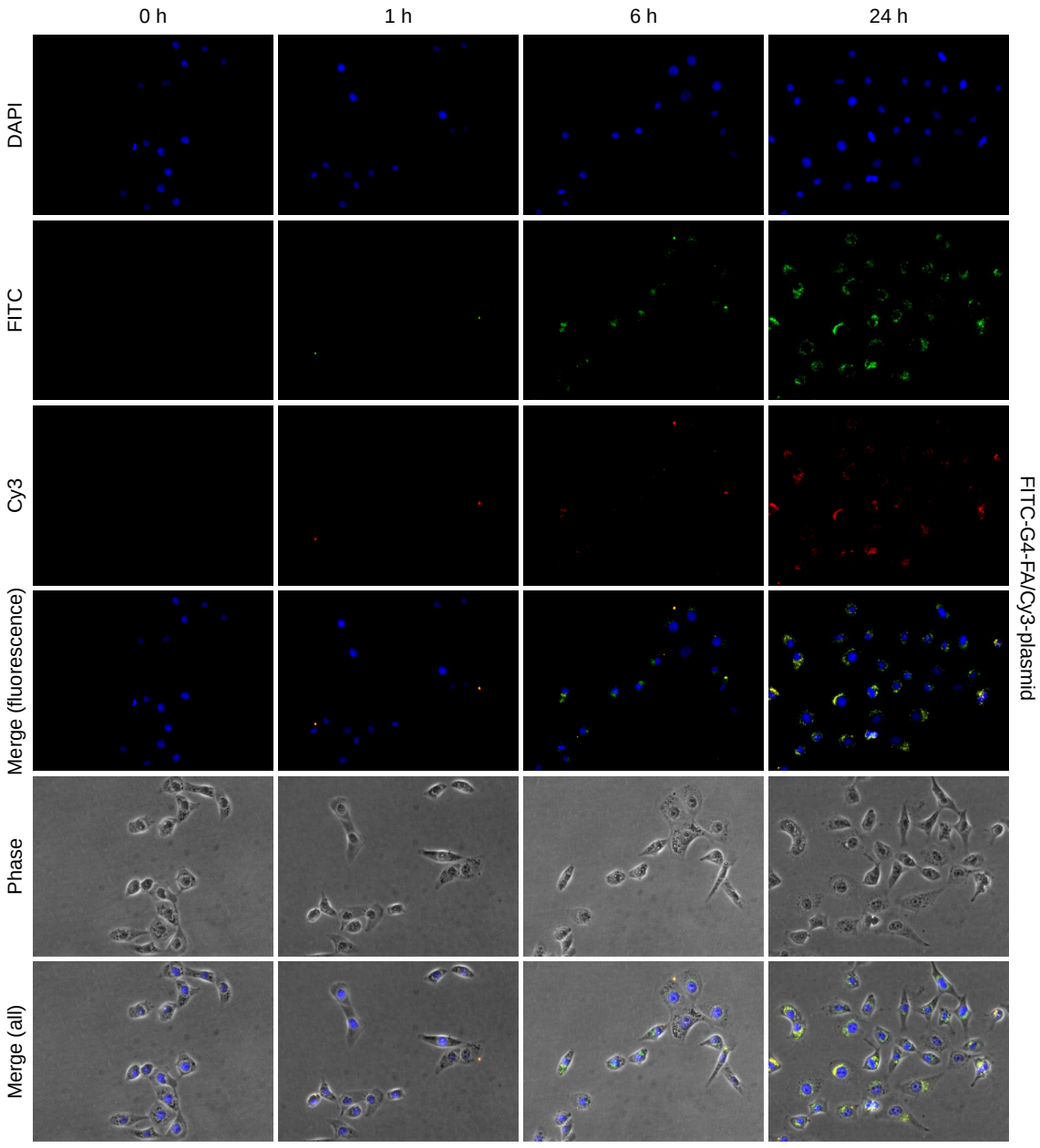

Figure 4.26: Cellular uptake of FITC-G4-FA/Cy3-plasmid polyplexes in HN12 cells.
HN12 cells were treated with FITC-G4-FA/Cy3-plasmid polyplexes (5:1, μg/μg) for 0, 1, 6, and 24 h, then fixed, counterstained with DAPI and imaged using fluorescence microscope. Original magnification, 200×. The images are representative of experiments conducted on three independent occasions.

endosomes and lysosomes. The proton sponge mechanism occurs because dendrimers contain a large number of secondary and tertiary amines. These amines enable the adsorption of protons released from ATPase and subsequently cause osmotic swelling and rupture of the endosome membrane to release the entrapped dendrimers [297]. To further investigate the mechanisms of G4-FA conjugates for gene delivery, we employed confocal microscopy to distribution of polyplexes and dissociation of plasmid and G4-FA conjugates from polyplexes. At 24 h-post transfection, both FITC and Cy3 fluorescence were observed within HN12 cells and close to the nuclei (Figure 4.27), which was consistent with fluorescence microscopy (Figure 4.26). Moreover, colocalization of FITC-G4-FA conjugates and Cy3-plasmid yields a yellow signal because of the overlay of FITC (green signal) and Cy3 (red signal). We clearly observed yellow, green, and red signals (Figure 4.28), indicating the dissociation of G4-FA/plasmid polyplexes could occur at or after 24 h-post transfection.

To confirm both fluorescence and confocal microscopy results, we quantified the cellular uptake of G4-FA/Cy3-plasmid and G4/Cy3-plasmid polyplexes in HN12 cells by using flow cytometric analysis. The Cy3 fluorescence histogram of cells incubated with G4-FA/Cy3-plasmid polyplexes (Figure 4.29) was similar to that of cells incubated with G4/Cy3-plasmid polyplexes (Figure 4.30). A distinguishable right shift was observed in the cells treated with both polyplexes in a time-dependent manner. By plotting the mean intensity of Cy3 against incubation time, we determined the cellular uptake kinetics of G4-FA/Cy3-plasmid and G4/Cy3-plasmid polyplexes (Figure 4.31a). By curve fitting, a dose-response-stimulation [log(agonist) vs. response - variable slope] model was found to best describe the data (Figure 4.31b). The kinetics of cellular uptake of G4-FA/Cy3-plasmid and G4/Cy3-plasmid polyplexes was different, which was similar to the kinetics of cellular uptake of FITC-G4-FA and FITC-G4 conjugates (Figure 4.17), suggesting that the mechanism of cellular uptake could be different from G4-FA/plasmid to G4/plasmid polyplexes. The cellular uptake of G4/plasmid polyplexes is nonspecific absorptive endocytosis via electrostatic interaction between cells and polyplexes. Therefore, HN12 cells kept taking up

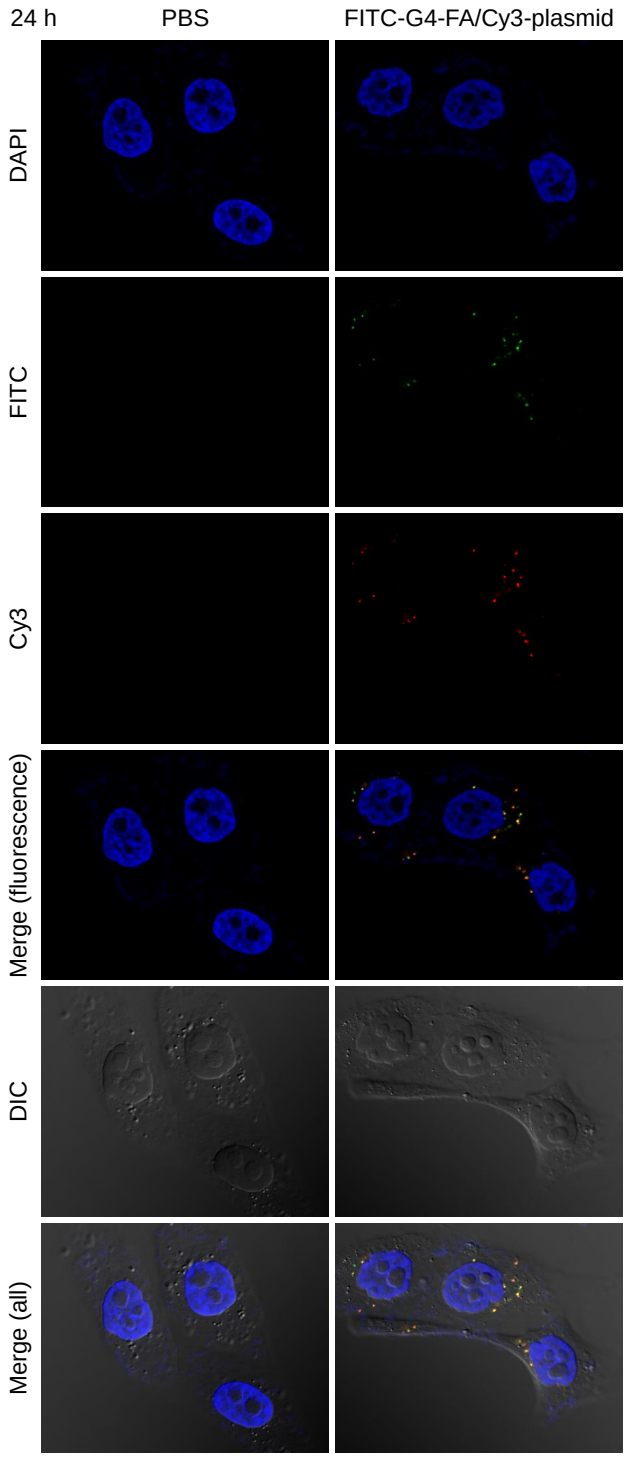

Figure 4.27: Intracellular trafficking of FITC-G4-FA/Cy3-plasmid polyplexes in HN12 cells.
HN12 cells were treated with FITC-G4-FA/Cy3-plasmid polyplexes (5:1, μg/μg) for 24 h, then fixed, counterstained with DAPI and imaged using confocal microscope. Original magnification, 630×. The images are representative of experiments conducted on three independent occasions.

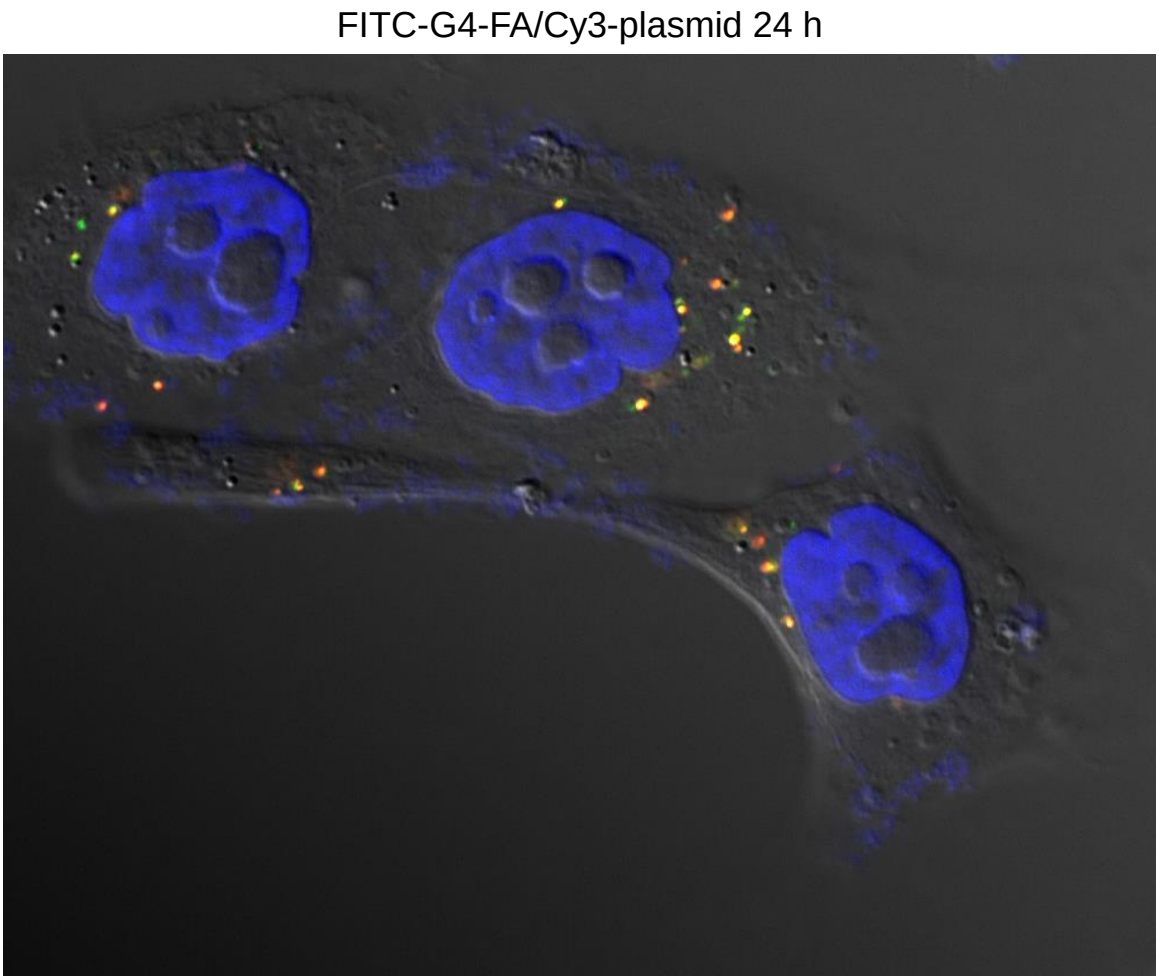

Figure 4.28: Intracellular trafficking of FITC-G4-FA/Cy3-plasmid polyplexes in HN12 cells.
HN12 cells were treated with FITC-G4-FA/Cy3-plasmid polyplexes (5:1, μg/μg) for 24 h, then fixed, counterstained with DAPI and imaged using confocal microscope. Original magnification, 630×. The images are representative of experiments conducted on three independent occasions.

G4/plasmid polyplexes. In contrast, it is reasonable to hypothesize that the cellular uptake of G4-FA/plasmid polyplexes is receptor-mediated endocytosis. The saturated receptor can then limit further cellular uptake of polyplexes, which causes the plateau of uptake curve.

To prove our hypothesis, we quantified the cellular uptake of G4-FA/Cy3-plasmid and G4/Cy3-plasmid polyplexes in the presence or absence of free FA. Compared to the cells treated with G4-FA/Cy3-plasmid in the absence of free FA, a distinguishable left shift of Cy3 fluorescence was observed in the cells treated with G4/Cy3-plasmid polyplexes in the presence of free FA (0.5 mg/mL) for 1 h and 2 h (Figure 4.32). In contrast, there was no distinguishable Cy3 fluorescence shift in the cells treated with G4/Cy3-plasmid polyplexes in the absence and presence of free FA (Figure 4.33). By plotting mean intensity of Cy3 against incubation time, we observed a significant decrease of mean intensity of Cy3 in the presence of free FA, compared to that in the absence of free FA, in the cells treated with either G4-FA/Cy3-plasmid or G4/Cy3-plasmid polyplexes (Figure 4.34). However, more predominant inhibition was observed in the cells treated with G4-FA/Cy3-plasmid than G4/Cy3-plasmid polyplexes in the presence of free FA (Figure 4.34). Additionally, the inhibition of G4-FA/Cy3-plasmid in HN12 cells by free FA was more predominant than that of FITC-G4-FA conjugates (Figure 4.23), most likely because dendrimer/plasmid complexation neutralized zeta potential of G4-FA (Figure 4.9, 4.12), which significantly reduced the non-specific cellular uptake. These results clearly demonstrate that FA-decorated dendrimer/plasmid polyplexes can trigger cellular uptake through FR-mediated endocytosis. Free FA can competitively bind to FR on the cell surface in early incubation time, and subsequently inhibit cellular uptake of G4-FA/plasmid polyplexes. Again, the expression level and recycling time of FR on cell membrane may serve as a rate-limiting step in cellular uptake of G4-FA/plasmid polyplexes, which is different as that of G4/plasmid polyplexes.

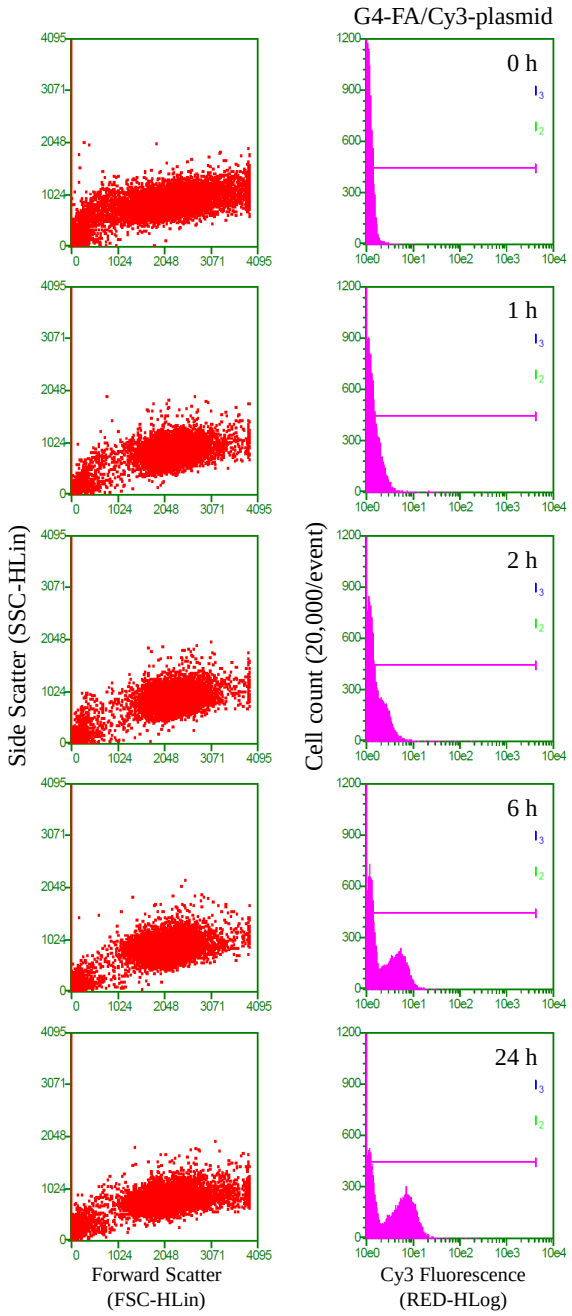

Figure 4.29: Cy3 fluorescence histogram of cells treated with G4-FA/Cy3-plasmid polyplexes.

HN12 cells were treated with G4-FA/Cy3-plasmid polyplexes (5:1, μg/μg) for 0, 1, 2, 6, and 24 h. The Cy3 fluorescence histogram of the cells at each treatment was determined by flow cytometry. The dot plot of cell scattering (forward verse side scattering) was presented on the left, and the histogram of FITC intensity against cell number was presented on the right. The histograms are representative of experiments conducted on three independent occasions.

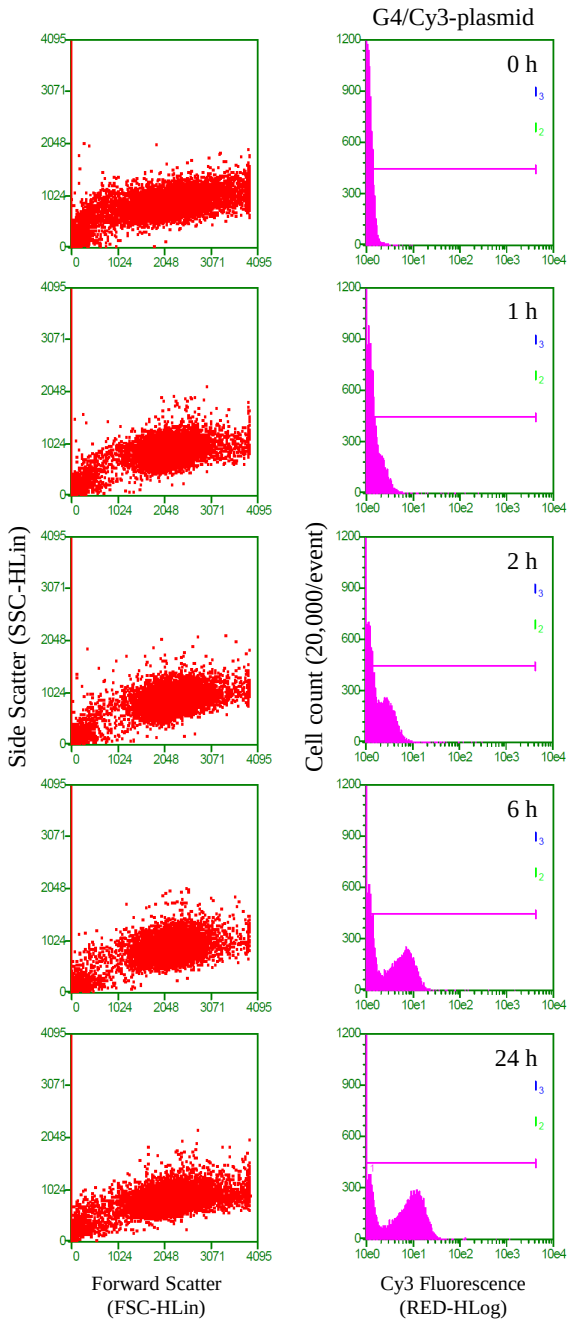

Figure 4.30: Cy3 fluorescence histogram of cells treated with G4/Cy3-plasmid polyplexes.
HN12 cells were treated with G4/Cy3-plasmid polyplexes (5:1, μg/μg) for 0, 1, 2, 6, and 24 h. The Cy3 fluorescence histogram of the cells at each treatment was determined by flow cytometry. The dot plot of cell scattering (forward verse side scattering) was presented on the left, and the histogram of FITC intensity against cell number was presented on the right. The histograms are representative of experiments conducted on three independent occasions.

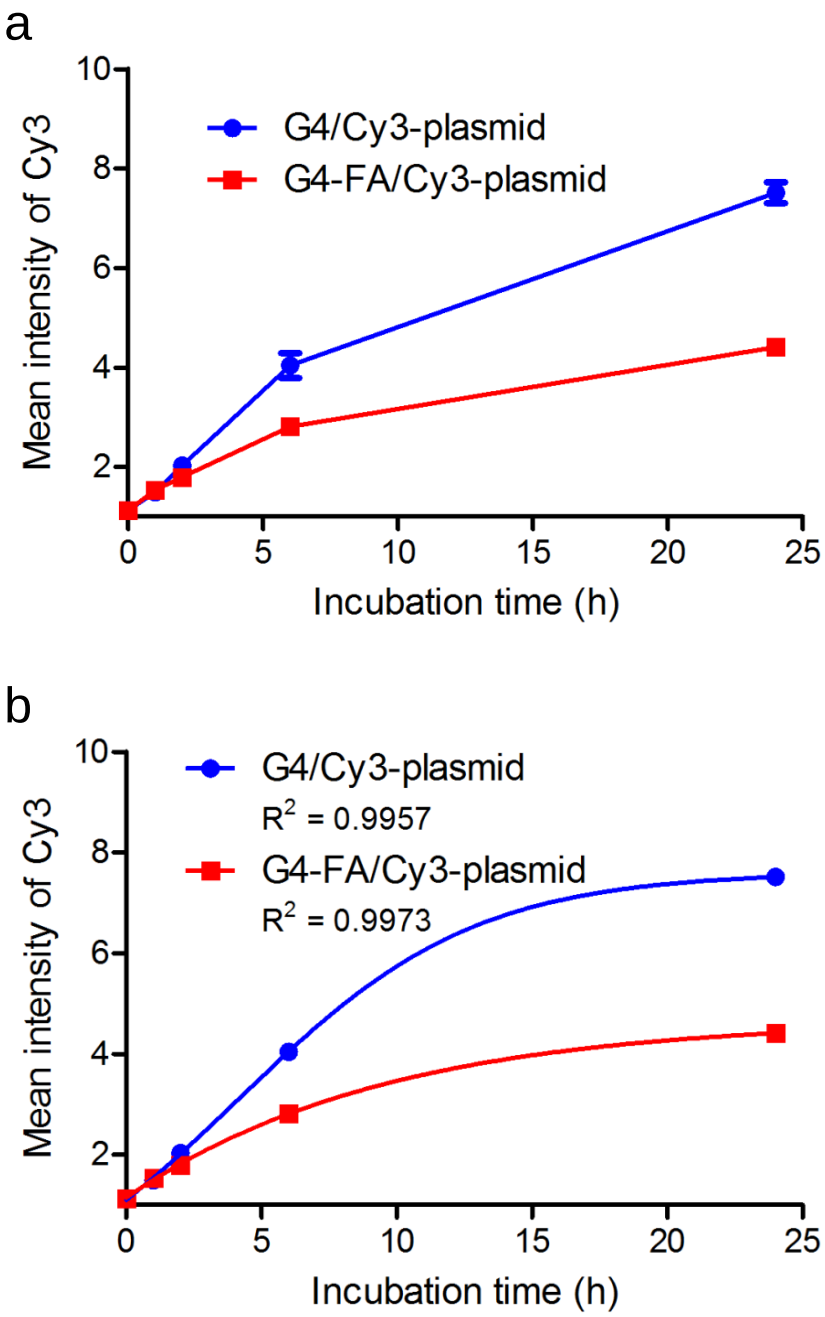

Figure 4.31: Cellular uptake kinetics of G4/Cy3-plasmid and G4-FA/Cy3-plasmid polyplexes in HN12 cells.
HN12 cells were treated with G4/Cy3-plasmid and G4-FA/Cy3-plasmid polyplexes (5:1, μg/μg) for 0, 1, 2, 6, and 24 h. The Cy3 fluorescence intensity of the cells at each treatment evaluated by flow cytometry (a). Time-response curves of FITC-G4 and FITC-G4-FA conjugates were determined (b). The dots and error bars are means $\pm$ SD. n = 5-6.

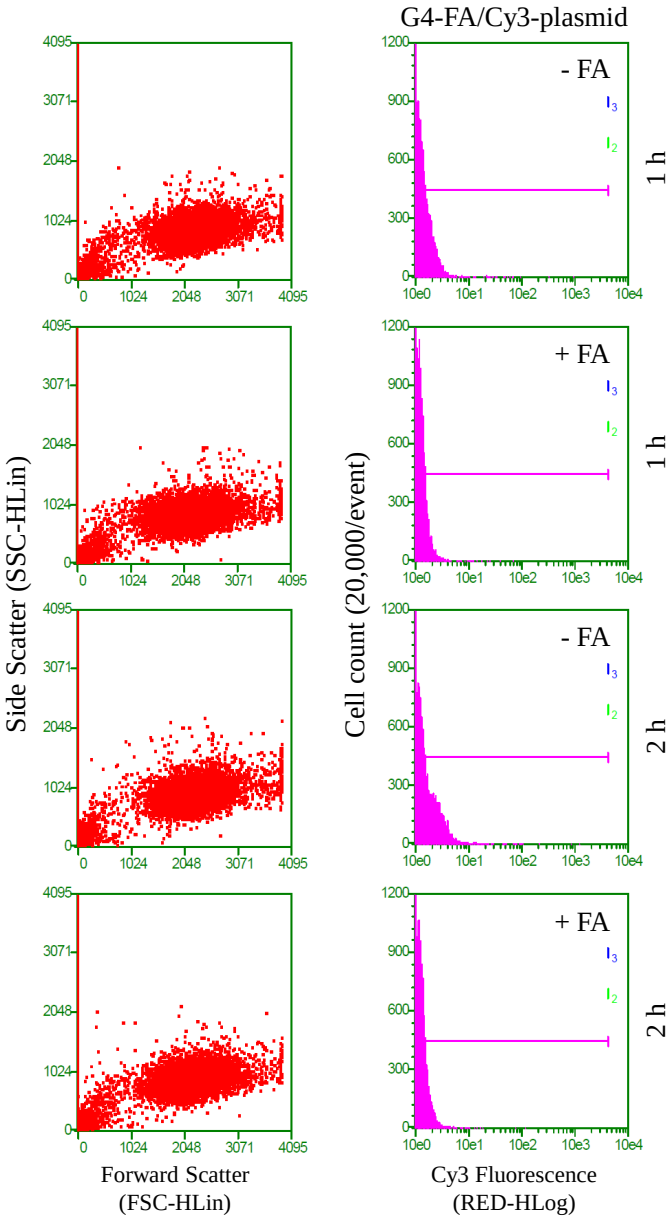

Figure 4.32: Effect of free FA on cellular uptake of G4-FA/Cy3-plasmid polyplexes in HN12 cells.
HN12 cells were treated with G4-FA/Cy3-plasmid polyplexes (5:1, μg/μg) for 1 and 2 h in the absence or presence of free FA (0.5 mg/mL). The Cy3 fluorescence histogram of the cells at each treatment was determined by flow cytometry. The dot plot of cell scattering (forward verse side scattering) was presented on the left, and the histogram of FITC intensity against cell number was presented on the right. The histograms are representative of experiments conducted on three independent occasions.

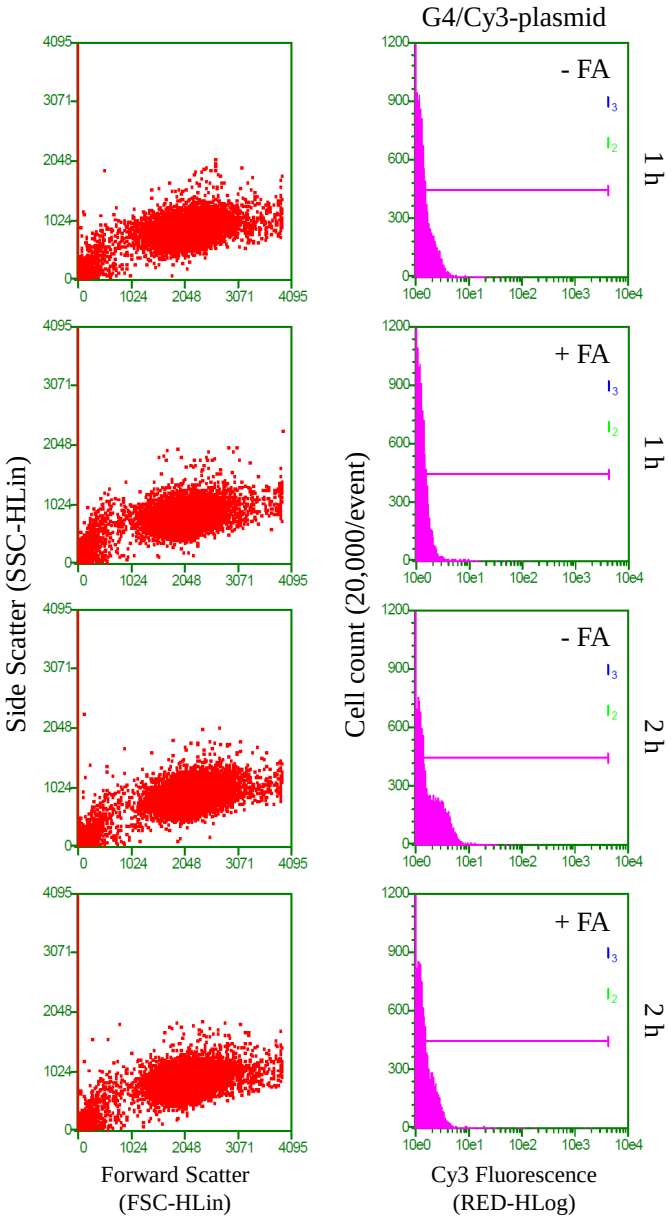

Figure 4.33: Effect of free FA on cellular uptake of G4/Cy3-plasmid polyplexes in HN12 cells.

HN12 cells were treated with G4/Cy3-plasmid polyplexes (5:1, μg/μg) for 1 and 2 h in the absence or presence of free FA (0.5 mg/mL). The Cy3 fluorescence histogram of the cells at each treatment was determined by flow cytometry. The dot plot of cell scattering (forward verse side scattering) was presented on the left, and the histogram of FITC intensity against cell number was presented on the right. The histograms are representative of experiments conducted on three independent occasions.

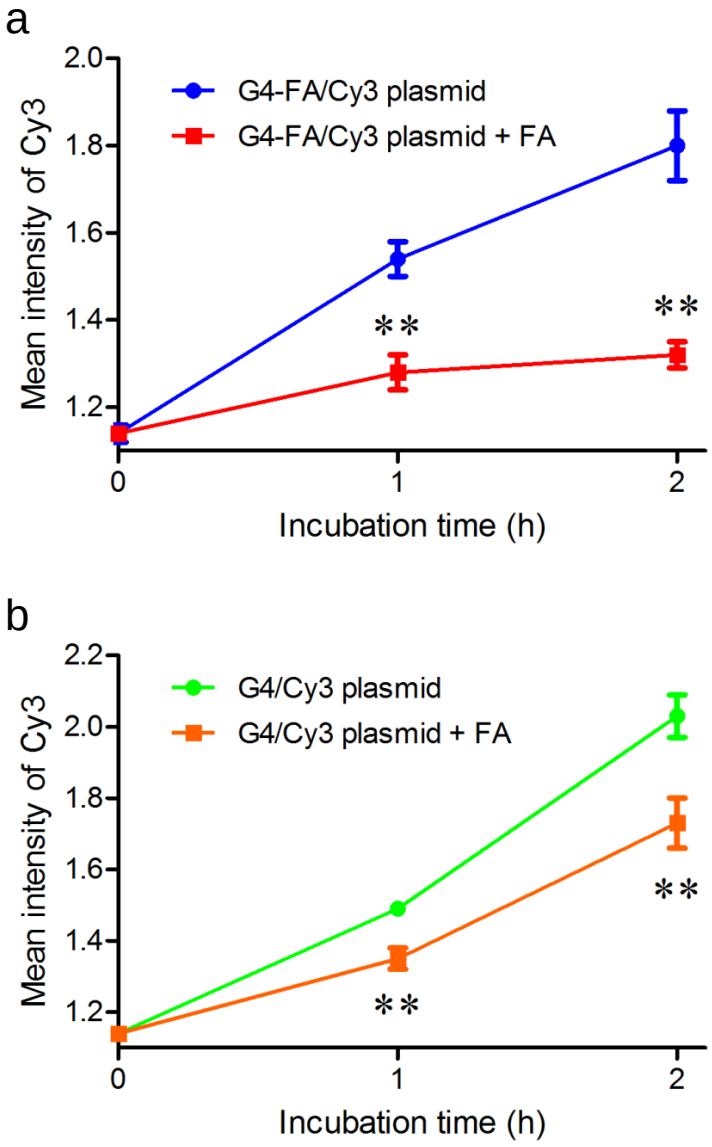

Figure 4.34: Effect of free FA on cellular uptake kinetics of G4/Cy3-plasmid and G4-FA/Cy3-plasmid polyplexes in HN12 cells.
HN12 cells were treated with HN12 cells were treated with G4/Cy3-plasmid and G4-FA/Cy3-plasmid polyplexes (5:1, μg/μg) for 1 and 2 h in the absence or presence of free FA (0.5 mg/mL). The Cy3 fluorescence intensity of the cells treated with G4-FA/Cy3-plasmid polyplexes was evaluated by flow cytometry (a). The Cy3 fluorescence intensity of the cells treated with G4/Cy3-plasmid polyplexes was evaluated by flow cytometry (b). The dots and error bars are means $\pm$ SD. n = 5-6. ** $p <$ 0.01 versus the treatment in the absence of free FA at each indicated time point.

Lastly, we setup a co-culture model, which contained FR-positive HN12 cells and FR-negative U87 cells, to further illustrate that cellular uptake of G4-FA/plasmid polyplexes is FR-dependent. In order to clearly identify HN12 cells and U87 cells, we hereby chose HN12 cells with YFP expression (HN12-YFP). As we expected, G4/Cy3-plasmid polyplexes were taken up by both HN12-YFP cells and U87 cells at 6 h-post transfection (Figure 4.35). No difference of polyplex uptake level was observed between HN12-YFP cells and U87 cells. In contrast, G4-FA/Cy3-plasmid polyplexes were most taken up by HN12-YFP cells at 6 h-post transfection (Figure 4.35). By calculating the percentage of cells which took up polyplexes, we found 92% HN12-YFP cells and 89% U87 cells took up G4/Cy3-plasmid polyplexes (Figure 4.36). No significant difference in cell percentage was observed between HN12-YFP cells and U87 cells. In contrast, we found 84% HN12-YFP cells but only 25% U87 cells took up G4-FA/Cy3-plasmid polyplexes (Figure 4.36). The uptake of G4-FA/Cy3-plasmid polyplexes in HN12-YFP cells was significant more than that in U87 cells. At 24 h-post transfection, a high uptake of G4/Cy3-plasmid polyplexes was observed in both HN12-YFP and U87 cells (Figure 4.37). However, the uptake of G4-FA/Cy3-plasmid polyplexes was higher in HN12-YFP cells than U87 cells as the more and stronger Cy3 fluorescence was colocalized with YFP fluorescence (Figure 4.37). Taken together, our results clearly demonstrate that FA decorated dendrimer/plasmid polyplexes can trigger cellular uptake through FR-mediated endocytosis which is highly FR-dependent. G4-FA/plasmid polyplexes are preferentially taken up by FR-postive cells compared to FR-negative cells. According to our early calculation (Table 4.2), the molar ratio of G4-FA to plasmid at a weight ratio of 5 is 671. Most likely, several G4-FA conjugates were coated onto one plasmid, which may yield a FA-decorated dendrimer-plasmid micelle. Based on our best understanding, plasmid does not shield FA on the dendrimer surface, which makes polyplexes retain targeting ability, same as FA-decorated dendrimers.

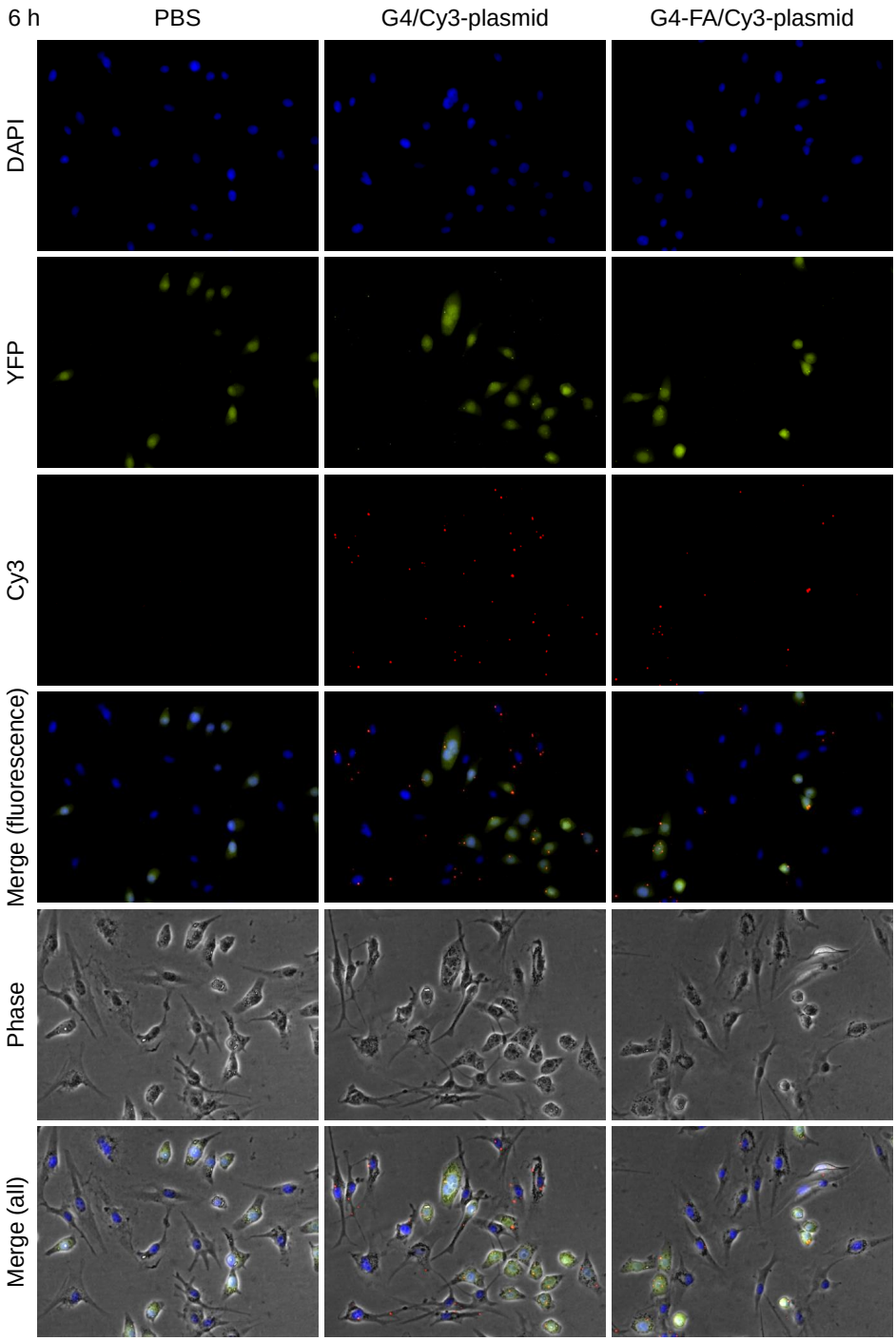

Figure 4.35: Cellular uptake of FITC-G4-FA/Cy3-plasmid polyplexes in the coculture model.
HN12 cells were cocultured with U87 cells at same seeding density. The cells were treated with FITC-G4-FA/Cy3-plasmid polyplexes (5:1, μg/μg) for 6 h, then fixed, counterstained with DAPI and imaged using fluorescence microscope. Original magnification, 200×. The images are representative of experiments conducted on three independent occasions.

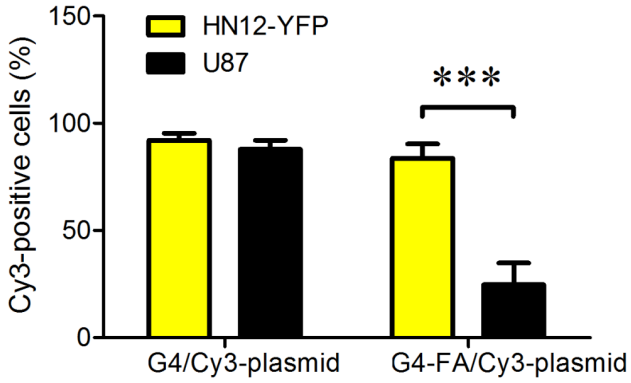

Figure 4.36: Cellular uptake of FITC-G4-FA/Cy3-plasmid polyplexes in the coculture model.
HN12-YFP cells were cocultured with U87 cells at same seeding density. The cells were treated with FITC-G4-FA/Cy3-plasmid polyplexes (5:1, μg/μg) for 6 h, then fixed, counterstained with DAPI and imaged using fluorescence microscope. The number of HN12-YFP cells and U87 cells transfected with Cy3-plasmid were counted and normalized to the total cell number for each cell line from 9 randomly selected fields. The bars and error bars are means $\pm$ SEM. n = 9. *** $p < 0.001$ versus HN12-YFP cells.

4.4.6 Transfection efficiency of polyplexes

By understanding the transfection mechanism, we tested the transfection efficiency of G4-FA/plasmid polyplexes. The in vitro gene transfection efficiency of G4-FA conjugates was evaluated using HN12 cells with GFP and YFP plasmid as reporters. To ascertain whether the use of targeting moiety FA would result in improved gene transfection, G4-mediated gene transfection was evaluated for direct comparison. Generally, increasing vector to plasmid ratio very likely augments gene transfection efficiency, but cytotoxicity of the vector may also increase at high concentrations, particularly for PEI, which has high toxicity [321]. Therefore, gene transfection of the vectors should be evaluated in conjunction with their potential toxic effects on transfected cells. G4-FA conjugates were complexed with GFP plasmid or p53 plasmid at a weight ratio of 1:1, 5:1, and 20:1, which were shown to generate stable complexation in gel retardation assay (Figure 4.11). The transfection efficiency was evaluated using GFP and YFP expression, which was qualitatively illustrated by fluorescence microscopy and quantified by both flow cytometery and Western blotting. The cell viability after

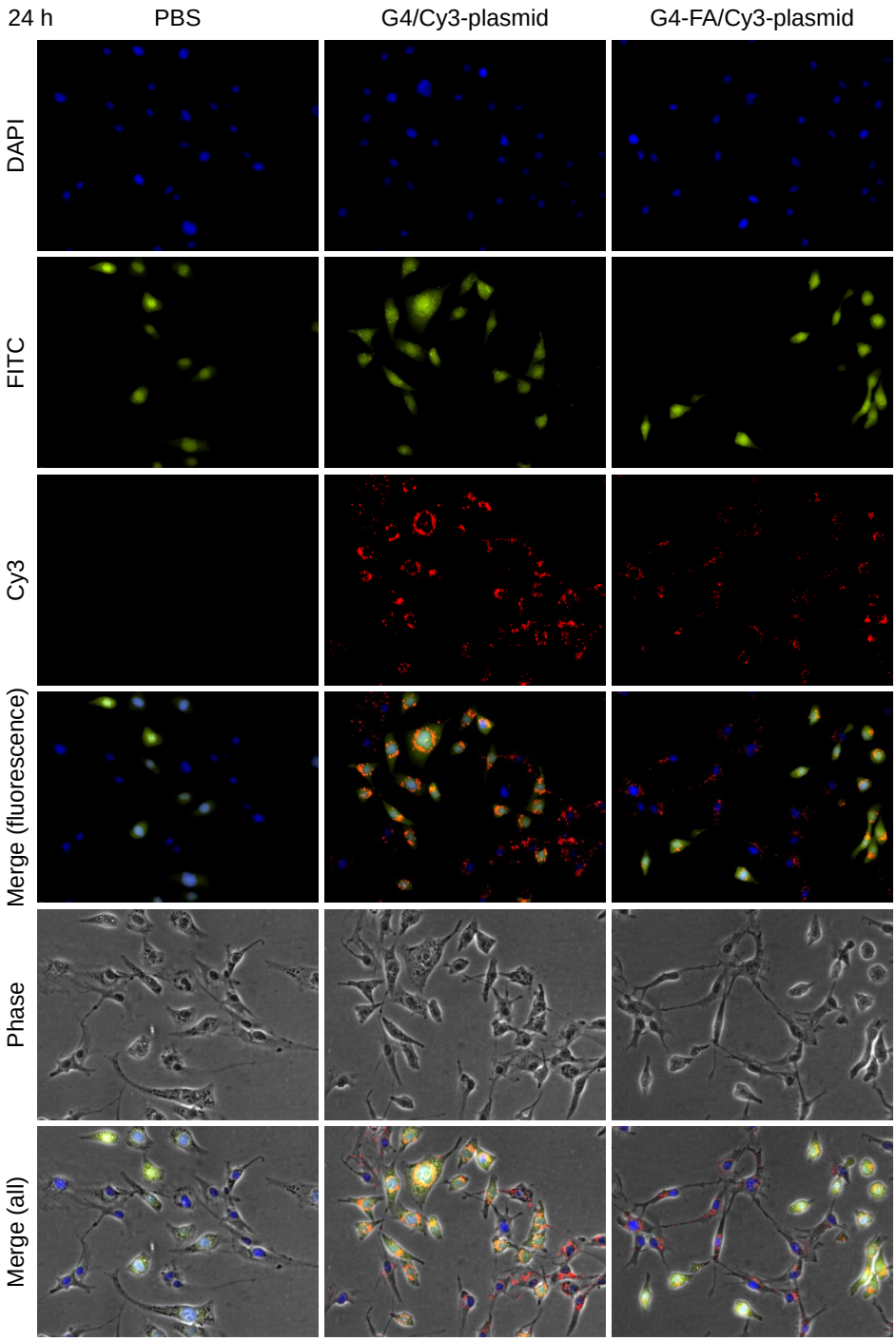

Figure 4.37: Cellular uptake of FITC-G4-FA/Cy3-plasmid polyplexes in the coculture model.
HN12 cells were cocultured with U87 cells at same seeding density. The cells were treated with FITC-G4-FA/Cy3-plasmid polyplexes (5:1, μg/μg) for 24 h, then fixed, counterstained with DAPI and imaged using fluorescence microscope. Original magnification, 200×. The images are representative of experiments conducted on three independent occasions.

transfection was assessed as well.

The fluorescence images of GFP-expressing HN12 cells were obtained following transfection (Figure 4.38). It is apparent that G4-FA/pGFP polyplexes at weight ratios of 1 and 5 showed the highest percentage of transfected HN12 cells with strong fluorescence. However, G4-FA/pGFP polyplexes at a weight ratio of 20 displayed a relatively low percentage of transfected HN12 cells. In contrast, G4/pGFP polyplexes at a weight ratio of 5 also yielded a low percentage of transfected HN12 cells with slightly low fluorescence intensity. To confirm the fluorescence microscopy results, we applied flow cytometry analysis to quantify the proportion of GFP-transfected HN12 cells. Compared to the cells treated with PBS, a distinguishable right shift of GFP fluorescence was observed in the cells treated with G4-FA/pGFP and G4/pGFP polyplexes (Figure 4.39). Noteworthy is that the cells treated with G4-FA/pGFP polyplexes at weight ratios of 1 and 5 displayed more both PI and GFP positive cells than those treated with G4-FA/pGFP polyplexes at a weight ratio of 20 and G4/pGFP polyplexes at a weight ratio of 5. Quantitative analysis revealed that the proportion of HN12 cells transfected was 14.9%, 22.6%, 6.8%, and 6.4% by G4-FA/pGFP polyplexes at weight ratios of 1, 5, 20, and G4/pGFP polyplexes at a weight ratio of 5, respectively (Figure 4.40). Among the presented transfection conditions, G4-FA/pGFP polyplexes at a weight ratio of 5 showed the highest transfection efficiency in HN12 cells. The transfection efficiency of G4-FA/pGFP polyplexes was 3.5 times that of non-targeting G4/pGFP polyplexes at the same weight ratio. To further confirm the fluorescence microscopy and flow cytometry results, we employed Western blot analysis to quantify the YFP expression levels in the transfected HN12 cells. Western blot analysis confirmed that G4-FA/pYFP polyplexes at weight ratios of 1 and 5 had the highest transfection efficiency in terms of the ability to induce YFP expression in HN12 cells (Figure 4.41). G4-FA/pYFP polyplexes resulted in an increase of 72% in the overall amount of YFP expressed in HN12 cells as compared to non-targeting G4/pYFP polyplexes at the same weight ratio.

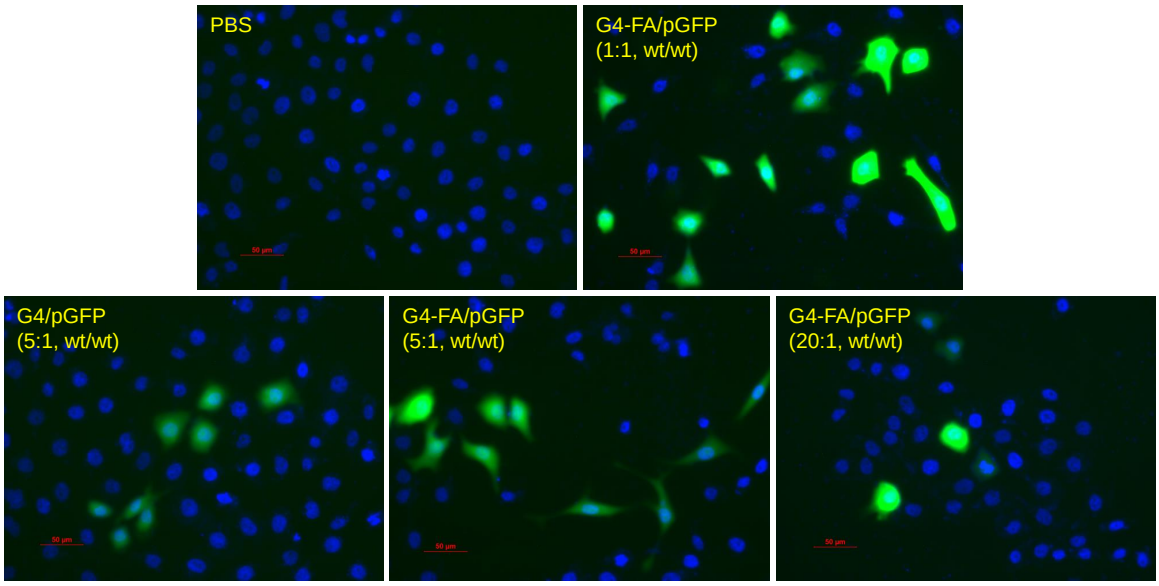

Figure 4.38: In vitro transfection efficacy of polyplexes.
HN12 cells were treated with G4-FA/pMAX-GFP plasmid (pGFP) polyplexes at weight ratios of 1, 5, and 20, and G4/pGFP polyplexes at a weight ratio of 5 for 48 h, followed by another 48 h culture. The cells treated with PBS were used as negative control. Then, the cells were fixed, counterstained with DAPI, and imaged using fluorescence microscope. Original magnification, 200×. The images are representative of experiments conducted on three independent occasions.

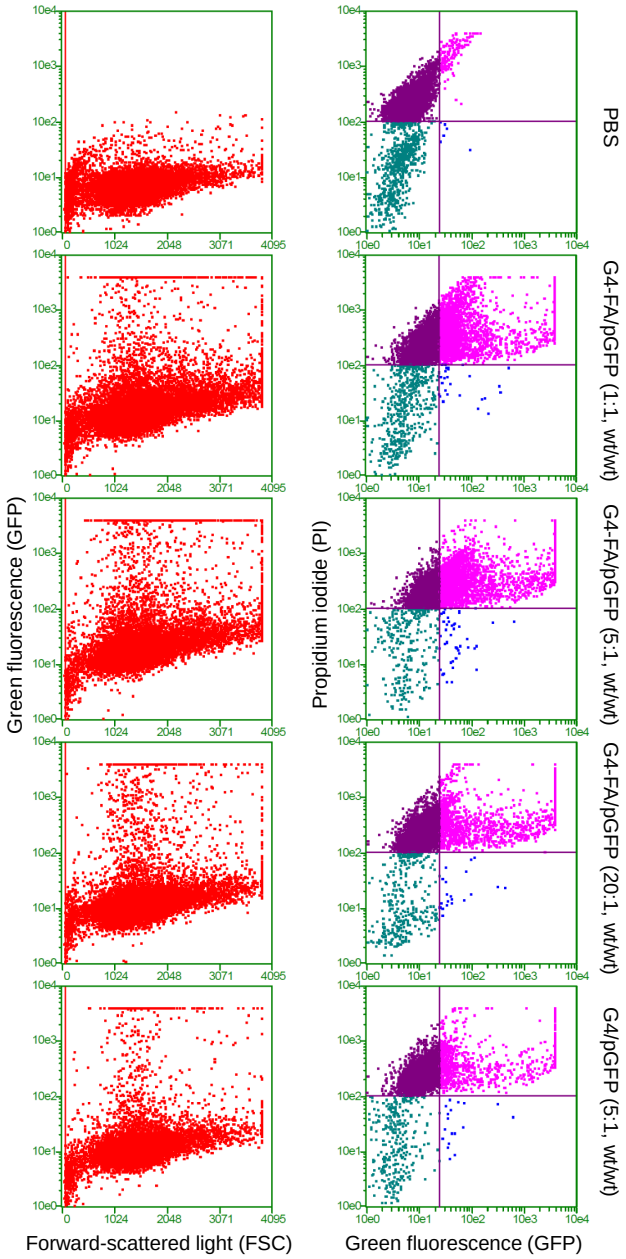

Figure 4.39: In vitro transfection efficacy of polyplexes.
HN12 cells were treated with G4-FA/pMAX-GFP plasmid (pGFP) polyplexes at weight ratios of 1, 5, and 20, and G4/pGFP polyplexes at a weight ratio of 5 for 48 h, followed by another 48 h culture. The cells treated with PBS were used as negative control. Then, the cells were fixed and counterstained with PI. The GFP expression was evaluated by flow cytometry. Dot plot of cell scattering (forward scattering verse green fluorescence intensity) was presented on the left, and the dot plot of cell scattering (green fluorescence intensity verse PI intensity) was presented on the right. The images are representative of experiments conducted on three independent occasions.

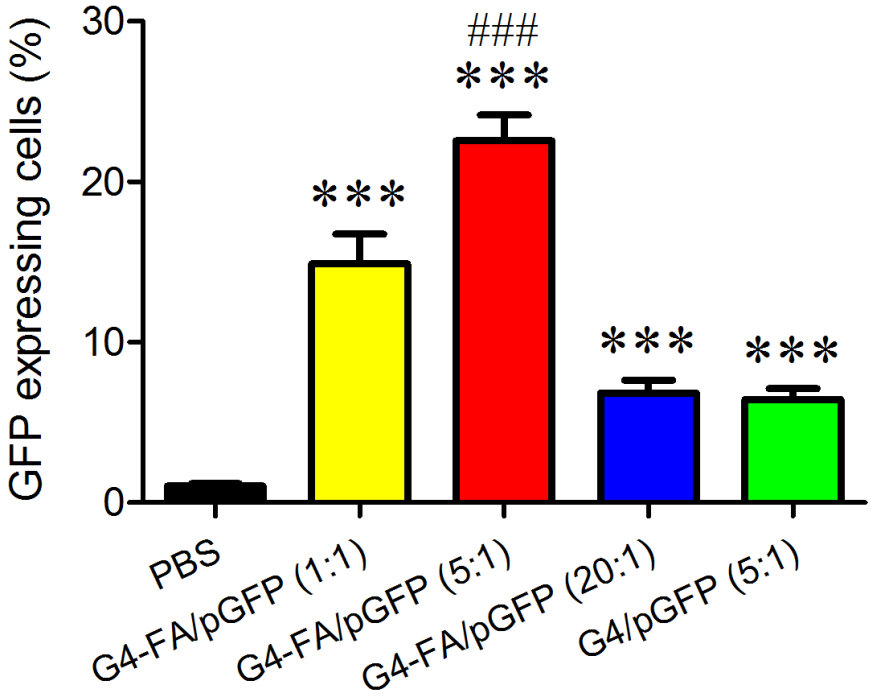

Figure 4.40: In vitro transfection efficiency of polyplexes.
HN12 cells were treated with G4-FA/pMAX-GFP plasmid (pGFP) polyplexes at weight ratios of 1, 5, and 20, and G4/pGFP polyplexes at a weight ratio of 5 for 48 h, followed by another 48 h culture. The cells treated with PBS were used as negative control. Then, the cells were fixed, counterstained with PI, and analyzed by flow cytometry. The bars and error bars are means ± SD. n = 8. *** $p < 0.001$ versus cells treated with PBS; ### $p < 0.001$ versus cells treated with G4/pGFP polyplexes at a weight ratio of 5.

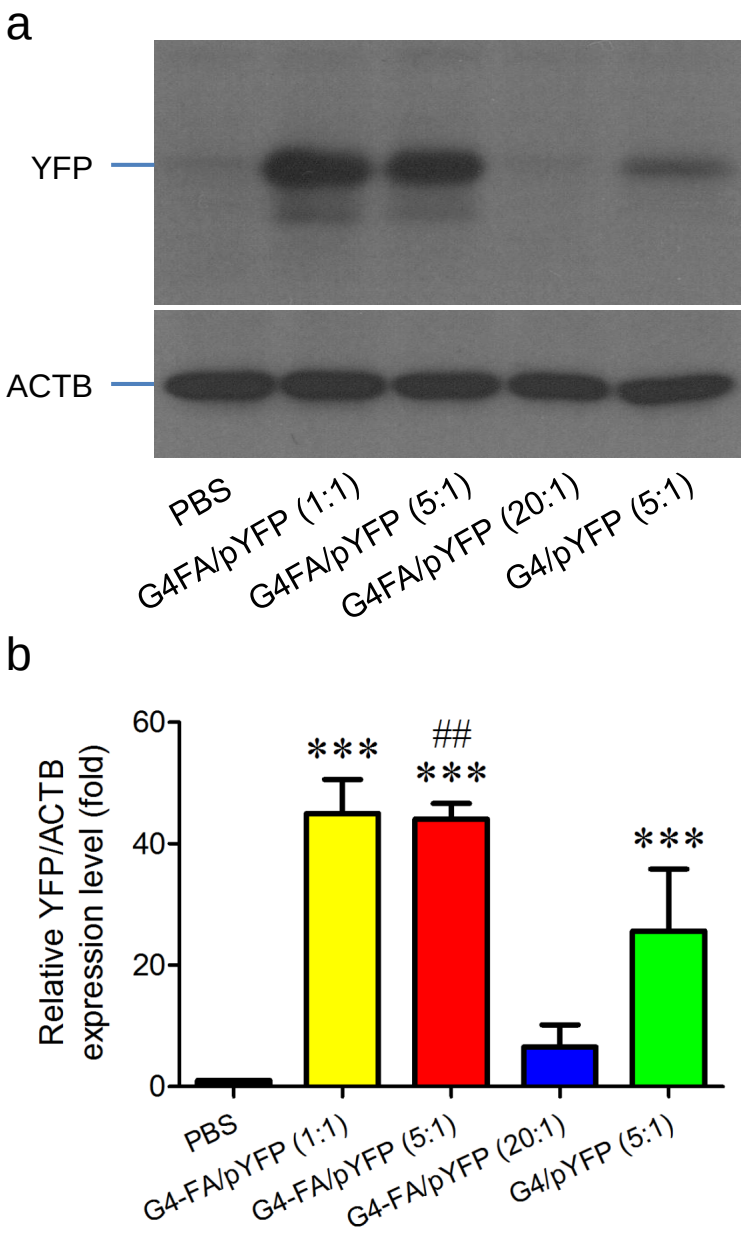

Figure 4.41: In vitro transfection efficiency of polyplexes.
HN12 cells were treated with G4-FA/pCEFL-YFP plasmid (pYFP) polyplexes at weight ratios of 1, 5, and 20, and G4/pYFP polyplexes at a weight ratio of 5 for 48 h, followed by another 48 h culture. The cells treated with PBS were used as negative control. The protein expression level of YFP was determined by Western blot analysis, and the expression level of β-actin (ACTB) was used as a loading control of total cellular protein (a). Each positive YFP band was normalized to ACTB and was quantified by NIH ImageJ (b). The data represents typical one of three experiments. The bars and error bars are mean $\pm$ SEM. n = 5. *** $p < 0.001$ versus cells treated with PBS; ### $p < 0.001$ versus cells treated with G4/pGFP polyplexes at a weight ratio of 5.

Taken together, our current work suggests that G4-FA/plasmid polyplexes at a weight ratio of 5 possess the highest transfection efficiency in HN12 cells in terms of transfected cell proportion and transgene expression. Increasing vector to plasmid ratio does not necessarily augment gene transfection efficiency for G4-FA conjugates. As early described previously, free FA works as a competitive ligand to inhibit uptake of G4-FA/Cy3-plasmid polyplexes in HN12 cells (Figure 4.32, 4.33, 4.34). Most likely, increasing vector to plasmid ratio yields excess amount of G4-FA conjugates in the polyplexes, which, in turn, function as competitive ligands to bind FR, and subsequently inhibit uptake of G4-FA/plasmid polyplexes in HN12 cells. Our results indicate that FA-decorated G4/plasmid polyplexes significantly increase transfection efficiency in HN12 cells in terms of transfected cell proportion and transgene expression. However, these results raised another question why G4/Cy3-plasmid polyplexes possessed higher cellular uptake (Figure 4.13, 4.14, 4.15, 4.16, 4.17) but lower transfection efficiency in HN12 cells than G4-FA/Cy3-plasmid polyplexes (Figure 4.38, 4.39, 4.40, 4.41). One possibility is that higher cellular uptake may yield higher cytotoxicity, which can compromise overall transfection efficiency.

To answer this question, we evaluated the cytocompatibility of polyplexes prepared at various weight ratios by using WST-1 assay. In our previous work, HN12 cells transfected with G4/pGFP polyplexes at a weight ratio of 100 showed a decrease of 32% in cell viability compared to untreated controls. In the current study, HN12 cells transfected with G4/pGFP polyplexes at a weight ratio of 5 also displayed a decrease of 16% in cell viability compared to PBS-treated cells (Figure 4.42). The difference could be explained as following. According to our previous work, HN12 cells were transfected with 100 μg of G4 dendrimer complexed with 1 μg of GFP plasmid for 1 day followed by 2 days culture, which led to a decrease of 32% in cell viability. Here, HN12 cells were transfected with 10 μg of G4 dendrimer complexed with 2 μg of GFP plasmid for 2 days followed by 2 days culture, which led to a decrease of 16% in cell viability. The overall amount of G4 dendrimer used in current study was one tenth of that in previous work, but transfection time was twice as long as previous work. Therefore, the cell viability in HN12 cells transfected with G4/pGFP polyplexes was

higher in the current work. In contrast, G4-FA/pGFP polyplexes were more cytocompatible than G4/pGFP polyplexes. HN12 cells transfected with G4-FA/pGFP polyplexes at weight ratios of 1, 5, and 20 showed a cell viability of 110%, 102%, and 83%, respectively, compared to PBS-treated cells (Figure 4.42). The decrease in cell viability in HN12 cells transfected with G4-FA/pGFP polyplexes was only observed at a weight ratio of 20. By comparing G4-FA/pGFP polyplexes with G4/pGFP polyplexes at the same weight ratio, HN12 cells transfected with G4-FA/pGFP polyplexes possessed significantly higher cell viability than the cells transfected with G4/pGFP polyplexes. This result agrees well with the cytocompatibility result of G4 and G4-FA vehicles alone that G4-FA conjugates were more cytocompatible than G4 dendrimer (Figure 4.10). Our early results suggest that the cellular uptake of G4-FA conjugates and G4-FA/plasmid polyplexes is via FR-mediated endocytosis. Therefore, the saturated FR on cell membrane may limit cellular uptake of G4-FA conjugates and G4-FA/plasmid polyplexes in high FR-expression cells, such as HN12 cells (Figure 4.13, 4.14, 4.15, 4.16, 4.17 and Figure 4.29, 4.30, 4.31). As a result, the cytocompatibility of G4-FA/plasmid polyplexes was enhanced (Figure 4.42), which in turn increased overall transfection efficiency in HN12 cells (Figure 4.38, 4.39, 4.40, 4.41).

4.5 Conclusions

FA-conjugated PAMAM dendrimer generation 4 (G4-FA) conjugates were successfully synthesized and evaluated as a new vector. G4-FA conjugates could complex tightly with plasmid DNA to form G4-FA/DNA polyplexes. The cellular uptake of G4-FA/DNA polyplexes was in a FR-dependent manner. Both free FA and excess G4-FA conjugates could competitively inhibit cellular uptake of G4-FA/DNA polyplexes. The transfection efficiency of G4-FA/DNA polyplexes is higher at a weight ratio of 5 than that of 1 and 20. At the same weight ratio of 5, the transfection efficiency of G4-FA/DNA polyplexes is higher than that of non-targeting G4/DNA polyplexes. This work has demonstrated that FA decoration on dendrimer/DNA polyplexes allows ac-

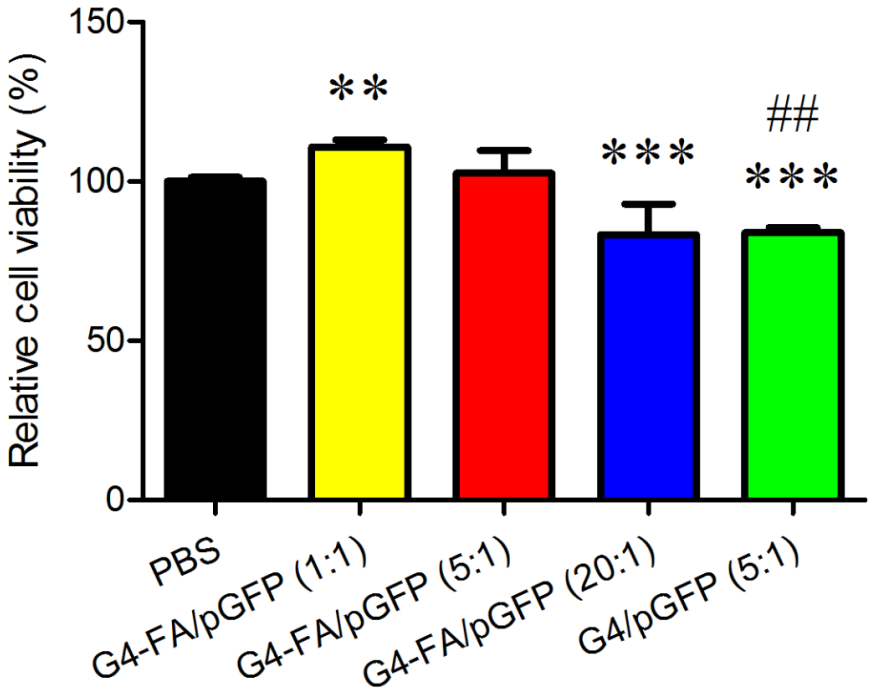

Figure 4.42: Cytocompatibility of polyplexes.
HN12 cells were treated with G4-FA/pMAX-GFP plasmid (pGFP) polyplexes at weight ratios of 1, 5, and 20, and G4/pGFP polyplexes at a weight ratio of 5 for 48 h, followed by another 48 h culture. The cells treated with PBS were used as negative control. Cell viability of HN12 cells treated with polyplexes was determined by WST-1 assay and normalized to the cells treated with PBS. The bars and error bars are means ± SD. n = 3. ** $p < 0.01$ *** $p < 0.001$ versus cells treated with PBS; ## $p < 0.01$ versus cells treated with G4/pGFP polyplexes at a weight ratio of 5.

tive targeting delivery, reduces cytotoxicity, and results in enhanced gene transfection efficiency.

Chapter 5

Folic Acid-Decorated PAMAM Dendrimer for Targeted Gene Delivery: In Vivo Studies for Head and Neck Cancer

Preface: This chapter has been prepared as a research article.

Leyuan Xu, W. Andrew Yeudall, Hu Yang

5.1 Abstract

To date, head and neck cancer presents high morbidity and low rates of survival. Cancer gene therapy is regarded as a promising approach but encounters delivery challenges. In this work, folic acid-conjugated polyamidoamine dendrimer generation 4 (G4-FA) conjugates were investigated for in vivo targeted delivery of siRNA against vascular endothelial growth factor A (siVEGFA) for cancer gene therapy. G4-FA conjugates were complexed with siVEGFA to form G4-FA/siVEGFA polyplexes. The zeta potential of G4-FA/siVEGFA polyplexes was characterized by DLS, and the in vitro knockdown efficiency was determined by real-time PCR and ELISA. Near infrared fluorescence dye was conjugated onto G4-FA conjugates (NIR-G4-FA)

for biodistribution imaging. The therapeutic efficacy of G4-FA/siVEGFA polyplexes was evaluated in a flank xenograft model of head and neck cancer. The level of angiogenesis in the tumor was analyzed by immunohistochemical staining of CD31. It was found G4-FA/siVEGFA polyplexes significantly knocked down VEGFA mRNA expression and reduced VEGFA protein release in HN12 cells. In the HN12 tumor-bearing nude mice, NIR-G4-FA conjugates were preferentially taken up by the tumor and retained in the tumor for at least 21 days via intratumoral (i.t.) administration. Two-dose administration of G4-FA/siVEGFA polyplexes significantly inhibited tumor growth by lowering tumor angiogenesis over an observation period of 3 weeks. These results show promise of using G4-FA conjugates for head and neck cancer gene delivery.

5.2 Introduction

Head and neck cancer includes malignancies arising in the mucosal surfaces of the oral cavity, pharynx and larynx, and is generally referred to as head and neck squamous cell carcinomas (HNSCC) [49]. HNSCC is the sixth most prevalent cancers in mankind and presents high morbidity and low rates of survival [22]. Treatment of HNSCC frequently requires multi-modality intervention involving surgical, medical, and radiation oncology [124]. These conventional therapies have been used for decades in HNSCC but they have several limitations. Surgery may cause disfigurement and reduce patient quality of life. Concurrent chemotherapy and radiation may lead to severe toxicity [57, 264]. The toxicities of conventional therapies are in large part due to their non-selective nature. Molecular targeted therapies are therefore in development with the goal of developing selective approaches to inhibit the growth of HNSCC cells.

To date, small-molecular-weight anticancer drugs remain dominant on the pharmaceutical market. Most anticancer drugs are designed to target DNA replication and cell division, subsequently causing cytotoxicity or apoptosis in cells. However, lack of tumor specificity is the common problem associated with this type of an-

ticancer drugs and causes poor clinical outcomes. Some anticancer drugs are designed to target cell signaling intermediates which contribute to cancer growth. However, development of acquired drug resistance is the common problem associated with this type of anticancer drugs and often leads to relapse [46]. Discovery and development of new cytotoxic agents for cancer therapy remains a key focus, but modification of existing drugs to improve their specificity and potency is also an important approach for anticancer chemotherapy.

Because cancer is an acquired genetic disorder, gene therapy may provide highly effective treatment that is precisely tailored to the gene structure of each tumor, which in turn reduces systemic toxicity [20]. Cancer gene therapy can be used in different approaches, such as mutation correction, enhancement of immune response against cancer cells, overexpression of suicide proteins and enzymes, RNA interference (RNAi), and antiangiogenesis [153]. Numerous suicide genes have been found in the laboratory, and some have undergone clinical trials, including tumor necrosis factor α (TNFα), TNF-related apoptosis-inducing ligand (TRAIL), caspase-9, and B-cell lymphoma 2 (Bcl-2)-interacting killer (Bik) [111]. Next, a paradigm shift in design of anticancer therapeutics has been brought about by groundbreaking discovery-RNAi. In the last decade, RNAi, especially small interference RNA (siRNA), is rapidly developed as an effective therapeutics for cancer therapy [296]. A number of siRNA and small hairpin RNA (shRNA) have shown promising therapeutic outcome in mouse xenograft tumor models, such as siVEGF (vascular endothelial growth factor), siSTAT3 (signal transducer and activator of transcription 3), siCDK1 (cyclin-dependent kinase 1) for breast cancer treatment [122, 45, 47, 168, 161]; sic-Myc, siSHMT1 (serine hydroxymethyltransferase isoform 1), shAnxA2 (Annexin A2) for lung cancer treatment [330, 195, 5]; siYB-1 (Y-box binding protein-1), siPLK-1 (serine/threonine-protein kinase), siNotch1 (Notch homolog 1, translocation-associated), siREV1, siREV3L for prostate cancer cancer [324, 288, 248, 300]; siVEGF for ovarian cancer treatment [56]; siRRM2 (ribonucleotide reductase M2), siEZH2 (Enhancer of zeste homolog 2)/siOct4 (octamer-binding transcription factor 4), and a combination of shVEGF, shTERT (telomerase reverse transcriptase), shBcl-xl (B-

cell lymphoma-extra large) for HNSCC treatment [88, 162, 216]. Among these siRNA and shRNA therapies, VEGFA knockdown has been widely explored for the treatment in different types of cancer. Indeed, VEGFA is one of the major regulators of angiogenesis. Angiogenesis is a prerequisite for tumor development in the tumor microenvironment, a crucial extracellular matrix for sustained tumor growth [20].

Cancer gene therapy is regarded as a promising approach but yet encounters delivery challenges [20, 296]. Therefore, numerous methods have been developed for gene delivery. Generally, there are two different categories of gene transfection methods based on the nature of the carriers, which are viruses and nonviral gene delivery carriers.[8] Viral vectors give high transfection efficiency and long-term gene expression but raise serious safety concerns, including limited size of carried gene, antigenicity, inflammation, insertion mutagenesis, and difficulty in a large scale. In contrast, nonviral vectors possess many advantages, including low immunogenicity, low toxicity, and potential targeting ability, which make nonviral vectors to serve as an alternative gene delivery system [20, 153].

In Chapter 4, we have successfully fabricated and characterized folic acid (FA) conjugated polyamidoamine dendrimer generation 4 (G4-FA) conjugates. G4-FA conjugates have shown to have the ability target folate receptor (FRα) and enhanced transfection efficiency in HN12 cells. In this chapter, we hypothesize that G4-FA conjugates can efficiently deliver siRNA into HN12 xenograft tumor. Near infrared fluorescence dye (NIR) was conjugated onto G4-FA conjugates and G4 dendrimer to monitor the biodistribution of the vehicles in the HN12 tumor-bearing mice. Both intratumoral (i.t.) and intravenous (i.v.) administration routes were evaluated. siRNA against VEGFA (siVEGFA) was chosen as a therapeutic siRNA and was complexed with G4-FA conjugates to form G4-FA/siVEGFA polyplexes. The therapeutic efficacy of G4-FA/siVEGFA polyplexes was studied and compared with siVEGFA alone, G4-FA/siGFP (control siRNA), and G4/siVEGFA. The angiogenesis in the tumor was analyzed as well.

5.3 Materials and Methods

5.3.1 Materials

Diaminobutane (DAB) core dendrimer generation 4.0 (technical grade) was purchased from NanoSynthons (Mt. Pleasant, MI). Dimethyl sulfoxide (DMSO), folic acid (FA), formaldehyde solution (37 wt. % in H2O), and 1-ethyl-3-[3-dimethylaminopropyl] carbodiimide hydrochloride (EDC) were purchased from Sigma-Aldrich (St. Louis, MO). Phosphate-buffered saline (PBS) and permount mounting medium were purchased from Fisher Scientific (Pittsburgh, PA). Dulbeccos modified Eagle medium (DMEM), trypsin-EDTA (0.25%), and penicillin-streptomycin (10,000 U/mL) were purchased from Life Technologies (Carlsbad, CA). Ingenio electroporation solution was purchased from Mirus Bio (Madison, WI). Vectastain ABC kit, 3,3'-Diaminobenzidine (DAB), and hematoxylin were purchased from Vector Laboratories (Burlingame, CA). Cosmic calf serum (CS) was purchased from Lonza (Walkersville, MD). β-actin (ACTBD11B7) antibody was purchased from Santa Cruz Biotechnology (Santa Cruz, CA). VEGFA (ab46154) and CD31 (ab28364) antibodies were purchased from Abcam (Cambridge, MA). Goat anti-rabbit antibody conjugated to horseradish peroxidase and goat anti-mouse antibody conjugated to horseradish peroxidase were purchased from Bio-Rad (Hercules, CA). Polyvinylidene difluoride (PVDF) membrane was purchased from Millipore (Billerica, MA). Western lightning Plus ECL was purchased from Perkin-Elmer (Waltham, MA). SnakeSkin dialysis tubing with 7,000 molecular weight cut-off (MWCO), human VEGF-A ELISA kit, ABsolute blue qPCR SYBR green low ROX mix, and Richard-Allan Scientific^{TM} signature series Clear-Rite 3 were purchased from Thermo Scientific (Rockford, IL). IRDye 800CW NHS Ester was purchased from Li-COR Biotechnology (Lincoln, NE). BD Retrievagen Antigen Retrieval Systems were purchased from BD Biosciences (San Jose, CA). siRNA and primers were synthesized and purchased from Sigma-Aldrich (St. Louis, MO).

5.3.2 Synthesis of PAMAM dendrimer conjugates

5.3.2.1 Synthesis of G4-FA

FA (18.6 mg, 42.2 μmol, MW = 441.4 g/mol) was allowed to react with EDC (113.3 mg, 590.9 μmol, MW = 191.71 g/mol) in a mixture of 12 mL of DMF and 4 mL of DMSO for 1 h. The organic reaction mixture was added dropwise to 50 mL of DI water solution containing 100 mg (7. 03 μmol) of PAMAM dendrimer G4 (MW = 14215 g/mol). The reaction mixture was vigorously stirred for 2 days and then dialyzed against DI water using dialysis tubing with MWCO of 7 kDa for 2 days. After lyophilization (Flexi-Dry^{TM} MP corrosion resistant freeze-dryer), the resultant G4-FA conjugates were obtained. The number of FA molecules coupled to each G4 dendrimer was quantified by using GENESYS 6 spectrophotometer (Thermo Scientific, Rockford, IL). The resultant G4-FA conjugates were analyzed by reverse-phase high performance liquid chromatography (RP-HPLC) and Proton nuclear magnetic resonance (^{1}H NMR) spectroscopy as described in Materials and Methods in Chapter 4.

5.3.2.2 Synthesis of NIR-G4-FA

IRDye 800CW NHS Ester (2 mg, 1.72 μmol, MW = 1162.2 g/mol) was dissolved in 1 mL of PBS. The dye solution was added dropwise to 9 mL of PBS containing 13.6 mg (0.86 μmol) of G4- FA conjugates (MW = 15783 g/mol by UV-Vis spectrophotometer). The reaction mixture was stirred in the dark for 1 day and then dialyzed against DI water using dialysis tubing with MWCO of 7 kDa for 2 days. After lyophilization, the resultant NIR-G4-FA conjugates were obtained.

5.3.2.3 Synthesis of NIR-G4

IRDye 800CW NHS Ester (2 mg, 1.72 μmol, MW = 1162.2 g/mol) was dissolved in 1 mL of PBS. The dye solution was added dropwise to 9 mL of PBS containing 12.2 mg (0.86 μmol) of G4 dendrimer (MW = 14215 g/mol). The reaction mixture was stirred in the dark for 1 day and then dialyzed against DI water using dialysis

tube with MWCO of 7 kDa for 2 days. After lyophilization, the resultant NIR-G4 conjugates were obtained.

The number of NIR molecules coupled to each G4-FA conjugate and G4 dendrimer was quantified by using GENESYS 6 spectrophotometer (Thermo Scientific, Rockford, IL) and Odyssey CLx infrared imaging system (Li-COR Biotechnology, Lincoln, NE).

5.3.3 Zeta potential measurements

PBS was filtered through a 20 nm filter. G4 dendrimer and its derivatives were dissolved in the filtered PBS at the concentration of 0.5 mg/mL. Various amounts of G4-FA conjugates (0 μg, 10 μg, 50 μg, and 200 μg) and G4 dendrimer (50 μg) were diluted in 600 μL of filtered PBS; while 10 μg of siRNA against VEGFA was diluted in 400 μL of filtered PBS. The solutions were vortexed for 10 s and then equilibrated for 10 min at room temperature. The dendrimer solution was added to the plasmid solution, homogenized for 10 s with a vortex, and equilibrated for 30 min at room temperature. The size and zeta potential of G4 dendrimer, its derivatives and polyplexes were measured at room temperature using a Malvern Zetasizer Nano ZS90 apparatus (Malvern Instruments, Worcestershire, U.K.).

5.3.4 Cell culture

HN12 and HN12-YFP cells were cultured as described previously in Dulbeccos modified Eagles medium (DMEM) supplemented with 10% Cosmic calf serum, 100 units/mL of penicillin, and 100 μg/mL of streptomycin at 37 °C in 95% air/5% CO_2 [272].

5.3.5 Polyplex formation and transfection

The custom designed siRNA against VEGFA (siVEGFA) and GFP (siGFP) were synthesized by Sigma-Aldrich (St. Louis, MO). The sequences of siRNAs were summarized in Table 5.1. A series of G4-FA/siRNA or G4/siRNA polyplex solutions were prepared accordingly. 2 μg, 10 μg, and 40 μg of G4-FA conjugates or 40 μg of G4

Table 5.1: Sequences of siRNA duplexes

Name	Forward sequence	Reverse sequence	Ref.
siVEGFA	GGAGUACCCUGAUGA GAUCdTdT	GAUCUCAUCAGGGUA CUCCdTdT	[251]
siGFP	GCACGACUUCUUCAA GUCCdTdT	GGACUUGAAGAAGUC GUGCdTdT	[119]

were diluted in 300 μL of DMEM; while 2 μg of siRNA (siVEGFA or siGFP) was diluted in 200 μL of DMEM. All the solutions were mixed by vortexing for 10 s and then equilibrated for 10 min at room temperature. The G4-FA conjugates solution or G4 dendrimer solution was added to the plasmid solution, homogenized for 10 s with a vortex, and equilibrated for 30 min at room temperature. Then 2.5 mL of the complete medium containing 10% serum was added into the polyplex solution, and the final volume brought to 3 mL [154, 159].

HN12 cells were seeded in the 6-well plates at a density of 20,000 cells/well and allowed to attach overnight. Before addition of the transfection medium, the spent medium was removed, and the cells were washed with PBS once. The cells were then incubated with 3 mL of polyplex-containing medium at 37 °C for 48 h. At the end of transfection, the spent medium was replaced with the complete medium containing 10% serum and maintained under normal growth conditions for another 48 h. The cells treated with plain PBS in the same conditions were used as negative controls.

5.3.6 Electroporation

Electroporation was used to knockdown VEGFA mRNA expression with siVEGFA function validation. Briefly, 1×10^6 HN12 cells were mixed with 1 μg of either siVEGFA or siGFP in 100 μL of Ingenio electroporation solution. Electroporation was carried out using Lonza-Amaxa nucleofector (Walkersville, MD) via a T-020 program. Cells were then recovered in 5 ml of growth medium containing 10% serum and plated into a 60-mm dish and treated for 48 h.

Table 5.2: Primer sets for real-time PCR analysis

Name	Forward sequence	Reverse sequence	Ref.
VEGFA	AGGGCAGAATCATCA CGAAGT	AGGGTCTCGATTGGA TGGCA	[11]
ACTB	CATGTACGTTGCTAT CCAGGC	CTCCTTAATGTCACG CACGAT	[95]

5.3.7 Real-time polymerase chain reaction (PCR) analysis

The relative mRNA levels were measured by real-time reverse-transcriptase PCR as previously described [291, 292]. Briefly, at 2 d-post transfection, total RNA was isolated from the cells using an ISOLATE II RNA Mini Kit (Bioline, London, UK) that included DNase treatment. The total RNA concentration from each sample was measured by a UV-Vis spectrophotometer (NanoDrop ND1000, Thermo Scientific, Wilmington, DE). 2 μg of total RNA was used in the first-strand cDNA synthesis. Real-time PCR was performed using SYBR green as a probe in an ABI 7500 Fast Real-Time PCR System (Applied Biosystems, Foster City, CA). Amplification of β-actin (ACTB) was used as internal controls. Relative mRNA expression was quantified with the comparative cycle threshold (Ct) method and expressed as $2^{-\Delta\Delta Ct}$. The sequences of the primers were summarized in Table 5.2.

5.3.8 Western blotting

Western blot analysis of total cellular protein was carried out following procedures described previously [293, 294, 298]. Briefly, at 2 d-post transfection, total cell lysates (30 μg) were separated on a 10% SDS-PAGE gel and transferred onto a polyvinylidene difluoride (PVDF) membrane. The membrane was blocked in Tris-buffered saline (TBS) containing 5% non-fat dry milk for 2 h at room temperature and then incubated in a 1:1000 dilution of primary antibody in blocking buffer overnight at 4 $\circ$C with shaking. The membrane was washed with TBS containing 0.5% Tween 20 (TBST) for three times and then incubated in a 1:3000 dilution of appropriate secondary antibody in TBST at room temperature for 2 h. The specific antigen-antibody interactions were

detected using enhanced chemiluminescence. The expression of ACTB was used as a loading control.

5.3.9 Enzyme-linked immunosorbent assay (ELISA) analysis

The levels of VEGFA protein secreted by HN12 cells in the media were determined by a VEGFA ELISA kit [99]. Briefly, at 2 d-post transfection, the spent media were collected, and VEGFA protein concentrations were measured by ELISA according to the manufacturers instructions. An anti-human VEGFA antibody was pre-coated to the 96-well microplate. The spent media/standards (50μL) were added to the antibody-coated wells and incubated for 2h. Unbound antigen was washed, followed by the addition of biotinylated secondary detecting antibody and subsequent incubation for 1h. Excess detecting antibody was washed, and streptavidin-HRP was added. It reacts with TMB (3,3',5,5'-tetramethylbenzidine) substrate to produce a colorimetric signal. This signal was detected by measuring the absorbance at 450nm using an Epoch plate spectrophotometer (BioTek, Winooski, VT). The number of the cells in each well was measured by Nexcelom Bioscience Cellometer Auto T4 (Nexcelom Bioscience, Lawrence, MA). Then, the VEGFA protein concentrations were normalized to the number of cells per well.

5.3.10 Animal studies

Animal studies were approved by the Institutional Animal Care and Use Committee (IACUC) of Virginia Commonwealth University, and were conducted in accordance with the Declaration of Helsinki, the Guide for the Care and Use of Laboratory Animals, and all applicable regulations.

5.3.10.1 Establishment of the xenograft tumor model of head and neck cancer

HN12 cells or HN12-YFP cells (5×10^6) were injected subcutaneously (s.c.) into 4-week-old female athymic nude mice (Harlan Sprague Dawley, Indianapolis, IN) [80,

Table 5.3: Mice assignment for in vivo biodistribution assessment

Group	Route	Nanoparticles	Dosage/tumor/mouse	Dose	n
1	i.t.	NIR dye	12 μg	1	5
2	i.t.	NIR-G4	175 μg	1	5
3	i.t.	NIR-G4-FA	175 μg	1	5
4	i.v.	NIR dye	12 μg	1	2
5	i.v.	NIR-G4-FA	175 μg	1	2
6	i.v.	NIR-G4-FA/pMAX-GFP	175 μg	1	2

Abbreviations: i.t., intratumoral; i.v., intravenous.

82]. When the tumors had developed to a volume of 80 mm^3 on average, the mice were divided into 14 groups (Tables 5.3, 5.5) in a way to minimize body weight and tumor size differences among the groups.

For the in vivo biodistribution assessment, the images were taken at 1 h, 1 d, 3d, 7 d, 14 d, and 21 d after i.t. administration, and 1 h, 6 h, 1 d, 2 d, 4 d, 7 d, and 14 d after i.v. administration, using Pearl Trilogy small animal imaging system (Li-COR Biotechnology, Lincoln, NE) at 800 nm channel. The mice were sacrificed by euthanasia using CO_2 inhalation at 21 d-post i.t. administration and 14 d-post i.v. administration, respectively. Organs including heart, kidney, spleen, lung, liver, brain, and tumor were collected and imaged using Pearl Trilogy small animal imaging system at 800 nm channel. The signal from each individual image was analyzed using Odyssey CLx infrared imaging system software (Li-COR Biotechnology, Lincoln, NE). Dye accumulation and retention in live animals and organs were evaluated by calculating the contrast index values [322].

For the in vivo anti-tumor assessment, the body weights were monitored, and the tumor size were measured by standard digital caliper (Tresna, Guangxi Province, China) every other day. The tumor volume was calculated using the formula $\text{Volume}_{tumor} = (\text{Length} \times \text{Width}^2)/2$, with the Width being smaller than the Length [80, 82, 81]. In the HN12-YFP tumor-bearing mice, the mice were imaged using IVIS 200 system to indicate the tumor size at 8 d-post injections. All tested mice were sacrificed by euthanasia using CO_2 inhalation at 24 d-post first i.t. injection.

Table 5.4: Mice assignment for in vivo anti-tumor assessment

Group	Route	Polyplexes	Dosage/tumor/mouse	Dose	n
7	i.t.	PBS	n/a	1	3
8	i.t.	G4-FA/siGFP	175 μg/35 μg	1	2
9	i.t.	G4-FA/siVEGFA	175 μg/35 μg	1	3
10	i.t.	PBS	n/a	2	6
11	i.t.	siVEGFA	175 μg/35 μg	2	6
12	i.t.	G4-FA/siGFP	175 μg/35 μg	2	6
13	i.t.	G4/siVEGFA	175 μg/35 μg	2	6
14	i.t.	G4-FA/siVEGFA	175 μg/35 μg	2	6

Abbreviations: n/a, not applicable; i.t., intratumoral.

The tumor was removed, imaged, and weighed. Then, equal portions of tumors were snap frozen and stored at -80 °C for further analysis, or fixed in 10% neutral-buffered formalin for histologic and immunohistochemical evaluation.

5.3.10.2 Hematoxylin and eosin staining (H&E staining)

The formalin-fixed tumor specimens were embedded in paraffin and sectioned at 5 μm. The H&E staining was performed at the VCU Massey Cancer Biological Macromolecule Core Facility. The tissues slides were imaged under a Nikon ECLIPSE E400 clinical microscope (Nikon Instruments Inc., Melville, NY) using a magnification of 100× and 200×.

5.3.10.3 Immunohistochemistry

The immunohistochemical staining was carried out following procedures described previously [328, 329]. Briefly, the formalin-fixed tumor specimens were embedded in paraffin, and sectioned at 5 μm, deparaffinized in Clear-Rite 3, and rehydrated in graded alcohols (100%, 95%, 90%, 80%, and 70%). For antigen retrieval, the sections were microwaved in antigen retrieval systems (BD retrievagen) for 10 min. Endogenous peroxidase activity was quenched by incubation in 3% (v/v) H_2O_2 for 15 min. The sections were incubated with the primary polyclonal antibody against CD31 for 1 h. After the sections were washed with TBS, the immobilized antibodies were detected

by avidin-biotin-peroxidase technique (Vectastain ABC kit). 3,3'-Diaminobenzidine and hematoxylin were used as the chromogen and the nuclear counterstain, respectively. The primary antibody was omitted as negative control. The tissues slides were then imaged under a Nikon ECLIPSE E400 clinical microscope using a magnification of 200×. The average microvessels counts (per 200× field) were quantitated as the number of CD31-positive vessels in six randomly selected fields for each sample, and each group included sections from 2 mice.

5.3.11 Statistical analysis

The data were expressed as means ± standard deviation (SD) or standard error of the mean (SEM). The statistical analysis was performed by Students *t*-test for comparison using GraphPad Prism 5 (La Jolla, CA). A value of $p < 0.05$ was considered statistically significant.

5.4 Results and Discussion

5.4.1 Synthesis and characterization of NIR-labeled G4-FA conjugates and G4 dendrimer

The preparation and characterizations of G4-FA conjugates were described in Chapter 4. For in vivo trafficking of G4-FA conjugates, near-infrared fluorescence dye (NIR) was conjugated onto G4 dendrimer and G4-FA conjugates. The strategy used to synthesize NIR-G4-FA conjugates is illustrated in Scheme 5.1. The UV-Visible absorption spectrum showed the characteristic maximum absorption wavelength of free NIR was at 780 nm (Figure 5.2a). Because the UV detection limitation of high performance liquid chromatography (HPLC) is from 190 to 700 nm, the purity of G4-FA conjugates could not be analyzed using HPLC. A fluorescence detector equipped HPLC may help to determine the purity of NIR-G4-FA and NIR-G4 conjugates in the future. UV-Visible (UV-Vis) spectroscopy was first employed to determine the coupling efficiency of NIR to G4-FA conjugates and G4 dendrimer. A standard curve

of NIR at absorption wavelength of 780 nm was generated by plotting the mean absorbance (y-axis) for each NIR concentration (x-axis) (Figure 5.2b). UV-Visible spectroscopy analysis showed that an average of 0.0082 and 0.0044 NIR molecules was conjugated onto each G4-FA conjugate and G4 dendrimer, respectively. These results were questionable because the color of resultant NIR-G4-FA and NIR-G4 conjugates were changed from yellow and transparent to dark blue, respectively. Therefore, the coupling efficiency of NIR to G4-FA conjugates and G4 dendrimer were determined by the Odyssey CLx infrared imaging system. A standard curve of NIR at 800 nm channel was generated by plotting the average signal counts (y-axis) for each NIR concentration (x-axis) (Figure 5.2c). Again, the result showed that an average of 0.0059 molecules was conjugated onto each G4-FA conjugate. Both results raised a question whether NIR coupling efficiency was extremely low in both conjugates. In order to find the truth, we measure the absorbance spectra of NIR-G4-FA and NIR-G4 conjugates. Surprisingly, we found the characteristic maximum absorption wavelength of NIR shifted from 780 nm to 620 nm, which left an absorbance tail at 780nm. These results explained why such low coupling efficiency was measured by the UV-Vis spectroscopy and the Odyssey CLx infrared imaging system. However, the reason to cause the absorbance shift remains unknown. One possible explanation could be that NIR dye was shielded from G4-FA conjugates and G4 dendrimer, which subsequently quenched its fluorescence. This interpretation needs to be validated by additional precise experiments in the future.

5.4.2 Characterization of NIR-G4, NIR-G4-FA conjugates, and polyplexes

G4-FA/siVEGFA, G4-FA/siGFP, and G4/siVEGFA polyplexes at different weight ratios were summarized in Table 5.2. By knowing the molecular weight and the number of primary amines of G4 dendrimer and G4-FA conjugate as well as the number of bases and phosphates of siVEGFA and siGFP, the molar ratios and the

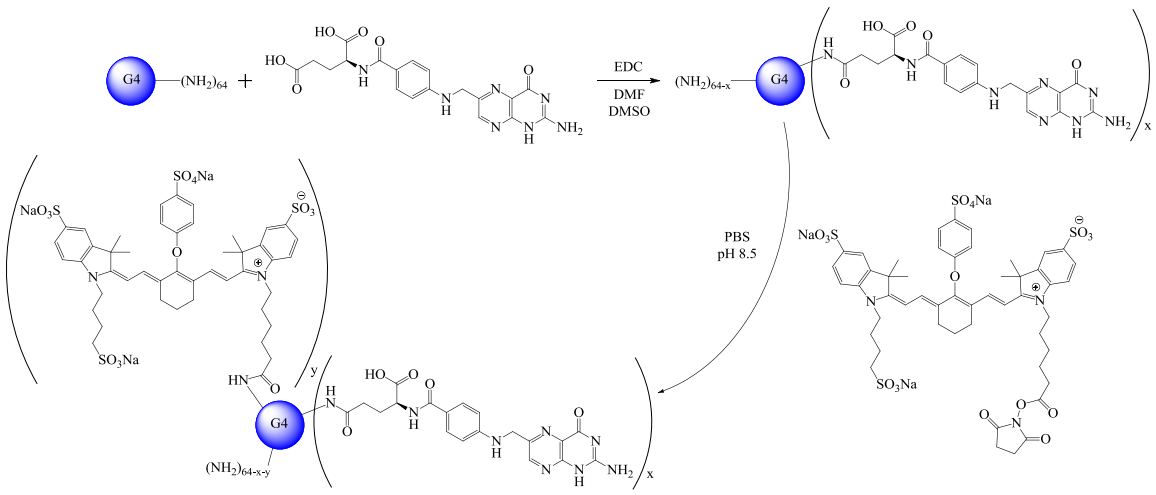

Figure 5.1: Synthetic scheme of NIR-G4-FA conjugate.
Synthesis of dendrimer-folic acid (G4-FA) conjugates (a). Labeling G4-FA conjugates with NIR (b).

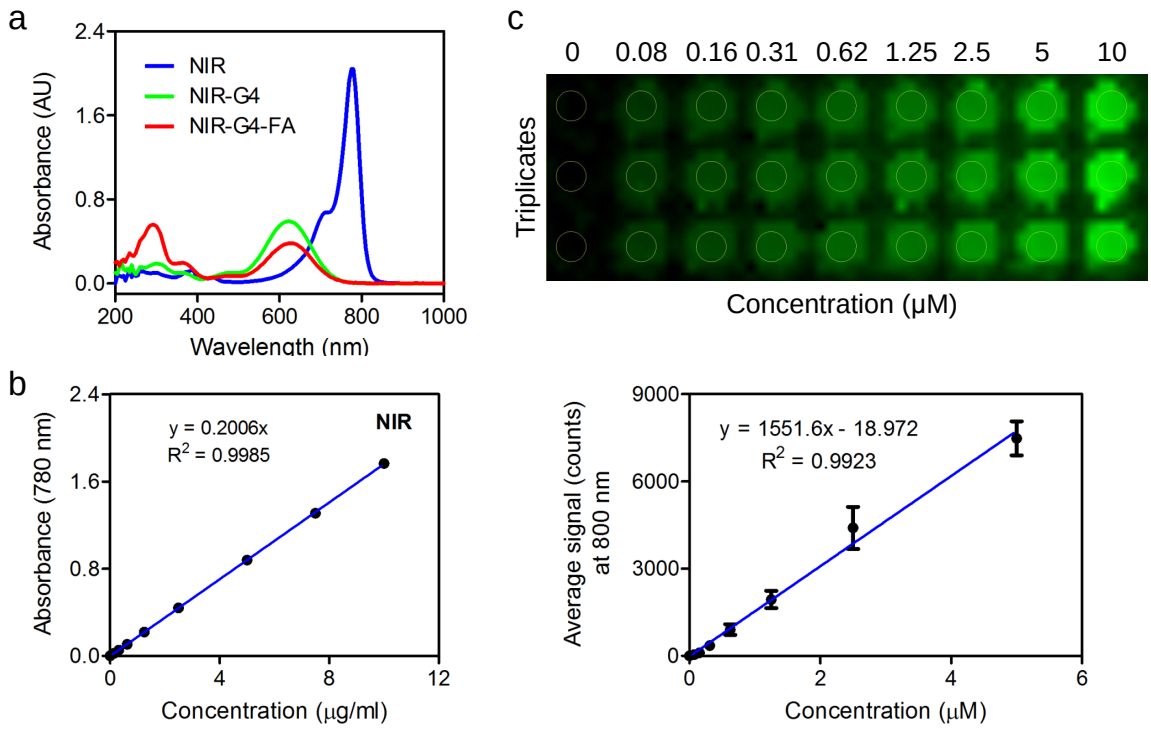

Figure 5.2: Characterization of NIR conjugated G4-FA conjugates and G4 dendrimer.
The absorption spectra of near-infrared fluorescence dye (NIR), NIR-G4-FA and NIR-G4 conjugates were determined by ultraviolet-visible (UV-Vis) spectroscopy (a). Standard curves of NIR were determined by UV-Vis spectroscopy (b) and Odyssey CLx infrared imaging system at 800 channel (c).

Table 5.5: Weight, molar, and nitrogen/phosphate (N/P) ratios of G4-FA conjugate and G4 dendrimer to siRNA

Polyplex	Weight ratio	Molar ratio	N/P ratio
G4-FA/siVEGFA	1	0.8	1.3
	5	4.2	6.4
	20	16.9	25.7
G4-FA/siGFP	5	4.2	6.4
G4/siVEGFA	5	4.7	7.1

nitrogen/phosphate (N/P) ratios of polyplexes were also calculated in Table 5.5.

The zeta potential of NIR-G4, NIR-G4-FA conjugates, and polyplexes was measured by DLS. First, no significant difference of zeta potential was observed between NIR-G4 and NIR-G4-FA conjugates (Figure 5.3a). Next, siRNA is double-stranded RNA molecule that possesses 21 base pairs in length (siVEGFA and siGFP). Each base pair contains a phosphate group, which results an overall negative charge of siRNA. As expected, siVEGFA possessed a negative zeta potential of -13.8 mV (Figure 5.3b). At a weight ratio of 1, G4-FA/siVEGFA polyplexes displayed a negative zeta potential of -14.8 mV, which was not significantly different from that of siVEGFA. At weight ratios of 5 and 20, the zeta potential of G4-FA/pGFP polyplexes significantly increased from -13.8 mV to 9.3 mV and 15.9, respectively. These results suggest that G4-FA/siVEGFA polyplexes can be formed at a weight ratio of 1 or above; however, at a weight ratio of 1 (molar ratio of 0.8), the number of G4-FA conjugate molecules was less than that of siVEGFA molecules. Thus, G4-FA conjugates may be not enough to cover the siVEGFA, which results an overall negative surface charge of -14.8 mV. At weight ratio of 5 and 20 (molar ratio of 4.2 and 16.9), the siVEGFA plasmid can be sufficiently shielded by G4-FA conjugates in complexation, which spiked the surface charge of polyplexes to positive. Moreover, the zeta potential of G4-FA/siVEGFA polyplexes was significantly lower than that of G4-FA conjugates, which indicates siVEGFA interacted with G4-FA conjugates by forming polyplexes. In contrast, the zeta potential of G4/siVEGFA polyplexes at a weight ratio of 5 was determined as 18.8 mV, which is higher than that of G4-FA/siVEGFA polyplexes at the same weight ratio. The increased zeta potential of G4/siVEGFA

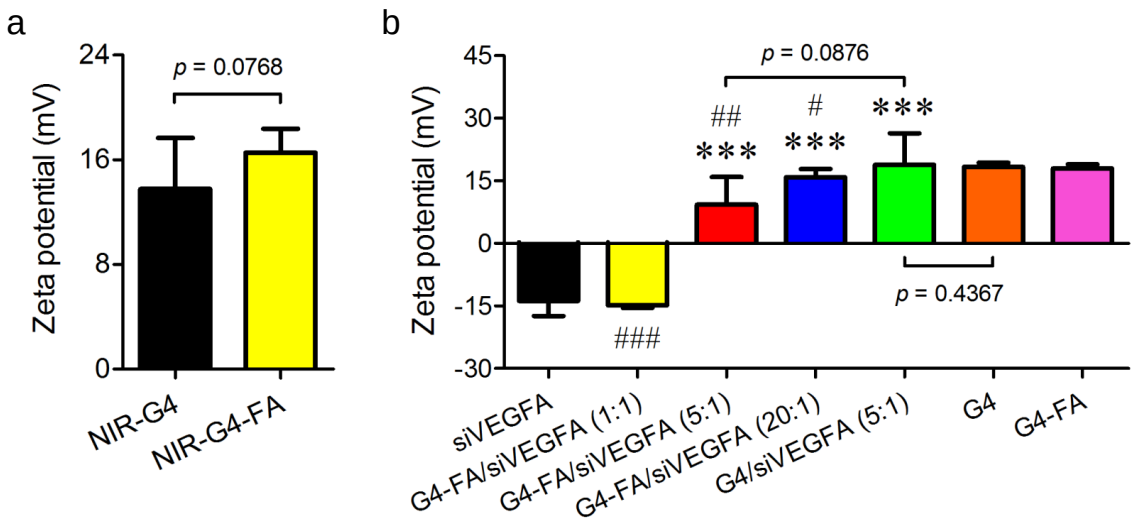

Figure 5.3: Zeta potentials of NIR-G4-FA and NIR-G4 conjugates (a), siVEGFA, G4-FA/siVEGFA, and G4/siVEGFA polyplexes, G4 dendrimer and G4-FA conjugates (b) were determined by dynamic light scattering (DLS).
The bars and error bars are means ± SEM. n = 3-6. *** $p < 0.001$ versus siVEGFA; # $p < 0.05$, ## $p < 0.01$, and ### $p < 0.001$ versus G4-FA conjugates.

polyplexes may lead a higher non-specific uptake than G4-FA/siVEGFA polyplexes, because the efficient adsorptive uptake of polyplexes by cells would be enabled by the net positive charge of polyplexes via electrostatic interaction [106]. On the other hand, because both NIR-G4 and NIR-G4-FA conjugates have high light absorption, the size of both conjugates was not able to be detected by DLS analysis.

5.4.3 Validation of siVEGFA

The sequences of siVEGFA duplex have been evaluated in several studies [251, 314, 31, 252], but these sequences of siVEGFA duplex have not been tested in HN12 cells. Thus, we tested the siVEGFA in HN12 cells using electroporation method. Electroporation transfection gives a stable transfection efficiency but a low cell viability, which is 40% to 70% cell viability under an optimal transfection condition [210]. Our results showed that siVEGFA significantly knocked down both mRNA (Figure 5.4a) and protein (Figure 5.4b) expression VEGFA in HN12 cells by 46% and 57%, re-

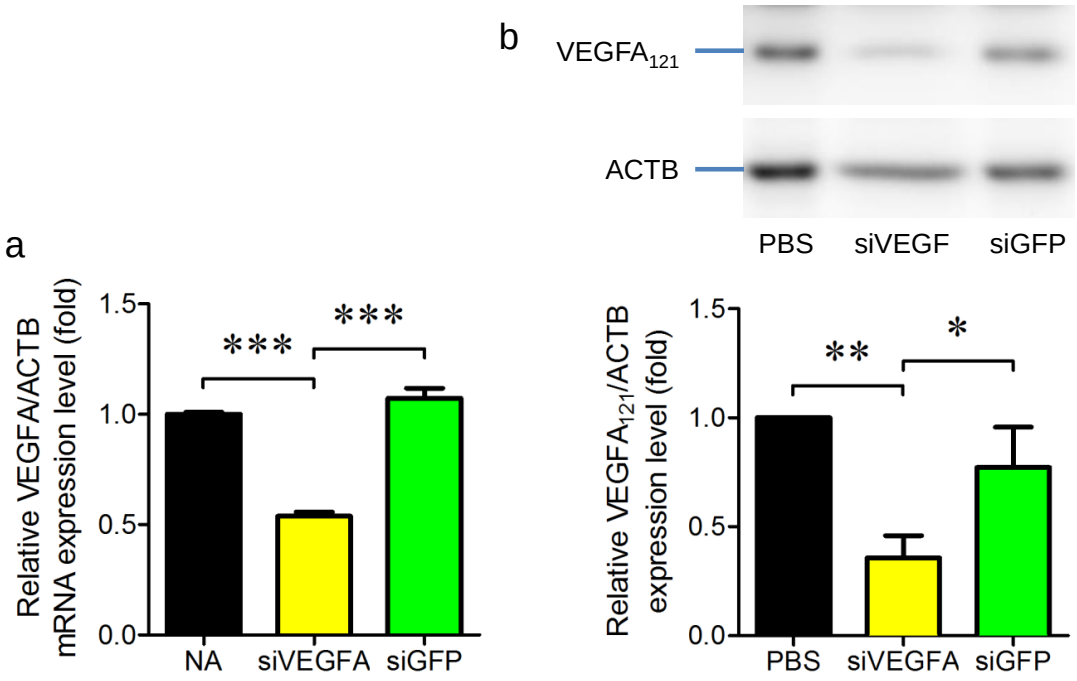

Figure 5.4: siVEGFA validation.
HN12 cells were transfected with siVEGFA and siGFP via electroporation, followed by 48 h culture. The relative mRNA expression of VEGFA was determined by real-time PCR analysis (a), and the relative intracellular protein expression of VEGFA was determined by Western blot analysis. The expression level of β-actin (ACTB) was used as a loading control. The bars and error bars are means $\pm$ SD. n =3. ** $p < 0.01$ and *** $p < 0.001$.

spectively. These results validated that siVEGFA duplex were able to knockdown VEGFA expression. Our results agree well with the previous reported findings. One report showed a 66% knockdown level of mRNA expression in prostate cancer PC3 cells [252], and a similar knockdown level of protein expression in colorectal cancer HCT116 cells was achieved [314], using Lipofectamine by the same set of siVEGFA duplexes. However, by giving a high transfection capability using electroporation, the gene silencing efficiency of VEGFA using this sequence was not very impressive, indicating silencing potency of a single set of siVEGFA duplex may be moderate in HN12 cells.

5.4.4 Transfection efficiency of poleplexes

By understanding the transfection mechanism and efficiency of G4-FA/plasmid polyplexes (Chapter 4), we tested the VEGFA knockdown efficiency of G4-FA/siVEGFA polyplexes. As we expected, G4-FA/siVEGFA polyplexes at weight ratios of 1, 5, and 20 significantly decreased the mRNA expression level of VEGFA by 8%, 28%, and 12%; while G4/siVEGFA polyplexes at a weight ratio of 5 significantly decreased the mRNA expression level of VEGFA by 18% (Figure 5.5). Among the presented transfection conditions, G4-FA/siVEGFA polyplexes at a weight ratio of 5 showed the highest VEGFA knockdown efficiency in HN12 cells. The knockdown efficiency of G4-FA/siVEGFA polyplexes was 1.6 times that of non-targeting G4/siVEGFA polyplexes at the same weight ratio. To confirm mRNA expression results, we quantified the sequential release of VEGFA after transfection of polyplexes in HN12 cells. The ELISA analysis showed that G4-FA/siVEGFA and G4/siVEGFA polyplexes at a weight ratio of 5 significantly decreased the release of VEGFA by 32% and 17%, respectively (Figure 5.6). G4-FA/siVEGFA polyplexes resulted in a decrease of 15% in the overall amount of VEGFA released in HN12 cells as compared to non-targeting G4/siVEGFA polyplexes at the same weight ratio. Although both G4-FA/siVEGFA and G4/siVEGFA polyplexes at a weight ratio of 5 showed significant knockdown of VEGFA mRNA expression and protein secretion, the knockdown efficiency was not very impressive. To our best knowledge, it could be due to the following two reasons. First, the silencing potency of single set of siVEGFA duplex was not very impressive in HN12 cells (Figure 5.4). Second, it has been reported that the presence of serum could significantly reduce the gene knockdown efficiency of both triethanolamine (TEA)-core PAMAM dendrimer G4 and arginine-terminated PAMAM dendrimer G4 (G4-Arg) siRNA polyplexes, especially G4/siRNA polyplexes [154]. In this work, the transfection was carried out in the presence serum, which raised the possibility that the serum proteins may interact with G4/siVEGFA or G4-FA/siVEGFA polyplexes and subsequently destabilize the polyplexes [154]. Therefore, to improve the knockdown efficiency of G4-FA/siVEGFA polyplexes, we could complex G4-FA

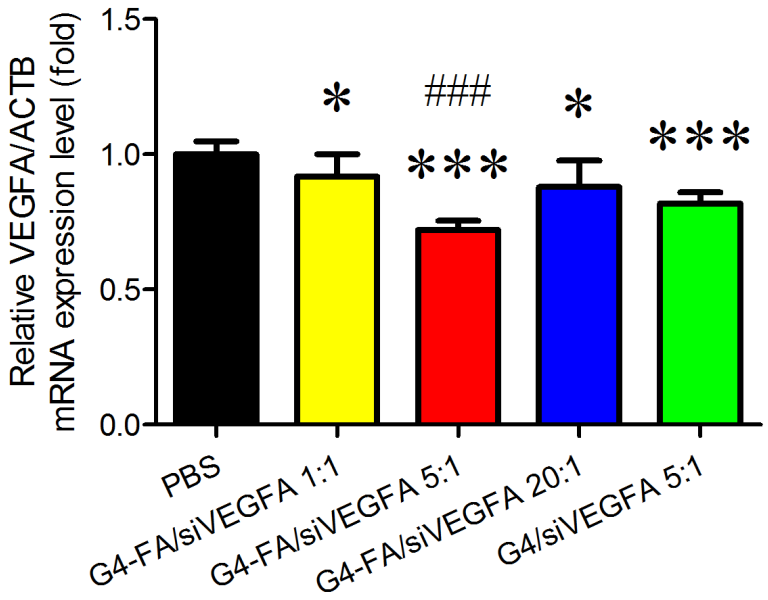

Figure 5.5: The effect of polyplexes on mRNA expression of VEGFA. HN12 cells were transfected with G4-FA/siVEGFA polyplexes at weight ratios of 1, 5, and 20, and G4/siVEGFA polyplexes at a weight ratio of 5 for 48 h, followed by 48 h culture. The relative mRNA expression of VEGFA was determined by real-time PCR analysis. The expression level of β-actin (ACTB) was used as a loading control. The bars and error bars are means $\pm$ SD. n = 3. * $p < 0.05$, *** $p < 0.001$ versus PBS; ### $p < 0.001$ versus G4/siVEGFA at a weight ratio of 5.

conjugates with a pool of siVEGFA duplex sets to increase the potency of siVEGFA itself and transfect cells with G4-FA/siVEGFA polyplexes in the absence of serum to limit serum interaction. However, these were not the purpose of this work. In this work, we aimed to investigate whether G4-FA conjugates could delivery siRNA into the tumor in vivo in a xenograft tumor model.

5.4.5 In vivo accumulation of G4-FA conjugates in a xenograft tumor model of head and neck cancer

One of the key advantages of using targeted NPs for anticancer drug delivery in vivo is that NPs facilitate drug accumulation within tumors. To investigate biodistribution and antitumor efficacy, we first established the xenograft tumor model by s.c. injection

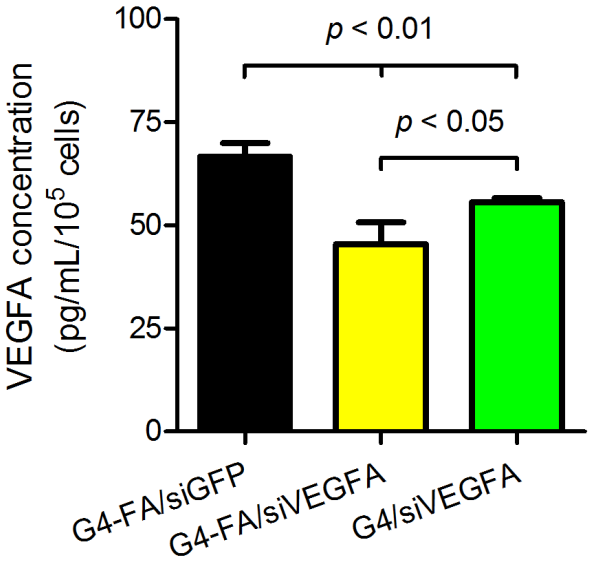

Figure 5.6: The effect of polyplexes on the release of VEGFA.
HN12 cells were transfected with G4-FA/siVEGFA and G4/siVEGFA polyplexes at a weight ratio of 5 for 48 h, followed by 48 h culture. The concentration of VEGFA in the medium was determined by ELISA, and normalized by the cell number. The bars and error bars are means ± SEM. n = 3.

of HN12 cells in the nude mice, yielding HN12 tumor-bearing mice. By monitoring the tumor volume, we determined HN12 tumor growth rate in the xenograft tumor model (Figure 5.7). The tumor growth rate showed that the tumor started to grow exponentially at 2 weeks-post s.c. injection of HN12 cells, indicating an effectively therapeutic window for siVEGFA gene therapy may be within 2 weeks.

5.4.5.1 Intratumoral (i.t.) administration

Near infrared fluorescence dye (NIR) shows great potential in tumor imaging, photothermal, and photodynamic therapies because of high tissue penetration depth and low tissue autofluorescence interference in the NIR spectrum window, which improve specificity to distinguish tumor from the normal tissues [318]. To investigate real-time biodistribution of G4-FA conjugates, we prepared NIR-labeled G4-FA (NIR-G4-FA) conjugates and NIR-labeled G4 dendrimer (NIR-G4) conjugates for comparison. Following local injection into tumor, the fluorescence signal was immediately detected

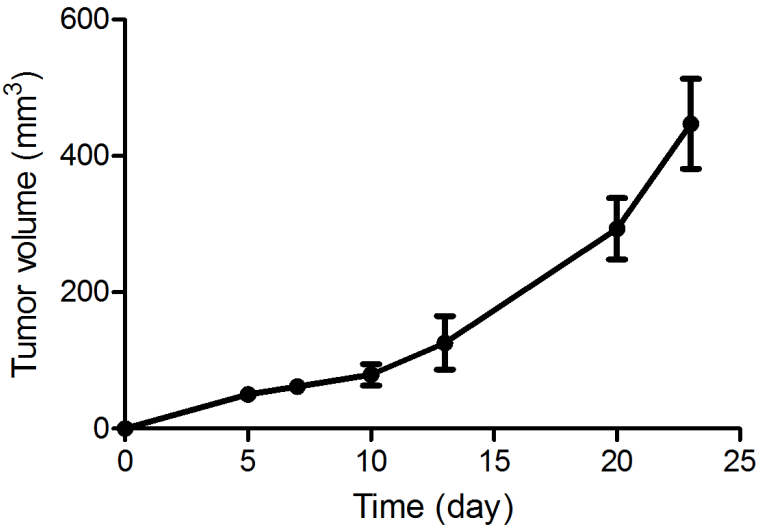

Figure 5.7: Establishment of the xenograft tumor model of head and neck cancer.
The tumor volume was measured at the predetermined time points after subcutaneous (s.c.) injection of HN12 cells in the nude mice. The dots and error bars are means ± SEM. n = 8-10.

in the tumors within 1 h (Figure 5.8, 5.9, 5.10). However, the fluorescence signal was significantly decreased at 1 d-post i.t. injection of free NIR, and was unable to be detected at and after 3 d-post i.t. injection (Figure 5.8). The ventral view of the mice at 1 h-post i.t. injection of free NIR showed a significant fluorescence signal in the bladder in addition to the whole body (Figure 5.11), indicating free NIR was rapidly eliminated from the body through renal clearance, and it possessed very low retention time in the tumor. In contrast, the fluorescence signal retained in the tumor region up to 21 d-post i.t. injection of both NIR-G4 and NIR-G4-FA conjugates (Figure 5.9, 5.10). The ventral view of the mice at 1-h post i.t. injection of NIR-G4 and NIR-G4-FA conjugates showed the fluorescence signal was highly localized in the tumor region and no fluorescence signal was detected from the other regions (Figure 5.11). These observations indicated both G4 dendrimers and G4-FA conjugates could retain in the tumor and its surrounding region for up to 21 days. At notice, the fluorescence signals spread from the tumor in both NIR-G4 and NIR-G4-FA conjugates injected mice. Therefore, we employed the Odyssey CLx infrared imaging system

to measure the fluorescence signal counts within the tumor region. Based on the real-time live imaging, no significant difference of the fluorescence signal counts could be found between the mice i.t. injected with NIR-G4 and those with NIR-G4-FA conjugates (Figure 5.12a). In addition, no significant difference of the body could be found in the mice i.t. injected with NIR, NIR-G4 and NIR-G4-FA conjugates (Figure 5.12b), which might indicate NIR-labeled G4 dendrimer and G4-FA conjugates were biocompatible at one-dose i.t. injection.

At 21 d-post i.t. injection, the heart, kidney, spleen, lung, liver, brain, and tumor tissues were collected. The fluorescence signal of each tissue was determined by Pearl Trilogy small animal imaging system. As expected, no fluorescence signal could be detected in the tissues from the mice i.t. injected with free NIR (Figure 5.13), consistent with the real-time biodistribution assessment (Figure 5.8). In contrast, a significant fluorescence signal was observed in the tumor tissue from the mice i.t. injected with NIR-G4 and NIR-G4-FA conjugates (Figure 5.13). The fluorescence intensity of each tissue was analyzed by CLx infrared imaging system software. In both NIR-G4 and NIR-G4-FA conjugates i.t. injected mice, the greatest fluorescence signal was observed in the tumor compared with the other tissues (Figure 5.14). The fluorescence intensities of kidney, spleen, liver, and tumor from the mice i.t. injected with NIR-G4-FA conjugates increased by 1.7, 1.8, 2.0, and 2.6 folds, compared to those from the mice i.t. injected with NIR-G4 conjugates. Collectively, these results indicate that both G4 dendrimers and G4-FA conjugates could facilitate in vivo tumor accumulation of NIR after i.t. administration. Moreover, FA-decoration onto G4 dendrimer could enhance tumor accumulation of NIR after i.t. administration. As we described in Chapter 4, the cellular uptake mechanism of G4 dendrimer was nonspecific absorptive endocytosis, whereas the cellular uptake mechanism of G4-FA conjugates was folate receptor (FR)-mediated endocytosis. The xenograft tumor was generated from HN12 cells, which highly express FRα. Besides, kidney, spleen, and

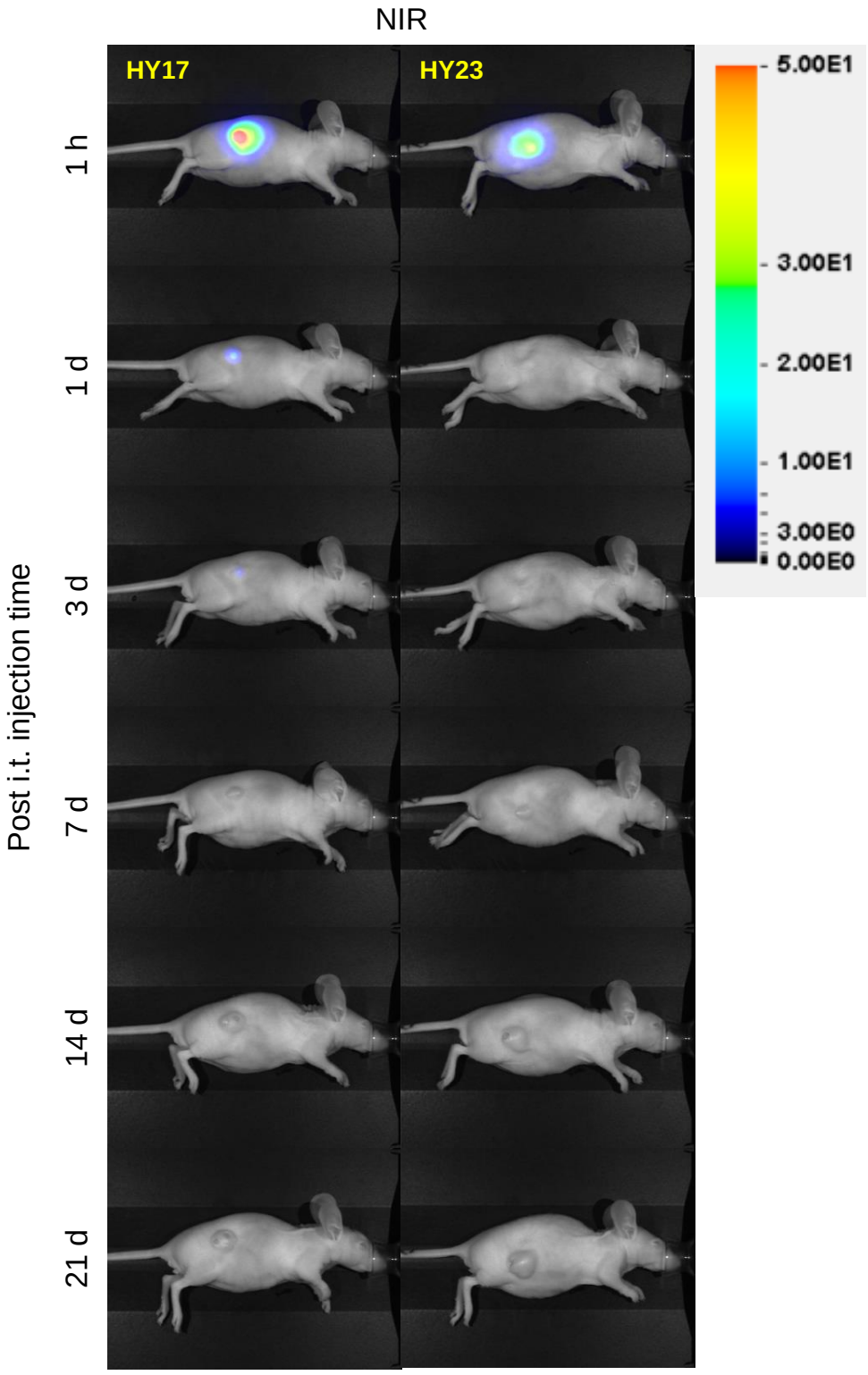

Figure 5.8: Lateral view of the mice at indicated time points after intratumoral (i.t.) injection of free near infrared fluorescence dye (NIR).

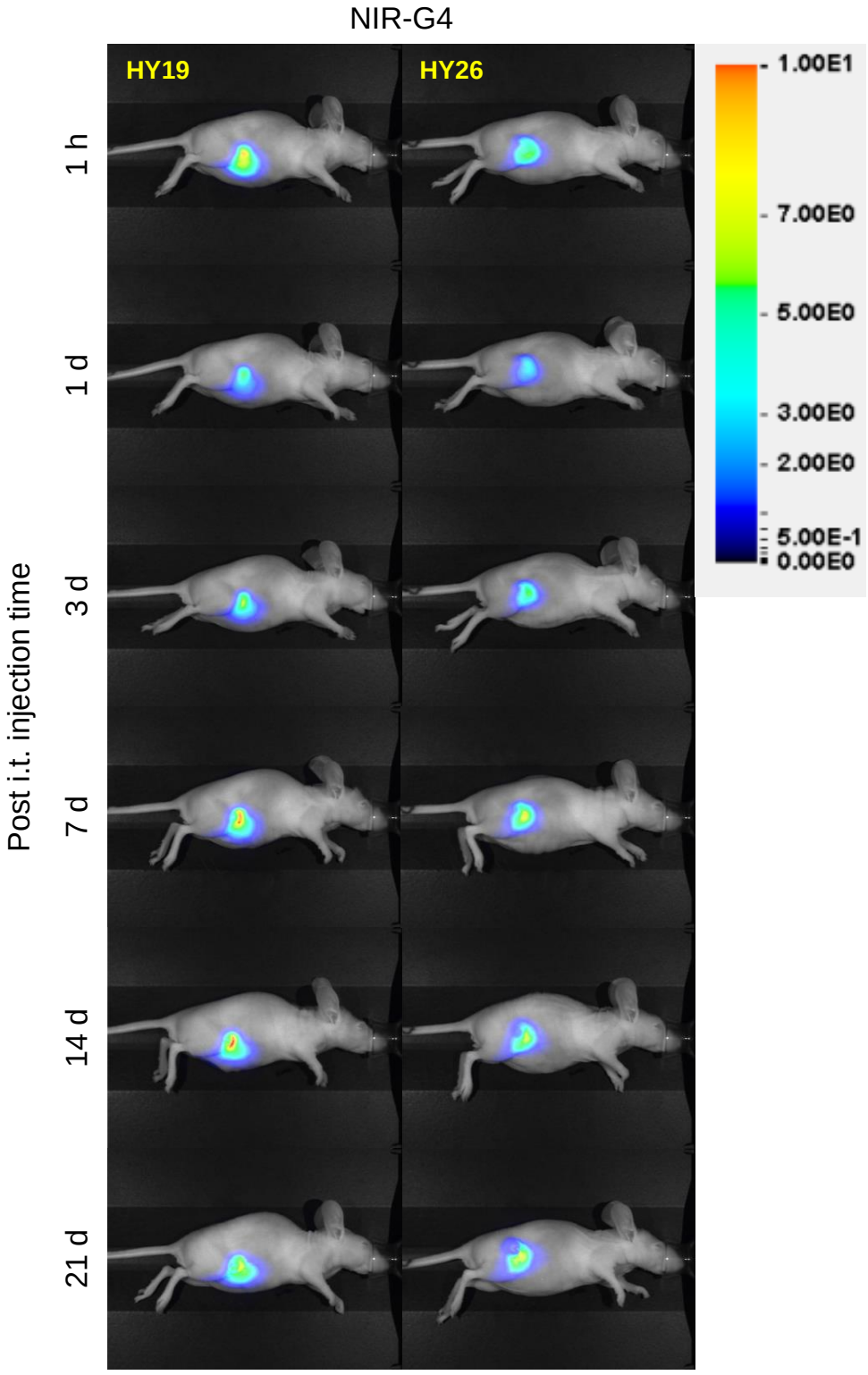

Figure 5.9: Lateral view of the mice at indicated time points after intratumoral (i.t.) injection of near infrared fluorescence dye-labeled G4 dendrimer (NIR-G4) conjugates.

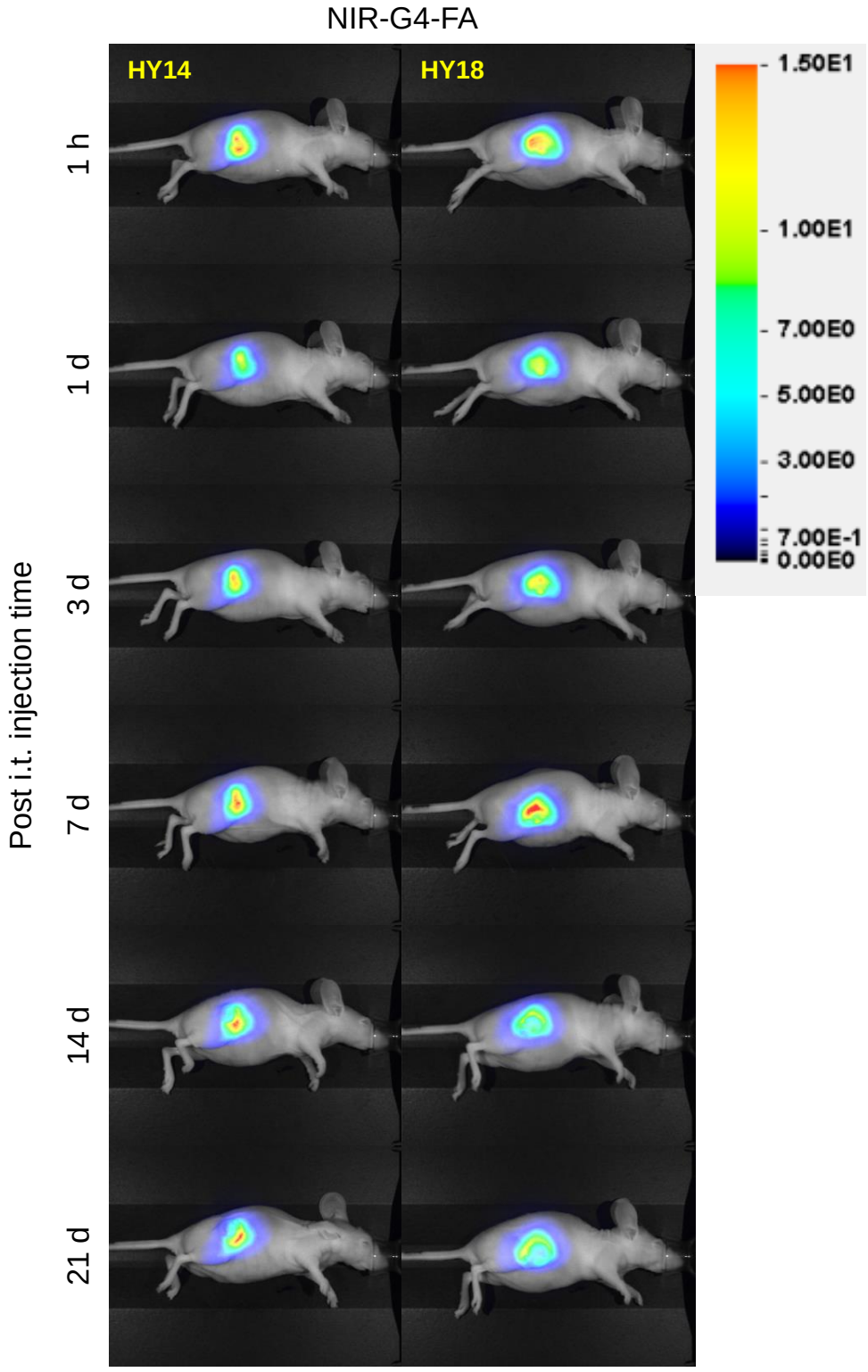

Figure 5.10: Lateral view of the mice at indicated time points after intratumoral (i.t.) injection of near infrared fluorescence dye-labeled G4-FA (NIR-G4-FA) conjugates.

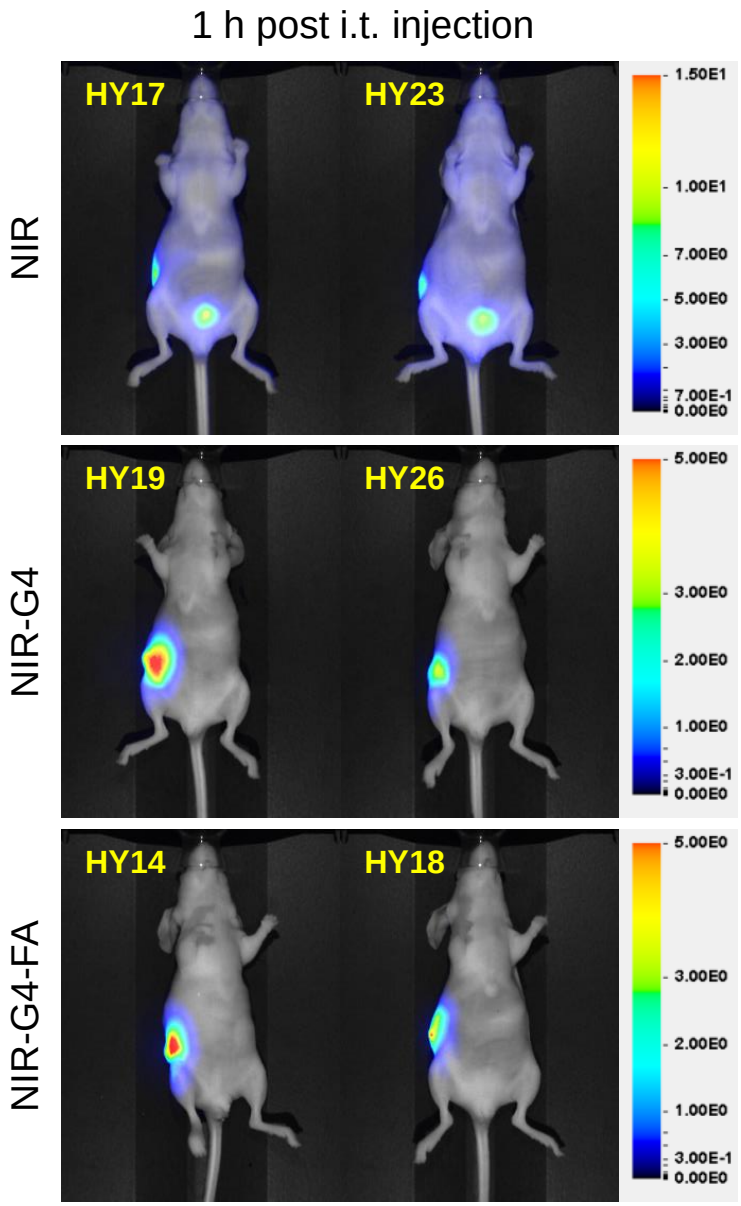

Figure 5.11: Ventral view of the mice at 1 h-post intratumoral (i.t.) injection of near infrared fluorescence dye (NIR), NIR-labeled G4 dendrimer (NIR-G4), and NIR-labeled G4-FA (NIR-G4-FA) conjugates.

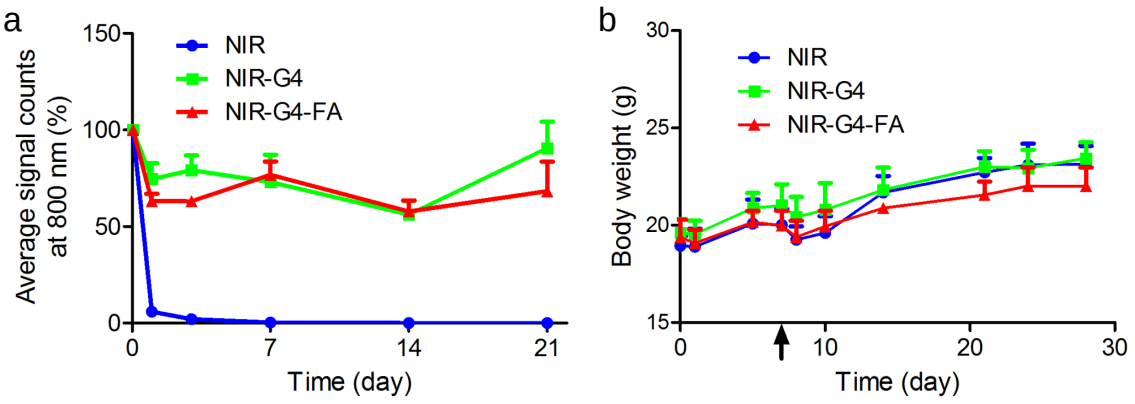

Figure 5.12: The real-time fluorescence intensity in the tumor region of the mice at indicated time points after intratumoral (i.t.) injection of near infrared fluorescence dye (NIR), NIR-labeled G4 dendrimer (NIR-G4), and NIR-labeled G4-FA (NIR-G4-FA) conjugates (a). The body weights were monitored at indicated time points after subcutaneous (s.c.) injection of HN12 cells (b). The dots and error bars are means SEM. n = 5.

liver have high FR expression because of folate resorption, presence of macrophages and Kupffer cells, respectively [29, 255]. Therefore, after local i.t. administration, G4-FA conjugates were preferentially taken up by tumor, and circulated G4-FA conjugates could be taken up by kidney, spleen, and liver.

From the literature search, we found both FA-modified trypsin-stabilized gold nanoclusters with NIR fluorescence (FA-try-AuNCs) and FA-modified dendrimer-entrapped gold nanoparticles (Au DENPs-FA) were synthesized for in vivo tumor bioimaging. NIR fluorescence signal could be detected immediately after i.t. injection of FA-try-AuNCs, and the signal in the tumor can remain up to 12 h in the HeLa tumor-bearing mice [155]. Au DENPs-FA could be detected in the tumor at 6 h-post i.t. injection in the KB tumor-bearing mice [271]. Both FA-try-AuNCs and Au DENPs-FA have shown great potentials for tumor imaging with good clearance, which helps to avoid potential toxicity from the imaging contrast agents and vehicle itself. However, by comparing with FA-try-AuNCs and Au DENPs-FA, our NIR-G4-FA conjugates offered significantly longer tumor retention time, which was

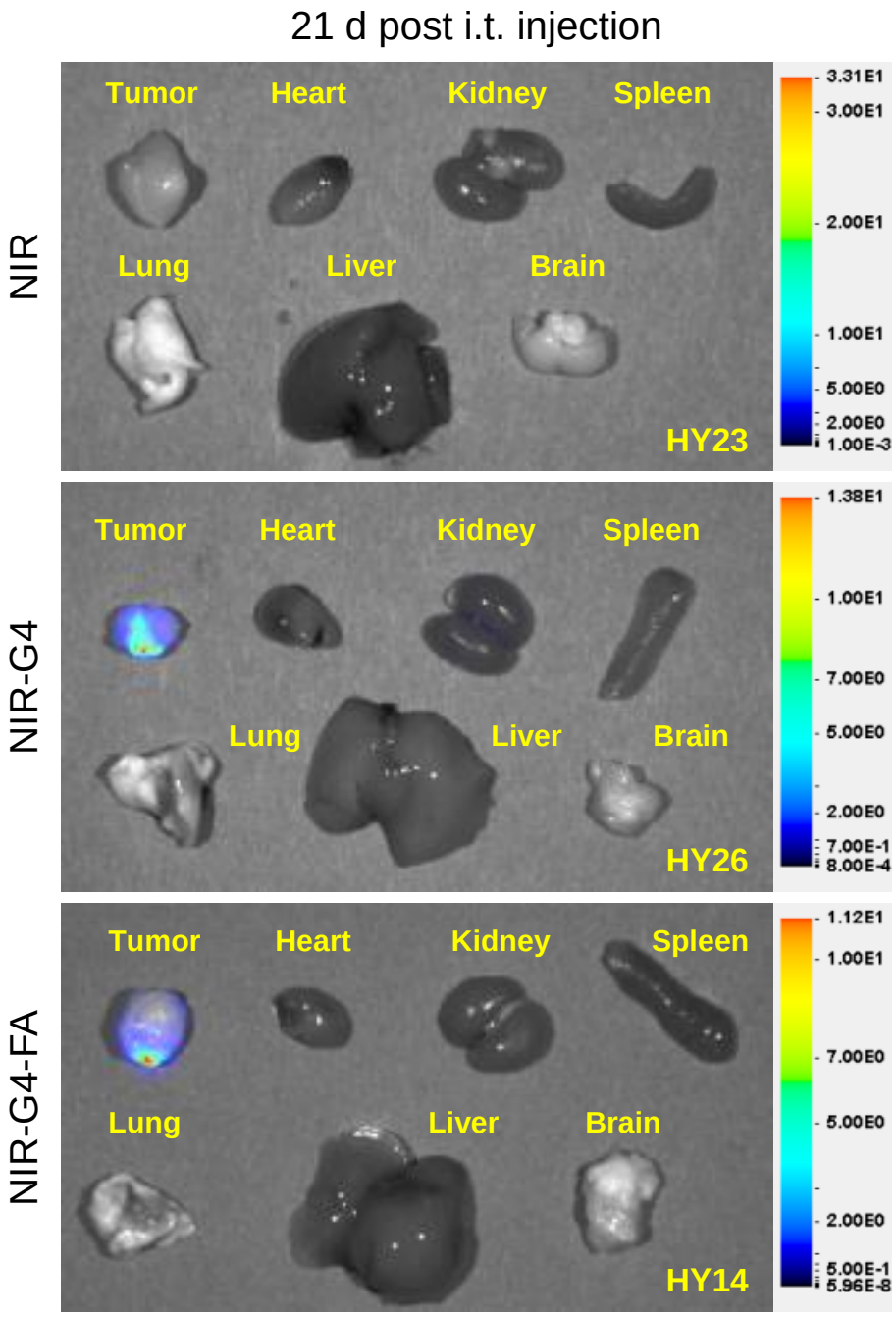

Figure 5.13: Qualitative biodistribution presentation of the tissues from the mice at 21 d-post i.t. injection of near infrared fluorescence dye (NIR), NIR-labeled G4 dendrimer (NIR-G4), and NIR-labeled G4-FA (NIR-G4-FA) conjugates.

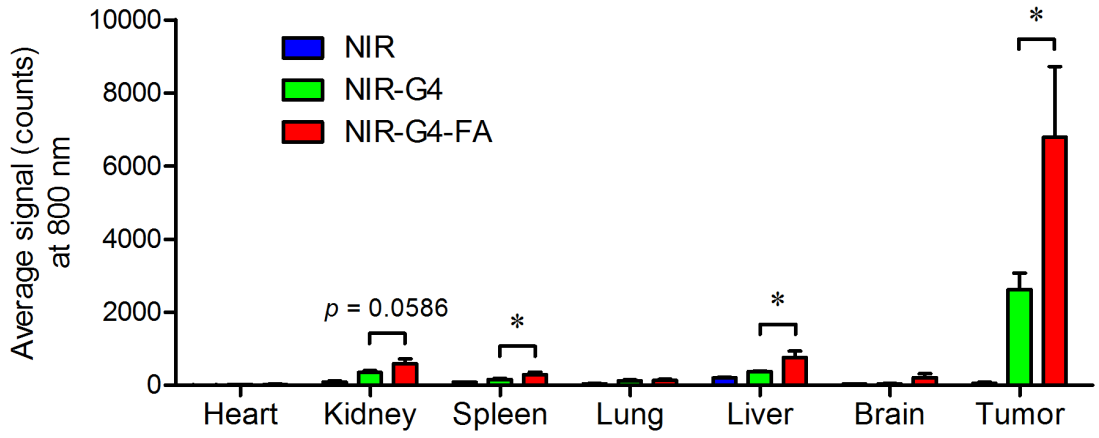

Figure 5.14: Quantitative biodistribution analysis of the tissues from the mice at 21 d-post i.t. injection of near infrared fluorescence dye (NIR), NIR-labeled G4 dendrimer (NIR-G4), and NIR-labeled G4-FA (NIR-G4-FA) conjugates. The bars and error bars are means SEM. n = 5.

at least 21 d. This prolonged tumor retention time would significantly contribute to the enhanced the gene and drug delivery efficacy of the vehicle.

5.4.5.2 Intravenous (i.v.) administration

The promising data generated from i.t. administration lead us to challenge i.v. administration in the xenograft tumor model. In this experiment, because NIR-G4-FA conjugates remained highly positively charged (Figure 5.3a), we complexed NIR-G4-FA conjugates with pMAX-GFP plasmid to neutralize the zeta potential of NIR-G4-FA conjugates. Following systemic injection of free NIR through the tail vein, the fluorescence signal was immediately detected in the whole body within 1 h (Figure 5.15). Then, the fluorescence signal was significantly decreased at 6 h-post i.v. injection of free NIR, and was unable to be detected at and after 1 d-post i.t. injection. The ventral view of the mice at 1 h-post i.v. injection of free NIR again showed a significant fluorescence signal in the bladder in addition to a the whole body (Figure 5.16), indicating free NIR was rapidly eliminated from the body through renal clearance and possessed very low retention time in the tumor. These results were consistent with those of i.t. administration (Figure 5.11). In contrast, the fluorescence signal retained

in the abdominal region at 1 h-post i.t. injection of both NIR-G4-FA conjugates and NIR-G4-FA/pGFP polyplexes (Figure 5.16), indicating the initial hepatic absorption of both conjugates and polyplexes was high after i.v. administration. The dorsal view of the mice at 1-h post i.v. injection of NIR-G4-FA conjugates and NIR-G4-FA/pGFP polyplexes showed the fluorescence signal was highly localized in the kidneys and no significant fluorescence signal was detected in the tumor region (Figure 5.17, 5.18), indicating the initial renal absorption of both conjugates and polyplexes was also high after i.v. administration. Based on the real-time biodistribution imaging from both ventral and dorsal views, the NIR could retain in liver and kidney for up to 14 d, but the fluorescence intensities in both liver and kidney were gradually decreased during these 14 d, indicating either NIR fluorescence was quenched over the time, or G4 dendrimers and G4-FA conjugates were slowly eliminated from the body. The lateral view of the mice after i.v. injection of NIR-G4-FA conjugates and NIR-G4-FA/pGFP polyplexes showed no significant increase of the fluorescence signal was detected in the tumor region compared to the rest of the body (Figure 5.19, 5.20). Then, we employed the Odyssey CLx infrared imaging system to measure the fluorescence signal counts within the tumor region. Based on the real-time live imaging, no significant increase of the fluorescence signal counts could be found in the mice i.v. injected with NIR-G4-FA conjugates and NIR-G4-FA/pGFP polyplexes (Figure 5.21a). In addition, no significant difference of the body weight could be found in the mice i.v. injected with NIR, NIR-G4-FA conjugates, and NIR-G4-FA/pGFP polyplexes (Figure 5.21b), indicating G4-FA conjugates and their polyplexes were biocompatible at one-dose i.v. injection, consistent with that of i.t. administration (Figure 5.12b).

At 14 d-post i.v. injection, the heart, kidney, spleen, lung, liver, brain, and tumor tissues were collected. The fluorescence signal of each tissue was determined by Pearl Trilogy small animal imaging system. As expected, no fluorescence signal could

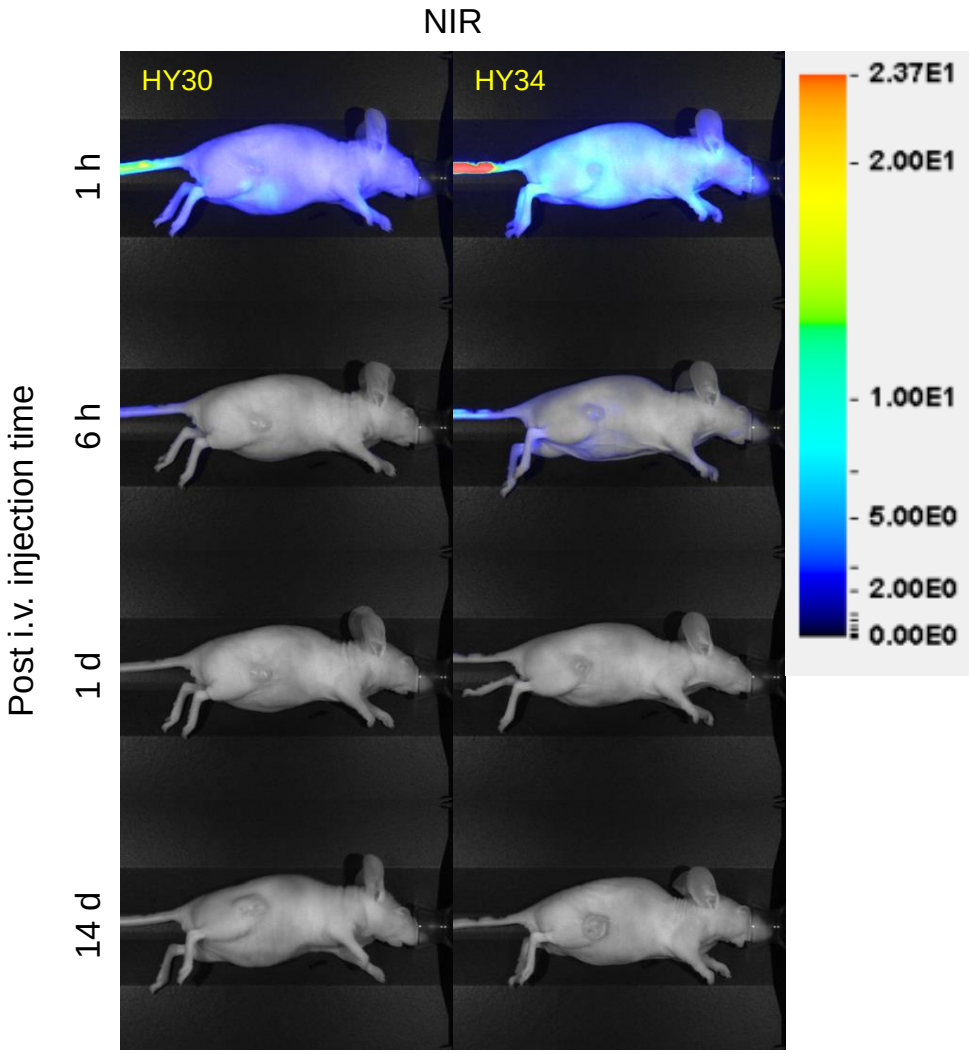

Figure 5.15: Lateral view of the mice at indicated time points after intravenous (i.v.) injection of free near infrared fluorescence dye (NIR).

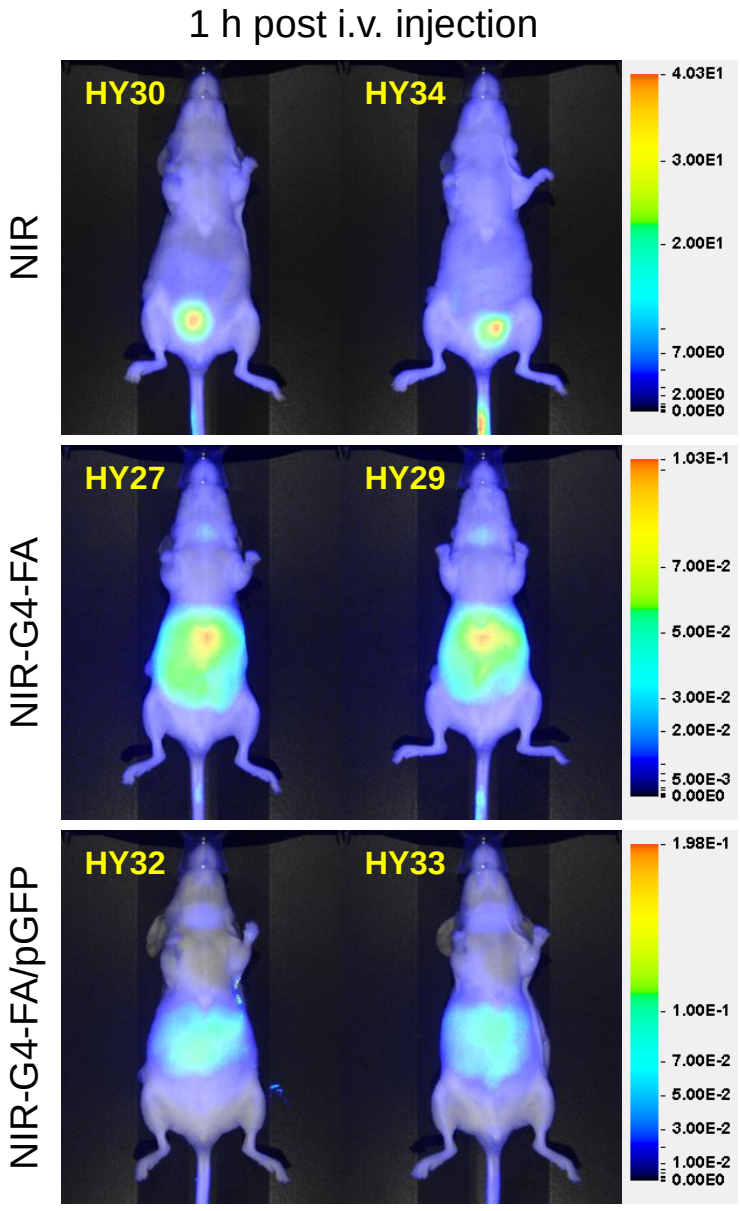

Figure 5.16: Ventral view of the mice at 1 h-post intravenous (i.v.) injection of near infrared fluorescence dye (NIR), NIR-labeled G4-FA (NIR-G4-FA) conjugates, and NIR-G4-FA/pGFP polyplexes. pGFP, pMAX-GFP plasmid.

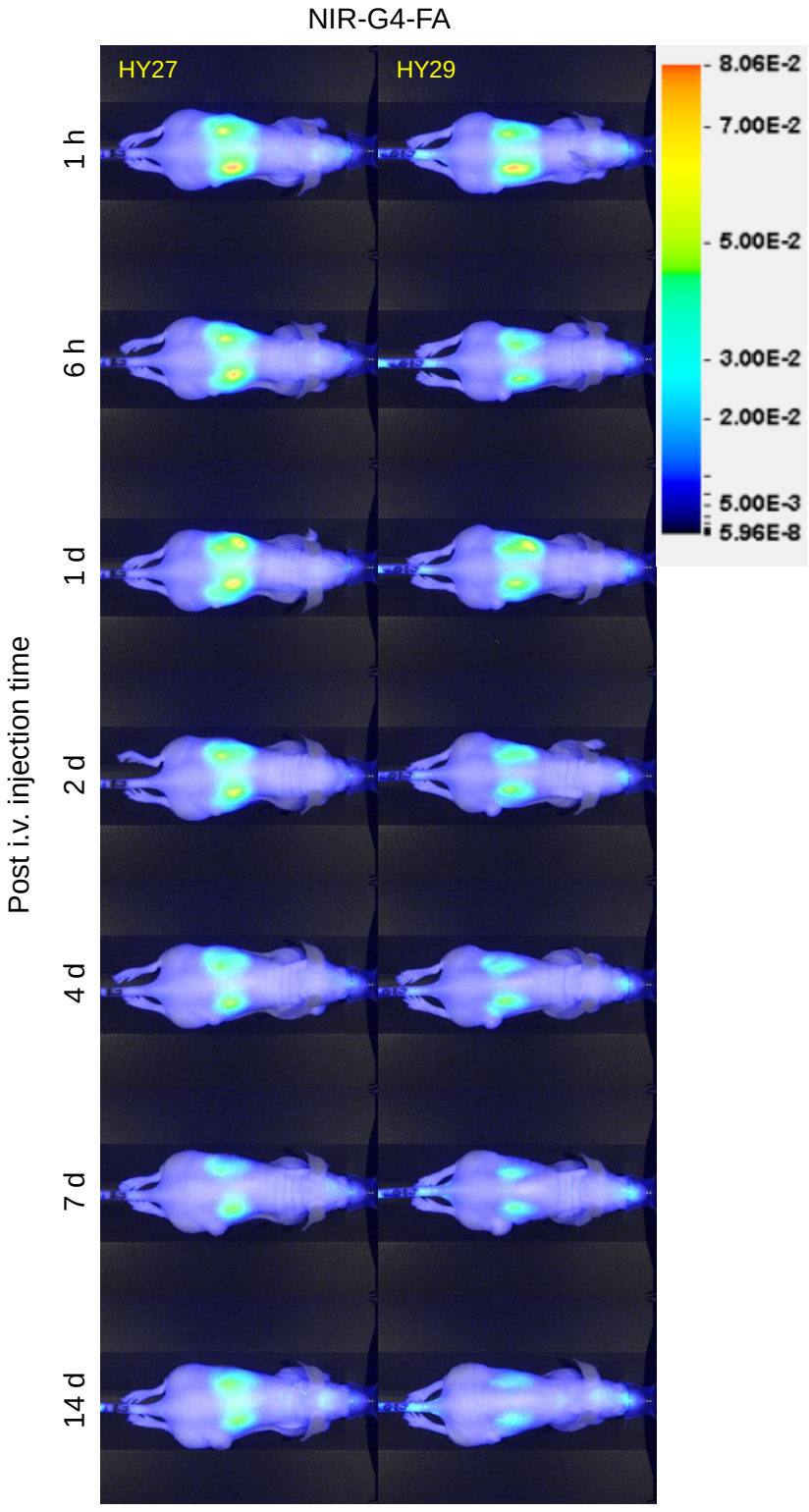

Figure 5.17: Dorsal view of the mice at indicated time points after intravenous (i.v.) injection of near infrared fluorescence dye-labeled G4-FA (NIR-G4-FA) conjugates.

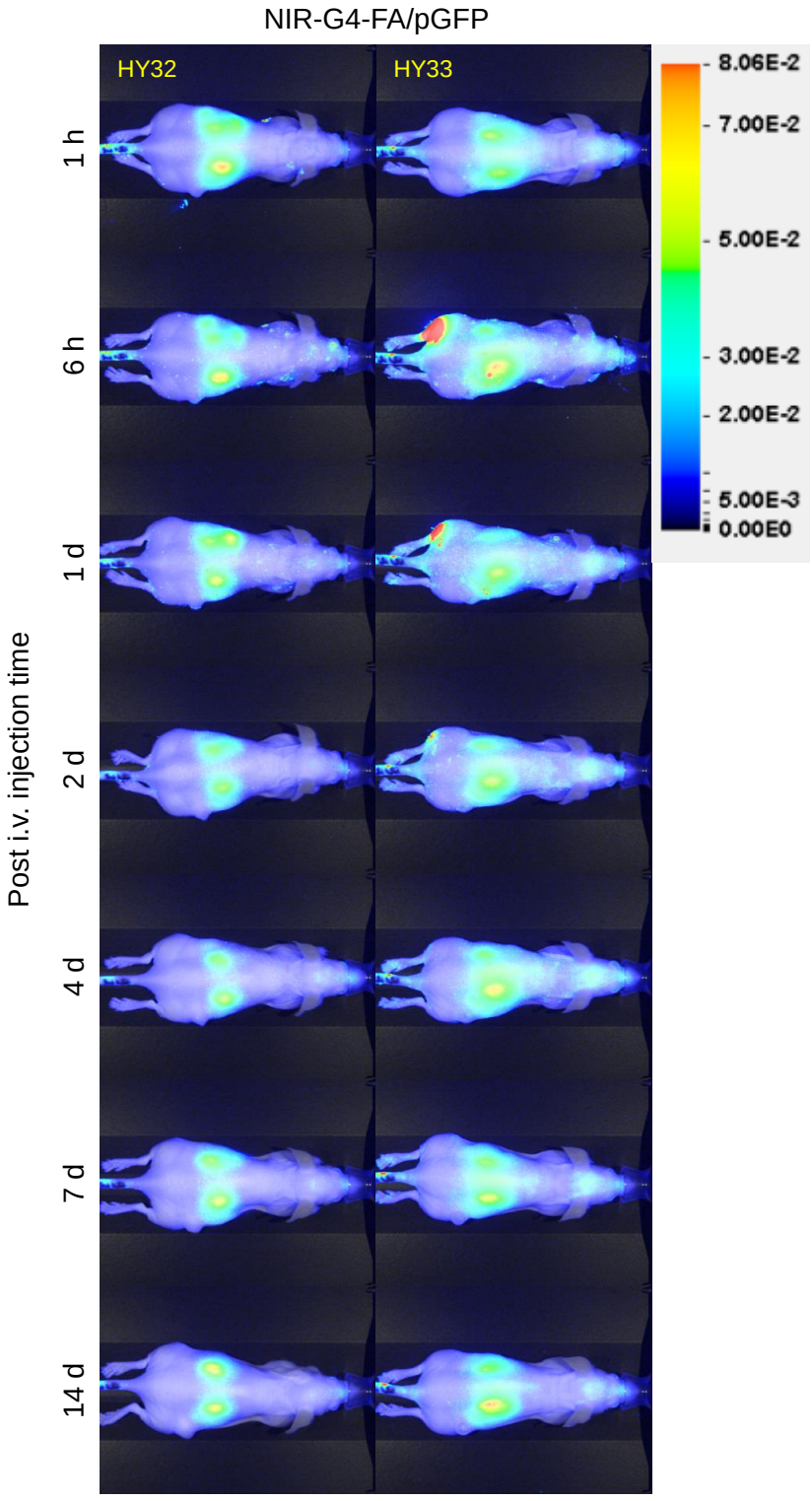

Figure 5.18: Dorsal view of the mice at indicated time points after intravenous (i.v.) injection of NIR-G4-FA/pGFP polyplexes. pGFP, pMAX-GFP plasmid.

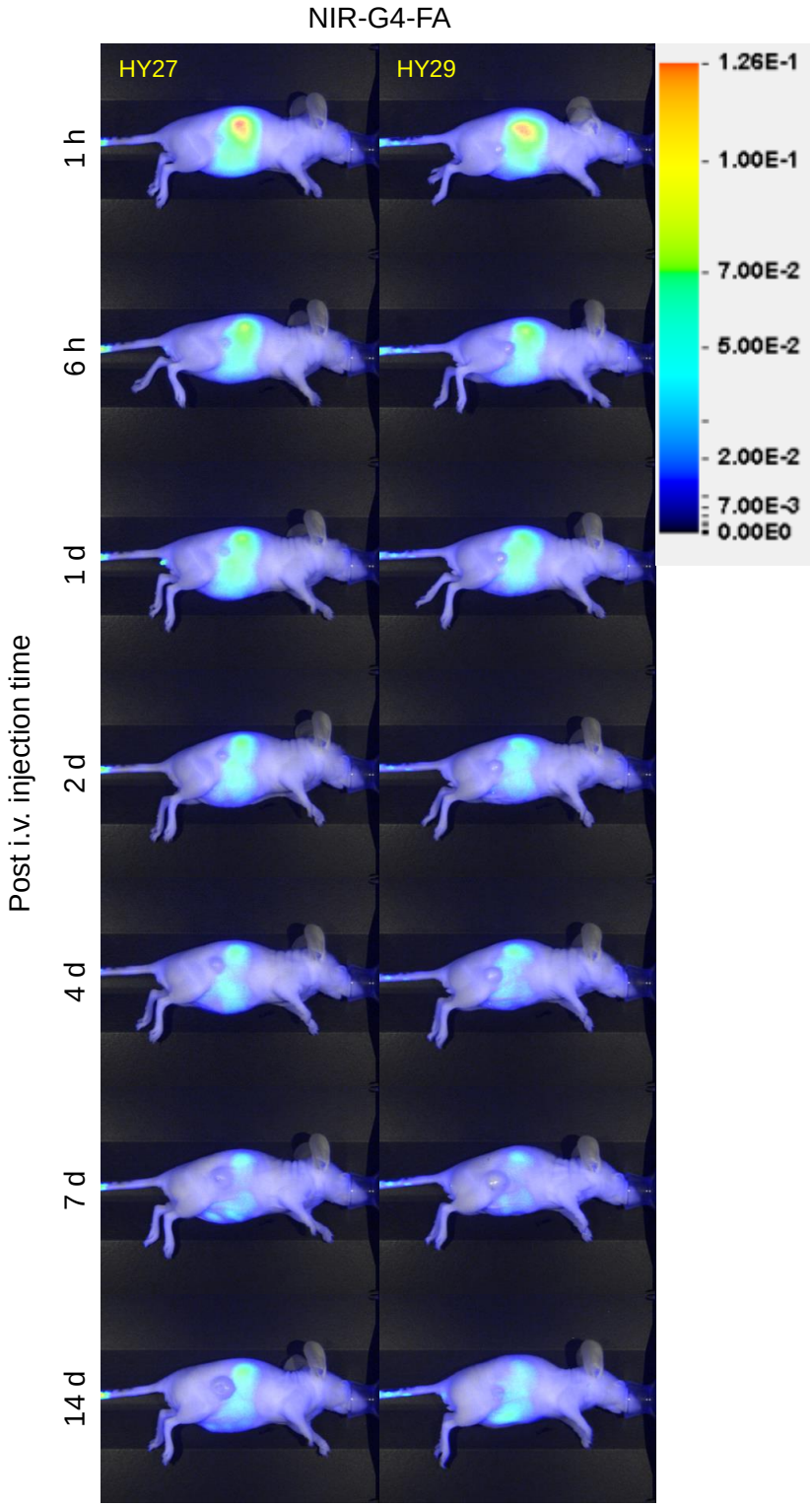

Figure 5.19: Lateral view of the mice at indicated time points after intravenous (i.v.) injection of near infrared fluorescence dye-labeled G4-FA (NIR-G4-FA) conjugates.

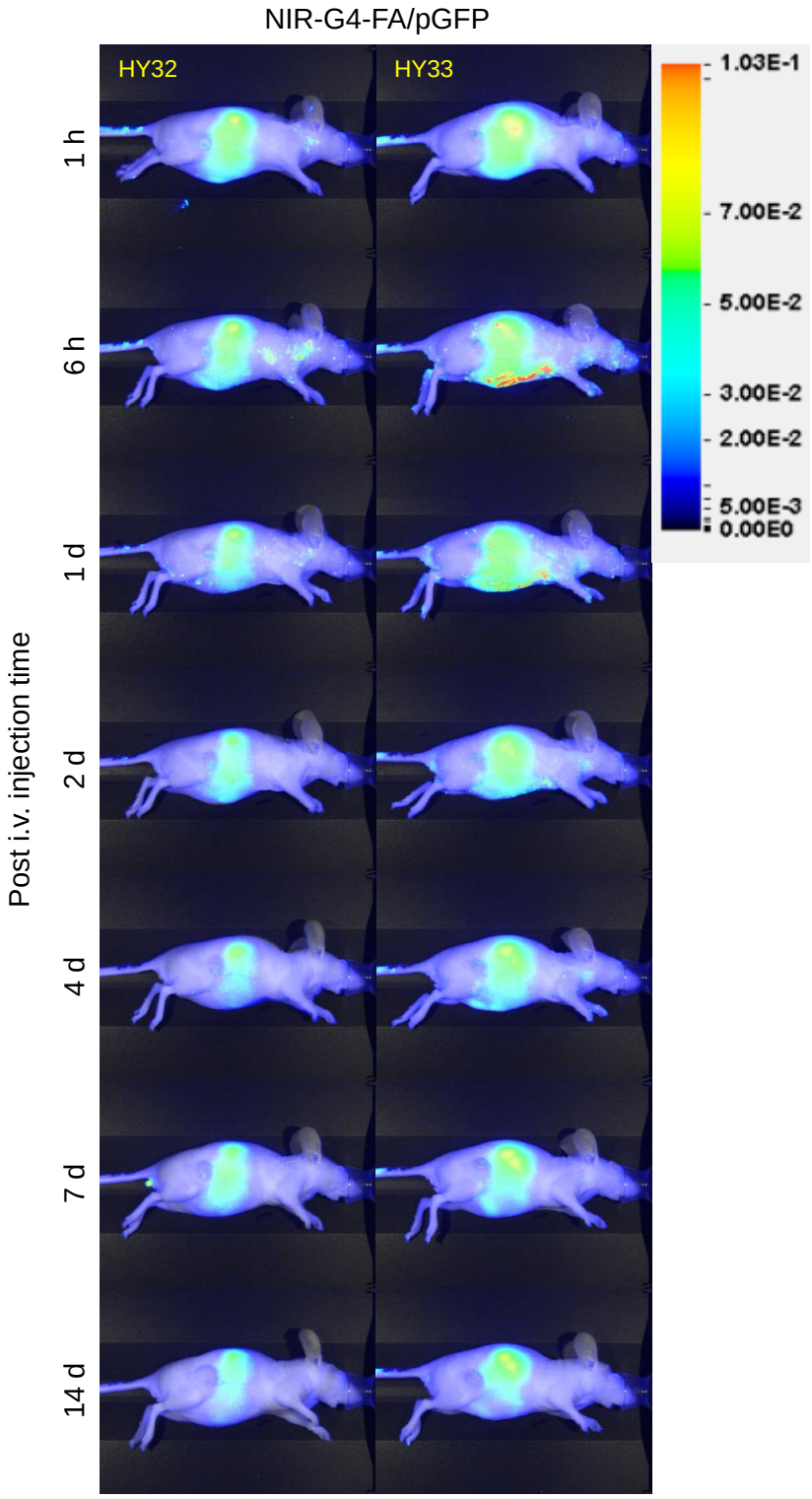

Figure 5.20: Lateral view of the mice at indicated time points after intravenous (i.v.) injection of NIR-G4-FA/pGFP polyplexes. pGFP, pMAX-GFP plasmid.

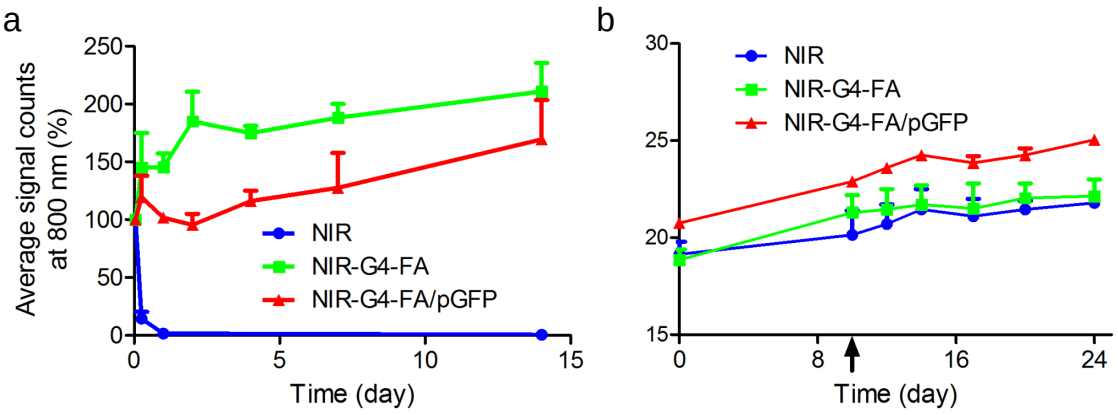

Figure 5.21: The real-time fluorescence intensity in the tumor region of the mice at indicated time points after intravenous (i.v.) injection of near infrared fluorescence dye (NIR), NIR-labeled G4-FA (NIR-G4-FA) conjugates, and NIR-G4-FA/pGFP polyplexes (a). The body weights were monitored at indicated time points after subcutaneous (s.c.) injection of HN12 cells (b). pGFP, pMAX-GFP plasmid. The dots and error bars are means SEM. n = 2.

be detected in the tissues from the mice i.v. injected with free NIR (Figure 5.22), consistent with the real-time biodistribution after i.t. administration (Figure 5.15). In contrast, a significant fluorescence signal was observed in the kidney, liver, and spleen tissues from the mice i.v. injected with NIR-G4-FA conjugates NIR-G4-FA/pGFP polyplexes (Figure 5.22). The fluorescence intensity of each tissue was analyzed by CLx infrared imaging system software. In both NIR-G4-FA conjugates and NIR-G4-FA/pGFP polyplexes i.v. injected mice, the greatest fluorescence signal was observed in the kidney, spleen, liver, but not tumor (Figure 5.23). Collectively, these results indicate that both G4-FA conjugates and G4-FA/plasmid polyplexes were not able to facilitate in vivo tumor accumulation of NIR after systemic administration. G4-FA conjugates and their polyplexes were rapidly taken up by kidney, spleen, and liver because their high FR expression [29, 255]. Therefore, systemic administration was not a suitable route for G4-FA conjugate administration. To our best knowledge, NIR-G4-FA conjugates and their polyplexes possess very short circulation half-life mainly because the submicron size, positive charge, and FA-targeting moiety of these nanoparticles can trigger rapid hepatic and renal clearance. It is well documented

that covalent or non-covalent surface modification of nanoparticles with polyethylene glycol (PEG) can significantly prolong the circulation time and increase the half-life of nanoparticles [199, 289, 332, 267]. Besides, PEG is non-toxic and non-immunogenetic and approved by Food and Drug Administration (FDA) for internal use in humans [267]. Therefore, PEGylation of G4-FA conjugates may serve as a better delivery carrier for siRNA via systemic administration. However, PEGylated PAMAM dendrimer causes the loss of primary amine on the PAMAM dendrimer and often results a decrease in their buffering capacity, which is essential for gene transfection [193]. Therefore, application of bis-aryl hydrazone (BAH) linkage onto PEGylated PAMAM dendrimer may compensate the loss of primary amine and help maintain or increase their buffering capacity [321]. On the other hand, the molecular weight of PEG and the degree of PEGylation remain to be justified by further evaluations in the future.

5.4.6 In vivo antitumor efficacy of G4-FA/siVEGFA polyplexes in the xenograft tumor model

The biodistribution assessment could be used to predict therapeutic outcome of G4-FA/siVEGFA polyplexes. VEGFs play central roles in regulation of angiogenesis. VEGFA, as the major factor for angiogenesis, binds to two tyrosine kinase receptors (VEGFR-1 and VEGFR-2), and subsequently regulates endothelial cell proliferation, migration, vascular permeability, secretion, and other endothelial functions [237]. VEGF-VEGFR is crucial not only for physiological angiogenesis from early embryonic to adult stages but also for pathological angiogenesis, such as in age-related macular degeneration and in cancer [237]. To data, a number of strategies have been developed to target VEGF-VEGFR system for anti-angiogenic therapy alone or in combination with other therapies in cancer treatment [119, 252, 120, 256]. In this work, we evaluated the antitumor efficacy of G4-FA/siVEGFA polyplexes via i.t. administration in HN12 tumor-bearing nude mice.

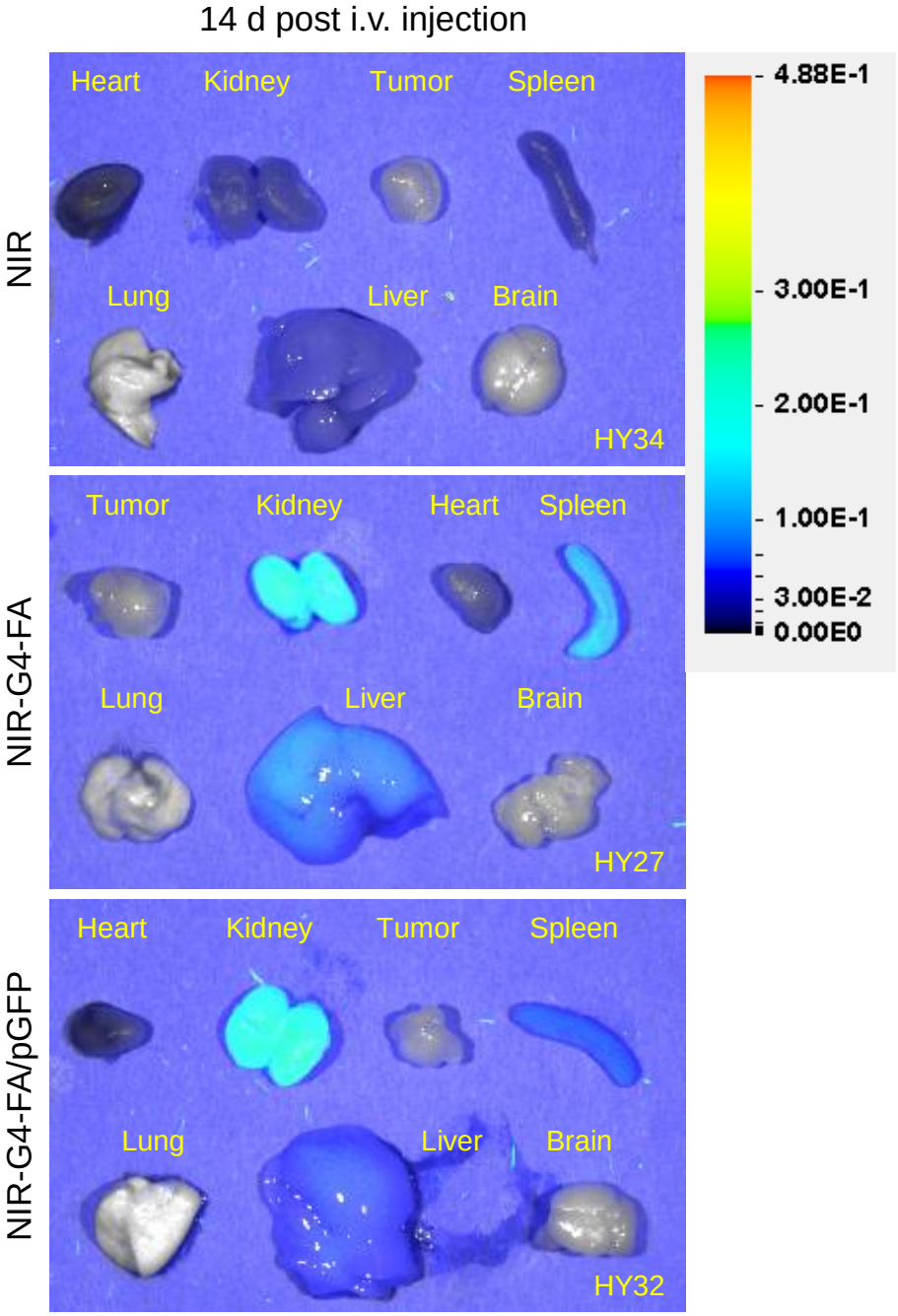

Figure 5.22: Qualitative biodistribution presentation of the tissues from the mice at 14 d post i.v. injection of near infrared fluorescence dye (NIR), NIR-labeled G4-FA (NIR-G4-FA) conjugates, and NIR-G4-FA/pGFP polyplexes. pGFP, pMAX-GFP plasmid.

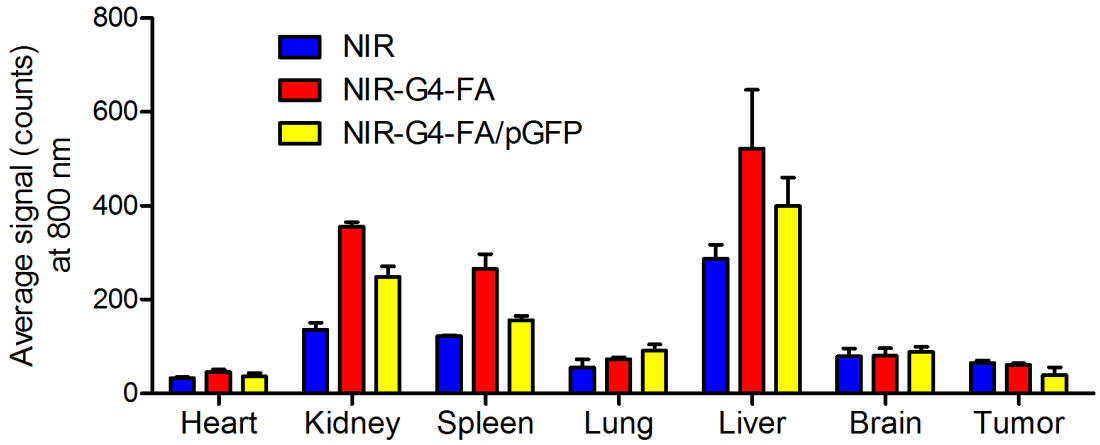

Figure 5.23: Quantitative biodistribution analysis of the tissues from the mice at 21 d post intratumoral (i.t.) injection of near infrared fluorescence dye (NIR), NIR-labeled G4-FA (NIR-G4-FA) conjugates, and NIR-G4-FA/pGFP polyplexes. pGFP, pMAX-GFP plasmid. The bars and error bars are means SEM. n = 2.

5.4.6.1 Single-dose administration

A single-dose of G4-FA/siVEGFA polyplexes, G4-FA/siGFP polyplexes control, and PBS control was injected intratumorally into HN12 xenograft tumor. Tumor volume was monitored every other day to indicate tumor growth rate. In the HN12 tumor-bearing mice, i.t. administration of G4-FA/siGFP polyplexes displayed no effect on tumor growth rate, compared to i.t. administration of PBS control (Figure 5.24a), because siGFP was used as a non-therapeutic control siRNA. This result indicated G4-FA conjugate may serve as a biocompatible gene delivery vehicle. In contrast, i.t. administration of G4-FA/siVEGFA polyplexes showed a delay in tumor growth rate, compared to i.t. administration of G4-FA/siGFP polyplexes and PBS control (Figure 5.24a). The live imaging of mice in each group was shown in Figure 5.25. Qualitatively, the tumors from the mice treated with G4-FA/siVEGFA polyplexes looked smaller than those from the mice treated with G4-FA/siGFP polyplexes and PBS control at 12 d-post i.t. injection (Figure 5.25). Due to the limited number of mice in each treatment group, we were unable to perform a comprehensive statistical analysis for this experiment. However, this result still indicated G4-FA conjugates

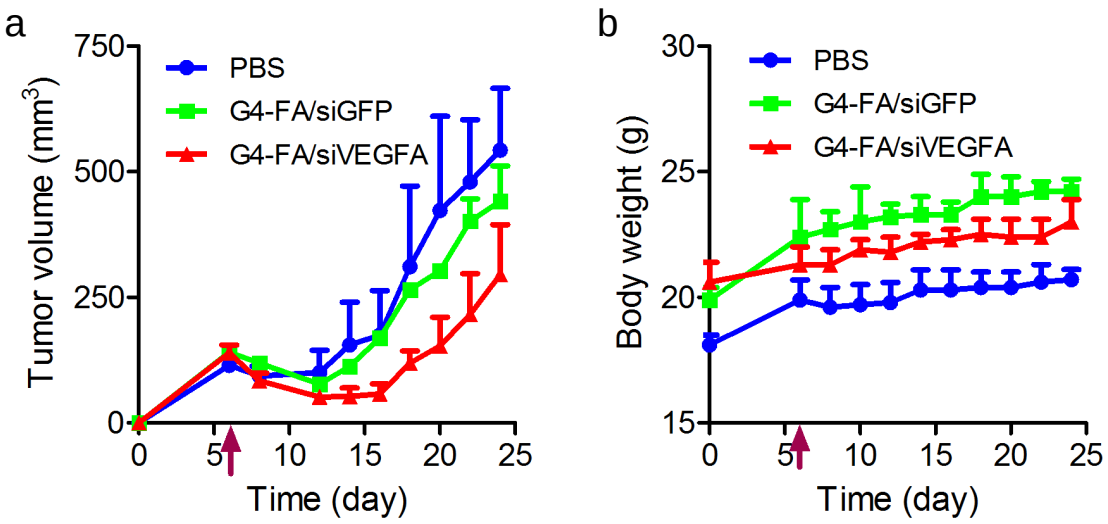

Figure 5.24: Antitumor effect of a single-dose injection of G4-FA/siVEGFA polyplexes.
The tumor volume from the mice was determined at indicated time after intratumoral (i.t.) injection of PBS, G4-FA/siGFP, and G4-FA/siVEGFA polyplexes (a). Body weights of mice in all groups were recorded (b). Arrow bars indicate the day when the mice were given injection. The dots and error bars are means SEM. n = 2-3.

might likely deliver siVEGFA to the tumor cells, knockdown VEGFA mRNA expression and reduce VEGFA secretion in the tumor cells, lower angiogenesis in the tumor, and subsequently delay the tumor growth. Additionally, the body weight of the mice treated with both polyplexes was similar to that of mice treated with PBS (Figure 5.24b), which further supported no acute toxicity after i.t. administration of G4-FA/siRNA polyplexes.

All the mice were sacrificed at 18 d-post i.t. injection, and the tumor tissues were collected (Figure 5.26a). It was observed that the weight of tumor mass from the mice i.t. injected with G4-FA/siVEGFA polyplexes decreased 55% compared to that from the mice i.t. injected with PBS control ($p = 0.0806$) (Figure 5.26b). Again, due to the limited number of mice in each treatment group, we were unable to perform a comprehensive statistical analysis for this experiment. However, these results indicate that G4-FA/siVEGFA polyplexes could slow the tumor growth via

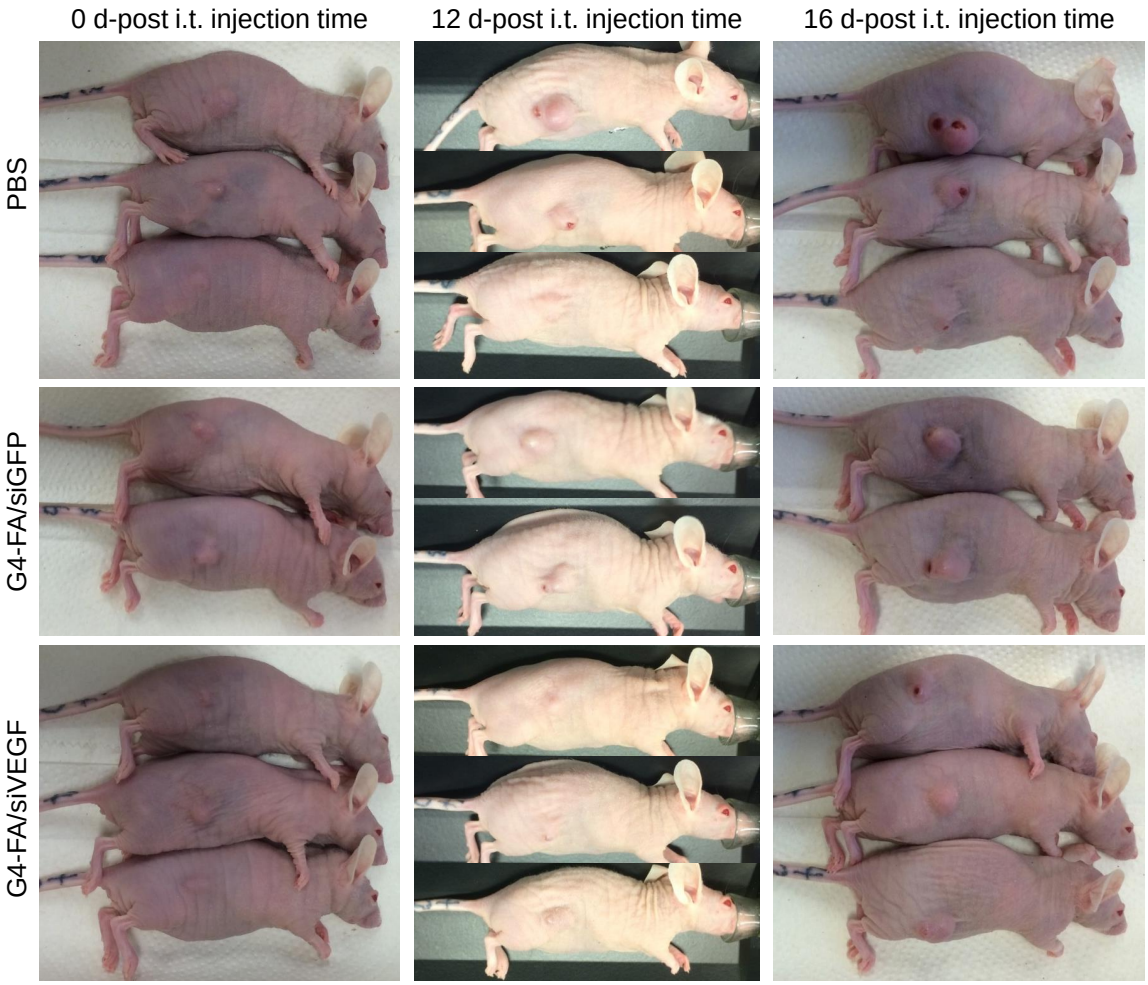

Figure 5.25: Qualitative presentations of the mice at indicated time after intratumoral (i.t.) injection of PBS, G4-FA/siGFP, and G4-FA/siVEGFA polyplexes.

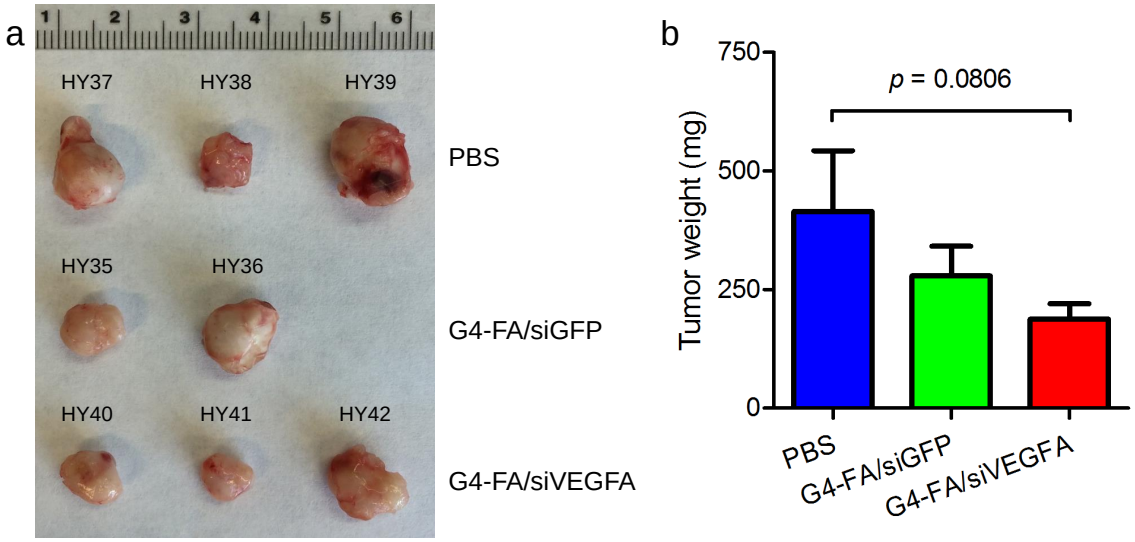

Figure 5.26: Antitumor effect of a single-dose injection of G4-FA/siVEGFA polyplexes.
All the mice were sacrificed at 18 d-post intratumoral (i.t.) injection of PBS, G4-FA/siGFP, and G4-FA/siVEGFA polyplexes. The tumor mass were then collected (a) and weighted (b). The bars and error bars are means SEM. n = 2-3.

i.t. administration in the xenograft tumor model.

5.4.6.2 Two-dose administration

Our preliminary results from single-dose administration showed potential therapeutic outcome of G4-FA/siVEGFA polyplexes. The noteworthy is that the tumors began to grow at 8 d-post i.t. injection of G4-FA/siGFP polyplexes and PBS control. In contrast, the tumors started to grow at 12 d-post i.t. injection of G4-FA/siVEGFA polyplexes, yielding a 4 d delay in tumor growth rate (Figure 5.24a). Next, we raised another question whether the tumor growth could be further inhibited by giving a second dose before it started to grow. To answer this question, we gave two-dose i.t. injection of G4-FA/siVEGFA polyplexes into HN12-YFP xenograft tumor and evaluated corresponding therapeutic outcomes. In this experiment, we generated the xenograft tumor by s.c. injection of HN12-YFP cells, which allowed real-time imaging of fluorescence intensity, in addition to tumor volume measurement, to monitor tumor growth. Besides, i.t. injections of PBS, siVEGFA alone, G4-FA/siVEGFA polyplexes, and G4/siVEGFA polyplexes were used as experiment controls.

i.t. administration of siVEGFA alone and G4-FA/siGFP polyplexes displayed no effect on tumor growth rate, compared to i.t. administration of PBS control (Figure 5.27a). In contrast, i.t. administration of G4-FA/siVEGFA polyplexes showed a significant inhibition in tumor growth rate, compared to i.t. administration of PBS control (Figure 5.27a). By given a second dose injection of G4-FA/siVEGFA polyplexes, the tumor growth kept inhibited (Figure 5.27a), compared to the single-dose injection (Figure 5.24a). The live imaging of mice (3/6 randomly selected) in each group was also shown in Figure 5.28. Qualitatively, the size of the tumors from the mice treated with G4-FA/siVEGFA polyplexes at 8 d-post second i.t. injection was similar to that before first injection, and it displaced much smaller than those from the mice treated with G4-FA/siGFP polyplexes, siRNA alone, and PBS control. In contrast, i.t. administration of non-targeting G4/siVEGFA polyplexes also yielded a decrease of tumor growth rate (Figure 5.24a). However, the inhibition was not as strong as that of G4-FA/siVEGFA polyplexes. In addition, a severe skin lesion from the tumor site was observed in the mice (6/6) after second dose i.t. injection of G4/siVEGFA polyplexes (Figure 5.28), indicating the non-targeting G4/siVEGFA polyplexes might accumulate in the skin tissue. The accumulated G4/siVEGFA polyplexes were potentially toxic to the skin tissues. According to the IACUC guidelines, we had to sacrifice G4/siVEGFA polyplexes-treated mice before the experiment end point. The body weight of the mice was similar in all the treatment groups except G4/siVEGFA polyplexes treatment group, in which the body weight dropped after second i.t. injection of G4/siVEGFA (Figure 5.24b). This result again supported that i.t. administration of G4-FA/siRNA polyplexes caused no acute toxicity, but the accumulated G4/siVEGFA polyplexes could cause acute toxicity to the mice.

Moreover, we employed IVIS 200 system to measure the fluorescence intensity of the tumors at predetermined time intervals. Before the first i.t. injection, the overall YFP fluorescence intensities of the tumors were similar among each treatment group (Figure 5.29). At 8 d-post first i.t. injection, the mice treated with single-dose of G4/siVEGFA and G4-FA/siVEGFA showed a decrease in the overall YFP fluores-

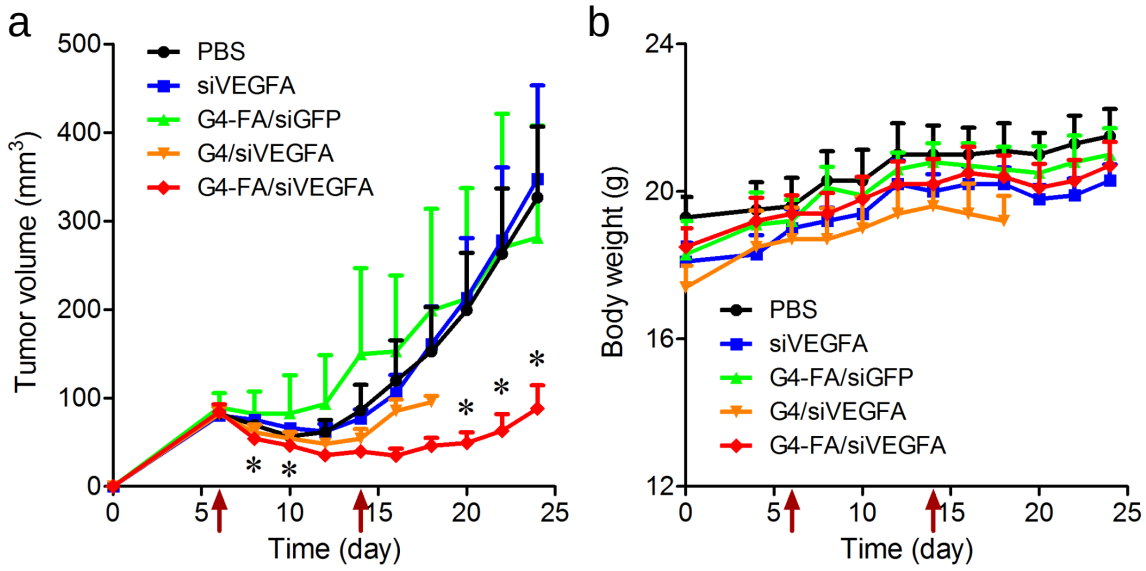

Figure 5.27: Antitumor effect of two-dose injection of G4-FA/siVEGFA polyplexes.
The tumor volume from the mice was determined at indicated time after intratumoral (i.t.) injection of PBS, siVEGFA alone, G4-FA/siGFP, G4/siVEGFA, and G4-FA/siVEGFA polyplexes (a). Body weights of mice in all groups were recorded (b). Arrow bars indicate the day when the mice were given injection. The dots and error bars are means SEM. n = 6. * $p < 0.05$ versus the mice i.t. injected with PBS.

Figure 5.28: Qualitative presentations of the mice at indicated time after intratumoral (i.t.) injection of PBS, siVEGFA alone, G4-FA/siGFP, G4/siVEGFA, and G4-FA/siVEGFA polyplexes.

cence intensities of tumors, compared to those treated with G4-FA/siGFP polyplexes, siVEGFA alone, and PBS controls (Figure 5.30). A further decreased in YFP fluorescence intensity was observed at 8 d-post second i.t. injection (Figure 5.31). The fluorescence intensity results well agreed with the tumor volume measurement, both of which were consistent with our preliminary results from single-dose administration (Figure 5.24a).

All the mice were sacrificed at 10 d-post second i.t. injection, and the tumor tissues were collected (Figure 5.32a). It was observed that the weight of tumor mass from the mice i.t. injected with G4-FA/siVEGFA polyplexes decreased 71% compared to that from the mice i.t. injected with PBS control ($p = 0.0172$) (Figure 5.32b). In contrast, siVEGFA alone treatment has no effect on tumor mass weight, compared to PBS control treatment. Although G4/siGFP polyplexes treatment slightly decreased the tumor mass weight ($p = 0.2020$), the data was not reliable because a significant tumor mass loss occurred at 8 d-post second i.t. injection of G4/siGFP polyplexes (Figure 5.28).

The major mechanism of action of G4-FA/siVEGFA polyplexes is to deliver siVEGFA into tumor cells and then reduce angiogenesis within the tumor. CD31 is an endothelial cell surface marker, primarily to demonstrate the presence of endothelial cells in histological tissue sections [175]. Then, CD31 has been widely used to evaluate the angiogenesis degree of tumor [256, 336, 280]. Finally, we evaluated the angiogenesis level in the tumor tissue by immunohistochemical (IHC) staining of CD31. The morphology of the tumor tissue was presented in Figure 5.33, indicating no tissue damage occurred in any tumor sample collected from PBS, siVEGFA, G4-FA/siGFP, and G4-FA/siVEGFA treatment groups. In the IHC staining assessment, an obvious decrease in CD31-positive tumor microvessels was observed upon G4-FA/siVEGFA treatment compared to those of G4-FA/siGFP, siVEGFA alone, and PBS treatments (Figure 5.34). The average microvessel counts (per 200× field) in PBS, siVEGFA alone, and G4-FA/siGFP polyplexes-treated tumor tissue were

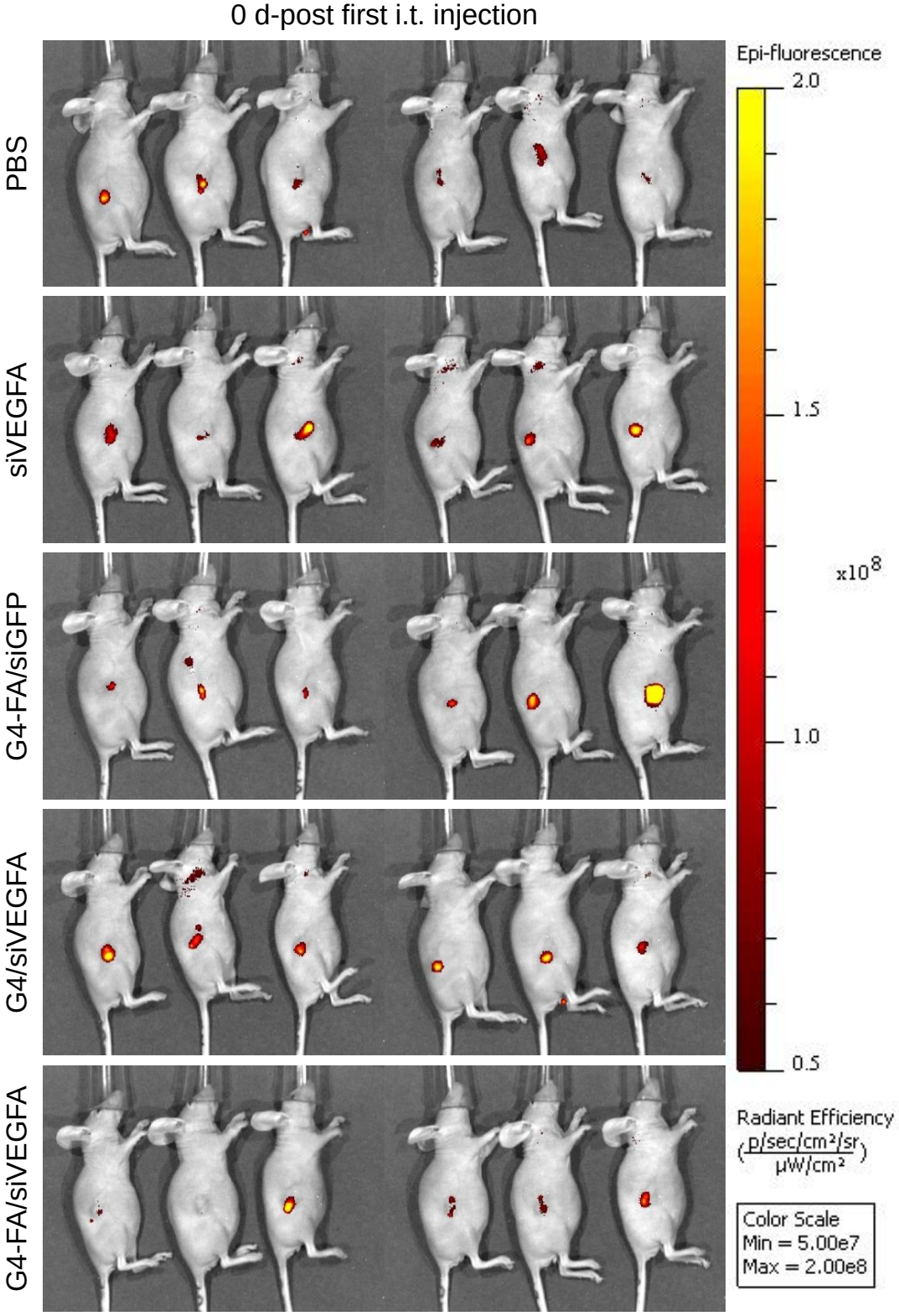

Figure 5.29: Fluorescence images of the mice at 6 d-post subcutaneous (s.c.) injection of HN12-YFP cells.

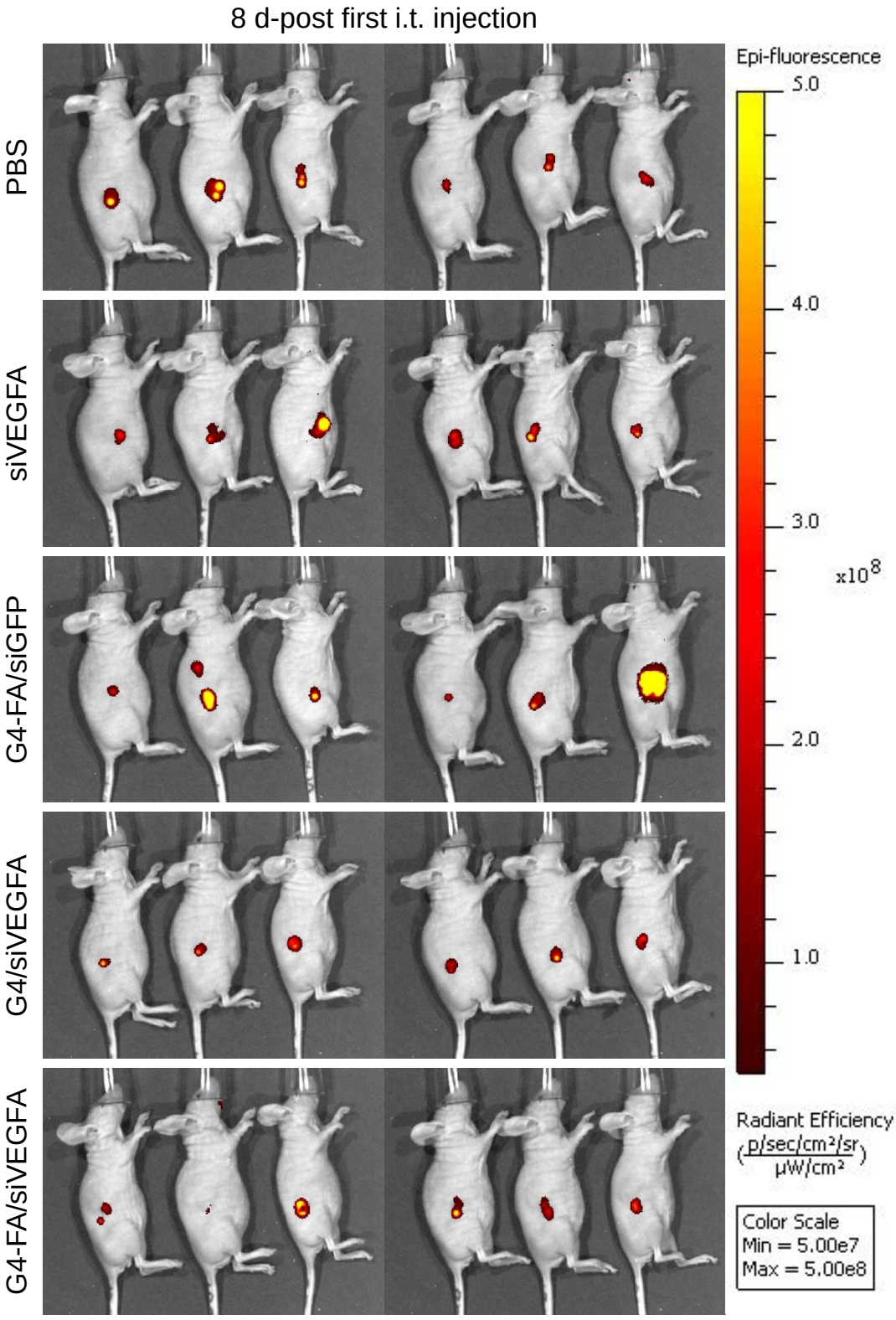

Figure 5.30: Fluorescence images of the mice at 8 d-post first intratumoral (i.t.) injection of PBS, siVEGFA alone, G4-FA/siGFP, G4/siVEGFA, and G4-FA/siVEGFA polyplexes.

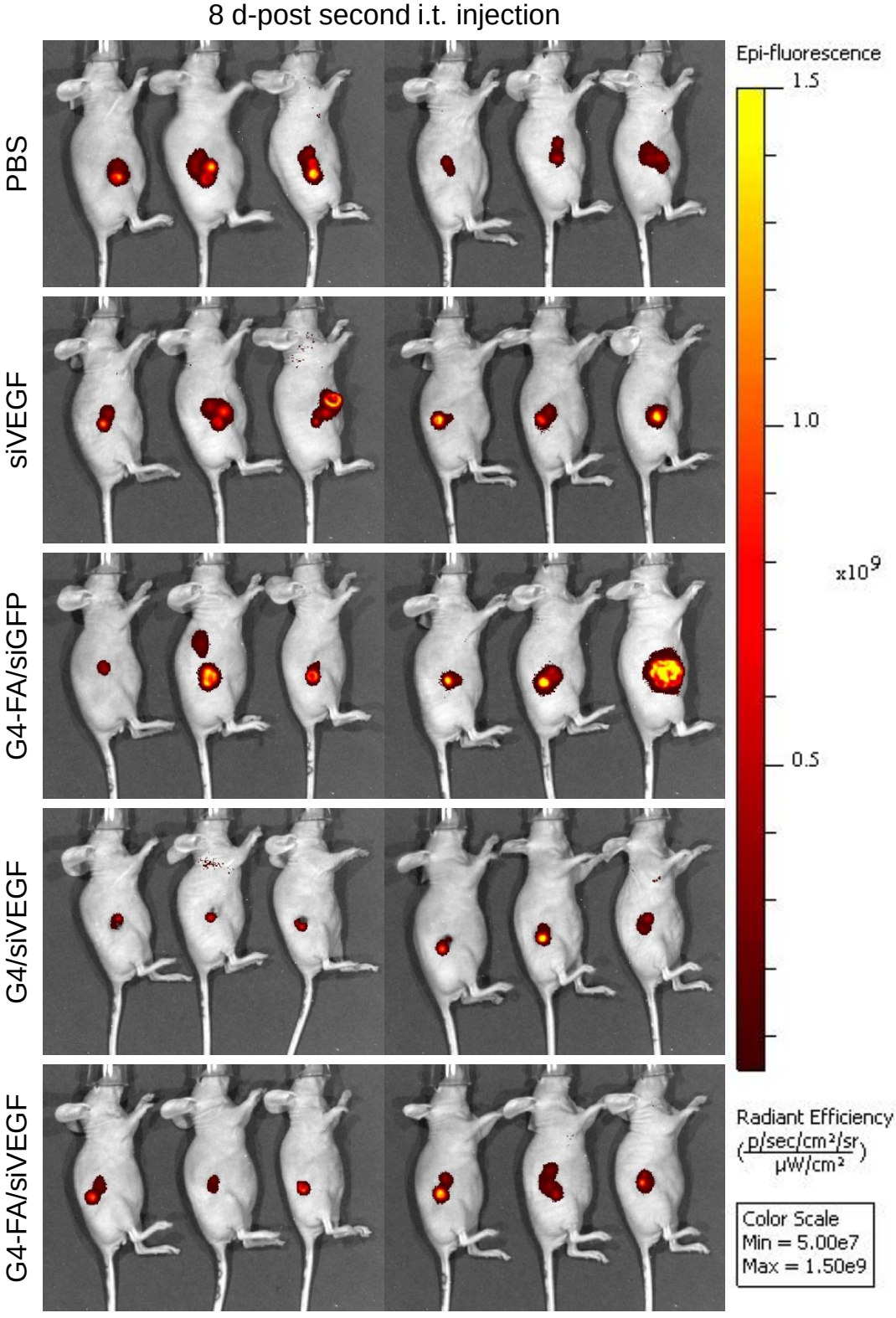

Figure 5.31: Fluorescence images of the mice at 8 d-post second intratumoral (i.t.) injection of PBS, siVEGFA alone, G4-FA/siGFP, G4/siVEGFA, and G4-FA/siVEGFA polyplexes.

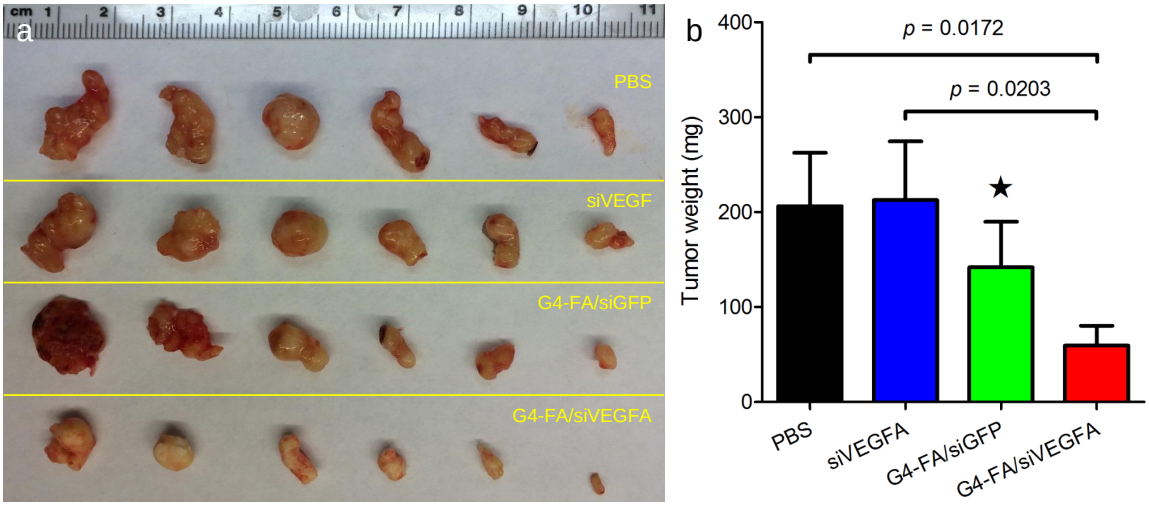

Figure 5.32: Antitumor effect of two-dose injection of G4-FA/siVEGFA polyplexes.
All the mice were sacrificed at 10 d-post second intratumoral (i.t.) injection of PBS, siVEGFA alone, G4-FA/siGFP, G4/siVEGFA, and G4-FA/siVEGFA polyplexes. The tumor mass were then collected (a) and weighted (b). The bars and error bars are means SEM. n = 6. $\star$, the data is not comparable to the others due to the tumor mass loss from the mouse in this group.

16.2, 16.3, and 15.0, respectively. These values were very close to the literature report, in which the average microvessel count (per 100× field) was 39.4 in the saline-treated KB-8-5 xenograft tumor [280]. In contrast, the average microvessels count in G4-FA/siVEGFA polyplexes-treated tumor tissue was 6.8. A 58% decrease in the average microvessels count was observed in the tumor treated with G4-FA/siVEGFA polyplexes, compared to that of the tumor treated with PBS (Figure 5.35). Taken together, our findings strongly suggest G4-FA conjugates can deliver siVEGFA to the tumor cells through local injection, knockdown VEGFA mRNA expression, reduce VEGFA secretion, lower angiogenesis in the tumor, and subsequently inhibit tumor growth.

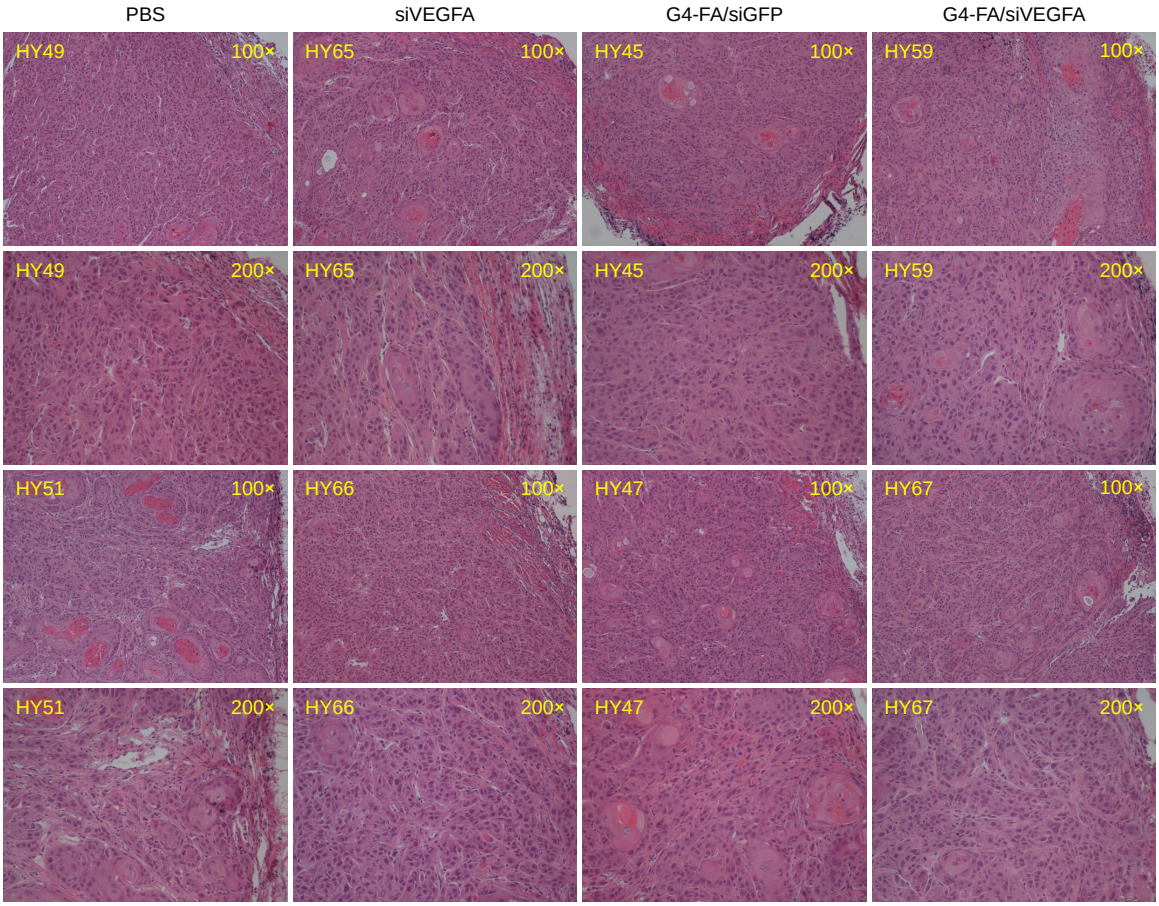

Figure 5.33: Histological analysis to tumor morphology.
All the mice were sacrificed at 10 d-post second intratumoral (i.t.) injection of PBS, siVEGFA alone, G4-FA/siGFP, G4/siVEGFA, and G4-FA/siVEGFA polyplexes. The tumor tissues were fixed, embedded, sectioned, stained with hematoxylin and eosin (H&E), and imaged using a magnification of 100× and 200×.

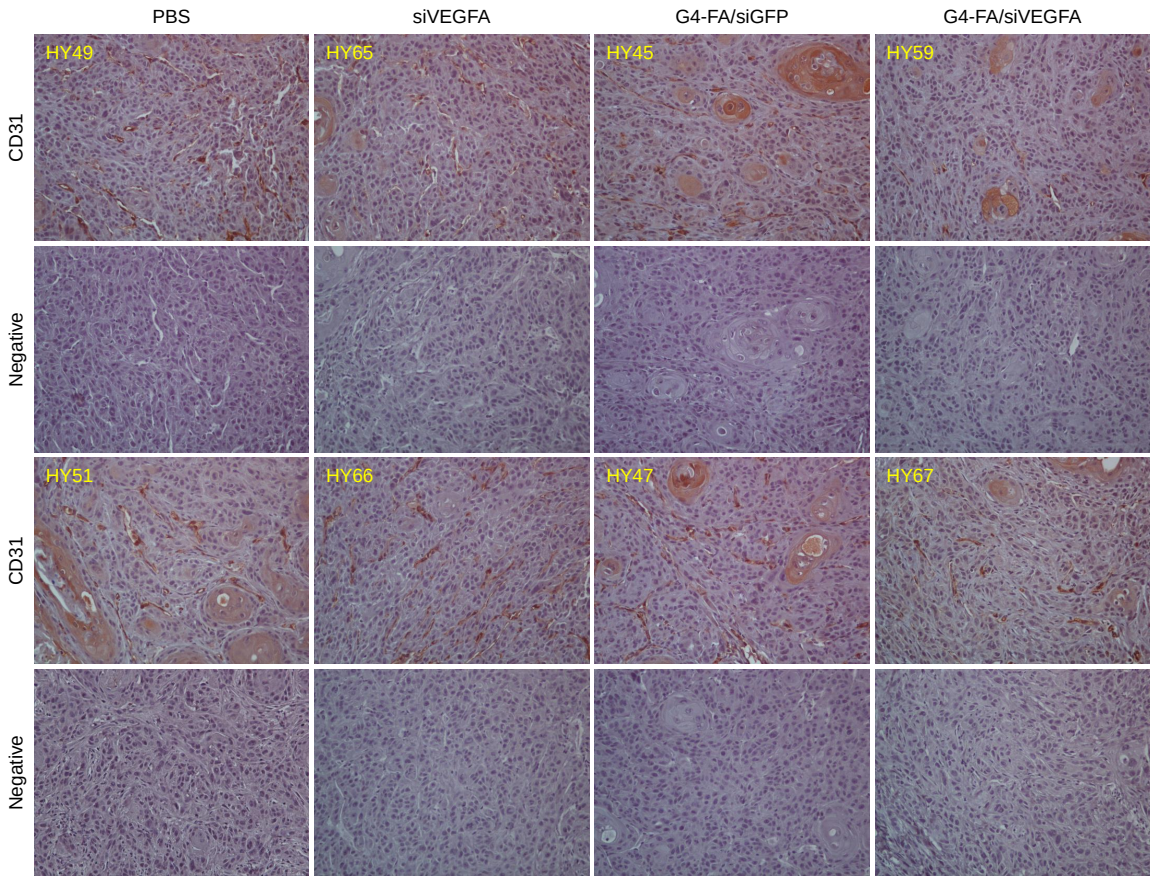

Figure 5.34: Angiogenesis evaluation of tumor.
All the mice were sacrificed at 10 d-post second intratumoral (i.t.) injection of PBS, siVEGFA alone, G4-FA/siGFP, G4/siVEGFA, and G4-FA/siVEGFA polyplexes. The tumor tissues were fixed, embedded, sectioned, immunostained with CD31, counter-stained with hematoxylin, and imaged using a magnification of 200×.

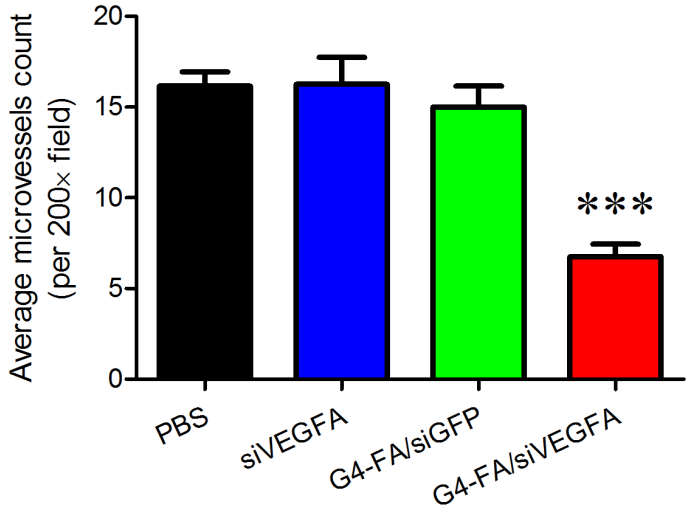

Figure 5.35: Angiogenesis evaluation of tumor.
All the mice were sacrificed at 10 d-post second intratumoral (i.t.) injection of PBS, siVEGFA alone, G4-FA/siGFP, G4/siVEGFA, and G4-FA/siVEGFA polyplexes. The average microvessels counts (per 200× field) were quantitated as the number of CD31-positive vessels in six randomly selected fields for each sample, and each group included sections from 2 mice. The bars and error bars are means SEM. *** $p < 0.001$ versus the mice i.t. injected with PBS.

5.5 Conclusions

Our work has demonstrated that FR-targeted PAMAM dendrimer G4, G4-FA conjugates, could significantly increase the silencing efficiency of siRNA in HN12 cells, which may contribute to reduced non-specific uptake of siRNA from peripheral tissues, enhanced biocompatibility of polyplexes, and prolonged retention of siRNA within tumors through i.t. administration. Using siVEGFA as a model siRNA, G4-FA/siVEGFA polyplexes markedly reduced angiogenesis within the tumor and subsequently inhibited tumor growth in an HN12 xenograft tumor model. These results indicate that G4-FA conjugates could serve as a specific and efficient siRNA delivery system for potential gene therapy in human head and neck squamous cell carcinoma (HNSCC).

Chapter 6

Click Synthesis of Polyamidoamine Dendrimer-Camptothecin Conjugates for Anticancer Drug Delivery

Preface: This chapter has been prepared as a research article.

Olga Yu. Zolotarskaya, Leyuan Xu, Kristoffer Valerie, Hu Yang

6.1 Abstract

In the present work we report on the synthesis of a new camptothecin (CPT)-carrying delivery system based on anionic polyamidoamine (PAMAM) dendrimer intended for glioblastoma multiforme therapy. We applied "click" chemistry to improve polymer-drug coupling reaction efficiency. Specifically, CPT was functionalized with a spacer, 1-azido-3,6,9,12,15-pentaoxaoctadecan-18-oic acid (APO), via EDC/DMAP coupling reaction. In parallel, propargylamine (PPA) and methoxypoly(ethylene glycol) amine were conjugated to PAMAM dendrimer G4.5 in sequence using an effective coupling agent 4-(4,6-dimethoxy-(1,3,5)triazin-2-yl)-4-methyl-morpholinium chloride (DMTMM). CPT-APO was then coupled to PEGylated PAMAM dendrimer G4.5-

PPA via a click reaction using copper bromide/2,2'-bipyridine/dimethyl sulfoxide (catalyst/ligand/solvent). Human glioma cells were exposed to the CPT-conjugate to determine toxicity and cell cycle effects using WST-1 assay and flow cytometry. The CPT-conjugate displayed a dose-dependent toxicity with an IC_{50} of 5 μM, a 185-fold increase relative to free CPT, presumably as a result of slow release. As expected, conjugated CPT resulted in G_2/M arrest and cell death while the dendrimer itself had little to no toxicity. Altogether, highly efficient click chemistry allows for the synthesis of multifunctional dendrimers for sustained drug delivery.

6.2 Introduction

Glioblastoma multiforme (GBM) is an aggressive form of brain cancer with poor prognosis and a median survival of only 12-15 months. In general, GBMs are resistant to standard treatment consisting of surgery followed by concurrent chemo- and radiotherapy [14]. New therapeutic approaches such as the use of small molecule radiosensitizers and gene therapy are under investigation for the treatment of GBM [15, 74]. However, treatment outcomes still depend largely on whether or not sufficient levels of therapeutic agent can be delivered to the brain tumor mass [305]. Considering that the blood-brain barrier (BBB), the blood cerebral spinal fluid, and the blood-tumor barrier hamper the administration of the therapeutic to the brain, efficient delivery still remains a challenge, and new technologies and delivery systems need to be developed [145, 104]. A number of carriers have been developed to facilitate drug entry into the brain, a topic which has been thoroughly reviewed [14, 305, 104, 127, 197]. Among them, dendrimers have attracted increasing attention as drug carriers in that they possess a high degree of molecular uniformity, high drug loading capacity, and the ability to accommodate various functional entities [260, 259, 173]. Thus, the dendrimer-based platform would be very attractive for building modular drug delivery vehicles12-15, and its utility for delivering anticancer drugs has been actively explored [84, 98, 169, 337].

Early studies have shown promising results with dendrimers as drug delivery

vehicle making it a feasible platform for further development [102, 113, 319]. Drugs along with BBB-specific ligands can be covalently coupled to the multivalent dendrimer for targeted drug delivery to the brain. Regardless, a commonly encountered problem is the heterogeneity of ligand and drug on the dendrimer surface during chemical synthesis [236]. It is essential to obtain a uniform distribution of ligand and drug for standardizing therapeutic effects and for the successful translation of dendrimer-based nanomedicines to clinical application. Robust and efficient coupling methods must be applied to overcome such issues. To develop an enabling modular dendrimer-based delivery system for GBM, the current study reports on the use of click chemistry for the synthesis of water soluble polyamidoamine (PAMAM) dendrimer-camptothecin (CPT) conjugates. Camptothecin is a plant alkaloid isolated from Camptotheca acuminata of the Nyssaceae family with remarkable anticancer activity by inhibiting both DNA and RNA synthesis [156]. Camptothecin has been used for the treatment of many different types of cancer despite its low water solubility and poor stability of the lactone form, a required form for therapeutic activity [338]. In particular, it is of advantage to use CPT to treat GBM as it selectively kills proliferating (S-phase) cells, thus exerting little to no toxicity to non-dividing normal cells resident of the brain [33, 157]. Although several dendrimer-CPT derivatives have been made in the past, the efficiency using high capacity of dendrimer to deliver CPT was low. For instance, Thiagarajan et al. applied EDC/NHS chemistry to conjugate CPT to the dendrimer via a glycine spacer [258]. Less than 20% of CPT used in the reaction was successfully attached to the dendrimer. Copper-catalyzed azide-alkyne cycloaddition (CuAAC), the best known example of a "click" reaction, is a highly efficient and selective synthetic method. It has proven to be a powerful strategy for precisely loading drugs to various polymeric carriers including dendrimers [134, 338, 97]. In the present study, we applied CuAAC for improving coupling reaction efficiency and to synthesize CPT-dendrimer conjugates. Anionic PAMAM dendrimer G4.5 was used as the carrier because of low toxicity and low non-specific cellular uptake. It was modified with polyethylene glycol (PEG) for improved water solubility and cytocompatibility. CPT was click coupled to the dendrimer carrier

via a short heterobifunctional spacer. The click synthesis and characterization of the resulting conjugates and their therapeutic activity are reported herein.

6.3 Experimental Section

6.3.1 Materials

EDA core PAMAM dendrimer G4.5 caboxylate sodium salt was purchased from Dendritech (Midland, MI). 2,2'-Bipyridine, 4-dimethylaminopyridine (DMAP), copper(II) sulfate (CuSO4), (+)-sodium L-ascorbate, 4-(4,6-dimethoxy-(1,3,5)triazin-2-yl)-4-methylmorpholinium chloride (DMTMM), deuterated solvents, dichloromethane (DCM), dimethyl sulfoxide (DMSO), and other organic solvents were purchased from Acros (Morris Plains, NJ). (S)-(+)-Camptothecin (CPT), propargylamine (PPA), copper bromide (CuBr), N-(3-dimethylaminopropyl)-N'-ethylcarbodiimide hydrochloride (EDC), and silica gel 60 (40-63 μm, 230-400 mesh) were purchased from Sigma-Aldrich (St. Louis, MO). 1-Azido-3,6,9,12,15-pentaoxaoctadecan-18-oic acid (APO) and methoxypoly(ethylene glycol) amine (mPEG-NH_2, 2000 g/mol) were purchased from Biomatrik (Jiaxing, Zhejiang, China) and JenKem Technology USA (Plano, TX), respectively. SnakeSkin dialysis tubing 3.5 kDa and 7 kDa MWCO and magnesium sulfate ($MgSO_4$) were purchased from Thermo Fisher Scientific (Pittsburg, PA).

6.3.2 Instrumentation

^{1}H NMR spectra were recorded on a Bruker AVANCEIII 600 MHz spectrometer. UV/Vis spectra were acquired on an Agilent 8453 spectrophotometer.

6.3.3 Synthesis of CPT-APO

To a suspension of CPT (200 mg, 0.57 mmol) in 60 mL of DCM were added EDC (330 mg, 1.73 mmol) and DMAP (140 mg, 1.14 mmol) followed by APO (290 mg, 0.86 mmol) pre-dissolved in 5 mL of DCM. After having been stirred for 24 h at room

temperature, the reaction mixture was poured into 50 mL of water. The organic phase was collected. The aqueous phase was extracted with DCM two times. The DCM fractions were combined and dried over MgSO4. Upon the removal of DCM by rotary evaporation, the obtained CPT-APO was further purified by column chromatography on silica gel using DCM/methanol mixture (90/2.5, v/v). Yield 67%. ^{1}H NMR (*d*6-DMSO, 600 MHz): δ (ppm) 8.68 (s, 1H), 8.15 (d, J=8.5 Hz, 1H), 8.12 (d, J=8.2 Hz, 1H), 7.86 (t, J= 7.9Hz, 1H), 7.71 (t, J=7.5 Hz, 1H), 7.16 (s, 1H,), 5.50 (s, 2H), 5.28 (q, 2H), 3.83-3.33 (m, 22H), 2.81 (m, 1H), 2.66 (m, 1H), 2.14 (m, 2H), 0.94 (t, J =7.4Hz, 3H).

6.3.4 Synthesis of G4.5-PPA

To a solution of PAMAM dendrimer G4.5 in carboxyl form (50 mg, 2.1 μmol) in 3 mL of 0.1M $NaHCO_3$ was added DMTMM (58 mg, 0.21 mmol) followed by addition of 0.5 mL of DMF containing 0.13 mmol PPA. The reaction mixture was stirred overnight. Upon removal of the solvent under reduced pressure, the remaining residue was dialyzed against water using dialysis tube with MWCO 3.5 kDa and freeze-dried to yield 53 mg of G4.5-PPA. ^{1}H NMR (D_2O, 600 MHz): δ (ppm) 3.98 (m, 2H, CH_2C≡CH), 2.43-3.69 (m, methylene protons of G4.5).

6.3.5 Synthesis of PPA-G4.5-PEG Conjugates

To a solution of G4.5-PPA (40 mg, 1.7 μmol) and DMTMM (17 mg, 0.061 mmol) in 4 mL of 0.1M $NaHCO_3$ was added mPEG-NH_2 (102 mg, 51 μmol). The obtained mixture was stirred overnight at room temperature, dialyzed against water using dialysis tubing with 7.0 kDa MWCO for 48 h, and then freeze-dried to obtain 86 mg of PPA-G4.5-PEG. ^{1}H NMR (D_2O, 600 MHz): δ (ppm) 3.99 (m, 2H), 3.73 (br.s, methylene protons in PEG repeat units), 3.41 (s, 3H), 3.40-2.42 (m, methylene protons of G4.5).

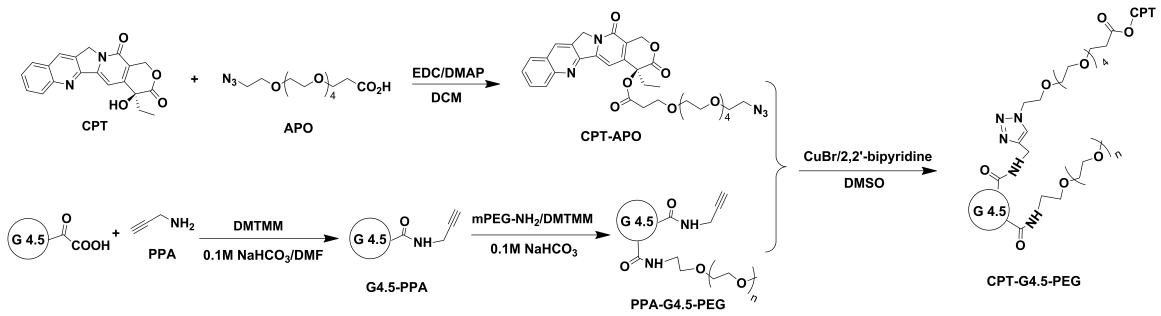

Figure 6.1: Synthesis of CPT-G4.5-PEG conjugates.

6.3.6 Synthesis of CPT-G4.5-PEG Conjugates

PPA-G4.5-PEG (20 mg, 0.26 μmol), CPT-APO (2.9 mg, 4.4 μmol), and 2,2-bipyridine (0.6 mg, 3.8 μmol) were mixed in 1 mL of DMSO. The molar feed ratio of CPT to dendrimer in this reaction was 17:1, which was determined based on availability assessment for the alkyne groups on the dendrimer (see Supporting Information). The obtained mixture underwent 3 times of freeze-pump-thaw cycling for degassing. Afterwards, CuBr (0.3 mg, 2.1 μmol) dissolved in 40 μL of DMSO was added to the mixture solution. The reaction mixture under nitrogen was stirred in dark overnight at room temperature and then poured into 5 mL of water. After 1 h-stirring, the solvents were removed under reduced pressure. Extraction of unreacted CPT-APO was conducted by vortexing the obtained solid residue with ether (1 mL each time) followed by centrifugation for liquid-solid separation. The extraction procedure was repeated until CPT-APO became undetectable in ether by UV-Vis spectrophotometer. The remaining solid was dissolved in 1 mL of water followed by centrifugation. The liquid phase was collected and freeze-dried to yield CPT-G4.5-PEG. UV-Vis spectroscopy analysis confirmed that conjugated CPT accounted for 6.4 wt.% of the product. ^{1}H NMR (d_6-DMSO, 600 MHz): δ (ppm) 8.64 (br.s, 1H), 8.12 (br.s, 2H), 7.85 (br.s, 2H), 7.68 (br.s, 1H), 7.14 (br.s, 1H), 5.50 (s, 2H), 5.26 (br.s, 2H), 4.44 (br.s, 2H), 4.26 (br.s, 2H), 3.50 (br.s, methylene protons in the repeat unit of PEG), 3.23 (s, 3H), 2.06-2.95 (m, methylene protons of G4.5), 0.94 (s, 3H).

6.3.7 Cell Culture

Human glioma U1242 cells were cultured in Dulbeccos modified Eagles medium (DMEM) supplemented with 10% Cosmic calf serum at 37 °C in 95% air/5% CO_2 [73].

6.3.8 Cytotoxicity Assay

Human glioma U1242 cells were seeded at a density of 1×10^4 cells/well in a 96-well cell culture plate and cultured for 1 day to allow cell attachment. The cells were then treated with various concentrations (0-50 μM) of CPT in either free or conjugated form for 2 days. For comparison, toxicity of PPA-G4.5-PEG conjugates at the same molar concentrations as CPT-G4.5-PEG conjugates was used as control. Cell viability relative to untreated and control-treated cells was then determined by WST-1 proliferation assay. GraphPad Prism 5 was used to perform the curve fitting and then determine the 50% maximal inhibitory concentrations of free CPT (IC_{50free}) and conjugated CPT ($IC_{50conjugated}$).

6.3.9 Cell Cycle Analysis

Human glioma U1242 cells (1×10^6) were seeded in a 100-mm cell culture dish and cultured for 1 day to allow cell attachment. The cells were treated with CPT at the concentration of $2\times IC_{50free}$, conjugated CPT at the concentration of $2\times IC_{50cojugated}$ and PPA-G4.5-PEG conjugates at the equivalent concentration of CPT-G4.5-PEG conjugates for various lengths of time (6, 12, and 24 h). The cells treated with PBS were used as a control. At the end of each treatment, the cells were washed with PBS and re-suspended in fresh cell culture medium following trypsinization. Following the centrifugal removal of the medium, the cells were fixed with cold 70% ethanol and maintained at 4 °C for 1 h. Finally, the cells were washed with PBS three times and incubated with RNase at a final concentration of 1 μg/mL and propidium iodide at a final concentration of 50 μg/mL at 37 °C for 30 min. The cells were then immediately analyzed by flow cytometry using a Guava EasyCyte mini flow cytometry system

(Millipore, Billerica, MA) [321].

6.4 Results and Discussion

6.4.1 Synthesis and characterization

We synthesized clickable PAMAM dendrimer G4.5 and used it as a carrier to deliver CPT. Taking into consideration that cell membranes are negatively charged, the use of anionic half-generated PAMAM dendrimers terminated with carboxylic acid groups is expected to minimize nonspecific cellular uptake and reduce drug side effect. Given the hydrophobicity of CPT, the dendrimer drug loading degree should be carefully controlled to avoid generating water insoluble entities. The incorporation of hydrophilic molecules such as PEG onto the dendrimer surface has proven effective in improving water solubility and enhancing cytocompatibility [308, 309]. Thus, this step was applied in the synthesis of our dendrimer-CPT conjugates. A short heterobifunctional spacer, i.e., APO bearing azide and carboxyl groups (Figure 6.2), was used to modify CPT. CPT was coupled to APO via EDC/DMAP chemistry. The reaction proceeded successfully in methylene chloride. A ^{1}H NMR spectrum clearly shows proton signals from both CPT and APO (Figure 6.3). In particular, multiple proton signals between 3.40 and 3.83 ppm are from methylene protons in APO. The signal at 5.28 ppm is assigned to the two methylene protons in the CPT lactone ring, indicating that therapeutically active lactone form remained. A double doublet for the methylene protons in the lactone ring was also clearly seen in the ^{1}H NMR spectrum based on $CDCl_3$ (Figure 6.4).

To make clickable dendrimers, alkyne groups were introduced onto the PAMAM dendrimer surface via reaction with PPA using coupling reagent DMTMM. ^{1}H NMR spectrum of G4.5-PPA (Figure 6.5) shows multiple peaks of dendrimer methylene protons in the range 2.43-3.69 ppm along with multiplet at 3.98 ppm assigned to methylene protons (a) adjacent to the alkyne group of PPA, confirming the successful

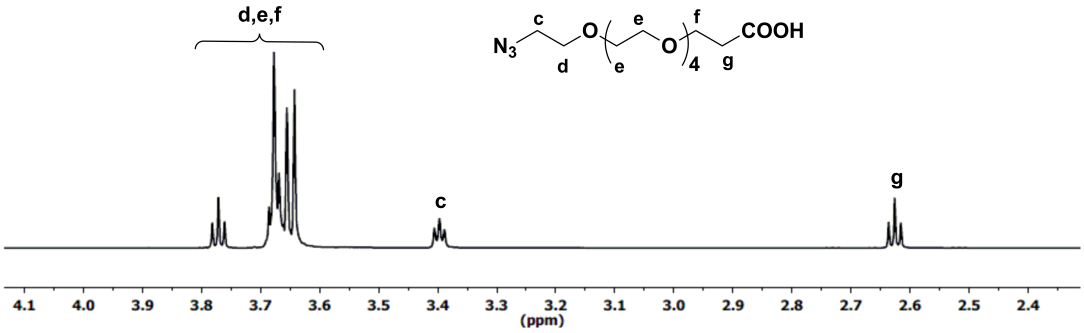

Figure 6.2: ^{1}H NMR spectrum of APO in $CDCl_3$.

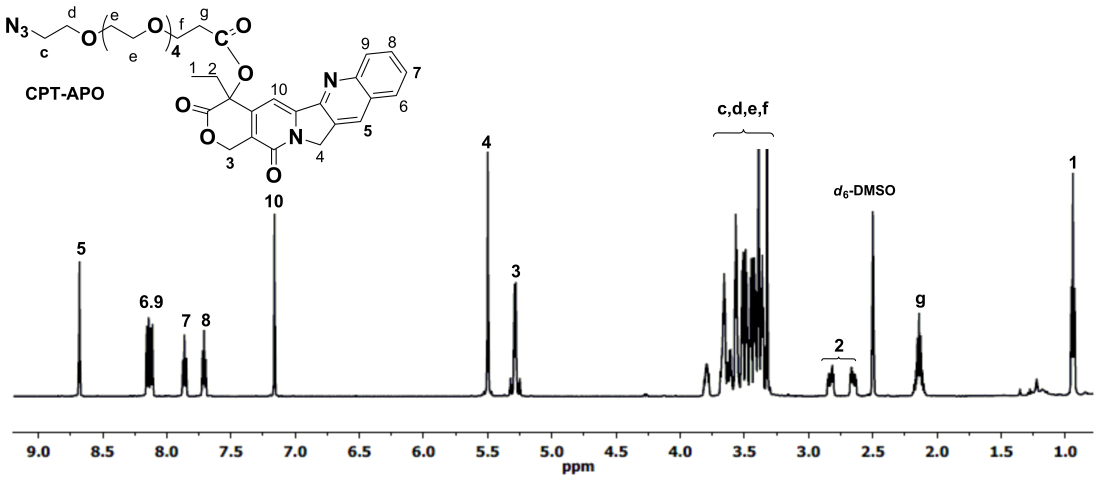

Figure 6.3: ^{1}H NMR spectrum of CPT-APO in d_6-DMSO.

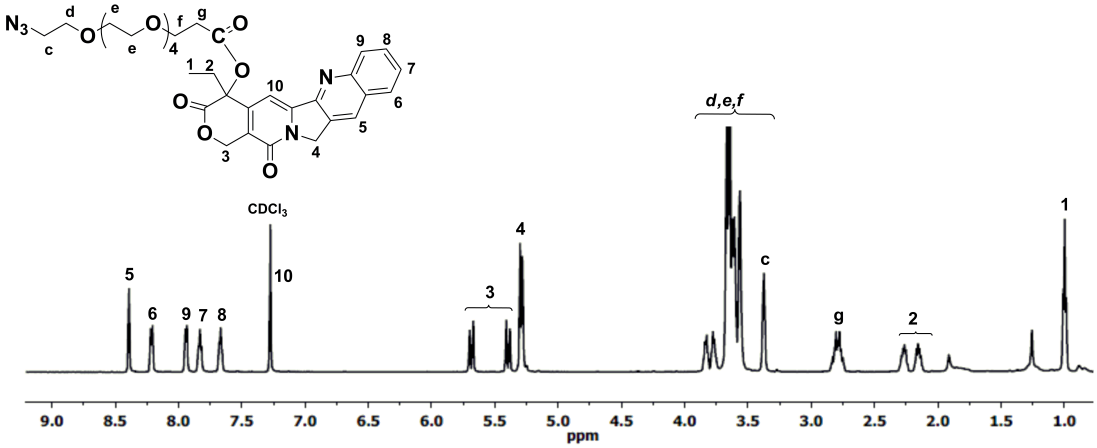

Figure 6.4: ^{1}H NMR spectrum of CPT-APO in $CDCl_3$.

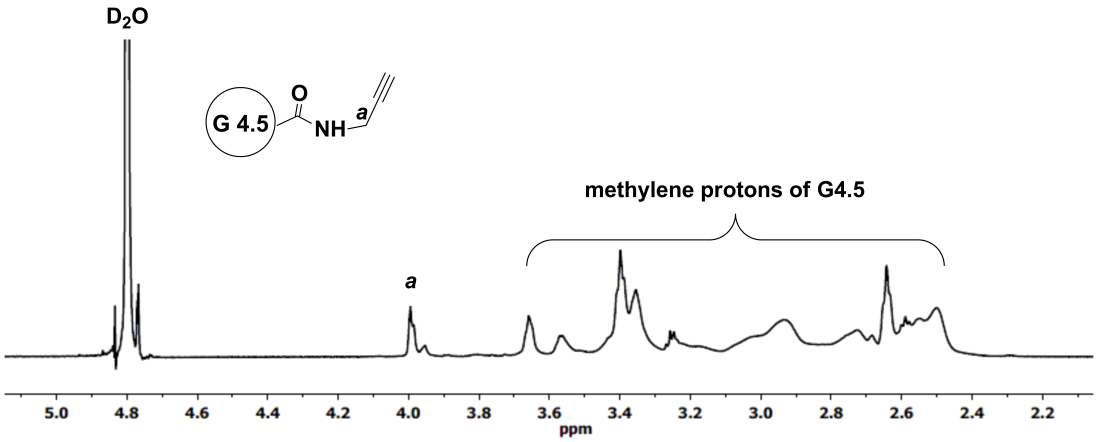

Figure 6.5: ^{1}H NMR spectrum of G4.5-PPA in D_2O.

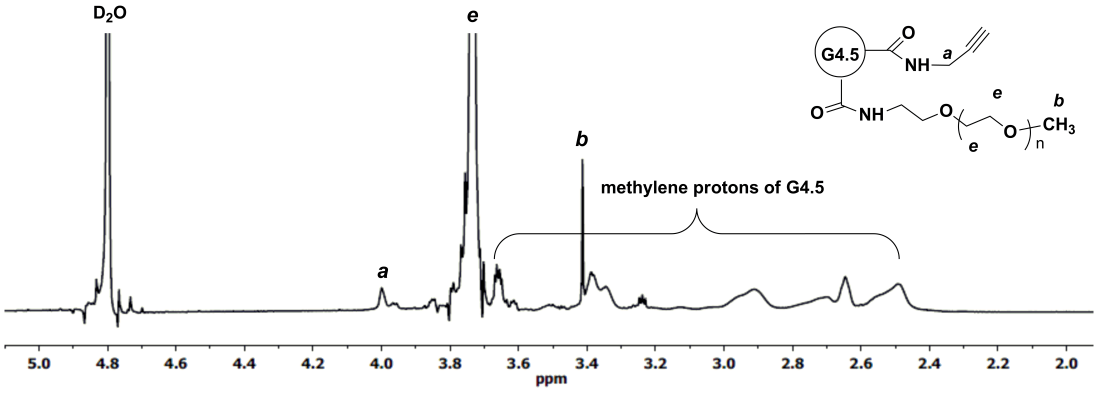

Figure 6.6: ^{1}H NMR spectrum of PPA-G4.5-PEG in D_2O.

amide bond formation. Based on the ^{1}H NMR integration analysis, the synthesized G4.5-PPA conjugates carried 30 alkyne groups per dendrimer.

G4.5-PPA was further PEGylated by coupling mPEG-NH2 (2000 Da) to the dendrimer surface in the presence of DMTMM. The ^{1}H NMR spectrum shown in Figure 6.6 confirms successful covalent attachment of mPEG to G4.5-PPA. In addition to the identification of the proton signals from PPA and dendrimer moieties, a broad singlet centered at 3.73 ppm is assigned to the methylene protons of PEG repeat units while a singlet at 3.41 ppm is due to the methyl protons. Based on the ^{1}H NMR spectrum, the degree of PEGylation was calculated to be 27.

The final step of the synthesis involves a click reaction between alkyne-carrying

PEGylated PAMAM dendrimer G4.5 (i.e., PPA-G4.5-PEG) and azide-carrying CPT (i.e., CPTAPO) in the presence of CuBr/2,2-bipyridine (catalyst/ligand) system in DMSO. The feed molar ratio (17:1) of CPT to dendrimer was first determined. To a water solution (4 mL) containing G4.5-PPA (8 mg, 0.34 μmol) and an excess amount of APO (14.6 mg, 43 μmol) was added CuSO4 (5.4 mg, 22 μmol) followed by sodium ascorbate (8.6 mg, 43 μmol). The obtained mixture was stirred overnight at 55 °C under nitrogen. After cooling down the reaction mixture was dialyzed against 5% aqueous solution of EDTA for 8 h, against water for 24 h and then freeze-dried. (D2O, 600 MHz): δ (ppm) 7.99 (m, 1H), 4.63 (br.s, 2H), 4.49 (m, 2H), 3.99 (m, 2H), 3.55-3.79 (m, methylene protons of PEG repeat units), 2.32-3.47 (m, methylene protons of G4.5). The formation of the triazole linker was supported by appearance of the signal at 7.99 ppm assigned to methine proton b. Furthermore, a broad singlet at 4.63 ppm and proton signals in the range 3.55-3.79 ppm are assigned to the methylene protons (c) adjacent to the triazole ring and the methylene protons (d', e', and f') of PEG, respectively. The simultaneous presence of multiplet at 4.49 ppm (a) assigned to methylene protons adjacent to the triazole ring and broad singlet at 3.99 ppm (a) assigned to the unreacted acetylene groups indicates not all alkynes on the dendrimer surface are available for click reaction. Proton NMR integrations showed that an average of 17 alkyne groups were successfully click coupled with azide-containing APO (Figure 6.7). Using the alkyne accessibility analysis result as a guide, the feed molar ratio (17:1) of CPT to dendrimer was used in the click reaction. The resulting CPT-G4.5-PEG conjugates were characterized by ^{1}H NMR spectroscopy. The proton signals of CPT and spacer APO in the conjugates are identified in Figure 6.8. A further downfield shift of the signal of methylene protons (a', 4.26 ppm) adjacent to the ring opposed to proton signal (a', 3.99 ppm) resulted from the triazole linkage formation. In addition, methine proton (b) in the triazole ring appears as a singlet at 7.85 ppm, overlapping the benzene proton signal of CPT. The proton signal at 3.99 ppm (a) indicates the presence of remaining alkyne groups. Because of proton signal interference by the deuterated solvent d_6-DMSO in the spectrum, CPT coupled to the conjugates was quantified by using UV-Vis spectroscopy. Based on the UV

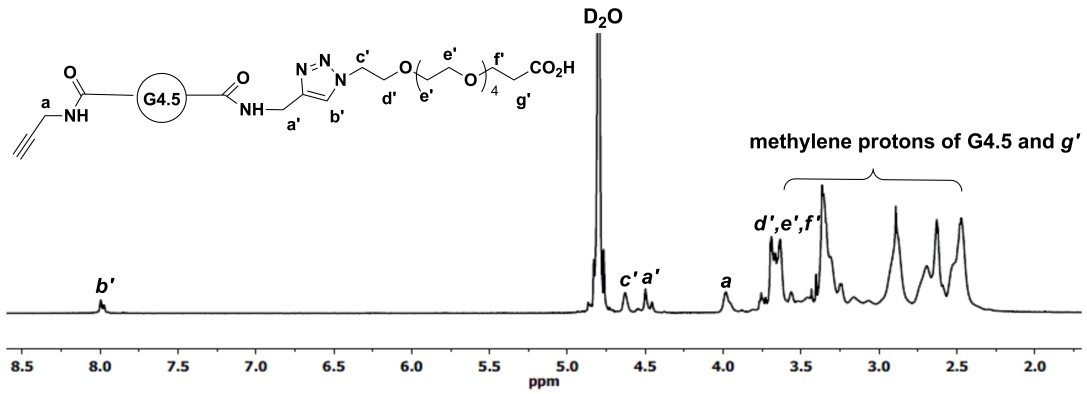

Figure 6.7: Assessment of reactivity and accessibility of alkyne in G4.5-PPA conjugates for click reaction.

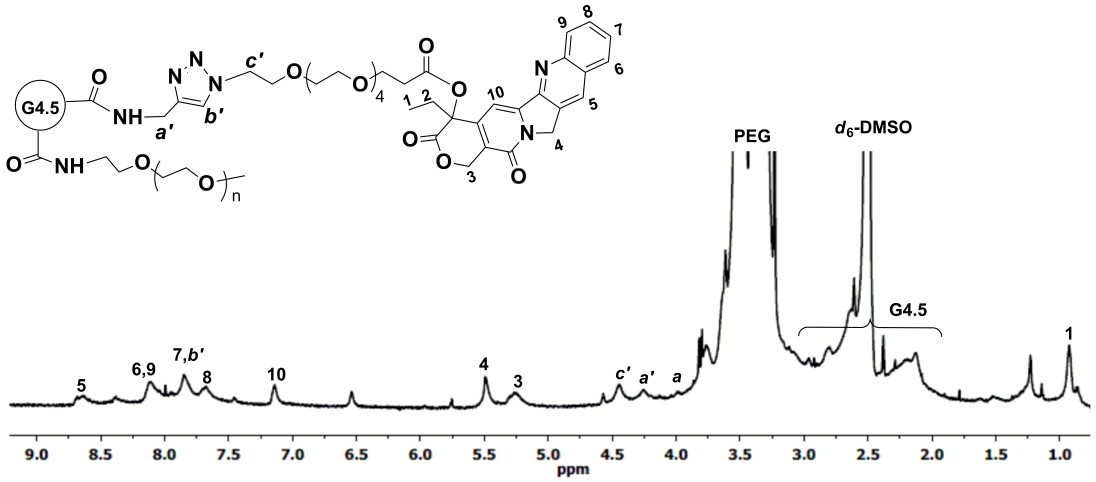

Figure 6.8: ^{1}H NMR spectrum of CPT-G4.5-PEG in d_6-DMSO.

absorbance at 347 nm, the final polymer-drug conjugates carried approximately 17 CPT molecules per dendrimer. The estimated drug loading degree matches the feed molar ratio used in the click reaction, indicating a 100% conversion rate for the utility of CPT in the click reaction. Making water soluble conjugates with a higher CPT loading will be explored in the future.

6.4.2 Cytotoxicity evaluation

CPT interferes with the breakage-reunion reaction of DNA topoisomerase I (Top1) often referred to as the cleavable complex necessary to relieve DNA stress during

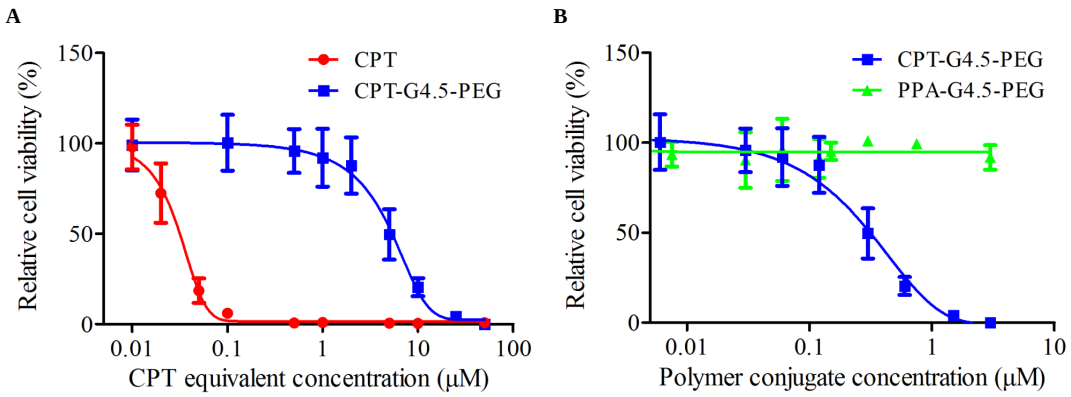

Figure 6.9: Cytotoxicity of free CPT, CPT-G4.5-PEG and PPA-G4.5-PEG conjugates in U1242 cells. The data points are mean ± SD.

DNA replication [156]. In doing so, a ternary complex between Top1-CPT-DNA is formed which is converted into single-strand breaks and subsequently into double-strand breaks during DNA replication. The cytotoxicity of the synthesized conjugates to human glioma U1242 cells was then assessed. CPT-G4.5-PEG cytotoxicity was found to be dose-dependent with an IC_{50} of 5 μM (Figure 6.9A). In comparison, the IC50 of free CPT was 27 nM. Conjugated CPT is expected to become therapeutically active following hydrolysis of the ester linkage between CPT and the dendrimer. As expected, the conjugated CPT exhibited much lower potency than free CPT at equivalent concentrations because of this slow release. Thus, the conjugates are capable of sustaining therapeutic activity for a longer period of time. PEGylated PAMAM dendrimer carrier without CPT is cytocompatible and does not cause toxicity to cells at concentrations up to 50 μM (Figure 6.9B).

Prolonged exposure to CPT is expected to bring about DNA double-strand breaks during replication hence resulting in an arrest in G_2/M of the cell cycle if not repaired [33, 245]. We performed cell cycle analyses following treatment with PBS, free CPT, CPT-G4.5-PEG or dendrimer carrier. As shown in Figure 6, cells treated with free CPT or CPT-G4.5-PEG conjugate exhibited a remarkable decrease in the G_0/G_1 cell population and an increase in G_2/M going from a little more than 20% to more than 40% over a period of 24 h. Untreated cells (PBS group) showed a normal

cell cycle distribution with a larger fraction in the G_0/G_1 phase. The cells treated with PPA-G4.5-PEG conjugate showed a similar cell cycle distribution as untreated cells, indicating that the PPA-G4.5-PEG conjugate had little to no effect on cell cycle progression. Consistent with cytotoxicity assessment, cell cycle analyses further demonstrated that CPT-G4.5-PEG induced an arrest in G_2/M and lead to apoptosis as indicated by a temporal increase in the sub-G_1 population.

6.5 Conclusions

CPT was coupled to PEGylated PAMAM dendrimer G4.5 via copper-catalyzed click reaction. Nearly 100% of CPT molecules used in the reaction were covalently conjugated to the dendrimer. The resulting conjugates carried an average of 17 CPT molecules per dendrimer and demonstrated dose-dependent toxicity against human glioma U1242 cells by causing an arrest in G_2/M and inducing cell death while the carrier itself had no toxicity. Conjugated CPT was found to have an IC50 of 5 μM, a 185-fold increase in comparison to the IC_{50} of free CPT as a result of slow release. One the other hand, the presence of a targeting moiety on the surface of a dendrimer molecule whose receptors are overexpressed on cancer cell membrane surface will provide the delivery of PAMAM dendrimer-drug conjugate to the tissue of the interest and improve specific uptake of the drug. In future studies, coupling tumor- and BBB-specific ligands or other functional moieties to the synthesized dendrimer-CPT conjugates via click chemistry will be explored for directing and enhancing drug uptake by brain tumor cells. The further utility of click chemistry based coupling strategy would make it possible to make large-scale polymerdrug-ligand conjugates of high quality possessing a uniform loading of ligand and drug on the dendrimer surface, a critical factor for achieving reproducible antitumor efficacy.

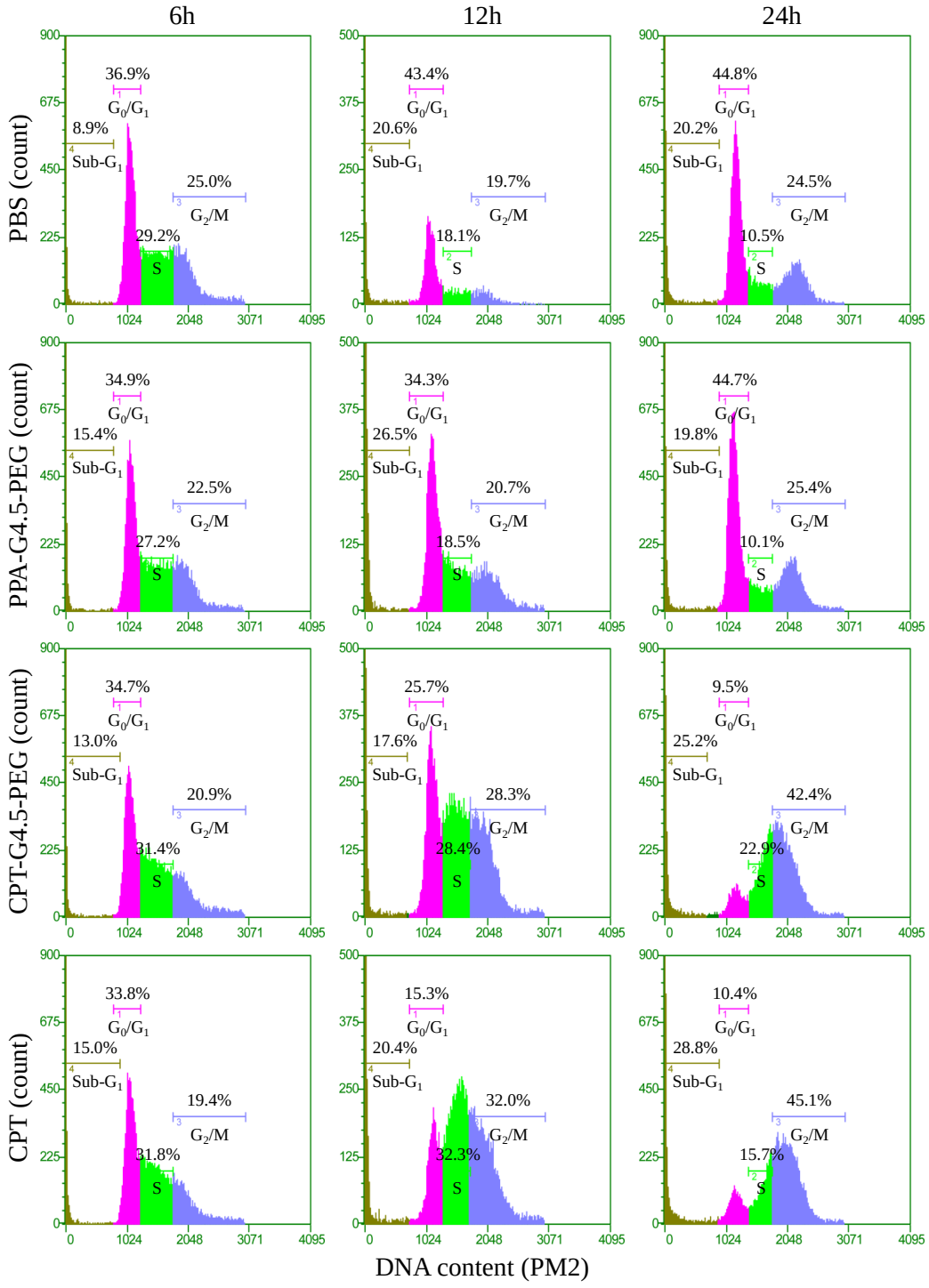

Figure 6.10: Cell cycle analysis.

U1242 cells were left untreated (control), CPT at the concentration of $2\times IC_{50free}$, conjugated CPT at the concentration of $2\times IC_{50cojugated}$, and PPA-G4.5-PEG conjugates at the equivalent concentration of CPT-G4.5-PEG conjugates for various lengths of time (6, 12, and 24 h).

Chapter 7

Click Hybridization of Immune Cells and Polyamidoamine Dendrimers

Preface: This chapter has been published as a research article.

Leyuan Xu, Olga Yu. Zolotarskaya, W. Andrew Yeudall, Hu Yang

Advanced Healthcare Materials: 2014; Volume 3, Issue 9, pages 1430-1438

7.1 Abstract

Immobilizing highly branched polyamidoamine (PAMAM) dendrimers to the cell surface represents an innovative method of enhancing cell surface loading capacity to deliver therapeutic and imaging agents. In this work, hybridized immune cells, that is, macrophage RAW264.7 (RAW), with PAMAM dendrimer G4.0 (DEN) on the basis of bioorthogonal chemistry are clicked. Efficient and selective cell surface immobilization of dendrimers is confirmed by confocal microscopy. Viability and motility of RAW-DEN hybrids remain the same as untreated RAW cells according to WST-1 assay and wound closure assay. Furthermore, Western blot analysis reveals that there are no significant alterations in the expression levels of signaling molecules AKT, p38, and NFκB (p65) and their corresponding activated (phosphorylated) forms in

RAW cells treated with azido sugar and dendrimer, indicating that the hybridization process neither induced cell stress response nor altered normal signaling pathways. Taken together, this work shows the feasibility of applying bioorthogonal chemistry to create cell-nanoparticle hybrids and demonstrates the noninvasiveness of this cell surface engineering approach.

7.2 Introduction

Immune cells such as monocytes and macrophages actively infiltrate the tumor mass in response to tumor invasion, recurrence, and metastasis or tumor hypoxia [61, 21]. Such cell types with their endogenous cancer-targeting and -attacking abilities are promising carriers to deliver therapeutics to the inner core of solid tumors, which is often inaccessible to standard modalities. A few early studies have demonstrated the use of macrophages as carriers to deliver anticancer genes and gold particles via phagocytosis [21, 77, 202, 35]. However, phagocytosis is not applicable to cell-based anticancer drug delivery. Anticancer drugs cannot be directly loaded into the cellular vehicle or loosely encapsulated on the cell surface because of the detrimental impact of their inherent toxicity on cell viability and functions. Resolution of this issue is critical to the realization of the potential of this therapeutic approach. Recently, we reported an innovative method of using macrophages as carriers by hybridizing them with polyamidoamine (PAMAM) dendrimers through cell surface modifications [92]. Dendrimers are well-fined highly branched macromolecules possessing a high density of surface groups [e.g., 64 primary amine groups for ethylenediamine (EDA) core PAMAM dendrimer G4.0] [261, 19]. As illustrated in Figure 7.1, anchoring dendrimer macromolecules at the cell surface would considerably expand cell surface loading capacity. This hybrid vector is envisioned to have several appealing characteristics. Because of the possession of a number of terminal groups by dendrimer, a high payload of anticancer drugs can be covalently conjugated to the cell surface without causing toxicity to the carrier cell as a result of avoidance of burst release. Highly adaptable structures of dendrimers are suitable for delivery of imaging reagents and

functional moieties that help with cancer treatment, diagnosis, or understanding of cellular behaviors in the context of tumorigenesis [8, 169, 170, 196, 337, 339]. In this way, nanoparticles become truly "stealth", sneaking past the body's immune system. Monocytes/macrophages themselves are native to the human body and take surface-anchored dendrimers to the therapeutically relevant tissue sites and this hybrid vector will serve as personalized medicine to treat individual patients, which may also result in enhanced therapeutic efficacy by making more anticancer drugs available to cancer cells or tumor mass.

In our previous approach, we chemically treated macrophages with sodium periodate to generate aldehyde groups on the cell surface and then made them react with amine-terminated PEG-dendrimers to form transient Schiff base linkages [92]. Further treatment with sodium cyanoborohydride converted the Schiff base linkages to stable amide linkages. This multistep chemical approach relies on existing sialic acids on the cell surface, which can be a potential limit for nanoparticle loading. To hybridize the surface of immune cells with dendrimers, it is critical to enhance cell-nanoparticle hybridization reaction efficiency and avoid extensive chemical modifications or damages to the cellular vehicle. Bioorthogonal chemistry developed by Bertozzi has emerged as a powerful tool for live cell surface labeling because of high efficiency and high selectivity [227, 240, 239, 25]. Strain-promoted azide-alkyne cycloaddition (SPAAC), commonly referred to as copper-free click chemistry, is the best known example. It has been shown that the copper-free click reaction proceeds within minutes on live cells with no apparent toxicity comparing to the copper-catalyzed reaction [13]. Furthermore, it minimally interferes with a biological system [240].

For the first time, we have applied this novel chemistry to develop an advanced nanosurface engineering method of creating cell-dendrimer hybrids. In this work, clickable dendrimers were synthesized by coupling dibenzocyclooctyne (DIBO) alkyne to PAMAM dendrimer G4.0 followed by FITC labeling. RAW264.7 macrophages (RAW) were cultured in the presence of azido sugar, in order to express azides on the cell surface. Azide-expressing macrophages were then hybridized with clickable dendrimers following SPAAC reaction. Localization of fluorescently-labeled dendrimers

following hybridization was determined using confocal microscopy. To ensure the preservation of cell viability and functions throughout the cell-nanoparticle hybridization process, the effects of the bioorthogonal chemistry-based hybridization process on biological functions of RAW cells were investigated. In particular, cell viability, motility, and key intracellular signaling pathways were examined.

7.3 Experimental Section

7.3.1 Materials

EDA core PAMAM dendrimer generation 4.0 (technical grade) was purchased from Dendritech (Midland, MI). *N*-hydroxysuccinimide (NHS), peracetylated *N*-azidoacetylmannosamine (Ac_4ManNAz), 1-ethyl-3-[3-dimethylaminopropyl] carbodiimide hydrochloride (EDC), *N*,*N*-diisopropylethylamine (DIPEA), Dimethyl sulfoxide (DMSO), and fluorescein isothiocyanate (FITC) were purchased from Sigma-Aldrich (St. Louis, MO). Click-IT succinimidyl ester DIBO alkyne (simply referred to as DIBO) was purchased from Life Technologies (Grand Island, NY). 4',6-diamidino-2-phenylindole (DAPI), sodium hydroxide, paraformaldehyde, and phosphate-buffered saline (PBS) were purchased from Fisher Scientific (Pittsburgh, PA). Cell proliferation reagent WST-1 was purchased from Roche Applied Science (Indianapolis, IN). NFκB p65, phospho-NFκB p65 (Ser536), p38 MAPK, phospho-p38 MAPK (Thr180/Tyr182), and phospho-Akt (Ser473) antibodies were purchased from Cell Signaling Technology (Danvers, MA). AKT1 (559028) antibody was purchased from BD Biosciences Pharmingen (Mississauga, ON, Canada). β-actin (ACTBD11B7) antibody was purchased from Santa Cruz Biotechnology (Santa Cruz, CA). Goat anti-rabbit antibody conjugated to horseradish peroxidase and goat anti-mouse antibody conjugated to horseradish peroxidase were purchased from Bio-Rad (Hercules, CA).

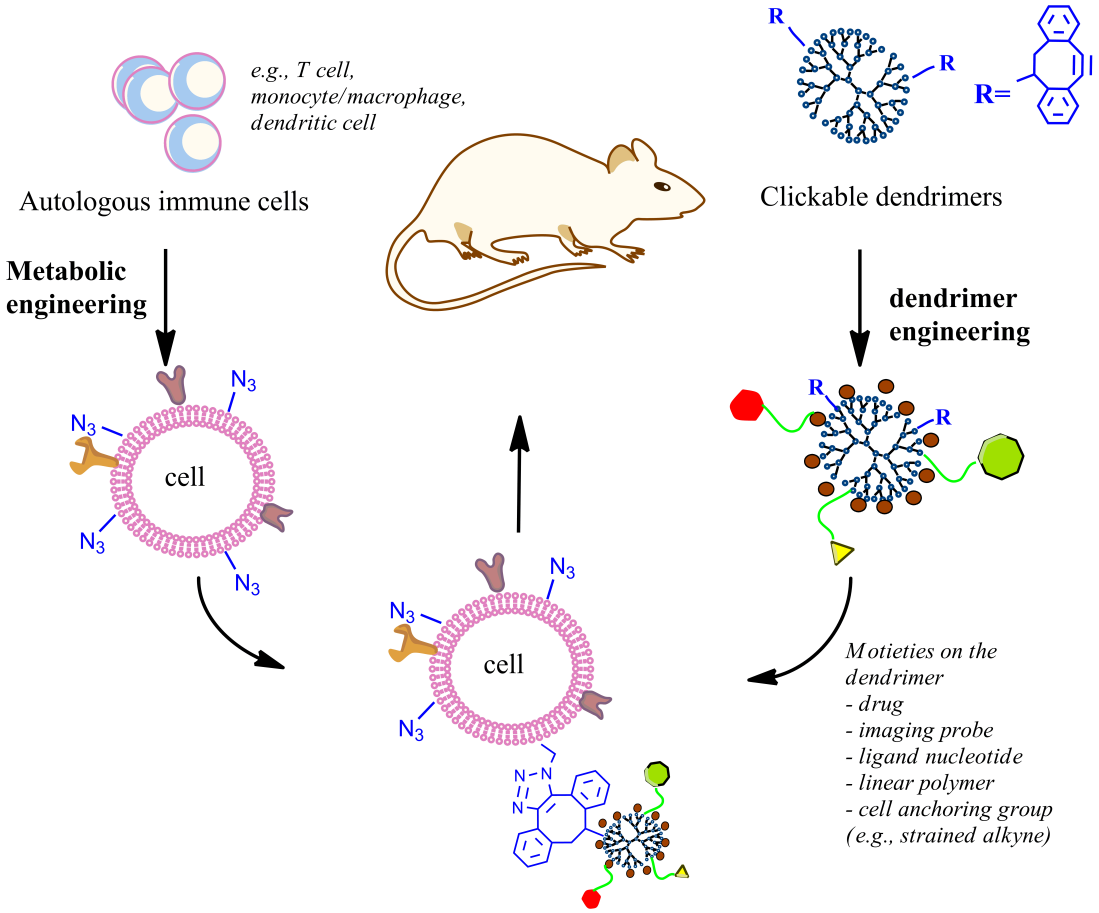

Figure 7.1: Immune cell-nanoparticle hybrid vector represents a novel platform for delivery of therapeutic and imaging reagents through cell surface modification.
Immune cells are removed from the animal, and azides are metabolically introduced into cell-surface glycans. Polyamidoamine (PAMAM) dendrimer undergoes a series of surface functionalization chemistries to possess strain-promoted alkyne, drug, imaging agent, and other moieties of interest. Azide-expressing cells are then incubated with functionalized clickable dendrimers to form cell-nanoparticle hybrids following a highly efficient selective bioorthogonal reaction, namely strain-promoted azide-alkyne cycloaddition in water under physiological conditions without using any additional reagents. Following ex vivo cell surface engineering, the hybrid vehicles are injected back to the same animal for therapeutic and/or diagnostic treatment.

7.3.2 Cell Culture

RAW264.7 (RAW), a mouse monocyte/macrophage cell line (purchased from ATCC, Manassas, VA), was used in this work. RAW cells were cultured in Dulbecco's modification of Eagle's medium (DMEM) (Life Technologies, Grand Island, NY) containing high glucose and supplemented with $_L$-glutamine, 10% (v/v) fetal bovine serum (FBS) (Fisher Scientific, Pittsburgh, PA), 100 units mL^{-1} of penicillin, and 100 μg mL^{-1} of streptomycin (both from Thermo Fisher Scientific, Ashville, NC) at 37 °C in a humid environment with 5% CO_2 [144].

7.3.3 Synthesis of Clickable PAMAM Dendrimers

As illustrated in Figure 7.2, the synthesis is a one-step reaction. Briefly, following removal of methanol from the stock solution, PAMAM dendrimer G4.0 (0.135 μmol, 1 equiv.) was dissolved in DMSO (300 μL) and then mixed with DIPEA (30 equiv.). DIBO (5 equiv.) was dissolved in DMSO (100 μL) and then added, dropwise, into the dendrimer solution while stirring. The reaction proceeded at room temperature overnight followed by removal of DMSO under vacuum.

7.3.4 FITC Labeling

FITC as a fluorescent probe (green) was used for dendrimer labeling. FITC was dissolved in DMSO and then added, dropwise, to DMSO solution of dendrimer (G4.0-DIBO or G4.0) in the presence of DIPEA, in which the molar ratio of DIPEA:FITC:dendrimer was 30:5:1. The reaction mixture was stirred overnight in the dark, followed by removal of DMSO under vacuum.

7.3.5 General Click Cell-Dendrimer Hybridization Procedures

Prior to surface treatment, azides were metabolically introduced to the surface of RAW cells by incubating RAW cells in culture medium containing azido sugar Ac_4ManNAz (50×10^{-6} M) for 2 d. The resulting RAW cells expressing azides on the surface

(i.e., RAW-N3 cells) were washed three times with pH 7.4 PBS. RAW-N3 cells were then treated with G4.0(FITC)-DIBO (25×10^{-6} M) (1:100 dilution in PBS from a 2.5 $\times$ 10^{-3} M dendrimer DMSO solution) for 10 min at room temperature to hybridize RAW-N3 cells with clickable dendrimer following copper-free click reaction on the cell surface. The resultant RAW-DEN hybrids were washed with PBS three times and subjected to the various assays described below. For comparison, hybridization between RAW cell and dendrimer devoid of complementarily reactive azide, DIBO, or both, was conducted under the same conditions as for RAW-DEN hybridization (i.e., RAW-N3/G4.0(FITC), RAW/G4.0(FITC), and RAW/G4.0(FITC)-DIBO), and the resulting treatment groups were investigated along with RAW-DEN hybrids.

7.3.6 Confocal Microscopy

To study uptake and localization of dendrimer nanoparticles, following the treatments described above, RAW cells were fixed with 4% paraformaldehyde immediately and nuclei were counterstained with DAPI (blue). The fixed cells were imaged under a Zeiss LSM 700 confocal laser scanning microscope using a magnification of 630×. Images were analyzed using ImageJ [229].

7.3.7 Cell Viability Assessment

Immediately following treatment, cell viability of five groups - RAW(control), RAW-DEN, RAW-N3, RAW/G4.0(FITC)-DIBO, RAW-N3/G4.0(FITC) - was determined by WST-1 cell proliferation assay following the manufacturer's protocol. The relative cell viability was normalized with respect to the viability of the control group. Briefly, the cells were incubated with WST-1 reagent (10 μL) in the cell culture media (100 μL) for 30 min. The absorbance of each sample solution was then measured at 450 nm against a background control as blank. The wavelength of 650 nm was used as the reference wavelength.

7.3.8 Western Blot Analysis

To examine whether or not key cellular signaling pathways in RAW cells might be affected by azido sugar culture and G4.0(FITC)-DIBO treatment, Western blot analysis of total cellular protein in RAW-N3 and RAW-DEN cellular vehicles was carried out following procedures described previously [292]. Briefly, total cell lysates (30 μg of protein) were separated on a 10% SDS-PAGE gel and transferred onto a polyvinylidene difluoride (PVDF) membrane. The membrane was blocked for 2 h in Tris-buffered saline (TBS) containing 5% non-fat dry milk. The specific proteins on the membrane were determined by incubation with primary antibodies overnight at 4 °C with shaking. After washing in TBS containing 0.5% Tween 20, the membrane was incubated in a 1:3000 dilution of appropriate secondary antibody at room temperature for 1 h in wash buffer. The specific antigen-antibody interactions were detected using enhanced chemiluminescence (Pierce ECL Western Blotting Substrate) (Thermo Scientific, Rockford, IL). β-actin was used as a loading control.

7.3.9 Wound Closure Assay

Motility of cellular vehicles (i.e., RAW, RAW-N3, and RAW-DEN, three wells for each type of cellular vehicle) was assessed using wound-closure (scratch) assays. Briefly, RAW cells were plated in 12-well cell culture plates. When the cells reached 80% confluence, the cell culture medium was replaced with fresh culture medium either containing 50×10^{-6} M $Ac_4ManNAz$ or free of azido sugar. When the cells reached 100% confluence, one group of RAW cells (three wells) fed with azido sugar was further treated with G4.0-DIBO (25×10^{-6} M) in PBS for 10 min to generate RAW-DEN hybrids. The fully confluent cells were washed three times with PBS. A sterile pipette tip was then used to denude the surface of each well. Following complete removal of the cells within the scratch area, each well was washed three times with PBS and then replaced with fresh cell culture medium. The width of the scratch was measured at three different points using a light microscope and AxioVision software (Carl Zeiss Microimaging, Thornwood, NY). Following 20-h culture at 37 °C, the scratch width

was measured again at the same positions. Cell migration rate was calculated as follows: Motility = ($\text{Width}_{average,0h}$ - $\text{Width}_{average,20h}$) / 20h [313].

7.3.10 Statistical Analysis

All the data were expressed as mean ± standard deviation (SD) and subjected to one way analysis of variance (ANOVA) followed by Student t-test for unpaired samples. A value of $p < 0.05$ was considered as statistically significant.

7.4 Results

7.4.1 Bioorthogonal Chemistry-Based Cell-Nanoparticle Hybridization

Our new bioorthogonal chemistry-based cellnanoparticle hybridization approach involves two steps: 1) metabolic incorporation of azido sugars into the cell surface with peracetylated N-azidoacetylmannosamine (Ac_4ManNAz, 50×10^{-6} M) for 48 h, and 2) copper-free click reaction on the cell surface in the presence of clickable dendrimers (Figure 7.2). Different from our previous approach using anionic carboxylate-terminated PAMAM dendrimer [92], we used cationic amine-terminated PAMAM dendrimer G4.0 as a model to investigate the hybridization efficiency and to explore the adaptability of dendrimers used for cell-dendrimer hybridization because both types of PAMAM dendrimers have been commonly utilized in drug and gene delivery applications [337, 207, 238, 146, 112, 320, 319]. To this end, a different synthetic route has been developed to apply bioorthogonal chemistry for cell-nanoparticle hybridization. In particular, succinimidyl ester DIBO alkyne (DIBO) was coupled to amine-terminated PAMAM dendrimer G4.0 to make clickable dendrimers. The resultant G4.0-DIBO conjugates were further labeled with FITC to allow fluorescent imaging for localization of nanoparticles. Except for the untreated cells (control), the other three groups were incubated with equimolar amounts of FITC.

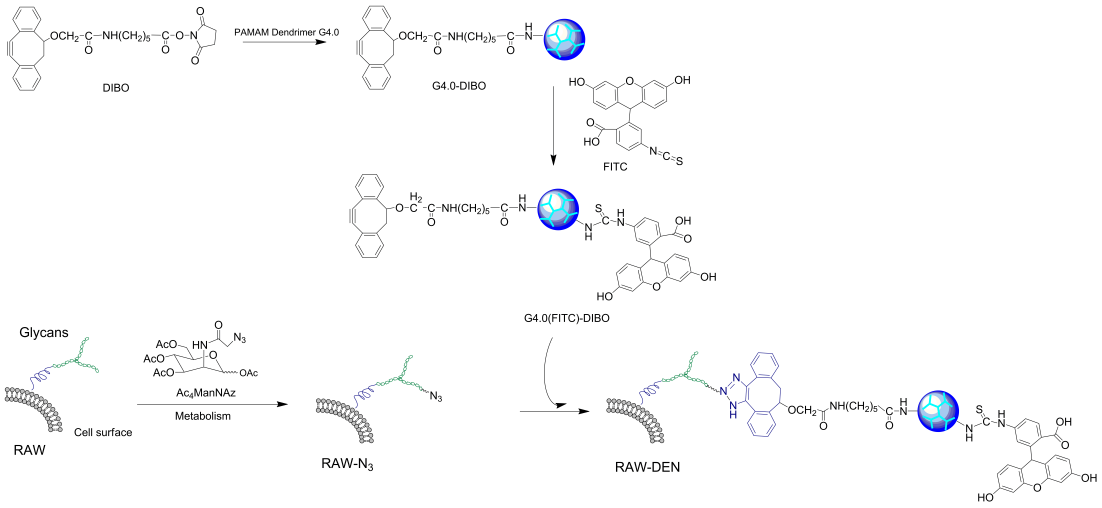

Figure 7.2: Schematic for hybridization of PAMAM dendrimer and macrophage through bioorthogonal chemistry.

As expected, untreated RAW cells lack the fluorescent label, whereas RAW cells treated with FITC show uniform distribution of fluorescence inside the cell due to nonspecific uptake (Figure 7.3a). FITC labeled PAMAM dendrimer G4.0 was found to be taken up more prominently by RAW-N3 cells and accumulated primarily in the cytoplasm. This observation was attributed to a high density of cationic charges on the dendrimer surface responsible for promoting nonspecific cellular uptake of FITC-labeled dendrimer. There was no obvious accumulation of dendrimers on the cell surface. Although RAW-N3 cells present azide groups on the surface, the click reaction did not take place because the dendrimer did not possess complementarily reactive alkynes on the surface. In contrast, a significant increase in fluorescence intensity was observed on the surface of the RAW-N3 cells following incubation with G4.0(FITC)-DIBO, indicating successful hybridization of dendrimer nanoparticles with the cell surface (Figure 7.3b). Significant reduction in uptake of the nanoparticles into the cell reaffirms the efficiency of bioorthogonal chemistry.

It is critical to ensure that RAW cells are minimally affected by the hybridization process. Therefore, cell morphology was monitored throughout the process. No abnormal morphological cell changes were observed. Some RAW-DEN cells undergoing mitosis were observed, suggesting a normal cell cycle. Detailed examination of

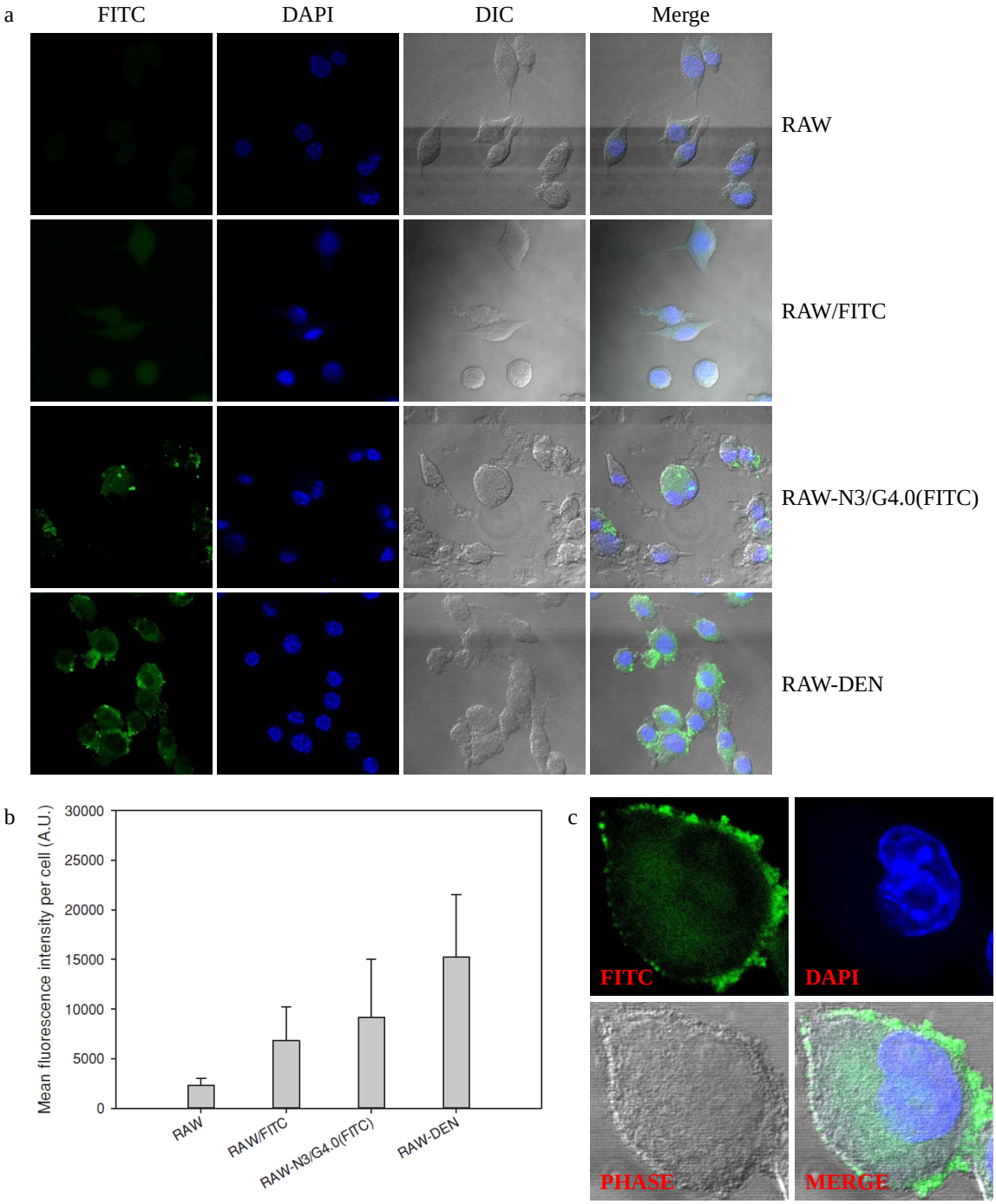

Figure 7.3: Hybridization of PAMAM dendrimer and macrophage through bioorthogonal chemistry and confirmation by confocal microscopy.
a) Colocalization assay of FITC-labeled G4.0 (green) with nuclei (blue) by confocal microscopy following different surface treatments. b) Quantitative analysis of cell fluorescence intensities using ImageJ. c) Representative confocal images of a single RAW-DEN cell. (Original magnification: 630×.)

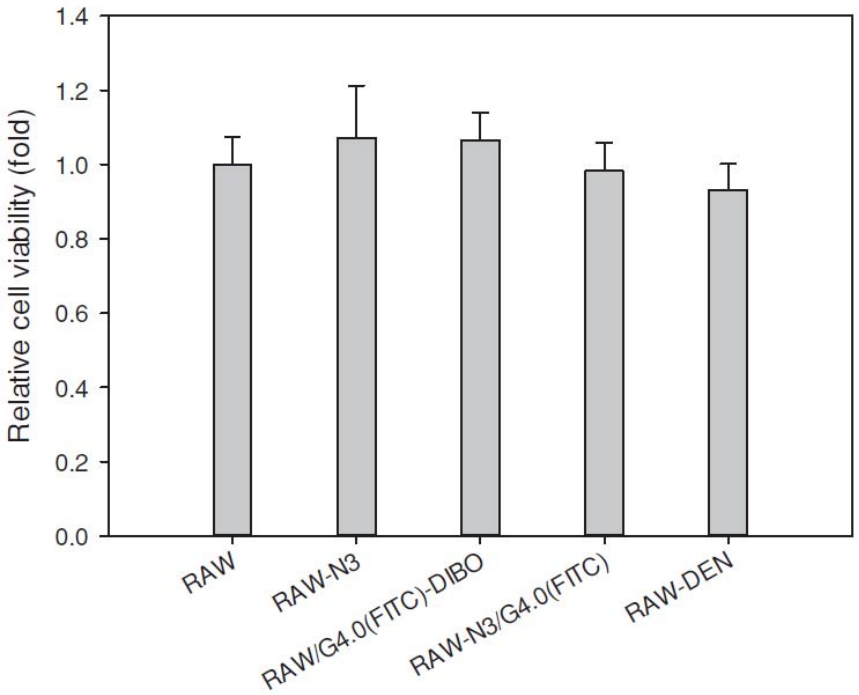

Figure 7.4: Cell viability of RAW cells following various treatments as determined by WST-1 cell proliferation assay following the manufacturer's protocol.
The relative cell viability was normalized with respect to the viability of the control group. The data are expressed as mean ± SD. No statistically significant difference was noted for comparisons between subgroups.

single hybrid cells (Figure 7.3c) clearly illustrates that the fluorescence is mainly localized on the cell surface as opposed to in the cytoplasm for those dendrimer particles uptaken by cells via endocytosis [183]. The heterogeneity of a dendrimer-immobilized cell surface reflects the distribution of azide groups that were metabolically integrated into the cell surface. RAW cells maintained good viability throughout the process, as shown in Figure 7.4. The doses of azido sugar and dendrimers used in the hybridization process had negligible toxicity effects on the cells.

7.4.2 Intracellular Signaling Pathways in the Hybrid Cell Vehicles

Cells utilize signaling pathways to regulate their biological functions as well as their interactions with the microenvironment. Common stress-activated signaling pathways include nuclear factor (NF)κB (p65), p38 mitogen-activated protein kinases (MAPKs), and AKT. In this work, we primarily examined whether or not these signaling pathways had been altered by the hybridization process. As judged by Western blot analysis, expression levels of AKT, p65, and p38 in RAW cells were similar before and after 48 h culture in the presence of Ac 4 ManNAz at various concentrations up to 50×10^{-6} M (Figure 7.5a,b). The levels of the phosphorylated forms of these key signaling molecules were also unchanged, indicating that azido sugar likely had not altered the signaling pathways involving AKT, p65, and p38. Consistent with the cytotoxicity assay, azido sugar is biocompatible with RAW cells.

The second step in the cell-nanoparticle hybridization process is to anchor polycationic PAMAM dendrimers at the cell surface. Inherent phagocytosis of macrophages and the cationic surface of dendrimers would be expected to enable entry of dendrimers into the cell, although bioorthogonal chemistry employed in this work has greatly reduced inadvertent dendrimer uptake by RAW cells. PAMAM dendrimers show doseand generation-dependent toxicity [307, 309]. The dendrimer concentrations used for cell-nanoparticle hybridization did not cause a decrease in cell viability. However, the effects of amine-terminated PAMAM dendrimers on intracellular signaling pathways are unknown. Therefore, we evaluated intracellular AKT, p65, and p38 signaling pathways in RAW cells following 10-min treatment of PAMAM dendrimer G4.0 at various concentrations up to 100×10^{-3} M.

The Western blot results showed that the acute exposure of PAMAM dendrimer G4.0 to RAW cells did not alter intracellular p65 and p38 signaling pathways (Figure 7.5c,d), indicating that no acute stress in RAW cells was induced by PAMAM dendrimer G4.0. Furthermore, normal activation of intracellular AKT was preserved although there was a minimal decrease in AKT and p-AKT levels, suggesting that

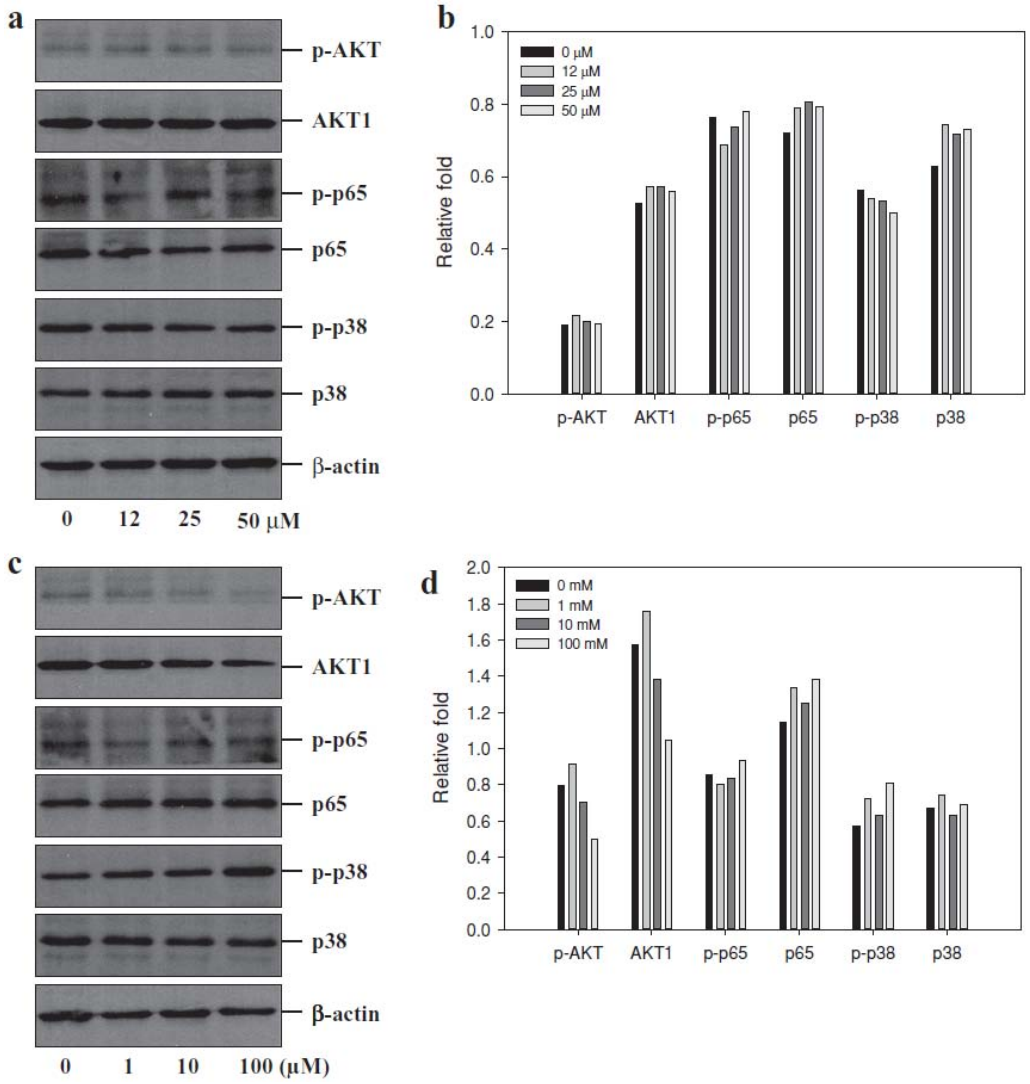

Figure 7.5: Biological effects of azido sugar and PAMAM dendrimers on intracellular signaling pathways in RAW cells during the hybridization process.

Western blot analysis and quantitative densitometry of signaling molecules AKT, p65 (NFκB), p38 MAPK, and their corresponding phosphorylated forms: a,b) in RAW cells treated with Ac_4ManNAz for 48 h at the indicated concentrations and c,d) in RAW cells treated with PAMAM dendrimer G4.0 for 10 min at the indicated concentrations.

the macrophages were able to survive and retain proliferative capacity, consistent with the results of viability assays. These observations are also consistent with the previous reports that dendrimers are biocompatible at relatively low concentrations and over a short exposure time [50, 108].

7.4.3 Assessment of Cell Motility

RAW cells are adherent cells. Assessment of their migration speed allows one to evaluate whether the bioorthogonal reaction at the cell surface causes loss of cell motility. To this end, we performed a 2D wound closure assay. We first introduced a "wound" by denuding confluent monolayers of RAW cells with a pipette tip, and determined their motility over 20 h (Figure 7.6a). As summarized in Figure 7.6b, untreated RAW cells migrated at a mean rate of 7.2 μm h^{-1}. The mean migration rates were 6.3 and 6.9 μm h^{-1} for RAW-N3 and RAW-DEN hybrids, respectively. No significant difference was observed between the control group and the surface-modified RAW cells. These results confirm that surface modification of macrophages via copper free click chemistry does not reduce cell motility.

7.5 Discussion

There are many advantages about nanoparticle-based anticancer drug delivery. The composition, shape, size, charge, and morphology of nanoparticles can be finely tuned to achieve some desirable pharmacokinetic and pharmacodynamic profiles for a drug such as prolonged release, reduced systemic toxicity, and tumor-specific efficacy [71, 60, 139]. However, this approach has two major limitations. First, because of heterogeneities of vascular permeability and the complex microenvironment of cancer biology, delivery of drug-carrying nanoparticles even including those decorated with tumor-specific ligand relies heavily on passive mechanisms such as the enhanced permeability and retention (EPR) effect. Second, only a small percentage of the injected drug can fi nally accumulate in the tumor with the aid of nanoparticles, in large part,

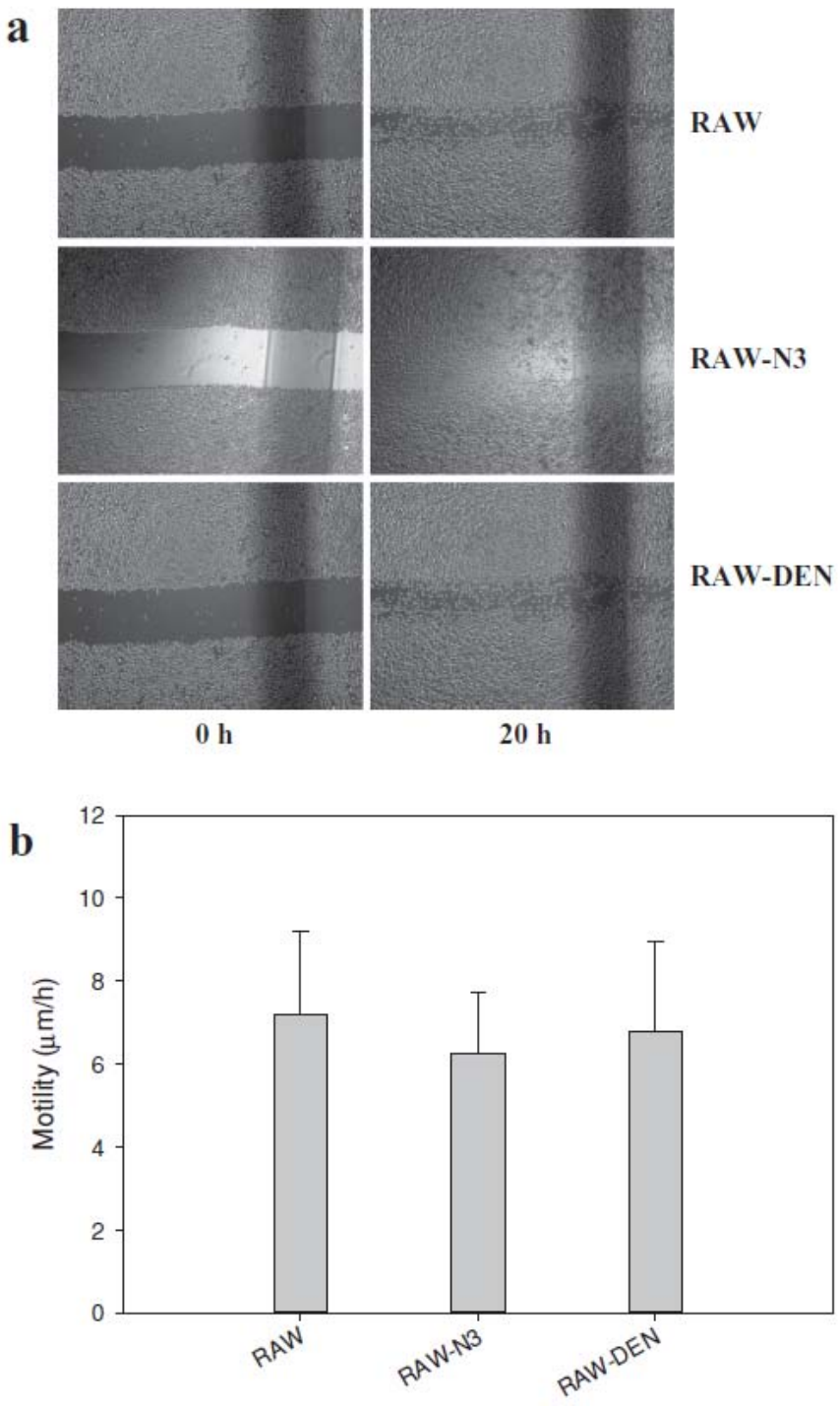

Figure 7.6: Wound closure assay to assess the motility of RAW cells following different treatments.
a) After RAW cells 100% confluence, the cell monolayer was denuded. The distance across the denuded area was measured at 0 h and at 20 h (original magnification: 50×). b) Motility is presented as mean ± SD (n = 18). Data are representative of experiments conducted on three independent occasions.

due to rapid clearance by immune cells in the liver and spleen, which is commonly known as the mononuclear phagocytic system (MPS). Immune cells including T cells and macrophages have been explored as drug carriers for cancer therapy because of their endogenous cancer-targeting or -attacking abilities. Unfortunately, loading therapeutic components into the cell via phagocytosis is the primary means for drug delivery [21, 77, 202, 35]. Covalently conjugating drug-loaded particles to the surface of immune cell such as T cell has emerged as an appealing method for cancer immunotherapy [247]. The highly localized drug on the cell surface can continuously and directly exert pseudoautocrine stimulation of transferred cells in vivo and avoid its systemic toxicity [247]. Nonetheless, none of the approaches mentioned above is applicable to cell-based anticancer drug delivery.

We proposed a new concept to take advantages of the best aspects of both types for anticancer drug delivery. Using the macrophage surface to covalently deliver anticancer drugs would prevent phagocytosis of those inherently toxic therapeutic agents, thus avoiding significant loss of cell viability and functions such as motility. High payloads of functional moieties such as drugs and fluorescent probes at cell surfaces can be achieved by virtue of the high loading capacity of dendrimers [158, 53]. Although various techniques have been developed to engineer cell surfaces [63, 244, 116, 23, 41], coupling nanoparticles such as dendrimers [92] and lipid-coated PLGA nanoparticles [247] to the cell surface represents a new way of utilizing cell surfaces, thus generating a great need to develop efficient chemistries for cell surface modifications to avoid inadvertent particle uptake by the cell and minimize cell function loss. Recently, a series of bioorthogonal reactions has been developed based on the Staudinger ligation and SPAAC [240]. SPAAC reactions employ cyclooctynes to boost click reactions in the absence of copper catalyst [37, 76, 110, 241], a source of toxicity in copper-catalyzed alkyne-azide cycloaddition (CuAAC) due to production of copper-induced reactive oxygen species (ROS) [240, 94]. Therefore, bioorthogonal chemistry, which has been acclaimed as a safe and noninvasive method to probe molecules in cells and live organisms [13, 43, 137, 138], has great potential for live cell surface modification with dendrimers.

An essential criterion for developing a clinically acceptable cell surface engineering protocol is to maintain cell viability and functions [246]. We examined the biological functions of the cellular vehicle via analysis of several key signaling molecules based on the following justification. p65 is a key mediator of inducible transcription in the innate immune system. It plays a central role in regulating cellular responses to a variety of stimuli, such as stress, cytokines, free radicals, ultraviolet irradiation, inflammation, and infection [83]. p38 MAPKs are a class of mitogen-activated protein kinases responding to stress stimuli, such as cytokines, ultraviolet irradiation, heat shock, and osmotic shock, and also play important roles in cell differentiation, apoptosis, and immune response [38]. As reported, p38 can be rapidly phosphorylated in response to lipopolysaccharide (LPS) stimulation, resulting in the production of proinflammatory cytokines such as interleukin-1 (IL-1) and tumor necrosis factor-α (TNF-α) [44]. AKT, also known as protein kinase B, is a serine/threonine-specific protein kinase that is involved in metastatic pathways and survival signaling pathways. Activation of AKT kinase may cause cell detachment, proliferation, invasion, angiogenesis, and protection against apoptosis [233].

We provided evidence to prove the proof-of-concept of click hybridizing macrophages with dendrimers and its noninvasiveness to the engineered cells [246]. It is also important to evaluate cell surface stability of dendrimers following copper free click chemistry and study potential effects of the factors including cell type, immobilized molecules, and immobilization technique on the fate of cell surface-immobilized moieties (i.e., dendrimers). In addition to these factors, dynamic intracellular dendrimer distribution and additional parameters including particle size, surface charge, particle geometry, cell type, cell membrane turnover, hybridization conditions (e.g., surface densities of azide and dendrimer concentrations) may affect dendrimer stability. Those factors will be investigated systematically in future work to gain insight into the cell surface engineering optimization for achieving targeted durability for cell surface-immobilized dendrimers. Future work also includes in vivo validation of macrophage homing following hybridization and assessment of therapeutic and diagnostic functions of the cell-dendrimer hybrids. Drugs or imaging probes can be

covalently conjugated to or complexed with the dendrimer prior to cell-dendrimer hybridization. The linkages between dendrimer and cell and the linkages between drug/imaging probe and dendrimer can be engineered to be cleavable in response to external stimuli such as pH or enzymes or be stable. We envision that the whole hybrid system is modular and capable of controlled drug release using molecular engineering approaches.

7.6 Conclusions

PAMAM dendrimer G4.0 was successfully immobilized to the RAW cell surface via bioorthogonal chemistry and confirmed by confocal microscopy. Both azido sugar and PAMAM dendrimer G4.0 are cytocompatible under the conditions used for cell-nanoparticle hybridization. The viability, intracellular signaling pathways, and motility of RAW cells remained unaltered. Although internalization of nanoparticles by macrophages seems to be an inevitable process because of their innate phagocytic capability, the application of bioorthogonal chemistry provides an efficient noninvasive method for cell surface modification and hybridization with nanoparticles, and it has greatly reduced the intracellular uptake of nanoparticles during the hybridization process.

Chapter 8

Summary and Future Directions

8.1 Summary

The background and significance of head and neck squamous cell carcinomas (HNSCC) have been reviewed in Chapter 1. HNSCC remains the sixth most prevalent cancers in mankind, and presents high morbidity and low rates of survival in the US [22]. Treatment of HNSCC frequently requires multi-modality intervention involving surgical, medical, and radiation oncology. Because surgery may cause disfigurement, concurrent chemotherapy and radiation is more patient compliant, but it also leads to more severe toxicity. Currently, most chemotherapeutics are small-molecular-weight drugs that target intracellular proteins, enzymes, and DNA. The anticancer drugs that block DNA replication and cell division have severe side effects due to non-specific uptake of normal cells. The anticancer drugs that target intracellular signal intermediates develop acquired drug resistance. The anticancer gene therapy that is precisely tailored to the gene structure of each tumor is obstructed from the cells because of the nature of these materials [20]. Although discovery and development of new cytotoxic agents for cancer chemotherapy remains a key focus, modification of existing anticancer drugs to improve their specificity and potency is also an important approach for anticancer chemotherapy.

Dendrimers possess numerous advantages including maintaining drug levels in a therapeutically desirable range, increased half-lives, increased solubility, stability

and permeability of drugs, capable to deliver a variety of drugs, reduced macrophage uptake, targeting ability, facile passage across biological barriers by transcytosis, rapid cellular entry, improved delivery efficiency, and reduced side effects by targeted delivery. All these advantages lead dendrimers to advance for anticancer drug delivery. Besides, polycationic dendrimers, bearing primary amines on the surface, have been shown great potential for gene transfection and cancer gene therapy, which have been discussed in Chapter 2.

Literature documents that folate receptors (FRs) are highly expressed in numerous cancers, including HNSCC, in order to meet the folate demand of rapidly dividing cells under low folate conditions. In the last decade, numerous formulations of FA-decorated nanoparticles have been developed for anticancer drug delivery and diagnosis, which have been reviewed in Chapter 3. Therefore, our aim was to engineer a folate acid (FA)-decorated dendrimer for HNSCC gene delivery and potential gene therapy. We chose HN12 cells as our model cell line because HN12 cells were derived from a primary synchronous lymph node metastasis that is a clinically relevant HNSCC cell line. In Chapter 4, a FA-conjugated polyamidoamine (PAMAM) dendrimer generation 4 (G4-FA) conjugate was successfully synthesized. Fluorescein isothiocyanate (FITC) was conjugated onto G4-FA conjugate for in vitro trafficking. G4-FA conjugate or G4 dendrimer was complexed with plasmid to form G4-FA/plasmid and G4/plasmid polyplexes. Our results strongly indicate that G4-FA conjugate and G4-FA/plasmid polyplex are taken up by HN12 cells through receptor-mediated endocytosis; whereas G4 dendrimer and G4/plasmid polyplex are taken up by HN12 cells through absorptive-mediated endocytosis triggered by electrostatic interaction. Because of the different cellular uptake mechanisms, G4-FA/plasmid polyplex displayed targeting capability, increased cytocompatibility, and enhanced transfection efficiency in HN12 cell, compared with G4/polyplex. In Chapter 5, near infrared fluorescence dye (NIR) was conjugated onto G4-FA conjugate for biodistribution imaging. G4-FA conjugate or G4 dendrimer was complexed with siRNA against vascular endothelial growth factor (siVEGFA) to form G4-FA/siVEGFA and G4/siVEGFA polyplexes. Our results showed that NIR-G4-FA and NIR-G4 conjugates could retain in the tu-

mor region at least 21 days after intratumoral (i.t.) administration in the HN12 tumor-bearing mice. However, NIR-G4-FA conjugate exhibited higher tumor uptake than NIR-G4 conjugate. Single-dose i.t. injection of G4-FA/siVEGFA polyplexes delayed tumor growth rate by 4 day, and two-dose intratumoral (i.t.) injection of G4-FA/siVEGFA polyplexes significantly inhibited tumor growth, by lowering angiogenesis in the tumor microenvironment, in HN12 tumor-bearing mice.

Besides gene transfection and gene delivery, we also explored the potential of using dendrimers for anticancer drug delivery. In Chapter 6, a new camptothecin (CPT)-carrying anionic PAMAM dendrimer generation 4.5 (G4.5) drug delivery system was designed for anticancer chemotherapy. Click chemistry was employed in this approach to improve polymer-drug coupling reaction efficiency. CPT was conjugated onto a PEGylated G4.5 dendrimer to form a CPT-G4.5-PEG conjugate via an ester linkage, which allows a controlled release. Our results showed the IC_{50} of CPT-G4.5-PEG conjugate increased 185 folds in comparison to that of free CPT as a result of slow release. The released CPT could induce an arrest in G2/M of cell cycle, which leads to apoptosis in HN12 cells.

Macrophages actively infiltrate the tumor mass in response to tumor invasion, recurrence, and metastasis or tumor hypoxia. In chapter 7, we hybridized macrophage with PAMAM dendrimer generation 4, as a potential alternative strategy for anticancer drug and gene delivery. The macrophage-dendrimer hybrids were formed based on bioorthogonal reaction, referred to as strain-promoted azide-alkyne cycloaddition. Our results strongly indicate dendrimer can be successfully immobilized onto macrophage surface, which has no impact on the intracellular signaling, such as AKT, p65, and p38, cell viability, and cell motility.

8.2 Discussion

8.2.1 G4-FA conjugate formulation for targeted gene delivery

In Chapter 4 and 5, we engineered a simplest PAMAM dendrimer-FA conjugates by direct coupling. We have shown a consistent successful synthesis and purification of G4-FA conjugates from batch to batch. From in vitro gene transfection aspect, G4-FA conjugates possess high cytocompatibility and excellent gene transfection efficiency in FR-positive cells. Although dendrimers have been extensively investigated for gene delivery, it is interesting to compare our findings to the others. It has been reported that surface modification of PAMAM dendrimers with triazine [282], hyaluronic acid (HA) [266], fluorobenzoic acid (FBA) [275], RRRK peptide from mouse fibroblast growth factor 3 [141], aminoglycoside (paromomycin and neomycin) [68], lysine (Lys) [278], arginine (Arg), phenylalanine (Phe), and histidine (His) [270] all showed an increased cytocompatibility and enhanced transfection efficiency in vitro. Triazine is a capable of binding DNA through complementary hydrogen bonds [282]. HA is a ubiquitous glycosaminoglycan (GAG) found in the extracellular matrix. HA is to interact electrostatically, shield surface charge, function as a targeting agent, improve biodistribution, and lower cytotoxicity [266]. Fluorinated molecules tend to assemble into a hydrophobic and lipophobic fluorous phase which can improve cellular uptake and endosomal escape [275]. RRRK peptide is to induce nuclear localization [141]. Aminoglycosides is to enhance cellular uptake due to their natural affinity for nucleic acids [68]. Lys is to enhance the electrostatic interaction with DNA molecules [278]. Arg is to stabilize complexes, Phe is to improve cellular uptake efficacy, and His is to increase buffering capacity and minimizes cytotoxicity of the cationic dendrimer [270]. Most of these approaches were aimed to employ positive charged natural materials to enhance cytocompatibility of PAMAM dendrimer without compromising electrostatic interaction with genetic materials. These approaches showed great potentials in general gene transfection compared to commercial available transfection reagents,

but they do not possess targeting capability. Our previous work showed that epidermal growth factor (EGF) conjugated PAMAM dendrimer G4 via a triglycine spacer can enhance gene transfection efficiency without activating epidermal growth factor receptor (EGFR) signaling. This approach is aimed to enhance cellular uptake by targeting EGFR in EGFR-overexpressing cells. Similarly, our current approach is aimed to enhance cellular uptake by targeting FR in FR-overexpressing cell, such as cancer cells. The co-culture experiment strongly indicates G4-FA/plasmid conjugates can be selectively and preferentially taken up in FR-positive cells. The cytocompatibility of G4-FA/plasmid polyplexes can be significantly improved by limiting uptake of polyplexes from saturating FR on the cell membrane. All these formulations showed great potential for in vitro gene transfection, but the transfection mechanism of G4-FA conjugates is different from those of surface modified dendrimers mentioned above. Any combination of these approaches may be interesting for future investigation.

From our literature search, most FR-targeting dendrimer delivery systems are investigated to actively deliver small molecular weight drugs and contrast agents, such as methotrexate [128, 180, 331], paclitaxel [169, 26], doxorubicin [186, 325], camptothecin [58, 258], fluorescence resonance energy transfer (FRET)-based substrates [181], but very few are designed for gene delivery. Both G3-PEG-FA conjugated with -cyclodextrin (Fol-PC) and FA-PEG-chitosan complexed with G4 (FPCPHD) nanoparticles were developed to enhance gene transfection in vitro and gene delivery in vivo [7, 276]. Plasmid pRL-CMV-Luc vector encoding Renilla luciferase and plasmid pDsRed-M-N1 vector encoding red fluorescence protein were employed in either of these two investigations. Noteworthy is that Fol-PC and FPCPHD can significantly enhance gene transfection in the tumor after i.t. and i.v. administration, respectively, in the KB tumor-bearing mice. Compared to these two formulations, FA-decorated dendrimer-based formulations for in vivo siRNA delivery has not been investigated. Although DNA plasmid and siRNA possess similar the number of phosphate and zeta potential per each base pair, but their geometry and size are significantly different. Plasmid is a circular, double-stranded DNA molecule; whereas siRNA is a linear, double-stranded RNA molecule. The size of a plasmid varies from 1,000 to 20,000

base pairs; whereas the size of an siRNA is 20-25 base pairs in length. This significant difference in size can impact on the shape of resultant dendrimer/gene polyplexes, which may further influence on cellular uptake and transfection efficiency. To this end, a comprehensive evaluation is needed to justify this assumption. Our current investigation shows that G4-FA conjugates can enhance gene silencing efficiency in vitro and siRNA delivery in vivo (Chapter 5). To further validate the FR-targeted gene delivery of our G4-FA formulation, we can complex G4-FA conjugates with plasmid vector encoding luciferase or fluorescence protein to form G4-FA/pDNA polyplexes, and evaluate the reporter gene expression in the tumor after i.t. administration in HN12 tumor-bearing mice. In addition, we can complex G4-FA conjugates with a plasmid encoding small heparin (sh)RNA against VEGFA (shVEGFA), and evaluate the therapeutic outcome after i.t. administration in HN12 tumor-bearing mice. By comparing the therapeutic outcome of G4-FA/siVEGFA and G4-FA/shVEGFA polyplexes, we may determine the G4-FA conjugate formulation is suitable for siRNA or DNA plasmid delivery.

On the other hand, our preliminary results indicate G4-FA conjugate formulation is not suitable for i.v. administration, because the rapid uptake and clearance from liver, kidney, and spleen. It has been reported that lower generation dendrimer are subjected to rapid renal clearance and surface charged (cationic and anionic) or hydrophobic dendrimers are subjected to rapid hepatic clearance [50]. PEGylation can prolong circulation time, allow for tumor-targeting, and minimize non-specific uptake from liver, kidney, and spleen [267]. However, PEGylation may compromise the buffering capacity and stability of dendrimer/gene polyplexes. Our previous study showed incorporation of a bis-aryl hydrazine (BAH) linkage can compensate the loss of primary amine from PEGylation, increase the buffering capacity, and stabilize dendrimer/gene complaxation [321]. Indeed, we are interested to explore G4-BAH-PEG-FA conjugate formulation for in vivo siRNA delivery through systemic administration.

Biocompatibility is always a safety concern for drug delivery systems. To date, very few toxicological investigations of dendrimers and their derivatives have been re-

ported. Acute administration (single-dose) and long-term administration (repeatedly once a week for 10 weeks) of 2.6, 10, and 45 mg/kg of PAMAM dendrimer G3 and G5 showed no behavioral changes, weight loss, or immunogenicity [220]. In our current work, single local injection of G4/siVEGFA polyplexes at a G4-concentration of 9.3 mg/kg showed no weight loss, but two local injections of G4/siVEGFA polyplexes at a G4-concentration of 9.3 mg/kg showed a weight loss and skin lesion, indicating a skin damage and potential local toxicity occurred after second injection. A large amount of G4/siVEGFA polyplexes might accumulate in the tumor and surrounding areas without entering circulation because of the local injection. G4/siVEGFA polyplexes can trigger rapid non-specific cellular uptake by absorptive endocytosis, which may cause the toxicity to the skin. In contrast, both single and two local injections of G4-FA/siVEGFA and G4-FA/siGFP polyplexes showed no weight loss. Our proposed mechanism is that the cellular uptake of G4-FA conjugate is via FR-mediate endocytosis, which is highly dependent on the FR availability on the cell surface. Due to the lack of FR in the surrounding tissues such as skin, G4-FA/siVEGFA polyplexes were preferentially taken up by HN12 xenograft tumor; while FR of the tumor again limited the amount of G4-FA/siVEGFA polyplexes uptake. Therefore, G4-FA/siRNA polyplexes displayed no toxicity to the HN12 tumor-bearing mice. However, further studies of multiple-dose injection are needed to verify our mechanism.

8.2.2 Challenges in siRNA delivery

siRNA may serve as a promising therapeutic molecule for treating human diseases such as cancer. Generally, the most serious obstacle to siRNA therapeutic development perhaps is the delivery. However, two recent studies illustrate other barriers that likely occur at the point of internalization (Figure 8.1) [283]. Gilleron et al. showed only 1-2% of internalized siRNA could escape from the endocytic system (Figure 8.1) [69]. Sahay et al. showed LNPs were internalized by macropinocytosis and trafficked directly into late endosomes. However, those dissociated siRNA was exocytosed, as a result of overall 70% siRNA loss after 24 h treatment (Figure 8.1) [224]. Together, both studies indicate endosomal escape and exocytosis need to be

considered in design of siRNA delivery system. In our current study, we determined the cellular uptake kinetics of plasmid which labeled with Cy3 fluorescence dye by flow cytometry and fluorescence microscopy. The results indicate G4-FA/plasmid polyplexes can be gradually taken up and the exocytosis of the polyplexes can be minor in 24 h, as the evidence shown Cy3 fluorescence increased in a time-dependent manner. In the co-localization assessment based on confocal microscopy, we found most of G4-FA conjugates were co-locolized with plasmid after 24 h treatment. This result indicates that dissociation of plasmid from polyplex may not be efficient for our formulation. Although most of the polyplexes were close to nucleus within the cell, it remains unknown where are the polyplexes located, late endosome, lysosome, or somewhere else. Further cellular component co-locolization investigations are needed to justify when and how the plasmid and polyplexes can escape from the endosome or lysosome. On the other hand, the intracellular response of siRNA and plasmid is different due to their different the biological and physicochemical properties. Plasmid needs to enter nucleus and integrate into host chromosomal target sites. siRNA needs to bind to its complementary messenger RNA and induce degradation of the passenger strand by incorporating into the RNA-induced silencing complex (RISC) in the cytosol. Therefore, the in vitro trafficking of G4-FA/plasmid polyplexes may not represent that for G4-FA/siRNA. Thus, a Cy3-labeled siRNA is needed to demonstrate the cellular uptake and intracellular trafficking of siRNA delivered by G4-FA conjugates. More importantly, we need to answer three fundamental questions: 1) whether or not the G4-FA/siRNA polyplex can escape from endosome, late endosome, or lysosome; 2) where the siRNA can be released from the polyplex; and 3) whether the released siRNA can retain in the cytosol or undergo exocytosis.

8.2.3 In vivo xenograft model

The in vivo xenograft tumor model used in this work is an HN12 tumor-bearing nude mouse model. Athymic nude mice are immunodeficient, particularly T-cell deficient, which allows for xenograft tumor. Athymic nude mice in turn become an

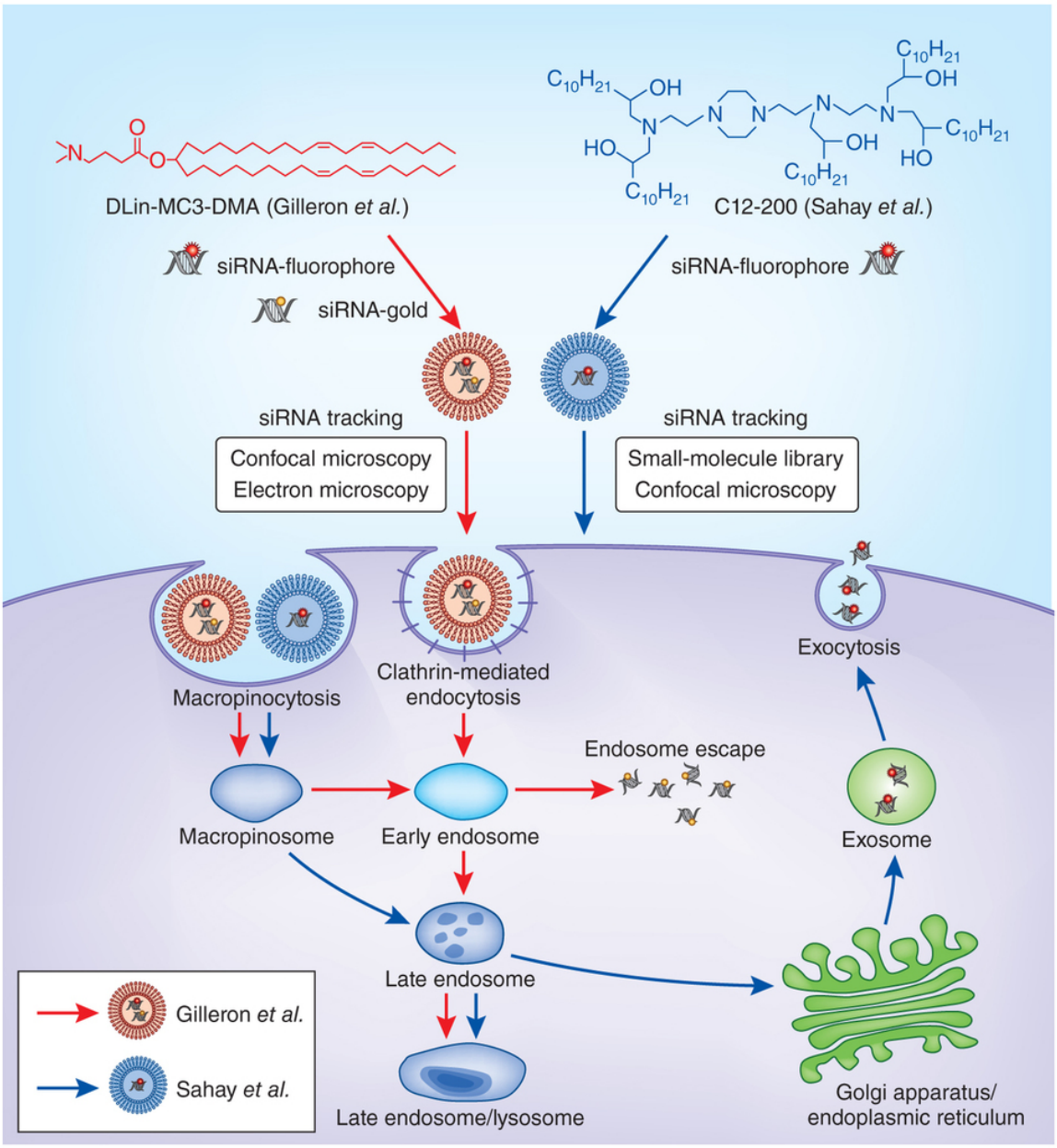

Figure 8.1: Schematic illustration of the approach used to study the uptake and intracellular trafficking of siRNA delivered by lipid nanoparticles (LNPs).
The major difference between these two LNPs is in the cationic lipids used to formulate the LNP that delivered the siRNA. (Reproduced reference [283]. Copyright 2013 Macmillan Publishers Ltd.)

excellent in vivo model for transplantation and tumor cell growth. However, it may not be an ideal in vivo model to investigate drug delivery systems. Those chemotherapeutics that target DNA or multicomponent machineries of cancer cells can cause substantial toxicity because they can affect both cancer and normal cells. This type of chemotherapeutics can compromise the rapidly dividing cells of immune system (hematopoiesis), gut, hair, and also the function of post-mitotic tissue such as heart muscle and peripheral nerves [46]. Thus, the patient receiving this type of chemotherapy will experience hair loss and infections (due to compromised immune system) and peripheral nerve pain. Because athymic nude mice are immunodeficient, it becomes difficult to evaluate the immune response after therapeutics-carried nanoparticles administration in the xenograft tumor model. Particularly, the immune system first responses therapeutics-carried nanoparticles once they enter circulation. Due to the T-cell deficiency, the effect of therapeutics-carried nanoparticles on T-cells remains unknown after therapeutics-carried nanoparticles administration in the xenograft tumor model, which may affect cell-mediated immunity of the body. On the other hand, these athymic nude mice may be an ideal in vivo model to investigate our immune cell-dendrimer hybrids. Because of the immunodeficiency, xenogeneic immune cells, such as monocytes, can be systemically injected to the tumor-bearing mice. These hybrids are cell-based vehicles, which can minimize non-specific uptake from liver, kidney, and immune system itself. It would be very interesting to further investigate the biodistribution of monocyte-dendrimer hybrids after i.v. administration.

8.3 Future Directions

8.3.1 Local delivery of highly potent genetic materials using G4-FA conjugates

In Chapter 5, we addressed the potency of the siVEGFA duplex used in our work might not be very high in HN12 cells. To enhance silencing efficacy, we can select an siVEGFA pool against VEGFA for G4-FA complexation. Besides siVEGFA, we

can employ an siRNA pool targeting to multiple intracellular signaling intermediates, which are oncoproteins, to improve the therapeutic outcomes. Among these signaling intermediates, epidermal growth factor receptor pathway substrate 8 (EPS8) is one of our interest targeting signaling intermediates. EPS8 plays an important role in HNSCC. Our early report has shown that overexpression of EPS8 activates AKT in a PI3K-dependent manner, leading to an increase mRNA expression of matrix metalloproteinase-9 (MMP9). This enhanced MMP-9 activity facilitates extracellular matrix degradation, thereby enhancing cell invasion [272]. In addition, our recent report has shown EPS8 enhances cell proliferation, migration and tumorigenicity in vitro and in vivo. A microarray screen identified EPS8 upregulates multiple cell cycle-related targets such as the transcription factor FOXM1 and several of its reported downstream mediators, including cdc20, cyclin B1, cyclin A, aurora-B kinase, cdc25C and MMP9 [273]. Thus, EPS8 knockdown represents a novel approach for gene therapy of HNSCC. In addition to siRNA delivery, we can complex G4-FA conjugates with plasmid encoding suicide genes, such as tumor necrosis factor (TNF), TNF-related apoptosis-inducing ligand (TRAIL), caspase-9, caspase-9, and B-cell lymphoma 2 (Bcl-2)-interacting killer (Bik), for cancer gene therapy. Overexpression of these suicide genes in cancer cells can trigger apoptosis in cancer cells, potentially leading to tumor regression.

8.3.2 Systemic gene delivery using PEGylated G4-FA conjugates

In Chapter 5, our results showed FA-conjugated G4 dendrimer failed to enhance tumor uptake through i.v. administration. A rapid hepatic and renal clearance was observed, indicating G4-FA conjugates possess a short circulation time. To prolong the circulation time, we can partially surface modify G4 dendrimer with PEG via a bis-aryl hydrazine (BAH) linkage and then conjugate FA onto the surface modified G4 dendrimer to form G4-BAH-PEG-FA conjugates (Figure 8.2). Incorporation of BAH linkage can help to compensate the loss of amine from PEGylation, which in

turn enhances the buffering capacity of dendrimer conjugates for gene delivery. We can conjugate Cy5 fluorescence dye onto dendrimer conjugates for in vitro trafficking and in vivo bioimaging. Therefore, our hypothesis is that G4-BAH-PEG-FA/siRNA polyplexes may prolong the circulation, increase tumor accumulation, and lead to an enhanced therapeutic outcome compared to G4-FA/siRNA polyplexes, in HN12 tumor-bearing nude mice after i.v. administration. The key rationale of this approach is to engineering a versatile dendrimer-based gene delivery system for tumor-targeted delivery of gene therapeutics, including siRNA, shRNA, plasmid, and any combination.

8.3.3 Synthesize FA-conjugated CPT-G4.5-PEG conjugates for targeted chemotherapy

In Chapter 6, we have shown a slow release of CPT from CPT-G4.5-PEG conjugates in U2142 cells. To further explore this formulation via click chemistry in the treatment of HNSCC, we can further couple FA onto CPT-G4.5-PEG conjugate, yielding a CPT-G4.5-PEG-FA conjugates (Figure 8.3). With understanding of cellular uptake mechanism, we expect to observe more therapeutic outcomes from CPT-G4.5-PEG-FA conjugates than CPT-G4.5-PEG conjugates in vitro in HN12 cells and in vivo in HN12 tumor-bearing mice. Additionally, we also want to investigate the effect of PEGylation of dendrimer on administration routes in this approach. In Chapter 5, we have clearly demonstrated non-PEGylated G4-FA conjugates can retain in the tumor region for at least 21 day after i.t. administration. However, G4-FA conjugates failed to accumulate in the tumor after systemic administration, mainly due to the rapid clearance by liver and kidney. Therefore, our hypothesis is that G4.5-PEG conjugates may prolong the circulation compared to G4-FA conjugates; G4.5-PEG-FA conjugates may increase tumor accumulation compared to G4.5-PEG; and CPT-G4.5-PEG-FA conjugates may lead to an enhanced therapeutic outcome compared to CPT-G4.5-PEG and free CPT, in HN12 tumor-bearing nude mice after i.v. administration. The key rationale of this approach is to apply click chemistry to increase the coupling

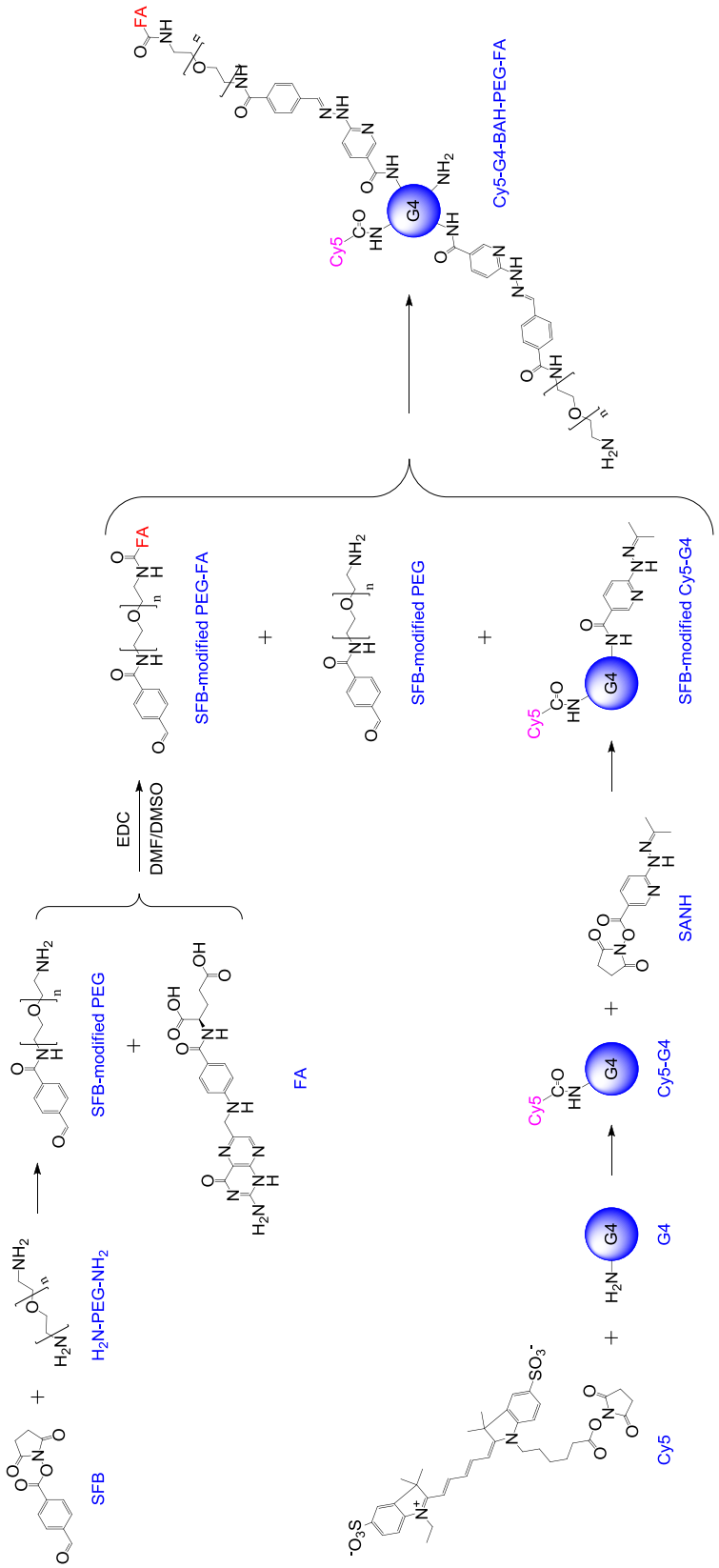

Figure 8.2: Synthesis of Cy5-G4-BAH-PEG-FA conjugates

efficiency in the dendrimer-based drug delivery system.

8.3.4 In vivo evaluation of monocyte-dendrimer hybrids

In Chapter 7, we have shown PAMAM dendrimer G4 can be successfully immobilized onto macrophage to form hybrids. Next step is to evaluate the biodistribution of these hybrids in the tumor-bearing mice. Our novel bioorthogonal chemistry-based cell-nanoparticle hybridization approach is proposed in Figure 8.4. First, we need to determine the stability of these hybrids in order to obtain an in vivo delivery time window. To improve the hybrid stability, we can partially conjugate PEG onto polycationic PAMAM dendrimer generation 4 (G4), which can neutralize zeta potential of G4, to minimize the uptake of dendrimer from the electrostatic interaction. Second, we can label the G4-PEG with Cy5 fluorescence dye (Cy5). Cy5 possesses high signal-to-noise ratio, which allows bioimaging, and it has a characteristic maximum absorption wavelength at 650 nm, which is within the UV detector range of our HPLC instrument. The purity of the resultant Cy5-G4-PEG conjugates can be determined by HPLC and 1H NMR. Third, monocytes, such as THP-1 monocytes, are suspending cells, which is more feasible for i.v. administration. Thus, we can hybrid monocytes with Cy5-G4-PEG conjugates based on bioorthogonal reaction. The stability and the biodistribution of these novel hybrids will be evaluated in vitro and in vivo in the tumor-bearing nude mice, respectively. Lastly, it would be important to determine drug loaded G4-PEG conjugates-monocyte hybrids. Doxorubicin (DOX) can be a good drug candidate in this approach, because the autofluorescent DOX can allow in vitro trafficking. The stability and anticancer efficiency can be evaluated in vitro and in vivo in the tumor-bearing nude mice. The key rationale is to utilize immune cells as vehicles to deliver therapeutics and imaging contrast agents to the tumor, which may significantly reduce non-specific uptake from liver, kidney, spleen, and immune system itself.

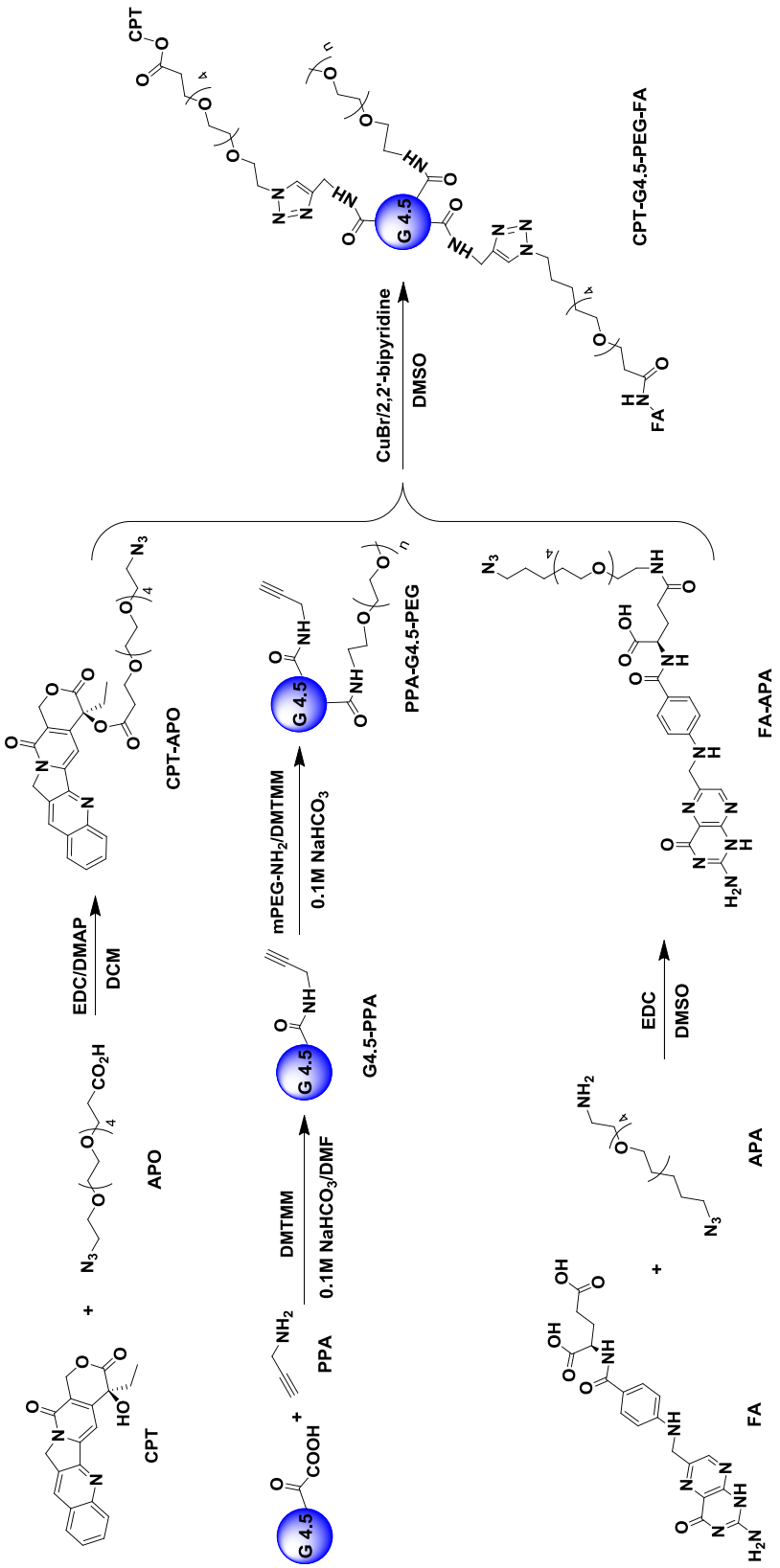

Figure 8.3: Synthesis of CPT-G4.5-PEG-FA conjugates

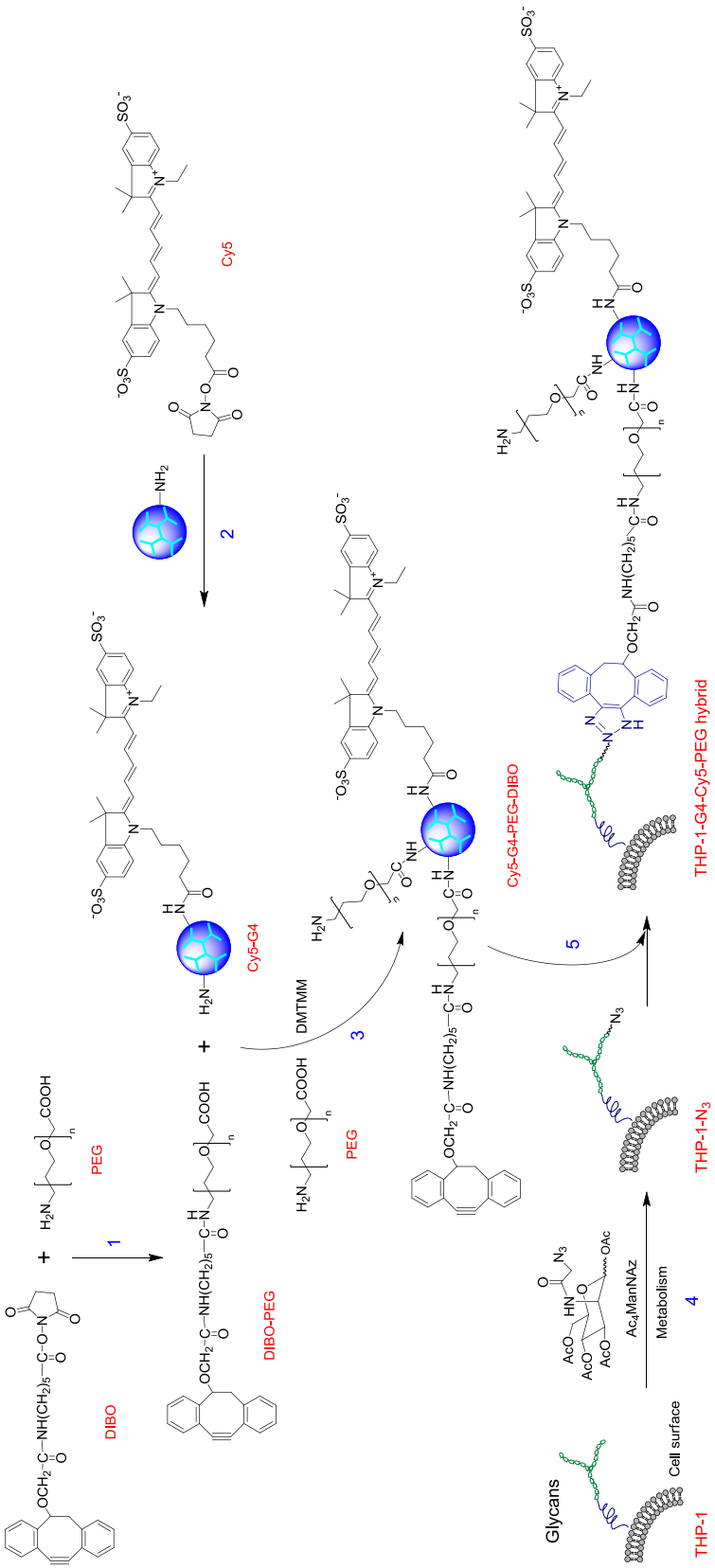

Figure 8.4: Schematic for hybridization of PEGylated PAMAM dendrimer and monocyte through bioorthogonal chemistry

Bibliography

[1] Sarbari Acharya and Sanjeeb K Sahoo. Plga nanoparticles containing various anticancer agents and tumour delivery by epr effect. *Adv Drug Deliv Rev*, 63(3):170–183, 2011.

[2] David J Adelstein, John A Ridge, Maura L Gillison, Anil K Chaturvedi, Gypsyamber D'Souza, Patti E Gravitt, William Westra, Amanda Psyrri, W Martin Kast, Laura A Koutsky, et al. Head and neck squamous cell cancer and the human papillomavirus: summary of a national cancer institute state of the science meeting, november 9–10, 2008, washington, dc. *Head Neck*, 31(11):1393–1422, 2009.

[3] Amit Agrawal, Dal-Hee Min, Neetu Singh, Haihao Zhu, Alona Birjiniuk, Geoffrey Von Maltzahn, Todd J Harris, Deyin Xing, Stephen D Woolfenden, Phillip A Sharp, et al. Functional delivery of sirna in mice using dendriworms. *ACS Nano*, 3(9):2495–2504, 2009.

[4] M Intakhab Alam, Sarwar Beg, Abdus Samad, Sanjula Baboota, Kanchan Kohli, Javed Ali, Alka Ahuja, and M Akbar. Strategy for effective brain drug delivery. *Eur J Pharm Sci*, 40(5):385–403, 2010.

[5] Terrick Andey, Srujan Marepally, Apurva Patel, Tanise Jackson, Shubhashish Sarkar, Malaney O'Connell, Rakesh C Reddy, Srikumar Chellappan, Pomila Singh, and Mandip Singh. Cationic lipid guided short-hairpin rna interference of annexin a2 attenuates tumor growth and metastasis in a mouse lung cancer stem cell model. *J Control Release*, 184:67–78, 2014.

[6] AC Antony. The biological chemistry of folate receptors. *Blood*, 79(11):2807–2820, 1992.

[7] Hidetoshi Arima, Masayo Arizono, Taishi Higashi, Ayumi Yoshimatsu, Haruna Ikeda, Keiichi Motoyama, Kenjiro Hattori, Tomoko Takeuchi, Fumitoshi Hirayama, and Kaneto Uekama. Potential use of folate-polyethylene glycol (peg)-appended dendrimer (g3) conjugate with α-cyclodextrin as dna carriers to tumor cells. *Cancer Gene Ther*, 19(5):358–366, 2012.

[8] Hidetoshi Arima, Ayumi Yoshimatsu, Haruna Ikeda, Ayumu Ohyama, Keiichi Motoyama, Taishi Higashi, Akira Tsuchiya, Takuro Niidome, Yoshiki Katayama, Kenjiro Hattori, et al. Folate-peg-appended dendrimer conjugate with α-cyclodextrin as a novel cancer cell-selective sirna delivery carrier. *Mol Pharm*, 9(9):2591–2604, 2012.

[9] Rohidas B Arote, Soon-Kyung Hwang, Hwang-Tae Lim, Tae-Hee Kim, Dhananjay Jere, Hu-Lin Jiang, You-Kyoung Kim, Myung-Haing Cho, and Chong-Su Cho. The therapeutic efficiency of fp-pea/tam67 gene complexes via folate receptor-mediated endocytosis in a xenograft mice model. *Biomaterials*, 31(8):2435–2445, 2010.

[10] Lynn B Bailey and Jesse F Gregory. Folate metabolism and requirements. *J Nutr*, 129(4):779–782, 1999.

[11] Tobias Bald, Thomas Quast, Jennifer Landsberg, Meri Rogava, Nicole Glodde, Dorys Lopez-Ramos, Judith Kohlmeyer, Stefanie Riesenberg, Debby van den Boorn-Konijnenberg, Cornelia Hömig-Hölzel, et al. Ultraviolet-radiation-induced inflammation promotes angiotropism and metastasis in melanoma. *Nature*, 2014.

[12] Nancy L Bartlett, Robert Chen, Michelle A Fanale, Pauline Brice, Ajay Gopal, S Smith, Ranjana Advani, J Matous, Radhakrishnan Ramchandren, J Rosenblatt, et al. Retreatment with brentuximab vedotin in patients with cd30-positive hematologic malignancies. *J Hematol Oncol*, 7(1):24, 2014.

[13] Jeremy M Baskin, Jennifer A Prescher, Scott T Laughlin, Nicholas J Agard, Pamela V Chang, Isaac A Miller, Anderson Lo, Julian A Codelli, and Carolyn R Bertozzi. Copper-free click chemistry for dynamic in vivo imaging. *Proc Natl Acad Sci U S A*, 104(43):16793–16797, 2007.

[14] Laura Biddlestone-Thorpe, Nicola Marchi, Kathy Guo, Chaitali Ghosh, Damir Janigro, Kristoffer Valerie, and Hu Yang. Nanomaterial-mediated cns delivery of diagnostic and therapeutic agents. *Adv Drug Deliv Rev*, 64(7):605–613, 2012.

[15] Laura Biddlestone-Thorpe, Muhammad Sajjad, Elizabeth Rosenberg, Jason M Beckta, Nicholas CK Valerie, Mary Tokarz, Bret R Adams, Alison F Wagner, Ashraf Khalil, Donna Gilfor, et al. Atm kinase inhibition preferentially sensitizes p53-mutant glioma to ionizing radiation. *Clin Cancer Res*, 19(12):3189–3200, 2013.

[16] Anna U Bielinska, Ann Yen, Huai Liang Wu, Kathleen M Zahos, Rong Sun, Norman D Weiner, James R Baker, and Blake J Roessler. Application of membrane-based dendrimer/dna complexes for solid phase transfection in vitro and in vivo. *Biomaterials*, 21(9):877–887, 2000.

[17] Kristen Bisanz, Jie Yu, Magnus Edlund, Bill Spohn, Mien-Chie Hung, Leland WK Chung, and Chia-Ling Hsieh. Targeting ecm–integrin interaction with liposome-encapsulated small interfering rnas inhibits the growth of human prostate cancer in a bone xenograft imaging model. *Mol Ther*, 12(4):634–643, 2005.

[18] Adela Bonoiu, Supriya D Mahajan, Ling Ye, Rajiv Kumar, Hong Ding, Ken-Tye Yong, Indrajit Roy, Ravikumar Aalinkeel, Bindukumar Nair, Jessica L Reynolds, et al. Mmp-9 gene silencing by a quantum dot–sirna nanoplex delivery to maintain the integrity of the blood brain barrier. *Brain Res*, 1282:142–155, 2009.

[19] AW Bosman, HM Janssen, and EW Meijer. About dendrimers: structure, physical properties, and applications. *Chem Rev*, 99(7):1665–1688, 1999.

[20] Malcolm K Brenner, Stephen Gottschalk, Ann M Leen, and Juan F Vera. Is cancer gene therapy an empty suit? *Lancet Oncol*, 14(11):e447–e456, 2013.

[21] J Martin Brown and William R Wilson. Exploiting tumour hypoxia in cancer treatment. *Nat Rev Cancer*, 4(6):437–447, 2004.

[22] M Brunotto, AM Zarate, A Bono, JL Barra, and S Berra. Risk genes in head and neck cancer: A systematic review and meta-analysis of last 5years. *Oral Oncol*, 50(3):178–188, 2014.

[23] JEB Burchenal, Christopher R Deible, Timothy E Deglau, Alan J Russell, Eric J Beckman, and William R Wagner. Polyethylene glycol diisocyanate decreases platelet deposition after balloon injury of rabbit femoral arteries. *J Thromb Thrombolysis*, 13(1):27–33, 2002.

[24] ALC Cardoso, S Simoes, LP De Almeida, N Plesnila, MC Pedroso de Lima, E Wagner, and C Culmsee. Tf-lipoplexes for neuronal sirna delivery: a promising system to mediate gene silencing in the cns. *J Control Release*, 132(2):113–123, 2008.

[25] Pamela V Chang, Jennifer A Prescher, Matthew J Hangauer, and Carolyn R Bertozzi. Imaging cell surface glycans with bioorthogonal chemical reporters. *J Am Chem Soc*, 129(27):8400–8401, 2007.

[26] Yulei Chang, Yapeng Li, Xinlei Meng, Nian Liu, Dexin Sun, Huan Liu, and Jingyuan Wang. Dendrimer functionalized water soluble magnetic iron oxide conjugates as dual imaging probe for tumor targeting and drug delivery. *Polym Chem*, 4(3):789–794, 2013.

[27] Anil K Chaturvedi, Eric A Engels, Ruth M Pfeiffer, Brenda Y Hernandez, Weihong Xiao, Esther Kim, Bo Jiang, Marc T Goodman, Maria Sibug-Saber, Wendy Cozen, et al. Human papillomavirus and rising oropharyngeal cancer incidence in the united states. *J Clin Oncol*, 29(32):4294–4301, 2011.

[28] Anumita Chaudhury, Surajit Das, Ralph M Bunte, and Gigi NC Chiu. Potent therapeutic activity of folate receptor-targeted liposomal carboplatin in the localized treatment of intraperitoneally grown human ovarian tumor xenograft. *Int J Nanomedicine*, 7:739, 2012.

[29] Chen Chen, Jiyuan Ke, X Edward Zhou, Wei Yi, Joseph S Brunzelle, Jun Li, Eu-Leong Yong, H Eric Xu, and Karsten Melcher. Structural basis for molecular recognition of folic acid by folate receptors. *Nature*, 500(7463):486–489, 2013.

[30] Hongwei Chen, Liya Wang, Julie Yeh, Xinying Wu, Zehong Cao, Yongqiang A Wang, Minming Zhang, Lily Yang, and Hui Mao. Reducing non-specific binding and uptake of nanoparticles and improving cell targeting with an antifouling peo-b-pγmps copolymer coating. *Biomaterials*, 31(20):5397–5407, 2010.

[31] Jing Chen, Shu Zhu, Liangqian Tong, Jiansha Li, Fei Chen, Yunfeng Han, Ming Zhao, and Wei Xiong. Superparamagnetic iron oxide nanoparticles mediated 131i-hvegf sirna inhibits hepatocellular carcinoma tumor growth in nude mice. *BMC cancer*, 14(1):114, 2014.

[32] Qian Chen, Kangan Li, Shihui Wen, Hui Liu, Chen Peng, Hongdong Cai, Mingwu Shen, Guixiang Zhang, and Xiangyang Shi. Targeted ct/mr dual mode imaging of tumors using multifunctional dendrimer-entrapped gold nanoparticles. *Biomaterials*, 34(21):5200–5209, 2013.

[33] F Cheng, J Liu, C Teh, SW Chong, V Korzh, YJ Jiang, and LW Deng. Camptothecin-induced downregulation of mll5 contributes to the activation of tumor suppressor p53. *Oncogene*, 30(33):3599–3611, 2011.

[34] Pei-Yu Chien, Jinkang Wang, Danielle Carbonaro, Sabrina Lei, Bruce Miller, Saifuddin Sheikh, Shoukath M Ali, Moghis U Ahmad, and Imran Ahmad. Novel cationic cardiolipin analogue-based liposome for efficient dna and small interfering rna delivery in vitro and in vivo. *Cancer Gene Ther*, 12(3):321–328, 2005.

[35] Mi-Ran Choi, Katie J Stanton-Maxey, Jennifer K Stanley, Carly S Levin, Rizia Bardhan, Demir Akin, Sunil Badve, Jennifer Sturgis, J Paul Robinson, Rashid Bashir, et al. A cellular trojan horse for delivery of therapeutic nanoparticles into tumors. *Nano Lett*, 7(12):3759–3765, 2007.

[36] R James Christie, Yu Matsumoto, Kanjiro Miyata, Takahiro Nomoto, Shigeto Fukushima, Kensuke Osada, Julien Halnaut, Frederico Pittella, Hyun Jin Kim, Nobuhiro Nishiyama, et al. Targeted polymeric micelles for sirna treatment of experimental cancer by intravenous injection. *ACS Nano*, 6(6):5174–5189, 2012.

[37] Julian A Codelli, Jeremy M Baskin, Nicholas J Agard, and Carolyn R Bertozzi. Second-generation difluorinated cyclooctynes for copper-free click chemistry. *J Am Chem Soc*, 130(34):11486–11493, 2008.

[38] Ana Cuadrado and Angel Nebreda. Mechanisms and functions of p38 mapk signalling. *Biochem J*, 429:403–417, 2010.

[39] Mark E Davis. The first targeted delivery of sirna in humans via a self-assembling, cyclodextrin polymer-based nanoparticle: from concept to clinic. *Mol Pharm*, 6(3):659–668, 2009.

[40] Mark E Davis, Jonathan E Zuckerman, Chung Hang J Choi, David Seligson, Anthony Tolcher, Christopher A Alabi, Yun Yen, Jeremy D Heidel, and Antoni Ribas. Evidence of rnai in humans from systemically administered sirna via targeted nanoparticles. *Nature*, 464(7291):1067–1070, 2010.

[41] PA De Bank, B Kellam, DA Kendall, and KM Shakesheff. Surface engineering of living myoblasts via selective periodate oxidation. *Biotechnol Bioeng*, 81(7):800–808, 2003.

[42] Stefaan C De Smedt, Joseph Demeester, and Wim E Hennink. Cationic polymer based gene delivery systems. *Pharm Res*, 17(2):113–126, 2000.

[43] Karen W Dehnert, Brendan J Beahm, Thinh T Huynh, Jeremy M Baskin, Scott T Laughlin, Wei Wang, Peng Wu, Sharon L Amacher, and Carolyn R Bertozzi. Metabolic labeling of fucosylated glycans in developing zebrafish. *ACS Chem Biol*, 6(6):547–552, 2011.

[44] Ivan del Barco Barrantes and AngelR Nebreda. Roles of p38 mapks in invasion and metastasis. *Biochem Soc Trans*, 40(1):79, 2012.

[45] Yang Ding, Yazhe Wang, Jianping Zhou, Xiaochen Gu, Wei Wang, Congyan Liu, Xiuli Bao, Cheng Wang, Yuanru Li, and Qiang Zhang. Direct cytosolic sirna delivery by reconstituted high density lipoprotein for target-specific therapy of tumor angiogenesis. *Biomaterials*, 35(25):7214–7227, 2014.

[46] Matthias Dobbelstein and Ute Moll. Targeting tumour-supportive cellular machineries in anticancer drug development. *Nat Rev Drug Discov*, 13(3):179–196, 2014.

[47] Dawen Dong, Wei Gao, Yujie Liu, and Xian-Rong Qi. Therapeutic potential of targeted multifunctional nanocomplex co-delivery of sirna and low-dose doxorubicin in breast cancer. *Cancer Lett*, 2015.

[48] XB Dou, Y Hu, NN Zhao, and FJ Xu. Different types of degradable vectors from low-molecular-weight polycation-functionalized poly (aspartic acid) for efficient gene delivery. *Biomaterials*, 35(9):3015–3026, 2014.

[49] Yu Du, Noah D Peyser, and Jennifer R Grandis. Integration of molecular targeted therapy with radiation in head and neck cancer. *Pharmacol Ther*, 142(1):88–98, 2014.

[50] Ruth Duncan and Lorella Izzo. Dendrimer biocompatibility and toxicity. *Adv Drug Deliv Rev*, 57(15):2215–2237, 2005.

[51] Jonathan D Eichman, Anna U Bielinska, Jolanta F Kukowska-Latallo, and James R Baker. The use of pamam dendrimers in the efficient transfer of genetic material into cells. *Pharm Sci Technolo Today*, 3(7):232–245, 2000.

[52] Hala Elnakat and Manohar Ratnam. Distribution, functionality and gene regulation of folate receptor isoforms: implications in targeted therapy. *Adv Drug Deliv Rev*, 56(8):1067–1084, 2004.

[53] Roseita Esfand and Donald A Tomalia. Poly(amidoamine)(pamam) dendrimers: from biomimicry to drug delivery and biomedical applications. *Drug Discov Today*, 6(8):427–436, 2001.

[54] Brian T Farrell, Bronwyn E Hamilton, Edit Dósa, Endre Rimely, Morad Nasseri, Seymur Gahramanov, Cynthia A Lacy, Eugene P Frenkel, Nancy D Doolittle, Paula M Jacobs, et al. Using iron oxide nanoparticles to diagnose cns inflammatory diseases and pcnsl. *Neurology*, 81(3):256–263, 2013.

[55] Andrew Fire, SiQun Xu, Mary K Montgomery, Steven A Kostas, Samuel E Driver, and Craig C Mello. Potent and specific genetic interference by double-stranded rna in caenorhabditis elegans. *Nature*, 391(6669):806–811, 1998.

[56] Stelios Florinas, Jaesung Kim, Kihoon Nam, Margit M Janát-Amsbury, and Sung Wan Kim. Ultrasound-assisted sirna delivery via arginine-grafted bioreducible polymer and microbubbles targeting vegf for ovarian cancer treatment. *J Control Release*, 183:1–8, 2014.

[57] Arlene A Forastiere, Helmuth Goepfert, Moshe Maor, Thomas F Pajak, Randal Weber, William Morrison, Bonnie Glisson, Andy Trotti, John A Ridge, Clifford Chao, et al. Concurrent chemotherapy and radiotherapy for organ preservation in advanced laryngeal cancer. *N Engl J Med*, 349(22):2091–2098, 2003.

[58] Megan E Fox, Steve Guillaudeu, Jean MJ Fréchet, Katherine Jerger, Nichole Macaraeg, and Francis C Szoka. Synthesis and in vivo antitumor efficacy of pegylated poly (l-lysine) dendrimer- camptothecin conjugates. *Mol Pharm*, 6(5):1562–1572, 2009.

[59] Joseph A Francisco, Charles G Cerveny, Damon L Meyer, Bruce J Mixan, Kerry Klussman, Dana F Chace, Starr X Rejniak, Kristine A Gordon, Ron DeBlanc,

Brian E Toki, et al. cac10-vcmmae, an anti-cd30–monomethyl auristatin e conjugate with potent and selective antitumor activity. *Blood*, 102(4):1458–1465, 2003.

[60] Robert A Freitas. What is nanomedicine? *Dis Mon*, 1(1):2–9, 2005.

[61] Wolf Herman Fridman, Franck Pagès, Catherine Sautès-Fridman, and Jérôme Galon. The immune contexture in human tumours: impact on clinical outcome. *Nat Rev Cancer*, 12(4):298–306, 2012.

[62] Takuma Fujii, Miyuki Saito, Eri Iwasaki, Takahiro Ochiya, Yoshifumi Takei, Shigenori Hayashi, Akiko Ono, Nobumaru Hirao, Masaru Nakamura, Kaneyuki Kubushiro, et al. Intratumor injection of small interfering rna-targeting human papillomavirus 18 e6 and e7 successfully inhibits the growth of cervical cancer. *Int J Oncol*, 29(3):541–548, 2006.

[63] Carl G Gahmberg and Martti Tolvanen. Nonmetabolic radiolabeling and tagging of glycoconjugates. *Methods Enzymol*, 230:32–44, 1994.

[64] Pieter J Gaillard, Chantal CM Appeldoorn, Jaap Rip, Rick Dorland, Susanne MA van der Pol, Gijs Kooij, Helga E de Vries, and Arie Reijerkerk. Enhanced brain delivery of liposomal methylprednisolone improved therapeutic efficacy in a model of neuroinflammation. *J Control Release*, 164(3):364–369, 2012.

[65] Fuping Gao, Linlin Li, Tianlong Liu, Nanjing Hao, Huiyu Liu, Longfei Tan, Hongbo Li, Xinglu Huang, Bo Peng, Chuanmiao Yan, et al. Doxorubicin loaded silica nanorattles actively seek tumors with improved anti-tumor effects. *Nanoscale*, 4(11):3365–3372, 2012.

[66] Lin Gao, Lisi Xie, Xiaojing Long, Zhiyong Wang, Cheng-Yi He, Zhi-Ying Chen, Lei Zhang, Xiang Nan, Hulong Lei, Xin Liu, et al. Efficacy of mri visible iron oxide nanoparticles in delivering minicircle dna into liver via intrabiliary infusion. *Biomaterials*, 34(14):3688–3696, 2013.

[67] Xiaoling Gao, Jun Chen, Jiyao Chen, Bingxian Wu, Hongzhuan Chen, and Xinguo Jiang. Quantum dots bearing lectin-functionalized nanoparticles as a platform for in vivo brain imaging. *Bioconjug Chem*, 19(11):2189–2195, 2008.

[68] Alessandra Ghilardi, Daniele Pezzoli, Maria Cristina Bellucci, Chiara Malloggi, Armando Negri, Aurora Sganappa, Gabriella Tedeschi, Gabriele Candiani, and Alessandro Volonterio. Synthesis of multifunctional pamam–aminoglycoside conjugates with enhanced transfection efficiency. *Bioconjug Chem*, 24(11):1928–1936, 2013.

[69] Jerome Gilleron, William Querbes, Anja Zeigerer, Anna Borodovsky, Giovanni Marsico, Undine Schubert, Kevin Manygoats, Sarah Seifert, Cordula Andree, Martin Stöter, et al. Image-based analysis of lipid nanoparticle-mediated sirna delivery, intracellular trafficking and endosomal escape. *Nat Biotechnol*, 31(7):638–646, 2013.

[70] Maura L Gillison, Gypsyamber D'Souza, William Westra, Elizabeth Sugar, Weihong Xiao, Shahnaz Begum, and Raphael Viscidi. Distinct risk factor profiles for human papillomavirus type 16–positive and human papillomavirus type 16–negative head and neck cancers. *J Natl Cancer Inst*, 100(6):407–420, 2008.

[71] Michael Goldberg, Robert Langer, and Xinqiao Jia. Nanostructured materials for applications in drug delivery and tissue engineering. *J Biomater Sci Polym Ed*, 18(3):241–268, 2007.

[72] David Goldenberg, Juna Lee, Wayne M Koch, Michael M Kim, Barry Trink, David Sidransky, and Chul-So Moon. Habitual risk factors for head and neck cancer. *Otolaryngol Head Neck Surg*, 131(6):986–993, 2004.

[73] Sarah E Golding, Elizabeth Rosenberg, Bret R Adams, Shayalini Wignarajah, Jason M Beckta, Mark J Oonnor, and Kristoffer Valerie. Dynamic inhibition of atm kinase provides a strategy for glioblastoma multiforme radiosensitization and growth control. *Cell Cycle*, 11(6):1167–1173, 2012.

[74] Sarah E Golding, Elizabeth Rosenberg, Nicholas Valerie, Isa Hussaini, Mark Frigerio, Xiaoling F Cockcroft, Wei Yee Chong, Marc Hummersone, Laurent Rigoreau, Keith A Menear, et al. Improved atm kinase inhibitor ku-60019 radiosensitizes glioma cells, compromises insulin, akt and erk prosurvival signaling, and inhibits migration and invasion. *Mol Cancer Ther*, 8(10):2894–2902, 2009.

[75] M Golzio, L Mazzolini, A Ledoux, A Paganin, M Izard, L Hellaudais, A Bieth, MJ Pillaire, C Cazaux, JS Hoffmann, et al. In vivo gene silencing in solid tumors by targeted electrically mediated sirna delivery. *Gene Ther*, 14(9):752–759, 2007.

[76] Chelsea G Gordon, Joel L Mackey, John C Jewett, Ellen M Sletten, KN Houk, and Carolyn R Bertozzi. Reactivity of biarylazacyclooctynones in copper-free click chemistry. *J Am Chem Soc*, 134(22):9199–9208, 2012.

[77] L Griffiths, K Binley, S Iqball, O Kan, P Maxwell, P Ratcliffe, C Lewis, A Harris, S Kingsman, and S Naylor. The macrophage-a novel system to deliver gene therapy to pathological hypoxia. *Gene Ther*, 7(3):255–262, 2000.

[78] Marius Grzelinski, Beata Urban-Klein, Tobias Martens, Katrin Lamszus, Udo Bakowsky, Sabrina Höbel, Frank Czubayko, and Achim Aigner. Rna interference-mediated gene silencing of pleiotrophin through polyethylenimine-complexed small interfering rnas in vivo exerts antitumoral effects in glioblastoma xenografts. *Hum Gene Ther*, 17(7):751–766, 2006.

[79] Neela Guha, Paolo Boffetta, Victor Wünsch Filho, Jose Eluf Neto, Oxana Shangina, David Zaridze, Maria Paula Curado, Sergio Koifman, Elena Matos, Ana Menezes, et al. Oral health and risk of squamous cell carcinoma of the head and neck and esophagus: results of two multicentric case-control studies. *Am J Epidemiol*, 166(10):1159–1173, 2007.

[80] Shutao Guo, C Michael Lin, Zhenghong Xu, Lei Miao, Yuhua Wang, and Leaf Huang. Co-delivery of cisplatin and rapamycin for enhanced anticancer ther-

apy through synergistic effects and microenvironment modulation. *ACS Nano*, 8(5):4996–5009, 2014.

[81] Shutao Guo, Lei Miao, Yuhua Wang, and Leaf Huang. Unmodified drug used as a material to construct nanoparticles: delivery of cisplatin for enhanced anti-cancer therapy. *J Control Release*, 174:137–142, 2014.

[82] Shutao Guo, Yuhua Wang, Lei Miao, Zhenghong Xu, Ching-Hsuan M Lin, and Leaf Huang. Turning a water and oil insoluble cisplatin derivative into a nanoparticle formulation for cancer therapy. *Biomaterials*, 35(26):7647–7653, 2014.

[83] Subash C Gupta, Chitra Sundaram, Simone Reuter, and Bharat B Aggarwal. Inhibiting nf-κb activation by small molecules as a therapeutic strategy. *Biochimica et Biophysica Acta*, 1799(10):775–787, 2010.

[84] Sezen Gurdag, Jayant Khandare, Sarah Stapels, Larry H Matherly, and Rangaramanujam M Kannan. Activity of dendrimer-methotrexate conjugates on methotrexate-sensitive and-resistant cell lines. *Bioconjug Chem*, 17(2):275–283, 2006.

[85] István Hajdu, Magdolna Bodnár, György Trencsényi, Teréz Márián, György Vámosi, József Kollár, and János Borbély. Cancer cell targeting and imaging with biopolymer-based nanodevices. *Int J Pharm*, 441(1):234–241, 2013.

[86] Jyotsnabaran Halder, Aparna A Kamat, Charles N Landen, Liz Y Han, Susan K Lutgendorf, Yvonne G Lin, William M Merritt, Nicholas B Jennings, Arturo Chavez-Reyes, Robert L Coleman, et al. Focal adhesion kinase targeting using in vivo short interfering rna delivery in neutral liposomes for ovarian carcinoma therapy. *Clin Cancer Res*, 12(16):4916–4924, 2006.

[87] Stephen J Hamilton-Dutoit, Marianne Hamilton Therkildsen, Nils Højgaard Nielsen, Henning Jensen, JP Hart Hansen, and Gorm Pallesen. Undifferentiated carcinoma of the salivary gland in greenlandic eskimos: demonstration

of epstein-barr virus dna by in situ nucleic acid hybridization. *Hum Pathol*, 22(8):811–815, 1991.

[88] Ji-Bo Han, Ze-Zhang Tao, Shi-Ming Chen, Yong-Gang Kong, and Bo-Kui Xiao. Adenovirus-mediated transfer of tris-shrnas induced apoptosis of nasopharyngeal carcinoma cell in vitro and in vivo. *Cancer Lett*, 309(2):162–169, 2011.

[89] Chunbai He, Yiping Hu, Lichen Yin, Cui Tang, and Chunhua Yin. Effects of particle size and surface charge on cellular uptake and biodistribution of polymeric nanoparticles. *Biomaterials*, 31(13):3657–3666, 2010.

[90] XW He, T Liu, YX Chen, DJ Cheng, XR Li, Y Xiao, and YL Feng. Calcium carbonate nanoparticle delivering vascular endothelial growth factor-c sirna effectively inhibits lymphangiogenesis and growth of gastric cancer in vivo. *Cancer Gene Ther*, 15(3):193–202, 2008.

[91] Richard I Hogrefe, Alexandre V Lebedev, Gerald Zon, Kathleen F Pirollo, Antonina Rait, Qi Zhou, Wei Yu, and Esther H Chang. Chemically modified short interfering hybrids (sihybrids): nanoimmunoliposome delivery in vitro and in vivo for rnai of her-2. *Nucleosides Nucleotides Nucleic Acids*, 25(8):889–907, 2006.

[92] Christopher A Holden, Quan Yuan, W Andrew Yeudall, Deborah A Lebman, and Hu Yang. Surface engineering of macrophages with nanoparticles to generate a cell–nanoparticle hybrid vehicle for hypoxia-targeted drug delivery. *Int J Nanomedicine*, 5:25, 2010.

[93] Guo-bin Hong, Jing-xing Zhou, and Ren-xu Yuan. Folate-targeted polymeric micelles loaded with ultrasmall superparamagnetic iron oxide: combined small size and high mri sensitivity. *Int J Nanomedicine*, 7:2863, 2012.

[94] Vu Hong, Nicole F Steinmetz, Marianne Manchester, and MG Finn. Labeling live cells by copper-catalyzed alkyne- azide click chemistry. *Bioconjug Chem*, 21(10):1912–1916, 2010.

[95] CC Hsu, CW Chiang, HC Cheng, WT Chang, CY Chou, HW Tsai, CT Lee, ZH Wu, TY Lee, A Chao, et al. Identifying lrrc16b as an oncofetal gene with transforming enhancing capability using a combined bioinformatics and experimental approach. *Oncogene*, 30(6):654–667, 2011.

[96] Siwen Hu-Lieskovan, Jeremy D Heidel, Derek W Bartlett, Mark E Davis, and Timothy J Triche. Sequence-specific knockdown of ews-fli1 by targeted, nonviral delivery of small interfering rna inhibits tumor growth in a murine model of metastatic ewing's sarcoma. *Cancer Res*, 65(19):8984–8992, 2005.

[97] Baohua Huang, Ankur Desai, Hong Zong, Shengzhuang Tang, Pascale Leroueil, and James R Baker. Copper-free click conjugation of methotrexate to a pamam dendrimer platform. *Tetrahedron Lett*, 52(13):1411–1414, 2011.

[98] Baohua Huang, Jolanta F Kukowska-Latallo, Shengzhuang Tang, Hong Zong, Kali B Johnson, Ankur Desai, Chris L Gordon, Pascale R Leroueil, and James R Baker. The facile synthesis of multifunctional pamam dendrimer conjugates through copper-free click chemistry. *Bioorg Med Chem Lett*, 22(9):3152–3156, 2012.

[99] Jian-Ming Huang, Guo-Nan Zhang, Yu Shi, Xiao Zha, Yi Zhu, Miao-Miao Wang, Qing Lin, Wen Wang, Hai-Yan Lu, Shi-Qi Ma, et al. Atractylenolide-i sensitizes human ovarian cancer cells to paclitaxel by blocking activation of tlr4/myd88-dependent pathway. *Sci Rep*, 4, 2014.

[100] Rongqin Huang, Liang Han, Jianfeng Li, Shuhuan Liu, Kun Shao, Yuyang Kuang, Xing Hu, Xuxia Wang, Hao Lei, and Chen Jiang. Chlorotoxin-modified macromolecular contrast agent for mri tumor diagnosis. *Biomaterials*, 32(22):5177–5186, 2011.

[101] Rongqin Huang, Weilun Ke, Liang Han, Jianfeng Li, Shuhuan Liu, and Chen Jiang. Targeted delivery of chlorotoxin-modified dna-loaded nanoparticles to glioma via intravenous administration. *Biomaterials*, 32(9):2399–2406, 2011.

[102] Rongqin Huang, Weilun Ke, Liang Han, Yang Liu, Kun Shao, Liya Ye, Jinning Lou, Chen Jiang, and Yuanying Pei. Brain-targeting mechanisms of lactoferrin-modified dna-loaded nanoparticles. *J Cereb Blood Flow Metab*, 29(12):1914–1923, 2009.

[103] Shixian Huang, Jianfeng Li, Liang Han, Shuhuan Liu, Haojun Ma, Rongqin Huang, and Chen Jiang. Dual targeting effect of angiopep-2-modified, dna-loaded nanoparticles for glioma. *Biomaterials*, 32(28):6832–6838, 2011.

[104] Grace H Huynh, Dennis F Deen, and Francis C Szoka. Barriers to carrier mediated drug and gene delivery to brain tumors. *J Control Release*, 110(2):236–259, 2006.

[105] Toyoko Imae. Physicochemical properties of dendrimers and dendrimer complexes. *Dendrimer-Based Drug Delivery Systems: From Theory to Practice*, pages 55–92, 2012.

[106] Nilesh P Ingle, Brett Malone, and Theresa M Reineke. Poly (glycoamidoamine) s: a broad class of carbohydrate-containing polycations for nucleic acid delivery. *Trends Biotechnol*, 29(9):443–453, 2011.

[107] Aimee L Jackson and Peter S Linsley. Recognizing and avoiding sirna off-target effects for target identification and therapeutic application. *Nat Rev Drug Discov*, 9(1):57–67, 2010.

[108] R Jevprasesphant, J Penny, R Jalal, D Attwood, NB McKeown, and A D'Emanuele. The influence of surface modification on the cytotoxicity of pamam dendrimers. *Int J Pharm*, 252(1):263–266, 2003.

[109] Rachaneekorn Jevprasesphant, Jeffrey Penny, David Attwood, and Antony D'Emanuele. Transport of dendrimer nanocarriers through epithelial cells via the transcellular route. *J Control Release*, 97(2):259–267, 2004.

[110] John C Jewett and Carolyn R Bertozzi. Synthesis of a fluorogenic cyclooctyne activated by cu-free click chemistry. *Org Lett*, 13(22):5937–5939, 2011.

[111] Lin-Tao Jia, Si-Yi Chen, and An-Gang Yang. Cancer gene therapy targeting cellular apoptosis machinery. *Cancer Treat Rev*, 38(7):868–876, 2012.

[112] Arunvel Kailasan, Quan Yuan, and Hu Yang. Synthesis and characterization of thermoresponsive polyamidoamine–polyethylene glycol–poly (d, l-lactide) core–shell nanoparticles. *Acta Biomater*, 6(3):1131–1139, 2010.

[113] Sujatha Kannan, Hui Dai, Raghavendra S Navath, Bindu Balakrishnan, Amar Jyoti, James Janisse, Roberto Romero, and Rangaramanujam M Kannan. Dendrimer-based postnatal therapy for neuroinflammation and cerebral palsy in a rabbit model. *Sci Transl Med*, 4(130):130ra46–130ra46, 2012.

[114] Tomoko Kawamata and Yukihide Tomari. Making risc. *Trends Biochem Sci*, 35(7):368–376, 2010.

[115] Weilun Ke, Kun Shao, Rongqin Huang, Liang Han, Yang Liu, Jianfeng Li, Yuyang Kuang, Liya Ye, Jinning Lou, and Chen Jiang. Gene delivery targeted to the brain using an angiopep-conjugated polyethyleneglycol-modified polyamidoamine dendrimer. *Biomaterials*, 30(36):6976–6985, 2009.

[116] Oliver T Keppler, Peer Stehling, Markus Herrmann, Holger Kayser, Detlef Grunow, Werner Reutter, and Michael Pawlita. Biosynthetic modulation of sialic acid-dependent virus-receptor interactions of two primate polyoma viruses. *J Biol Chem*, 270(3):1308–1314, 1995.

[117] Prashant Kesharwani and Arun K Iyer. Recent advances in dendrimer-based nanovectors for tumor-targeted drug and gene delivery. *Drug Discov Today*, 2014.

[118] Jee Seon Kim, Mi Hwa Oh, Jae Yoon Park, Tae Gwan Park, and Yoon Sung Nam. Protein-resistant, reductively dissociable polyplexes for in vivo systemic delivery and tumor-targeting of sirna. *Biomaterials*, 34(9):2370–2379, 2013.

[119] Sun Hwa Kim, Ji Hoon Jeong, Tae-il Kim, Sung Wan Kim, and David A Bull. Vegf sirna delivery system using arginine-grafted bioreducible poly (disulfide amine). *Mol Pharm*, 6(3):718–726, 2008.

[120] Won Jong Kim, Lane V Christensen, Seongbong Jo, James W Yockman, Ji Hoon Jeong, Yong-Hee Kim, and Sung Wan Kim. Cholesteryl oligoarginine delivering vascular endothelial growth factor sirna effectively inhibits tumor growth in colon adenocarcinoma. *Mol Ther*, 14(3):343–350, 2006.

[121] You-Kyoung Kim, Arash Minai-Tehrani, Jae-Ho Lee, Chong-Su Cho, Myung-Haing Cho, and Hu-Lin Jiang. Therapeutic efficiency of folated poly (ethylene glycol)-chitosan-graft-polyethylenimine-pdcd4 complexes in h-ras12v mice with liver cancer. *Int J Nanomedicine*, 8:1489, 2013.

[122] Young-Min Kim and Soo-Chang Song. Targetable micelleplex hydrogel for long-term, effective, and systemic sirna delivery. *Biomaterials*, 35(27):7970–7977, 2014.

[123] Gordon J Kirkpatrick, Jane A Plumb, Oliver B Sutcliffe, David J Flint, and Nial J Wheate. Evaluation of anionic half generation 3.5–6.5 poly (amidoamine) dendrimers as delivery vehicles for the active component of the anticancer drug cisplatin. *J Inorg Biochem*, 105(9):1115–1122, 2011.

[124] Jonathan Klein, Jonathan Livergant, and Jolie Ringash. Health related quality of life in head and neck cancer treated with radiation therapy with or without chemotherapy: a systematic review. *Oral Oncol*, 50(4):254–262, 2014.

[125] Walter Kolch and Andrew Pitt. Functional proteomics to dissect tyrosine kinase signalling pathways in cancer. *Nat Rev Cancer*, 10(9):618–629, 2010.

[126] Joy L Kovar, William M Volcheck, Jiyan Chen, and Melanie A Simpson. Purification method directly influences effectiveness of an epidermal growth factor-coupled targeting agent for noninvasive tumor detection in mice. *Anal Biochem*, 361(1):47–54, 2007.

[127] Jörg Kreuter. Drug delivery to the central nervous system by polymeric nanoparticles: what do we know? *Adv Drug Deliv Rev*, 71:2–14, 2014.

[128] Jolanta F Kukowska-Latallo, Kimberly A Candido, Zhengyi Cao, Shraddha S Nigavekar, Istvan J Majoros, Thommey P Thomas, Lajos P Balogh, Mohamed K Khan, and James R Baker. Nanoparticle targeting of anticancer drug improves therapeutic response in animal model of human epithelial cancer. *Cancer Res*, 65(12):5317–5324, 2005.

[129] Iben Kümler, Malgorzata K Tuxen, and Dorte Lisbet Nielsen. A systematic review of dual targeting in her2-positive breast cancer. *Cancer Treat Rev*, 40(2):259–270, 2014.

[130] Yunus E Kurtoglu, Raghavendra S Navath, Bing Wang, Sujatha Kannan, Robert Romero, and Rangaramanujam M Kannan. Poly (amidoamine) dendrimer–drug conjugates with disulfide linkages for intracellular drug delivery. *Biomaterials*, 30(11):2112–2121, 2009.

[131] Kenji Kusumoto, Hidetaka Akita, Taichi Ishitsuka, Yu Matsumoto, Takahiro Nomoto, Ryo Furukawa, Ayman El-Sayed, Hiroto Hatakeyama, Kazuaki Kajimoto, Yuma Yamada, et al. Lipid envelope-type nanoparticle incorporating a multifunctional peptide for systemic sirna delivery to the pulmonary endothelium. *ACS Nano*, 7(9):7534–7541, 2013.

[132] Albert Kwok, Gabriela A Eggimann, Jean-Louis Reymond, Tamis Darbre, and Florian Hollfelder. Peptide dendrimer/lipid hybrid systems are efficient dna transfection reagents: structure–activity relationships highlight the role of charge distribution across dendrimer generations. *ACS Nano*, 7(5):4668–4682, 2013.

[133] Il Keun Kwon, Sang Cheon Lee, Bumsoo Han, and Kinam Park. Analysis on the current status of targeted drug delivery to tumors. *J Control Release*, 164(2):108–114, 2012.

[134] Enrique Lallana, Ana Sousa-Herves, Francisco Fernandez-Trillo, Ricardo Riguera, and Eduardo Fernandez-Megia. Click chemistry for drug delivery nanosystems. *Pharm Res*, 29(1):1–34, 2012.

[135] Charles N Landen, Arturo Chavez-Reyes, Corazon Bucana, Rosemarie Schmandt, Michael T Deavers, Gabriel Lopez-Berestein, and Anil K Sood. Therapeutic epha2 gene targeting in vivo using neutral liposomal small interfering rna delivery. *Cancer Res*, 65(15):6910–6918, 2005.

[136] Charles N Landen, William M Merritt, Lingegowda S Mangala, Angela M Sanguino, Corazon Bucana, Chunhua Lu, Yvonne G Lin, Liz Y Han, Aparna A Kamat, Rosemarie E Schmandt, et al. Intraperitoneal delivery of liposomal sirna for therapy of advanced ovarian cancer. *Cancer Biol Ther*, 5(12):1708–1713, 2006.

[137] Scott T Laughlin, Jeremy M Baskin, Sharon L Amacher, and Carolyn R Bertozzi. In vivo imaging of membrane-associated glycans in developing zebrafish. *Science*, 320(5876):664–667, 2008.

[138] Scott T Laughlin and Carolyn R Bertozzi. In vivo imaging of caenorhabditis elegans glycans. *ACS Chem Biol*, 4(12):1068–1072, 2009.

[139] David A Lavan, Terry McGuire, and Robert Langer. Small-scale systems for in vivo drug delivery. *Nat Biotechnol*, 21(10):1184–1191, 2003.

[140] Cameron C Lee, John A MacKay, Jean MJ Fréchet, and Francis C Szoka. Designing dendrimers for biological applications. *Nat Biotechnol*, 23(12):1517–1526, 2005.

[141] Jeil Lee, Jinwoo Jung, Youn-Joong Kim, Eunji Lee, and Joon Sig Choi. Gene delivery of pamam dendrimer conjugated with the nuclear localization signal peptide originated from fibroblast growth factor 3. *Int J Pharm*, 459(1):10–18, 2014.

[142] Kyung Dong Lee, Seon-Hee Choi, Da Hye Kim, Hye-Young Lee, and Ki-Choon Choi. Self-organized nanoparticles based on chitosan-folic acid and dextran succinate-doxorubicin conjugates for drug targeting. *Arch Pharm Res*, 37(12):1546–1553, 2014.

[143] Sangmin Lee, Heebeom Koo, Jin Hee Na, Kyung Eun Lee, Seo Young Jeong, Kuiwon Choi, Sun Hwa Kim, Ick Chan Kwon, and Kwangmeyung Kim. Dna amplification in neutral liposomes for safe and efficient gene delivery. *ACS Nano*, 8(5):4257–4267, 2014.

[144] Bokai Lei, Weibin Zha, Yun Wang, Cong Wen, Elaine J Studer, Xuan Wang, Fang Jin, Guangji Wang, Luyong Zhang, and Huiping Zhou. Development of a novel self-microemulsifying drug delivery system for reducing hiv protease inhibitor-induced intestinal epithelial barrier dysfunction. *Mol Pharm*, 7(3):844–853, 2010.

[145] Maciej S Lesniak and Henry Brem. Targeted therapy for brain tumours. *Nat Rev Drug Discov*, 3(6):499–508, 2004.

[146] Wojciech G Lesniak, Manoj K Mishra, Amar Jyoti, Bindu Balakrishnan, Fan Zhang, Elizabeth Nance, Roberto Romero, Sujatha Kannan, and Rangaramanujam M Kannan. Biodistribution of fluorescently labeled pamam dendrimers in neonatal rabbits: Effect of neuroinflammation. *Mol Pharm*, 10(12):4560–4571, 2013.

[147] Jin-Ming Li, Yuan-Yuan Wang, Wei Zhang, Hua Su, Liang-Nian Ji, and Zong-Wan Mao. Low-weight polyethylenimine cross-linked 2-hydroxypopyl-β-cyclodextrin and folic acid as an efficient and nontoxic sirna carrier for gene silencing and tumor inhibition by vegf sirna. *Int J Nanomedicine*, 8:2101, 2013.

[148] Jin-Ming Li, Mei-Xia Zhao, Hua Su, Yuan-Yuan Wang, Cai-Ping Tan, Liang-Nian Ji, and Zong-Wan Mao. Multifunctional quantum-dot-based sirna delivery for hpv18 e6 gene silence and intracellular imaging. *Biomaterials*, 32(31):7978–7987, 2011.

[149] Tony Shing Chau Li, Toshio Yawata, and Koichi Honke. Efficient sirna delivery and tumor accumulation mediated by ionically cross-linked folic acid–poly (ethylene glycol)–chitosan oligosaccharide lactate nanoparticles: For the potential targeted ovarian cancer gene therapy. *Eur J Pharm Sci*, 52:48–61, 2014.

[150] Yan Li, Hai He, Xinru Jia, Wan-Liang Lu, Jinning Lou, and Yen Wei. A dual-targeting nanocarrier based on poly (amidoamine) dendrimers conjugated with transferrin and tamoxifen for treating brain gliomas. *Biomaterials*, 33(15):3899–3908, 2012.

[151] Xuhua Liang, Yang Sun, Wenyuan Zeng, Lusha Liu, Xuan Ma, Yingyong Zhao, and Jun Fan. Synthesis and biological evaluation of a folate-targeted rhaponticin conjugate. *Bioorg Med Chem*, 21(1):178–185, 2013.

[152] Yong-beom Lim, Seon-mi Kim, Hearan Suh, and Jong-sang Park. Biodegradable, endosome disruptive, and cationic network-type polymer as a highly efficient and nontoxic gene delivery carrier. *Bioconjug Chem*, 13(5):952–957, 2002.

[153] Guimei Lin, Hong Zhang, and Leaf Huang. Smart polymeric nanoparticles for cancer gene delivery. *Mol Pharm*, 2014.

[154] Cheng Liu, Xiaoxuan Liu, Palma Rocchi, Fanqi Qu, Juan L Iovanna, and Ling Peng. Arginine-terminated generation 4 pamam dendrimer as an effective nanovector for functional sirna delivery in vitro and in vivo. *Bioconjug Chem*, 25(3):521–532, 2014.

[155] Jing-Min Liu, Jia-Tong Chen, and Xiu-Ping Yan. Near infrared fluorescent trypsin stabilized gold nanoclusters as surface plasmon enhanced energy transfer biosensor and in vivo cancer imaging bioprobe. *Anal Biochem*, 85(6):3238–3245, 2013.

[156] Leroy F Liu. Dna topoisomerase poisons as antitumor drugs. *Annu Rev Biochem*, 58(1):351–375, 1989.

[157] Leroy F Liu, Shyamal D Desai, Tsai-Kun Li, Yong Mao, Mei Sun, and Sai-Peng Sim. Mechanism of action of camptothecin. *Ann N Y Acad Sci*, 922(1):1–10, 2000.

[158] Mingjun Liu and Jean MJ Fréchet. Designing dendrimers for drug delivery. *Pharm Sci Technolo Today*, 2(10):393–401, 1999.

[159] Xiaoxuan Liu, Cheng Liu, Erik Laurini, Paola Posocco, Sabrina Pricl, Fanqi Qu, Palma Rocchi, and Ling Peng. Efficient delivery of sticky sirna and potent gene silencing in a prostate cancer model using a generation 5 triethanolamine-core pamam dendrimer. *Mol Pharm*, 9(3):470–481, 2012.

[160] Yang Liu, Rongqin Huang, Liang Han, Weilun Ke, Kun Shao, Liya Ye, Jinning Lou, and Chen Jiang. Brain-targeting gene delivery and cellular internalization mechanisms for modified rabies virus glycoprotein rvg29 nanoparticles. *Biomaterials*, 30(25):4195–4202, 2009.

[161] Yang Liu, Yan-Hua Zhu, Cheng-Qiong Mao, Shuang Dou, Song Shen, Zi-Bin Tan, and Jun Wang. Triple negative breast cancer therapy with cdk1 sirna delivered by cationic lipid assisted peg-pla nanoparticles. *J Control Release*, 192:114–121, 2014.

[162] Wen-Liang Lo, Yueh Chien, Guang-Yuh Chiou, Ling-Ming Tseng, Han-Shui Hsu, Yuh-Lih Chang, Kai-Hsi Lu, Chian-Shiu Chien, Mong-Lien Wang, Yi-Wei Chen, et al. Nuclear localization signal-enhanced rna interference of ezh2 and oct4 in the eradication of head and neck squamous cell carcinoma-derived cancer stem cells. *Biomaterials*, 33(14):3693–3709, 2012.

[163] Jian-Ming Lü, Xinwen Wang, Christian Marin-Muller, Hao Wang, Peter H Lin, Qizhi Yao, and Changyi Chen. Current advances in research and clinical applications of plga-based nanotechnology. 2009.

[164] Danièle Luce, Annette Leclerc, Denis Bégin, Paul A Demers, Michel Gérin, Ewa Orlowski, Manolis Kogevinas, Stefano Belli, Isabelle Bugel, Ulrich Bolm-

Audorff, et al. Sinonasal cancer and occupational exposures: a pooled analysis of 12 case–control studies. *Cancer Causes Control*, 13(2):147–157, 2002.

[165] Dan Luo and W Mark Saltzman. Synthetic dna delivery systems. *Nat Biotechnol*, 18(1):33–37, 2000.

[166] Zheng Ma, Jiang Li, Fengtian He, Annette Wilson, Bruce Pitt, and Song Li. Cationic lipids enhance sirna-mediated interferon response in mice. *Biochem Biophys Res Commun*, 330(3):755–759, 2005.

[167] Ram I Mahato, James Henry, Ajit S Narang, Omaima Sabek, Daniel Fraga, Malak Kotb, and A Osama Gaber. Cationic lipid and polymer-based gene delivery to human pancreatic islets. *Mol Ther*, 7(1):89–100, 2003.

[168] Junhua Mai, Yi Huang, Chaofeng Mu, Guodong Zhang, Rong Xu, Xiaojing Guo, Xiaojun Xia, David E Volk, Ganesh L Lokesh, Varatharasa Thiviyanathan, et al. Bone marrow endothelium-targeted therapeutics for metastatic breast cancer. *J Control Release*, 187:22–29, 2014.

[169] István J Majoros, Andrzej Myc, Thommey Thomas, Chandan B Mehta, and James R Baker. Pamam dendrimer-based multifunctional conjugate for cancer therapy: synthesis, characterization, and functionality. *Biomacromolecules*, 7(2):572–579, 2006.

[170] H Maruyama-Tabata, Y Harada, T Matsumura, E Satoh, F Cui, M Iwai, M Kita, S Hibi, J Imanishi, T Sawada, et al. Effective suicide gene therapy in vivo by ebv-based plasmid vector coupled with polyamidoamine dendrimer. *Gene Ther*, 7(1):53–60, 2000.

[171] Valentina Medici and Charles H Halsted. Folate, alcohol, and liver disease. *Mol Nutr Food Res*, 57(4):596–606, 2013.

[172] Ira Mellman, Renate Fuchs, and Ari Helenius. Acidification of the endocytic and exocytic pathways. *Annu Rev Biochem*, 55(1):663–700, 1986.

[173] Anupa R Menjoge, Rangaramanujam M Kannan, and Donald A Tomalia. Dendrimer-based drug and imaging conjugates: design considerations for nanomedical applications. *Drug Discov Today*, 15(5):171–185, 2010.

[174] William M Merritt, Yvonne G Lin, Whitney A Spannuth, Mavis S Fletcher, Aparna A Kamat, Liz Y Han, Charles N Landen, Nicholas Jennings, Koen De Geest, Robert R Langley, et al. Effect of interleukin-8 gene silencing with liposome-encapsulated small interfering rna on ovarian cancer cell growth. *J Natl Cancer Inst*, 100(5):359–372, 2008.

[175] Markku Miettinen, A Earle Lindenmayer, and Abhijeet Chaubal. Endothelial cell markers cd31, cd34, and bnh9 antibody to h-and y-antigens–evaluation of their specificity and sensitivity in the diagnosis of vascular tumors and comparison with von willebrand factor. *Mod Pathol*, 7(1):82–90, 1994.

[176] C Yu Mimi and Jian-Min Yuan. Epidemiology of nasopharyngeal carcinoma. In *Semin Cancer Biol*, volume 12, pages 421–429. Elsevier, 2002.

[177] Martina Miteva, Kellye C Kirkbride, Kameron V Kilchrist, Thomas A Werfel, Hongmei Li, Christopher E Nelson, Mukesh K Gupta, Todd D Giorgio, and Craig L Duvall. Tuning pegylation of mixed micelles to overcome intracellular and systemic sirna delivery barriers. *Biomaterials*, 38:97–107, 2015.

[178] Axel Montagne, Maxime Gauberti, Richard Macrez, Amandine Jullienne, Aurélien Briens, Jean-Sébastien Raynaud, Gaelle Louin, Alain Buisson, Benoit Haelewyn, Fabian Docagne, et al. Ultra-sensitive molecular mri of cerebrovascular cell activation enables early detection of chronic central nervous system disorders. *Neuroimage*, 63(2):760–770, 2012.

[179] Douglas E Morse, Ralph V Katz, David G Pendrys, Theodore R Holford, David J Krutchkoff, Ellen Eisenberg, Diane Kosis, and Susan T Mayne. Smoking and drinking in relation to oral epithelial dysplasia. *Cancer Epidem Biomar*, 5(10):769–777, 1996.

[180] Andrzej Myc, Jolanta Kukowska-Latallo, Peter Cao, Ben Swanson, Julianna Battista, Thomas Dunham, and James R Baker Jr. Targeting the efficacy of a dendrimer-based nanotherapeutic in heterogeneous xenograft tumors in vivo. *Anticancer Drugs*, 21(2):186, 2010.

[181] Andrzej Myc, István J Majoros, Thommey P Thomas, and James R Baker. Dendrimer-based targeted delivery of an apoptotic sensor in cancer cells. *Biomacromolecules*, 8(1):13–18, 2007.

[182] NA. Reducing treatment side effects for head and neck cancer. *Br Dent J*, 199(9):555, 2005.

[183] Raghavendra S Navath, Yunus E Kurtoglu, Bing Wang, Sujatha Kannan, Robert Romero, and Rangaramanujam M Kannan. Dendrimer- drug conjugates for tailored intracellular drug release based on glutathione levels. *Bioconjug Chem*, 19(12):2446–2455, 2008.

[184] George R Newkome, Zhongqi Yao, Gregory R Baker, and Vinod K Gupta. Micelles. part 1. cascade molecules: a new approach to micelles. a [27]-arborol. *J Org Chem*, 50(11):2003–2004, 1985.

[185] Ion Niculescu-Duvaz. Trastuzumab emtansine, an antibody-drug conjugate for the treatment of her2+ metastatic breast cancer. *Curr Opin Mol Ther*, 12(3):350–360, 2010.

[186] Saumya Nigam, Sudeshna Chandra, Donald F Newgreen, Dhirendra Bahadur, and Qizhi Chen. Poly (ethylene glycol)-modified pamam-fe3o4-doxorubicin triads with the potential for improved therapeutic efficacy: Generation-dependent increased drug loading and retention at neutral ph and increased release at acidic ph. *Langmuir*, 30(4):1004–1011, 2014.

[187] Ari Nowacek and Howard E Gendelman. Nanoart, neuroaids and cns drug delivery. *Nanomedicine*, 4(5):557–574, 2009.

[188] Natalia V Nukolova, Hardeep S Oberoi, Samuel M Cohen, Alexander V Kabanov, and Tatiana K Bronich. Folate-decorated nanogels for targeted therapy of ovarian cancer. *Biomaterials*, 32(23):5417–5426, 2011.

[189] Yusuke Oe, R James Christie, Mitsuru Naito, Stewart A Low, Shigeto Fukushima, Kazuko Toh, Yutaka Miura, Yu Matsumoto, Nobuhiro Nishiyama, Kanjiro Miyata, et al. Actively-targeted polyion complex micelles stabilized by cholesterol and disulfide cross-linking for systemic delivery of sirna to solid tumors. *Biomaterials*, 35(27):7887–7895, 2014.

[190] Nuri Oh and Ji-Ho Park. Endocytosis and exocytosis of nanoparticles in mammalian cells. *Int J Nanomedicine*, 9(Suppl 1):51, 2014.

[191] Yu-Kyoung Oh and Tae Gwan Park. sirna delivery systems for cancer treatment. *Adv Drug Deliv Rev*, 61(10):850–862, 2009.

[192] Risako Onodera, Keiichi Motoyama, Ayaka Okamatsu, Taishi Higashi, and Hidetoshi Arima. Potential use of folate-appended methyl-[bgr]-cyclodextrin as an anticancer agent. *Sci Rep*, 3, 2013.

[193] Daniel W Pack, Allan S Hoffman, Suzie Pun, and Patrick S Stayton. Design and development of polymers for gene delivery. *Nat Rev Drug Discov*, 4(7):581–593, 2005.

[194] Ajai Pal, Ateeq Ahmad, Sumsullah Khan, Isamu Sakabe, Chuanbo Zhang, Usha N Kasid, and Imran Ahmad. Systemic delivery of rafsirna using cationic cardiolipin liposomes silences raf-1 expression and inhibits tumor growth in xenograft model of human prostate cancer. *Int J Oncol*, 26(4):1087–1091, 2005.

[195] Shambhavi Pandey, Pankaj Garg, Somin Lee, Han-Wool Choung, Yun-Hoon Choung, Pill-Hoon Choung, and Jong Hoon Chung. Nucleotide biosynthesis arrest by silencing shmt1 function via vitamin b 6-coupled vector and effects on tumor growth inhibition. *Biomaterials*, 35(34):9332–9342, 2014.

[196] Aristarchos Papagiannaros, Kostas Dimas, George Th Papaioannou, and Costas Demetzos. Doxorubicin–pamam dendrimer complex attached to liposomes: cytotoxic studies against human cancer cell lines. *Int J Pharm*, 302(1):29–38, 2005.

[197] William M Pardridge. shrna and sirna delivery to the brain. *Adv Drug Deliv Rev*, 59(2):141–152, 2007.

[198] Nikki Parker, Mary Jo Turk, Elaine Westrick, Jeffrey D Lewis, Philip S Low, and Christopher P Leamon. Folate receptor expression in carcinomas and normal tissues determined by a quantitative radioligand binding assay. *Anal Biochem*, 338(2):284–293, 2005.

[199] Gianfranco Pasut, Donatella Paolino, Christian Celia, Anna Mero, Adrian Steve Joseph, Joy Wolfram, Donato Cosco, Oddone Schiavon, Haifa Shen, and Massimo Fresta. Polyethylene glycol (peg)-dendron phospholipids as innovative constructs for the preparation of super stealth liposomes for anticancer therapy. *J Control Release*, 199:106–113, 2015.

[200] Vyomesh Patel, John F Ensley, J Silvio Gutkind, and W Andrew Yeudall. Induction of apoptosis in head-and-neck squamous carcinoma cells by γ-irradiation and bleomycin is p53-independent. *Int J Cancer*, 88(5):737–743, 2000.

[201] Mahesh L Patil, Min Zhang, and Tamara Minko. Multifunctional triblock nanocarrier (pamam-peg-pll) for the efficient intracellular sirna delivery and gene silencing. *ACS Nano*, 5(3):1877–1887, 2011.

[202] Stephane Paul, David Snary, Johan Hoebeke, Deborah Allen, Jean-Marc Balloul, Nadine Bizouarne, Karine Dott, Michel Geist, Joseph Hilgers, Marie Paule Kieny, et al. Targeted macrophage cytotoxicity using a nonreplicative live vector expressing a tumor-specific single-chain variable region fragment. *Hum Gene Ther*, 11(10):1417–1428, 2000.

[203] Chrystal M Paulos, Joseph A Reddy, Christopher P Leamon, Mary Jo Turk, and Philip S Low. Ligand binding and kinetics of folate receptor recycling in vivo: impact on receptor-mediated drug delivery. *Mol Pharmacol*, 66(6):1406–1414, 2004.

[204] Chad V Pecot, George A Calin, Robert L Coleman, Gabriel Lopez-Berestein, and Anil K Sood. Rna interference in the clinic: challenges and future directions. *Nat Rev Cancer*, 11(1):59–67, 2011.

[205] Shu-Fen Peng, Chun-Jen Su, Ming-Cheng Wei, Chun-Yu Chen, Zi-Xian Liao, Po-Wei Lee, Hsin-Lung Chen, and Hsing-Wen Sung. Effects of the nanostructure of dendrimer/dna complexes on their endocytosis and gene expression. *Biomaterials*, 31(21):5660–5670, 2010.

[206] FC Perez-Martinez, AV Ocana, MD Perez-Carrion, and V Cena. Dendrimers as vectors for genetic material delivery to the nervous system. *Curr Med Chem*, 19(29):5101–5108, 2012.

[207] Omathanu P Perumal, Rajyalakshmi Inapagolla, Sujatha Kannan, and Rangaramanujam M Kannan. The effect of surface functionality on cellular trafficking of dendrimers. *Biomaterials*, 29(24):3469–3476, 2008.

[208] Fabio Petrocca and Judy Lieberman. Promise and challenge of rna interference–based therapy for cancer. *J Clin Oncol*, 29(6):747–754, 2011.

[209] Paola Posocco, Xiaoxuan Liu, Erik Laurini, Domenico Marson, Chao Chen, Cheng Liu, Maurizio Fermeglia, Palma Rocchi, Sabrina Pricl, and Ling Peng. Impact of sirna overhangs for dendrimer-mediated sirna delivery and gene silencing. *Mol Pharm*, 10(8):3262–3273, 2013.

[210] Huntington Potter and Richard Heller. Transfection by electroporation. *Curr Protoc Neurosci*, pages A–1E, 2001.

[211] Norbert Prenzel, OM Fischer, S Streit, S Hart, and A Ullrich. The epidermal growth factor receptor family as a central element for cellular signal transduction and diversification. *Endocr Relat Cancer*, 8(1):11–31, 2001.

[212] Susan Preston-Martin, Duncan C Thomas, Stuart C White, and Dierdre Cohen. Prior exposure to medical and dental x-rays related to tumors of the parotid gland1. *J Natl Cancer Inst*, 80(12):943–949, 1988.

[213] Lifeng Qi and Xiaohu Gao. Quantum dot- amphipol nanocomplex for intracellular delivery and real-time imaging of sirna. *ACS Nano*, 2(7):1403–1410, 2008.

[214] Li-Yan Qiu, Lu Yan, Lu Zhang, Yang-Min Jin, and Qing-He Zhao. Folate-modified poly (2-ethyl-2-oxazoline) as hydrophilic corona in polymeric micelles for enhanced intracellular doxorubicin delivery. *Int J Pharm*, 456(2):315–324, 2013.

[215] Quincy A Quick and David A Gewirtz. An accelerated senescence response to radiation in wild-type p53 glioblastoma multiforme cells. *J Neurosurg*, 105(1):111–118, 2006.

[216] Mohammad Aminur Rahman, ARM Ruhul Amin, Xu Wang, Jonathan E Zuckerman, Chung Hang J Choi, Bingsen Zhou, Dongsheng Wang, Sreenivas Nannapaneni, Lydia Koenig, Zhengjia Chen, et al. Systemic delivery of sirna nanoparticles targeting rrm2 suppresses head and neck tumor growth. *J Control Release*, 159(3):384–392, 2012.

[217] Donald D Rao, John S Vorhies, Neil Senzer, and John Nemunaitis. sirna vs. shrna: similarities and differences. *Adv Drug Deliv Rev*, 61(9):746–759, 2009.

[218] Josefine Reber, Harriet Struthers, Thomas Betzel, Alexander Hohn, Roger Schibli, and Cristina Muler. Radioiodinated folic acid conjugates: evaluation of a valuable concept to improve tumor-to-background contrast. *Mol Pharm*, 9(5):1213–1221, 2012.

[219] Arlette Rémy-Kristensen, Jean-Pierre Clamme, Constance Vuilleumier, Jean-Georges Kuhry, and Yves Mély. Role of endocytosis in the transfection of l929 fibroblasts by polyethylenimine/dna complexes. *Biochim Biophys Acta*, 1514(1):21–32, 2001.

[220] Jeanette C Roberts, Mahesh K Bhalgat, and Richard T Zera. Preliminary biological evaluation of polyamidoamine (pamam) starburst dendrimers. *J Biomed Mater Res*, 30(1):53–65, 1996.

[221] John F Ross, Prabir K Chaudhuri, and Manohar Ratnam. Differential regulation of folate receptor isoforms in normal and malignant tissues in vivo and in established cell lines. physiologic and clinical implications. *Cancer*, 73(9):2432–2443, 1994.

[222] S Sadekar, G Thiagarajan, K Bartlett, D Hubbard, A Ray, LD McGill, and H Ghandehari. Poly(amidoamine) dendrimers as absorption enhancers for oral delivery of camptothecin. *Int J Pharm*, 456(1):175–185, 2013.

[223] Cyrus R Safinya and Kai K Ewert. Materials chemistry: Liposomes derived from molecular vases. *Nature*, 489(7416):372–374, 2012.

[224] Gaurav Sahay, William Querbes, Christopher Alabi, Ahmed Eltoukhy, Sovan Sarkar, Christopher Zurenko, Emmanouil Karagiannis, Kevin Love, Delai Chen, Roberto Zoncu, et al. Efficiency of sirna delivery by lipid nanoparticles is limited by endocytic recycling. *Nat Biotechnol*, 31(7):653–658, 2013.

[225] MJ Santander-Ortega, IF Uchegbu, and AG Schätzlein. Dendrimer-based gene delivery systems: Administration routes and in vivo evaluation. *Dendrimer-Based Drug Delivery Systems: From Theory to Practice*, pages 329–354, 2012.

[226] A Santel, M Aleku, O Keil, J Endruschat, V Esche, B Durieux, K Löffler, M Fechtner, T Röhl, G Fisch, et al. Rna interference in the mouse vascular endothelium by systemic administration of sirna-lipoplexes for cancer therapy. *Gene Ther*, 13(18):1360–1370, 2006.

[227] Eliana Saxon and Carolyn R Bertozzi. Cell surface engineering by a modified staudinger reaction. *Science*, 287(5460):2007–2010, 2000.

[228] Andreas G Schatzlein, Bernd H Zinselmeyer, Adurrahim Elouzi, Christine Dufes, Ya Tsz A Chim, Clive J Roberts, Martyn C Davies, Avril Munro, Alexander I Gray, and Ijeoma F Uchegbu. Preferential liver gene expression with polypropylenimine dendrimers. *J Control Release*, 101(1):247–258, 2005.

[229] Caroline A Schneider, Wayne S Rasband, and Kevin W Eliceiri. Nih image to imagej: 25 years of image analysis. *Nat Methods*, 9(7):671–675, 2012.

[230] Dan Shao, Qinghui Zeng, Zheng Fan, Jing Li, Ming Zhang, Youlin Zhang, Ou Li, Li Chen, Xianggui Kong, and Hong Zhang. Monitoring hsv-tk/ganciclovir cancer suicide gene therapy using cdte/cds core/shell quantum dots. *Biomaterials*, 33(17):4336–4344, 2012.

[231] Kun Shao, Jiqin Wu, Zhongqing Chen, Shixian Huang, Jianfeng Li, Liya Ye, Jinning Lou, Liping Zhu, and Chen Jiang. A brain-vectored angiopep-2 based polymeric micelles for the treatment of intracranial fungal infection. *Biomaterials*, 33(28):6898–6907, 2012.

[232] Wei Shao, Arghya Paul, Bin Zhao, Crystal Lee, Laetitia Rodes, and Satya Prakash. Carbon nanotube lipid drug approach for targeted delivery of a chemotherapy drug in a human breast cancer xenograft animal model. *Biomaterials*, 34(38):10109–10119, 2013.

[233] Shijie Sheng, Meng Qiao, and Arthur B Pardee. Metastasis and akt activation. *J Cell Physiol*, 218(3):451–454, 2009.

[234] Jinjin Shi, Hongling Zhang, Lei Wang, Lulu Li, Honghong Wang, Zhenzhen Wang, Zhi Li, Chengqun Chen, Lin Hou, Chaofeng Zhang, et al. Pei-derivatized fullerene drug delivery using folate as a homing device targeting to tumor. *Biomaterials*, 34(1):251–261, 2013.

[235] Xiangyang Shi, Xiangdong Bi, T Rose Ganser, Seungpyo Hong, Lukasz A Myc, Ankur Desai, Mark M Banaszak Holl, and James R Baker. Hplc analysis of functionalized poly (amidoamine) dendrimers and the interaction between a folate-dendrimer conjugate and folate binding protein. *Analyst*, 131(7):842–848, 2006.

[236] Xiangyang Shi, István J Majoros, Anil K Patri, Xiangdong Bi, Mohammad T Islam, Ankur Desai, T Rose Ganser, and James R Baker Jr. Molecular heterogeneity analysis of poly (amidoamine) dendrimer-based mono-and multifunctional nanodevices by capillary electrophoresis. *Analyst*, 131(3):374–381, 2006.

[237] Masabumi Shibuya. Vascular endothelial growth factor and its receptor system: physiological functions in angiogenesis and pathological roles in various diseases. *J Biochem*, 153(1):13–19, 2013.

[238] Ugir Hossain Sk, Siva P Kambhampati, Manoj K Mishra, Wojciech G Lesniak, Fan Zhang, and Rangaramanujam M Kannan. Enhancing the efficacy of ara-c through conjugation with pamam dendrimer and linear peg: a comparative study. *Biomacromolecules*, 14(3):801–810, 2013.

[239] Ellen M Sletten and Carolyn R Bertozzi. Bioorthogonal chemistry: fishing for selectivity in a sea of functionality. *Angew Chem Int Ed Engl*, 48(38):6974–6998, 2009.

[240] Ellen M Sletten and Carolyn R Bertozzi. From mechanism to mouse: a tale of two bioorthogonal reactions. *Acc Chem Res*, 44(9):666–676, 2011.

[241] Ellen M Sletten, Hitomi Nakamura, John C Jewett, and Carolyn R Bertozzi. Difluorobenzocyclooctyne: Synthesis, reactivity, and stabilization by β-cyclodextrin. *J Am Chem Soc*, 132(33):11799–11805, 2010.

[242] Nitin D Sonawane, Francis C Szoka, and AS Verkman. Chloride accumulation and swelling in endosomes enhances dna transfer by polyamine-dna polyplexes. *J Biol Chem*, 278(45):44826–44831, 2003.

[243] Erwei Song, Pengcheng Zhu, Sang-Kyung Lee, Dipanjan Chowdhury, Steven Kussman, Derek M Dykxhoorn, Yi Feng, Deborah Palliser, David B Weiner, Premlata Shankar, et al. Antibody mediated in vivo delivery of small interfering rnas via cell-surface receptors. *Nat Biotechnol*, 23(6):709–717, 2005.

[244] Geeta Srivastava, KJ Kaur, O Hindsgaul, and MM Palcic. Enzymatic transfer of a preassembled trisaccharide antigen to cell surfaces using a fucosyltransferase. *J Biol Chem*, 267(31):22356–22361, 1992.

[245] Bart L Staker, Kathryn Hjerrild, Michael D Feese, Craig A Behnke, Alex B Burgin, and Lance Stewart. The mechanism of topoisomerase i poisoning by a camptothecin analog. *Proc Natl Acad Sci U S A*, 99(24):15387–15392, 2002.

[246] Matthias T Stephan and Darrell J Irvine. Enhancing cell therapies from the outside in: cell surface engineering using synthetic nanomaterials. *Nano Today*, 6(3):309–325, 2011.

[247] Matthias T Stephan, James J Moon, Soong Ho Um, Anna Bershteyn, and Darrell J Irvine. Therapeutic cell engineering with surface-conjugated synthetic nanoparticles. *Nat Med*, 16(9):1035–1041, 2010.

[248] Yansheng Su, Liang Yu, Na Liu, Zhangyan Guo, Guodong Wang, Jia Zheng, Ming Wei, He Wang, An-gang Yang, Weijun Qin, et al. Psma specific single chain antibody-mediated targeted knockdown of notch1 inhibits human prostate cancer cell proliferation and tumor growth. *Cancer Lett*, 338(2):282–291, 2013.

[249] Sönke Svenson and Donald A Tomalia. Dendrimers in biomedical applications–reflections on the field. *Adv Drug Deliv Rev*, 57(15):2106–2129, 2005.

[250] Toshinari Takahashi, Atsushi Harada, Nobuhiko Emi, and Kenji Kono. Preparation of efficient gene carriers using a polyamidoamine dendron-bearing lipid: improvement of serum resistance. *Bioconjug Chem*, 16(5):1160–1165, 2005.

[251] Yoshifumi Takei, Kenji Kadomatsu, Yukio Yuzawa, Seiichi Matsuo, and Takashi Muramatsu. A small interfering rna targeting vascular endothelial growth factor as cancer therapeutics. *Cancer Res*, 64(10):3365–3370, 2004.

[252] Yoshifumi Takei, Toshio Nemoto, Ping Mu, Tatsuya Fujishima, Takuji Ishimoto, Yasuhiko Hayakawa, Yukio Yuzawa, Seiichi Matsuo, Takashi Muramatsu, and Kenji Kadomatsu. In vivo silencing of a molecular target by short interfering rna electroporation: tumor vascularization correlates to delivery efficiency. *Mol Cancer Ther*, 7(1):211–221, 2008.

[253] GP Tang, JM Zeng, SJ Gao, YX Ma, L Shi, Y Li, H-P Too, and S Wang. Polyethylene glycol modified polyethylenimine for improved cns gene transfer: effects of pegylation extent. *Biomaterials*, 24(13):2351–2362, 2003.

[254] Yin Tang, Yang-Bing Li, Bo Wang, Ri-Yuan Lin, Mallory van Dongen, Danielle M Zurcher, Xiao-Yan Gu, Mark M Banaszak Holl, George Liu, and Rong Qi. Efficient in vitro sirna delivery and intramuscular gene silencing using peg-modified pamam dendrimers. *Mol Pharm*, 9(6):1812–1821, 2012.

[255] Giovanni Tarantino, Antonella Scalera, and Carmine Finelli. Liver-spleen axis: Intersection between immunity, infections and metabolism. *World J Gastroenterol*, 19(23):3534, 2013.

[256] Bart Thaci, Ilya V Ulasov, Atique U Ahmed, Sherise D Ferguson, Yu Han, and Maciej S Lesniak. Anti-angiogenic therapy increases intratumoral adenovirus distribution by inducing collagen degradation. *Gene Ther*, 20(3):318–327, 2013.

[257] Premal H Thaker, Liz Y Han, Aparna A Kamat, Jesusa M Arevalo, Rie Takahashi, Chunhua Lu, Nicholas B Jennings, Guillermo Armaiz-Pena, James A Bankson, Murali Ravoori, et al. Chronic stress promotes tumor growth and angiogenesis in a mouse model of ovarian carcinoma. *Nat Med*, 12(8):939–944, 2006.

[258] Giridhar Thiagarajan, Abhijit Ray, Alexander Malugin, and Hamidreza Ghandehari. Pamam-camptothecin conjugate inhibits proliferation and induces nuclear fragmentation in colorectal carcinoma cells. *Pharm Res*, 27(11):2307–2316, 2010.

[259] Donald A Tomalia. Birth of a new macromolecular architecture: dendrimers as quantized building blocks for nanoscale synthetic polymer chemistry. *Prog Polym Sci*, 30(3):294–324, 2005.

[260] Donald A Tomalia, H Baker, J Dewald, M Hall, G Kallos, S Martin, J Roeck, J Ryder, and P Smith. A new class of polymers: starburst-dendritic macromolecules. *Polym J*, 17(1):117–132, 1985.

[261] Donald A Tomalia, H Baker, J Dewald, M Hall, G Kallos, S Martin, J Roeck, J Ryder, and P Smith. Dendritic macromolecules: synthesis of starburst dendrimers. *Macromolecules*, 19(9):2466–2468, 1986.

[262] Donald A Tomalia, Jørn B Christensen, and Ulrik Boas. *Dendrimers, dendrons, and dendritic polymers: discovery, applications, and the future*. Cambridge University Press, 2012.

[263] Lingxia Tong, Wei Chen, Jing Wu, and Hongxia Li. Folic acid-coupled nanopaclitaxel liposome reverses drug resistance in skov3/tax ovarian cancer cells. *Anticancer Drugs*, 25(3):244–254, 2014.

[264] Anne S Tsao, Adam S Garden, Merrill S Kies, William Morrison, Lei Feng, J Jack Lee, Fadlo Khuri, Ralph Zinner, Jeffery Myers, Vassiliki Papadimitrakopoulou, et al. Phase i/ii study of docetaxel, cisplatin, and concomitant boost radiation for locally advanced squamous cell cancer of the head and neck. *J Clin Oncol*, 24(25):4163–4169, 2006.

[265] B Urban-Klein, S Werth, S Abuharbeid, F Czubayko, and A Aigner. Rnai-mediated gene-targeting through systemic application of polyethylenimine (pei)-complexed sirna in vivo. *Gene Ther*, 12(5):461–466, 2005.

[266] Koldo Urbiola, Carmen Sanmartín, Laura Blanco-Fernández, and Conchita Tros de Ilarduya. Efficient targeted gene delivery by a novel pamam/dna dendriplex coated with hyaluronic acid. *Nanomedicine*, 9(18):2787–2801, 2014.

[267] Lilian E van Vlerken, Tushar K Vyas, and Mansoor M Amiji. Poly (ethylene glycol)-modified nanocarriers for tumor-targeted and intracellular delivery. *Pharm Res*, 24(8):1405–1414, 2007.

[268] Sunil Verma, David Miles, Luca Gianni, Ian E Krop, Manfred Welslau, José Baselga, Mark Pegram, Do-Youn Oh, Véronique Diéras, Ellie Guardino, et al. Trastuzumab emtansine for her2-positive advanced breast cancer. *N Engl J Med*, 367(19):1783–1791, 2012.

[269] C Wagner. Cellular folate binding proteins; function and significance. *Annu Rev Nutr*, 2(1):229–248, 1982.

[270] Fei Wang, Yitong Wang, Hui Wang, Naimin Shao, Yuanyuan Chen, and Yiyun Cheng. Synergistic effect of amino acids modified on dendrimer surface in gene delivery. *Biomaterials*, 35(33):9187–9198, 2014.

[271] Han Wang, Linfeng Zheng, Chen Peng, Mingwu Shen, Xiangyang Shi, and Guixiang Zhang. Folic acid-modified dendrimer-entrapped gold nanoparticles as nanoprobes for targeted ct imaging of human lung adencarcinoma. *Biomaterials*, 34(2):470–480, 2013.

[272] Huixin Wang, Vyomesh Patel, Hiroshi Miyazaki, J Silvio Gutkind, and W Andrew Yeudall. Role for eps8 in squamous carcinogenesis. *Carcinogenesis*, 30(1):165–174, 2009.

[273] Huixin Wang, Muy-Teck Teh, Youngmi Ji, Vyomesh Patel, Shahrzad Firouzabadian, Anisha A Patel, J Silvio Gutkind, and W Andrew Yeudall. Eps8 upregulates foxm1 expression, enhancing cell growth and motility. *Carcinogenesis*, page bgq058, 2010.

[274] Lili Wang, Min Li, and Na Zhang. Folate-targeted docetaxel-lipid-based-nanosuspensions for active-targeted cancer therapy. *Int J Nanomedicine*, 7:3281, 2012.

[275] Mingming Wang and Yiyun Cheng. The effect of fluorination on the transfection efficacy of surface-engineered dendrimers. *Biomaterials*, 35(24):6603–6613, 2014.

[276] Mingyue Wang, Haiyang Hu, Yuqi Sun, Lipeng Qiu, Jie Zhang, Guannan Guan, Xiuli Zhao, Mingxi Qiao, Liang Cheng, Lifang Cheng, et al. A ph-sensitive gene delivery system based on folic acid-peg-chitosan–pamam-plasmid dna complexes for cancer cell targeting. *Biomaterials*, 34(38):10120–10132, 2013.

[277] Rui Wang, Xiuli Hu, Sai Wu, Haihua Xiao, Haidong Cai, Zhigang Xie, Yubin Huang, and Xiabin Jing. Biological characterization of folate-decorated biodegradable polymer–platinum (ii) complex micelles. *Mol Pharm*, 9(11):3200–3208, 2012.

[278] Xiaoting Wang, Yang Dai, Song Zhao, Jianxia Tang, Hongjun Li, Yuntian Xing, Guoli Qu, Xinsong Li, Jianrong Dai, Yinchang Zhu, et al. Pamam-lys, a novel vaccine delivery vector, enhances the protective effects of the sjc23 dna vaccine against schistosoma japonicum infection. *PloS One*, 9(1):e86578, 2014.

[279] Xu Wang, Jun Li, Yiqing Wang, Kwang Jae Cho, Gloria Kim, Ada Gjyrezi, Lydia Koenig, Paraskevi Giannakakou, Hyung Ju C Shin, Mourad Tighiouart, et al. Hft-t, a targeting nanoparticle, enhances specific delivery of paclitaxel to folate receptor-positive tumors. *ACS Nano*, 3(10):3165–3174, 2009.

[280] Xu Wang, Jun Li, Yuxiang Wang, Lydia Koenig, Ada Gjyrezi, Paraskevi Giannakakou, Edwin H Shin, Mourad Tighiouart, Zhuo Chen, Shuming Nie, et al. A folate receptor-targeting nanoparticle minimizes drug resistance in a human cancer model. *ACS Nano*, 5(8):6184–6194, 2011.

[281] Xuhua Wang, Alma R Morales, Takeo Urakami, Lifu Zhang, Mykhailo V Bondar, Masanobu Komatsu, and Kevin D Belfield. Folate receptor-targeted aggregation-enhanced near-ir emitting silica nanoprobe for one-photon in vivo and two-photon ex vivo fluorescence bioimaging. *Bioconjug Chem*, 22(7):1438–1450, 2011.

[282] Yu Wang, Lei Li, Naimin Shao, Zhiqi Hu, Hui Chen, Leqin Xu, Changping Wang, Yiyun Cheng, and Jianru Xiao. Triazine-modified dendrimer for efficient trail gene therapy in osteosarcoma. *Acta Biomater*, 2015.

[283] Yuhua Wang and Leaf Huang. A window onto sirna delivery. *Nat Biotechnol*, 31(7):611–612, 2013.

[284] Michael E Werner, Jonathan A Copp, Shrirang Karve, Natalie D Cummings, Rohit Sukumar, Chenxi Li, Mary E Napier, Ronald C Chen, Adrienne D Cox, and Andrew Z Wang. Folate-targeted polymeric nanoparticle formulation of docetaxel is an effective molecularly targeted radiosensitizer with efficacy dependent on the timing of radiotherapy. *ACS Nano*, 5(11):8990–8998, 2011.

[285] SN Wickramasinghe. Diagnosis of megaloblastic anaemias. *Blood Rev*, 20(6):299–318, 2006.

[286] Ho Lun Wong, Xiao Yu Wu, and Reina Bendayan. Nanotechnological advances for the delivery of cns therapeutics. *Adv Drug Deliv Rev*, 64(7):686–700, 2012.

[287] Wenbin Wu, Yonghui Zheng, Rui Wang, Weili Huang, Lei Liu, Xiuli Hu, Shi Liu, Jun Yue, Ti Tong, and Xiabin Jing. Antitumor activity of folate-targeted, paclitaxelloaded polymeric micelles on a human esophageal ec9706 cancer cell line. *Int J Nanomedicine*, 7:3487, 2012.

[288] Bai Xiang, Da-Wen Dong, Nian-Qiu Shi, Wei Gao, Zhen-Zhen Yang, Yi Cui, De-Ying Cao, and Xian-Rong Qi. Psa-responsive and psma-mediated multifunctional liposomes for targeted therapy of prostate cancer. *Biomaterials*, 34(28):6976–6991, 2013.

[289] Jisheng Xiao, Xiaopin Duan, Qi Yin, Zhiwen Zhang, Haijun Yu, and Yaping Li. Nanodiamonds-mediated doxorubicin nuclear delivery to inhibit lung metastasis of breast cancer. *Biomaterials*, 34(37):9648–9656, 2013.

[290] Cheng-Xiong Xu, Dhananjay Jere, Hua Jin, Seung-Hee Chang, Youn-Sun Chung, Ji-Young Shin, Ji-Eun Kim, Sung-Jin Park, Yong-Hoon Lee, Chan-Hee Chae, et al. Poly (ester amine)-mediated, aerosol-delivered akt1 small interfering rna suppresses lung tumorigenesis. *Am J Respir Crit Care Med*, 178(1):60–73, 2008.

[291] Leyuan Xu, Jin Koung Kim, Qianming Bai, Xin Zhang, Genta Kakiyama, Hae-ki Min, Arun J Sanyal, William M Pandak, and Shunlin Ren. 5-cholesten-3β, 25-diol 3-sulfate decreases lipid accumulation in diet-induced nonalcoholic fatty liver disease mouse model. *Mol Pharmacol*, 83(3):648–658, 2013.

[292] Leyuan Xu, Shanwei Shen, Yongjie Ma, Jin Koung Kim, Daniel Rodriguez-Agudo, Douglas M Heuman, Phillip B Hylemon, William M Pandak, and Shunlin Ren. 25-hydroxycholesterol-3-sulfate attenuates inflammatory response via pparγ signaling in human thp-1 macrophages. *Am J Physiol Endocrinol Metab*, 302(7):E788–E799, 2012.

[293] Leyuan Xu, Natasha Sheybani, Shunlin Ren, Gary L Bowlin, W Andrew Yeudall, and Hu Yang. Semi-interpenetrating network (sipn) co-electrospun gelatin/insulin fiber formulation for transbuccal insulin delivery. *Pharm Res*, 32(1):275–285, 2015.

[294] Leyuan Xu, Natasha Sheybani, W Andrew Yeudall, and Hu Yang. The effect of photoinitiators on intracellular akt signaling pathway in tissue engineering application. *Biomater Sci*, 3(2):250–255, 2015.

[295] Leyuan Xu and Hu Yang. Nanopreparations for central nervous system diseases.

[296] Leyuan Xu, Andrew W Yeudall, and Hu Yang. Dendrimer-based rna interference delivery for cancer therapy. *Tailored Polymer Architectures for Pharmaceutical and Biomedical Applications*, pages 197–213, 2013.

[297] Leyuan Xu, Hao Zhang, and Yue Wu. Dendrimer advances for the central nervous system delivery of therapeutics. *ACS Chem Neurosci*, 5(1):2–13, 2013.

[298] Leyuan Xu, Olga Yu Zolotarskaya, W Andrew Yeudall, and Hu Yang. Click hybridization of immune cells and polyamidoamine dendrimers. *Adv Healthc Mater*, 3(9):1430–1438, 2014.

[299] Long Xu, Jamie Betker, Hao Yin, and Thomas J Anchordoquy. Ligands located within a cholesterol domain enhance gene delivery to the target tissue. *J Control Release*, 160(1):57–63, 2012.

[300] Xiaoyang Xu, Kun Xie, Xue-Qing Zhang, Eric M Pridgen, Ga Young Park, Danica S Cui, Jinjun Shi, Jun Wu, Philip W Kantoff, Stephen J Lippard, et al. Enhancing tumor cell response to chemotherapy through nanoparticle-mediated codelivery of sirna and cisplatin prodrug. *Proc Natl Acad Sci U S A*, 110(46):18638–18643, 2013.

[301] Yuma Yamada, Mai Tabata, Yukari Yasuzaki, Masatoshi Nomura, Atsushi Shibata, Yuta Ibayashi, Yosuke Taniguchi, Shigeki Sasaki, and Hideyoshi Harashima. A nanocarrier system for the delivery of nucleic acids targeted to a pancreatic beta cell line. *Biomaterials*, 35(24):6430–6438, 2014.

[302] K Yamato, T Yamada, M Kizaki, K Ui-Tei, Y Natori, M Fujino, T Nishihara, Y Ikeda, Y Nasu, K Saigo, et al. New highly potent and specific e6 and e7 sirnas for treatment of hpv16 positive cervical cancer. *Cancer Gene Ther*, 15(3):140–153, 2008.

[303] Chengbiao Yang, Dongxia Li, Qianqi FengZhao, Lianyong Wang, Ling Wang, and Zhimou Yang. Disulfide bond reduction-triggered molecular hydrogels of folic acid–taxol conjugates. *Org Biomol Chem*, 11(40):6946–6951, 2013.

[304] Han Na Yang, Ji Sun Park, Su Yeon Jeon, Wooram Park, Kun Na, and Keun-Hong Park. The effect of quantum dot size and poly (ethylenimine) coating on the efficiency of gene delivery into human mesenchymal stem cells. *Biomaterials*, 35(29):8439–8449, 2014.

[305] Hu Yang. Nanoparticle-mediated brain-specific drug delivery, imaging, and diagnosis. *Pharm Res*, 27(9):1759–1771, 2010.

[306] Hu Yang and Weiyuan John Kao. Dendrimers for pharmaceutical and biomedical applications. *J Biomater Sci Polym Ed*, 17(1-2):3–19, 2006.

[307] Hu Yang and Weiyuan John Kao. Synthesis and characterization of nanoscale dendritic rgd clusters for potential applications in tissue engineering and drug delivery. *Int J Nanomedicine*, 2(1):89, 2007.

[308] Hu Yang and Stephanie T Lopina. In vitro enzymatic stability of dendritic peptides. *J Biomed Mater Res A*, 76(2):398–407, 2006.

[309] Hu Yang, Stephanie T Lopina, Linda P DiPersio, and Steven P Schmidt. Stealth dendrimers for drug delivery: correlation between pegylation, cytocompatibility, and drug payload. *J Mater Sci Mater Med*, 19(5):1991–1997, 2008.

[310] Hu Yang, Puneet Tyagi, Rajendra S Kadam, Christopher A Holden, and Uday B Kompella. Hybrid dendrimer hydrogel/plga nanoparticle platform sustains drug delivery for one week and antiglaucoma effects for four days following one-time topical administration. *ACS Nano*, 6(9):7595–7606, 2012.

[311] Yang Yang, YanFang Yang, XiangYang Xie, ZhiYuan Wang, Wei Gong, Hui Zhang, Ying Li, FangLin Yu, ZhiPing Li, and XingGuo Mei. Dual-modified liposomes with a two-photon-sensitive cell penetrating peptide and ngr ligand for sirna targeting delivery. *Biomaterials*, 48:84–96, 2015.

[312] Junichi Yano, Kazuko Hirabayashi, Shin-ichiro Nakagawa, Tohru Yamaguchi, Masaki Nogawa, Isao Kashimori, Haruna Naito, Hidetoshi Kitagawa, Kouichi

Ishiyama, Tadaaki Ohgi, et al. Antitumor activity of small interfering rna/cationic liposome complex in mouse models of cancer. *Clin Cancer Res*, 10(22):7721–7726, 2004.

[313] W Andrew Yeudall, Katharine H Wrighton, and Sumitra Deb. Mutant p53 in cell adhesion and motility. pages 135–146. Springer, 2013.

[314] Yu Yin, Li-Yu Cao, Wen-Qing Wu, Hao Li, Yan Jiang, and Hong-Fu Zhang. Blocking effects of sirna on vegf expression in human colorectal cancer cells. *World J Gastroenterol*, 16(9):1086, 2010.

[315] Takashi Yoshizawa, Yoshiyuki Hattori, Motoki Hakoshima, Kimiko Koga, and Yoshie Maitani. Folate-linked lipid-based nanoparticles for synthetic sirna delivery in kb tumor xenografts. *Eur J Pharm Biopharm*, 70(3):718–725, 2008.

[316] Anas Younes, Ajay K Gopal, Scott E Smith, Stephen M Ansell, Joseph D Rosenblatt, Kerry J Savage, Radhakrishnan Ramchandren, Nancy L Bartlett, Bruce D Cheson, Sven de Vos, et al. Results of a pivotal phase ii study of brentuximab vedotin for patients with relapsed or refractory hodgkin's lymphoma. *J Clin Oncol*, 30(18):2183–2189, 2012.

[317] Haijun Yu, Yonglong Zou, Yiguang Wang, Xiaonan Huang, Gang Huang, Baran D Sumer, David A Boothman, and Jinming Gao. Overcoming endosomal barrier by amphotericin b-loaded dual ph-responsive pdma-b-pdpa micelleplexes for sirna delivery. *ACS Nano*, 5(11):9246–9255, 2011.

[318] Ahu Yuan, Jinhui Wu, Xiaolei Tang, Lili Zhao, Feng Xu, and Yiqiao Hu. Application of near-infrared dyes for tumor imaging, photothermal, and photodynamic therapies. *J Pharm Sci*, 102(1):6–28, 2013.

[319] Quan Yuan, Yao Fu, Weiyuan John Kao, Damir Janigro, and Hu Yang. Transbuccal delivery of cns therapeutic nanoparticles: synthesis, characterization, and in vitro permeation studies. *ACS Chem Neurosci*, 2(11):676–683, 2011.

[320] Quan Yuan, Eunmee Lee, W Andrew Yeudall, and Hu Yang. Dendrimer-triglycine-egf nanoparticles for tumor imaging and targeted nucleic acid and drug delivery. *Oral Oncol*, 46(9):698–704, 2010.

[321] Quan Yuan, W Andrew Yeudall, and Hu Yang. Pegylated polyamidoamine dendrimers with bis-aryl hydrazone linkages for enhanced gene delivery. *Biomacromolecules*, 11(8):1940–1947, 2010.

[322] Caixia Yue, Peng Liu, Mingbin Zheng, Pengfei Zhao, Yiqing Wang, Yifan Ma, and Lintao Cai. Ir-780 dye loaded tumor targeting theranostic nanoparticles for nir imaging and photothermal therapy. *Biomaterials*, 34(28):6853–6861, 2013.

[323] Qingbing Zeng, Hanbin Wen, Qing Wen, Xiaohui Chen, Yuegang Wang, Wanlin Xuan, Jiansheng Liang, and Shanhe Wan. Cucumber mosaic virus as drug delivery vehicle for doxorubicin. *Biomaterials*, 34(19):4632–4642, 2013.

[324] San Zeng and May P Xiong. Trilayer micelles for combination delivery of rapamycin and sirna targeting y-box binding protein-1 (siyb-1). *Biomaterials*, 34(28):6882–6892, 2013.

[325] Chengyuan Zhang, Dayi Pan, Kui Luo, Wenchuan She, Chunhua Guo, Yang Yang, and Zhongwei Gu. Peptide dendrimer–doxorubicin conjugate-based nanoparticles as an enzyme-responsive drug delivery system for cancer therapy. *Adv Healthc Mater*, 3(8):1299–1308, 2014.

[326] Pengcheng Zhang, Luojuan Hu, Qi Yin, Zhiwen Zhang, Linyin Feng, and Yaping Li. Transferrin-conjugated polyphosphoester hybrid micelle loading paclitaxel for brain-targeting delivery: synthesis, preparation and in vivo evaluation. *J Control Release*, 159(3):429–434, 2012.

[327] Qin-Fang Zhang, Wen-Jing Yi, Bing Wang, Ji Zhang, Laifeng Ren, Qian-Ming Chen, Liandi Guo, and Xiao-Qi Yu. Linear polycations by ring-opening polymerization as non-viral gene delivery vectors. *Biomaterials*, 34(21):5391–5401, 2013.

[328] Xin Zhang, Qianming Bai, Genta Kakiyama, Leyuan Xu, Jin Kyung Kim, William M Pandak, and Shunlin Ren. Cholesterol metabolite, 5-cholesten-3β-25-diol-3-sulfate, promotes hepatic proliferation in mice. *J Steroid Biochem Mol Biol*, 132(3):262–270, 2012.

[329] Xin Zhang, Qianming Bai, Leyuan Xu, Genta Kakiyama, William M Pandak, Zhigang Zhang, and Shunlin Ren. Cytosolic sulfotransferase 2b1b promotes hepatocyte proliferation gene expression in vivo and in vitro. *Am J Physiol Gastrointest Liver Physiol*, 303(3):G344–G355, 2012.

[330] Yuan Zhang, Lei Peng, Russell J Mumper, and Leaf Huang. Combinational delivery of c-myc sirna and nucleoside analogs in a single, synthetic nanocarrier for targeted cancer therapy. *Biomaterials*, 34(33):8459–8468, 2013.

[331] Yuehua Zhang, Thommey P Thomas, Ankur Desai, Hong Zong, Pascale R Leroueil, Istvan J Majoros, and James R Baker Jr. Targeted dendrimeric anticancer prodrug: a methotrexate-folic acid-poly (amidoamine) conjugate and a novel, rapid,one pot synthetic approach. *Bioconjug Chem*, 21(3):489–495, 2010.

[332] Yulong Zhang, Omar Velasco, Xinli Zhang, Kang Ting, Chia Soo, and Benjamin M Wu. Bioactivity and circulation time of pegylated nell-1 in mice and the potential for osteoporosis therapy. *Biomaterials*, 35(24):6614–6621, 2014.

[333] Zhuohan Zhang, Xiaoying Yang, Yuan Zhang, Bin Zeng, Shujing Wang, Tianhui Zhu, Richard BS Roden, Yongsheng Chen, and Rongcun Yang. Delivery of telomerase reverse transcriptase small interfering rna in complex with positively charged single-walled carbon nanotubes suppresses tumor growth. *Clin Cancer Res*, 12(16):4933–4939, 2006.

[334] Peiqi Zhao, Hanjie Wang, Man Yu, Shuzhen Cao, Fei Zhang, Jin Chang, and Ruifang Niu. Paclitaxel-loaded, folic-acid-targeted and tat-peptide-conjugated polymeric liposomes: in vitro and in vivo evaluation. *Pharm Res*, 27(9):1914–1926, 2010.

[335] Rongbao Zhao, Larry H Matherly, and I David Goldman. Membrane transporters and folate homeostasis: intestinal absorption and transport into systemic compartments and tissues. *Expert Rev Mol Med*, 11:e4, 2009.

[336] H Zhu, Z Li, S Mao, B Ma, S Zhou, L Deng, T Liu, D Cui, Y Zhao, J He, et al. Antitumor effect of sflt-1 gene therapy system mediated by bifidobacterium infantis on lewis lung cancer in mice. *Cancer Gene Ther*, 18(12):884–896, 2011.

[337] Saijie Zhu, Minghuang Hong, Lihong Zhang, Guotao Tang, Yanyan Jiang, and Yuanying Pei. Pegylated pamam dendrimer-doxorubicin conjugates: in vitro evaluation and in vivo tumor accumulation. *Pharm Res*, 27(1):161–174, 2010.

[338] Olga Yu Zolotarskaya, Alison F Wagner, Jason M Beckta, Kristoffer Valerie, Kenneth J Wynne, and Hu Yang. Synthesis of water-soluble camptothecin–polyoxetane conjugates via click chemistry. *Mol Pharm*, 9(11):3403–3408, 2012.

[339] Hong Zong, Thommey P Thomas, Kyung-Hoon Lee, Ankur M Desai, Ming-hsin Li, Alina Kotlyar, Yuehua Zhang, Pascale R Leroueil, Jeremy J Gam, Mark M Banaszak Holl, et al. Bifunctional pamam dendrimer conjugates of folic acid and methotrexate with defined ratio. *Biomacromolecules*, 13(4):982–991, 2012.

Vita

Leyuan Xu was born in Shanghai, China, on September 22, 1984 and did most of his schooling in Shanghai. He attended Shanghai Normal University and earned a Bachelor of Science degree in Biotechnology in 2007. Upon the completion of his Bachelors degree, he moved to the United States to work as a research assistant in Hunter Holmes McGuire VA Medical Center affiliated to Virginia Commonwealth University for three and half years. In August 2011, he joined Dr. Hu Yang's laboratory to pursue his doctoral degree in Biomedical Engineering at Virginia Commonwealth University. During the course of his doctoral studies, he earned his Master of Science degree in Biomedical Engineering in 2013, and he was awarded the Alex M. Clark award for excellence in Biomedical Engineering in 2014 and the outstanding graduate research award by the School of Engineering for the academic year 2013-2014. Leyuan defended his doctoral degree on April 29, 2015 to earn his Doctor of Philosophy degree in Biomedical Engineering.